SEISMIC WAVE SCATTERING FROM ROUGH INTERFACES

by

Michael D. Prange

B.S., University of California (1982)

Submitted to the Department of Earth, Atmospheric, and Planetary Sciences
in partial fulfillment of the requirements for the degree of

Doctor of Philosophy

at the

MASSACHUSETTS INSTITUTE OF TECHNOLOGY

September 1, 1989

Signature of Author .....
Department of Earth, Atmospheric, and Planetary Sciences
September 1, 1989

Certified by .....
M. Nafi Toksöz
Professor of Geophysics
Thesis Supervisor

Accepted by .....
Thomas H. Jordan
Chairman
Department of Earth, Atmospheric, and Planetary Sciences

SEISMIC WAVE SCATTERING FROM ROUGH INTERFACES

by

Michael D. Prange

Submitted to the Department of Earth, Atmospheric, and Planetary Sciences
on September 1, 1989, in partial fulfillment of the
requirements for the degree of
Doctor of Philosophy

ABSTRACT

In this thesis I present a perturbation method which can model three-dimensional scattering from an arbitrary elastic-elastic rough interface with great computational efficiency. Using this method, I examine the changes introduced into the scattered wavefield by the presence of interface roughness. The matrix method used is appropriate for direct implementation in existing propagator matrix-based seismogram synthesis programs. It is derived using a perturbation approach which requires interface height perturbations to be small relative to the wavelengths of scattered waves, and interface slope perturbations to be much less than unity. These conditions are numerically investigated by comparison of frequency-wavenumber domain and time domain perturbation results with those generated by a second-order finite difference method for several rough interface models with Gaussian autocorrelation functions. Error is acceptable for RMS height deviations of less than about 20 percent and RMS slopes of less than about 0.25. A three-dimensional scattering kernel is introduced which represents the scattered field response to a delta function interface height function. This must be convolved with an interface height function in order to produce a scattering coefficient, but by itself illustrates the general scattering behavior of an interface contrast and source configuration independent of any particular interface roughness function. These scattering kernels show that waves are maximally scattered in directions for which the scattered wave particle motion coincides with that of the incident wave. Scattering kernels also show that the critical angles in rough interface scattering, *i.e.*, those angles at which amplitude maxima or minima appear, correspond to the critical angles of the mean planar interface problem with one qualification: since the spectrum of the interface height function modulates the scattering kernel, an interface whose spectrum does not contain energy at the critical angles will not have these maxima or minima in its scattering coefficient. By assuming material contrasts across the interface are small, further approximations can be made, yielding simple equations for the scattering coefficients which separate the influence of contrasts in P and S velocities

and density on the scattered wavefield. From these forms it is seen that the scattered field wavelet is the time derivative of the source field wavelet. Scattering coefficients and seismograms for normally incident waves illustrate the relative contributions of the separate material contrasts on the scattered wavefield. Scattering coefficients for obliquely incident waves show that the scattered wave amplitudes, excluding the background specular field, are not necessarily maximum in the direction of specular scattering. Finally, I present seismic data from a vertical seismic profile experiment which contains evidence of rough interface scattering. By generating scattering coefficients and seismograms for several rough interface models, I explore the particular scattering mechanism at work at this site.

Thesis Supervisor: M. Nafi Toksöz
Title: Professor of Geophysics

Contents

ACKNOWLEDGMENTS

I gratefully acknowledge the friendship, help, and guidance I have received that made my stay at M.I.T. an enjoyable experience. My advisor, Nafi Toksöz, was a wellspring of new ideas and approaches, and provided me with a well-equipped environment in which to work. The staff and visiting scientists at E.R.L. have always been an invaluable resource for me. Vernon Cormier, Arthur Cheng, Michel Bouchon, and Anas Abo Zena gave me a good start during my early work with stratified media formulations, and Batakrishna Mandal worked with me on optimizing these formulations. Roger Turpening and Carol Caravana are a continuing source of unbelievably high quality seismic data, and have been ever helpful in long discussions concerning these data. Special thanks to the support staff: Stephen Gildea and Jane Maloof for keeping the computers running, and Sara Brydges, Liz Henderson, Sue Turbak, Naida Buckingham, and Kelly Worrall for keeping the office right-side-up.

As we all learn in the course of our studies, a student learns most from his interactions with fellow students. I have spent untold hours discussing the finer points of finite difference, finite element, discrete wavenumber, etc. problems with Mike Mellen, Jim Mendelson, Bob Nowack, Ken Tubman, Rob Stewart, Fico Pardo-Casas, Dominique Dubucq, Christophe Gonguet, Eric Shortt, Carl Godkin, Wafik Beydoun, Ted Charrette, Bob Cicerone, Stephen Gildea, Henri Michel, Jeff Meredith, Karl Ellefsen, Arcangelo Sena, Alain Clo, and many others. Thank you. Ru Shan Wu, in particular, has taught me that to be good in research one mustn't be afraid to explore messy theoretical approaches in order to find a good solution.

My parents have encouraged and supported me throughout my schooling. From my brother Gary I learned to make education a way of life, and from my sister Cheryl I learned to make life a way of life. I also acknowledge the support of a special group of friends whom I grew up with back in California: Joseph and Cathy Baker, Kevin Kuwata, Michael Loeffler, and Alex and Harry Van. They are always there when I need them. I thank William Samaras, my high school biology teacher, for these words of advice, "Pay attention to the details and the big things will take care of themselves".

I gratefully acknowledge fellowship support from Chevron, Amoco, and Sohio. This work was further supported by the M.I.T Vertical Seismic Profiling and Reservior Delineation Consortium and the Air Force Office of Scientific Research. I thank Thinking Machines Corporation for providing me unlimited access to their Connection Machine, a massively parallel computer.

Finally, a special thanks to my wife Anne, who provided me the emotional support that I needed, and proved to be a good and usually willing editor as well. As a geophysicist herself, she also provided helpful criticism.

Chapter 1

GENERAL INTRODUCTION

A fundamental component of forward modeling and inversion procedures in elastic wave propagation problems is the ability to model scattering from sharp contrasts in the elastic properties of the propagation medium. Although scattering from smooth interfaces is easily modeled and well understood, the roughness inherent in many natural interfaces introduces a nonspecular, incoherent component to the scattered field which is poorly understood. Most current methods for computing the scattered field are limited to small, two-dimensional models by computational constraints, or apply only to oversimplified versions of the real interface. In this thesis I present a perturbation method which can model three-dimensional scattering from an arbitrary elastic-elastic rough interface with great computational efficiency. Furthermore, this method allows realistic interface shapes, and is limited only by the RMS height and slope of the interface height function. A three-dimensional scattering kernel is introduced which represents the scattered field response to a delta function interface height function. This must be convolved with an interface height function in order to produce a scattering coefficient, but by itself illustrates the general scattering behavior of an interface contrast and source configuration independent of any particular interface roughness function. Using these methods, I am able to examine the changes introduced into the scattered wavefield by the presence of interface roughness

Scattering is typically formulated in terms of reflection and transmission coefficients which relate the amplitude and phase of an incident wave in medium one to the amplitudes and phases of the waves scattered into media one and two, respectively. Exact analytical solutions for these coefficients are available in the literature (Pao and Mow, 1973) for interface shapes which are coordinate surfaces of coordinate systems in which the wave equation is separable, *e.g.,* planar, cylindrical, and spherical interfaces. In all, there are eleven coordinate systems in which the wave equation is separable (Ben-Menahem and Singh, 1981). In reality, natural processes do not create interfaces which can be exactly described by these simple surfaces. Numerical methods, such as the finite difference (Levander and Hill, 1985; Virieux, 1986; Bayliss et al., 1986) and boundary element (DeSanto, 1985; Campillo and Bouchon, 1985; Paul and Campillo, 1988) methods, are available which can cope with arbitrarily shaped interfaces. In addition to their flexibility in handling interfaces, such numerical methods provide complete scattered field solutions, including all diffracted, multiply scattered, and evanescent waves. The applicability of these methods is limited, however, by the large computational memory and time requirements which limit their usefulness to two-dimensional elastic wave scattering problems. Furthermore, since the numerical solutions are not expressed in terms of closed form analytical expressions, they cannot be directly decomposed and analyzed for the sensitivity of the solution to model parameter variations.

An alternative to the exact methods are the formulations which describe elastic wave scattering from bosses on a plane. The first of these methods describes elastic wave scattering from rigid or free bosses on a planar interface (Twersky, 1957; Lucas and Twersky, 1984). In this development, the bosses have shapes which are coordinate surfaces of coordinate systems in which the wave equation is separable. Exact analytical solutions for scattering from a single boss are combined to model multiple scattering, and an image field on the other side of the interface is used to match the boundary conditions at the interface. This approach, which is capable of providing an exact solution and has been successfully tested against experimental data (Chu and Stanton, 1989), allows the contri-

butions of successively higher orders of multiple scattering to be studied separately. The drawbacks are that natural interfaces can only be approximated by such simply shaped bosses on a planar surface, and that the method requires the interface to be rigid or free. An extension of this approach, based on work by Biot (1968), allows the scattering bosses to be elastic (Menke, 1982). This is done by approximating the scattering from each boss by a single source term. This extension, however, only describes the low-frequency component of the scattered field.

Many times, an interface can be described as the sum of one of the separable coordinate surfaces and a small perturbation surface. In this case, an analytical solution for the reflection and transmission coefficients can be developed which expresses the three-dimensional scattered wave field as the sum of a background field solution for the separable coordinate surface and a scattered field solution which accounts for the perturbations in this surface needed to describe the interface. Such solutions place restrictions on the magnitude and shape of the interface perturbations necessary to obtain an accurate solution, but for problems for which they are appropriate, a fully three-dimensional solution is obtained as a simple, closed form expression which can be efficiently evaluated, and which is convenient for analytical analysis of the properties of the scattered wave field. Perturbation approaches are frequently used to evaluate rough interface scattering in ocean acoustics problems. A two-dimensional formulation based on the T-matrix method (Dacol and Berman, 1988) and one based on the approach of Kennett (1972) (Kuperman and Schmidt, 1989) have been used to compare the scattered field response of a fluid-elastic rough interface with that of a fluid-rigid rough interface. The fluid-rigid approximation is commonly used to simplify modeling in ocean acoustics problems, but fluid-elastic models are more realistic. Comparison of the two ocean floor models showed that there is a greater loss of energy in the fluid-elastic model due to transmission into the elastic medium, and that the presence of the elastic medium introduces critical angles at which there are sharp maxima and minima in the scattering coefficients.

The perturbation approach is the most promising way to compute three-dimensional

seismic wave scattering from rough interfaces given realistic constraints on computer resources. Kennett (1972) applied a perturbation approach to the analysis of surface wave scattering from two-dimensionally rough interfaces. Our approach was to extend the perturbation approach of Kennett (1972) to handle three-dimensional body wave scattering (Prange and Toksöz, 1989). It differs from that of Kuperman and Schmidt (1989) in that we evaluate a deterministic scattered field and they work with the coherent component of a stochastic scattered wave field. A single-scattering approximation is used to replace the rough interface contribution to the scattered wavefield by a planar distribution of sources at the mean depth of the rough interface. This source is in the form of a discontinuity in the displacement-stress vector at the source depth, and as such is suitable for direct insertion into an exact solution algorithm for propagation of elastic waves through a vertically stratified medium (Kennett, 1983). Integration of the perturbation methods into stratified media formulations has been demonstrated for two-dimensional models by Kuperman and Schmidt (1989).

In this thesis we study the scattering from interfaces consisting of small perturbations about a planar surface bounding two elastic half-spaces. In chapter 2 a perturbation formulation is developed to model three-dimensional scattering from such interfaces. The method is formulated in terms of simple matrix operators. The range of interface parameters for which the perturbation method is valid is determined by comparison of seismograms and scattering coefficients with those generated by a highly accurate finite difference formulation. The models used in this comparison have Gaussian autocorrelation functions. The concept of a scattering kernel is introduced as a convenient way to separate influences on the scattered field into two parts: the effects of the interface roughness function and those of the material contrast and the source parameters. Scattering kernels and scattering coefficients are then used to discuss the properties of converted waves in the three-dimensional scattering.

In chapter 3 the perturbation method is used to examine the effect of P and S velocity and density contrasts on the scattered wavefield. In order to separate the effects of these

three material contrasts, a small material contrast approximation is made which reduces the three-dimensional scattered field equations to simple linear forms which decouple the influences of the three contrasts. From these simple expressions, we discuss the three-dimensional behavior of the scattered wavefield relative to changes in interface properties. We then present and discuss the influence of obliquely incident P and SV waves on scattered P, SV, and SH waves.

In chapter 4 we present seismic data from a vertical seismic profile[1] which contains evidence of rough interface scattering. Our perturbation formulation is applied to generate scattering coefficients and seismograms for several rough interface models for this data set in a effort to explore the particular scattering mechanism at work at this site.

Discussion and conclusions are contained in chapter 5.

References

Bayliss, A., K. Jordan, J. LeMesurier, and E. Turkel, 1986, A fourth-order accurate finite-difference scheme for the computation of elastic waves, *Bull. Seism. Soc. Am., 76,* 1115–1132.

Ben-Menahem, A. and S. Singh, 1981, *Seismic Waves and Sources,* Springer-Verlag, New York, 1108 pp.

Biot, M.A., 1968, Generalized boundary condition for multiple scatter in acoustic reflection, *J. Acoust. Soc. Am.,*, 44, 1616–1622.

Campillo, M. and M. Bouchon, 1985, Synthetic SH seismograms in a laterally varying medium by the discrete wavenumber method, *Geophys J. R. Astr. Soc.,* 83, 307–317.

Chu, D., and T. K. Stanton, 1989, Application of Twersky's boss scattering theory to laboratory measurements of sound scattered by a rough surface, submitted to *J. Acoust. Soc. Am.*

[1]A vertical seismic profile (VSP) is a seismic experiment in which a source is located at or near the surface of the earth and receivers are located in a borehole. For an indepth discussion of the VSP geometry and the associated interpretational techniques, see Gal'perin (1974) or Balsh *et al.,* (1982).

Dacol, D. K., and D. H. Berman, 1988, Sound scattering from a randomly rough fluid-solid interface, *J. Acoust. Soc. Am.*, 84, 292–302.

DeSanto, J., 1985, Exact spectral formalism from rough-surface scattering, *J. Opt. Soc. Am.*, 12, 2202-2207.

Kennett, B.L.N., 1972, Seismic wave scattering by obstacles on interfaces, *Geophys. J. R. astr. Soc., 28,* 249–266.

Kennett, B.L.N., 1983, *Seismic Wave Propagation in Stratified Media,* Cambridge University Press, New York, 339.

Kuperman, W., and H. Schmidt, 1989, Self-consistent perturbation approach to rough surface scattering in stratified elastic media, submitted to *J. Acoust. Soc. Am.*

Levander, A.R., and N.R. Hill, 1985, P-SV resonances in irregular low-velocity surface layers, *Bull. Seism. Soc. Am., 75,* 847–864.

Lucas, R.J., and V. Twersky, 1984, Coherent response to a point source irradiating a rough plane, *J. Acoust. Soc. Am.*, 76, 1847–1863.

Menke, W., 1982, On extending Biot's theory of multiple scattering at low frequencies from acoustic to elastic media, *Geophys. J. R. astr. Soc.*, 69, 819–830.

Pao, Y., and C. Mow, 1973, *Diffraction of Elastic Waves and Dynamic Stress Concentrations,* Crane, Russak, and Company Inc., New York, 694 pp.

Paul, A. and M. Campillo, 1988, Diffraction and conversion of elastic waves at a corrugated interface, *Geophysics,* 53, 1415–1424.

Prange, M., and M. N. Toksöz, 1989, Perturbation approximation of 3-D seismic scattering, submitted to *Geophysical Journal.*

Twersky, V., 1957, On scattering and reflection of sound by rough surfaces, *J. Acoust. Soc. Am.*, 29, 209–225.

Virieux, J., 1986, P-SV wave propagation in heterogeneous media: velocity-stress finite-difference method, *Geophysics, 51,* 889–901.

Chapter 2

PERTURBATION APPROXIMATION OF 3-D SEISMIC SCATTERING

2.1 ABSTRACT

A method is presented for computing three-dimensional seismic wave scattering from a rough interface. The matrix method used is appropriate for direct implementation in existing propagator matrix-based seismogram synthesis programs. It is derived using a perturbation approach which requires interface height perturbations to be small relative to the wavelengths of scattered waves, and interface slope perturbations to be much less than unity. These validity conditions are based on an order-of-error analysis of the truncation of the perturbation series. These conditions are numerically investigated by comparison of frequency-wavenumber domain and time domain perturbation results with those generated by a second-order finite difference method for several rough interface models with Gaussian autocorrelation functions. In the ω-k domain comparisons, the perturbation method is accurate for RMS interface height deviations of less than about 10 percent of the smallest wavelength in the scattered field. This result is

independent of RMS interface slope in the tested range of 0.037 to 0.99. Comparisons of seismograms generated by the two methods show that error does increase with increasing RMS slope, but at half the rate of error growth with increasing height. Time domain error is acceptable for RMS height deviations of less than about 20 percent and RMS slopes of less than about 0.25. A three-dimensional scattering kernel is defined which facilitates analysis of two- and three-dimensional scattered field results.

2.2 INTRODUCTION

The presence of a rough interface can strongly affect seismic waves reflected from and transmitted through that interface, even when the scale of roughness is much less than a wavelength. These effects include changes in the amplitude, scattering angle, frequency content, and wave-type conversion of the scattered wave. Available exact solutions take the form of integral equations (DeSanto and Brown, 1986) or finite difference/finite element formulations (Levander and Hill, 1985) that are prohibitively expensive to solve in three dimensions. In this paper, I present a perturbation approach to the solution of the three-dimensional elastic wave equation which satisfies welded boundary conditions at a rough interface. This solution is an extension of two-dimensional surface wave scattering formulations (Kennett, 1972; Gilbert and Knopoff, 1960). The method requires the height and slope of interface irregularities to be small with respect to the wavelengths of the elastic waves present. The accuracy of the perturbation method is then explored for two-dimensional models by comparing solutions for a series of rough interface models with those generated by a second-order finite difference method. The scattering results are first compared in the frequency-wavenumber domain in the form of scattering coefficients. The scattered wave fields computed with the perturbation and finite difference methods are separated into up- and down-going P and SV waves, and these scattering coefficients are individually compared. Comparisons are also made in the time-space domain using seismograms. Finally, we discuss the features of the three-dimensional scattered field.

2.3 THREE-DIMENSIONAL SCATTERING FORMULATION

A fine-scale blow-up of a three-dimensional rough interface is shown in Figure 2-1. The irregular interface is described by $z = h(x,y)$, and has a downward normal $\underline{n}(x,y)$. It separates an upper medium, described by compressional and shear wave velocities α_1 and β_1 and density ρ_1, from a lower medium, described by α_2, β_2, and ρ_2. The essence of the formulation is to project displacements and stresses on the two sides of the rough interface onto a planar surface whose depth equals the mean depth of the rough interface. These projected fields are then expanded in a perturbation series in h about a background field consisting of the known planar interface solution. This procedure results in a formulation in which the rough interface scattering problem is replaced by a planar interface scattering problem with sources along the planar interface generating the rough interface component of the scattered field.

The general form of the elastic wave equation which is valid for small displacements in the absence of body forces is

$$-\rho\omega^2 u_i = \tau_{ji,j}, \qquad i,j \in \{x,y,z\}, \tag{2.1}$$

where u_i is the ith component of the displacement vector, τ_{ji} is the i,j component of the Cauchy stress tensor, the comma denotes differentiation of τ_{ji} in the j-th coordinate direction, ω is the temporal frequency, and the Einstein summation convention applies. Throughout this paper, the Fourier transform in x, y, and t uses an implied phase factor of $\exp(ik_x x + ik_y y - i\omega t)$. For an isotropic solid, stresses are related to displacements by the constitutive relation

$$\tau_{ij} = \lambda u_{k,k}\delta_{ij} + \mu(u_{i,j} + u_{j,i}), \tag{2.2}$$

where δ_{ij} is the Kroniker symbol, and λ and μ are the Lamé parameters. Equations (2.1) and (2.2) can be expressed as a 6×6 matrix wave equation in the form

$$\frac{d\underline{r}}{dz} = \underline{\underline{A}}\,\underline{r}, \tag{2.3}$$

where $\underline{r}$ is the displacement-stress vector defined by $\underline{r} = [u_x,\ u_y,\ u_z,\ \tau_{xz},\ \tau_{yz},\ \tau_{zz}]^T$ and $\underline{\underline{A}}$ is defined by

$$\underline{\underline{A}} = \begin{bmatrix} 0 & 0 & -\partial_x & \frac{1}{\mu} & 0 & 0 \\ 0 & 0 & -\partial_y & 0 & \frac{1}{\mu} & 0 \\ \frac{-\lambda}{\lambda+2\mu}\partial_x & \frac{-\lambda}{\lambda+2\mu}\partial_y & 0 & 0 & 0 & \frac{1}{\lambda+2\mu} \\ -\rho\omega^2 - \zeta\partial_{xx} - \mu\partial_{yy} & -\mu(1+\frac{2\lambda}{\lambda+2\mu})\partial_{xy} & 0 & 0 & 0 & \frac{-\lambda}{\lambda+2\mu}\partial_x \\ -\mu(1+\frac{2\lambda}{\lambda+2\mu})\partial_{xy} & -\rho\omega^2 - \mu\partial_{xx} - \zeta\partial_{yy} & 0 & 0 & 0 & \frac{-\lambda}{\lambda+2\mu}\partial_y \\ 0 & 0 & -\rho\omega^2 & -\partial_x & -\partial_y & 0 \end{bmatrix} \tag{2.4}$$

with $\zeta = 4\mu(\lambda+\mu)/(\lambda+2\mu)$.

Welded boundary conditions at the rough interface require continuity of displacement and traction at each point on the interface. These tractions are measured with respect to the local tangent plane at each point on the interface, and are given by $T_j = \sigma_{jk}n_k$, where the downward unit normal n_k is defined by

$$\begin{bmatrix} n_x \\ n_y \\ n_z \end{bmatrix} = \frac{1}{\sqrt{1+h_{,x}^2+h_{,y}^2}} \begin{bmatrix} -h_{,x} \\ -h_{,y} \\ 1 \end{bmatrix} \tag{2.5}$$

A new displacement-stress vector $\underline{\hat{r}}$ is defined using these tangent plane tractions so that $\underline{\hat{r}}$ is continuous at the rough interface. $\underline{\hat{r}}$ is defined as

$$\begin{bmatrix} u_x \\ u_y \\ u_z \\ T_x\sqrt{1+h_{,x}^2+h_{,y}^2} \\ T_y\sqrt{1+h_{,x}^2+h_{,y}^2} \\ T_z\sqrt{1+h_{,x}^2+h_{,y}^2} \end{bmatrix} = \begin{bmatrix} 1 & 0 & 0 & 0 & 0 & 0 \\ 0 & 1 & 0 & 0 & 0 & 0 \\ 0 & 0 & 1 & 0 & 0 & 0 \\ -h_{,x}\zeta\partial_x & -h_{,x}\frac{2\lambda\mu}{\lambda+2\mu}\partial_y & 0 & 1 & 0 & h_{,x}\frac{-\lambda}{\lambda+2\mu} \\ -h_{,y}\mu\partial_y & -h_{,y}\mu\partial_x & & & & \\ -h_{,x}\mu\partial_y & -h_{,x}\mu\partial_x & 0 & 0 & 1 & h_{,y}\frac{-\lambda}{\lambda+2\mu} \\ -h_{,y}\frac{2\lambda\mu}{\lambda+2\mu}\partial_x & -h_{,y}\zeta\partial_y & & & & \\ 0 & 0 & 0 & -h_{,x} & -h_{,y} & 1 \end{bmatrix} \begin{bmatrix} u_x \\ u_y \\ u_z \\ \tau_{xz} \\ \tau_{yz} \\ \tau_{zz} \end{bmatrix} \tag{2.6}$$

Writing (2.6) in a form which explicitly expresses the h dependence, this transformation takes the form

$$\underline{\hat{r}}(x,y;h) = (\underline{\underline{I}} + h_{,x}\underline{\underline{Q}}_x + h_{,y}\underline{\underline{Q}}_y)\underline{r}(x,y;h) \tag{2.7}$$

where $\underline{\hat{r}}$ and $\underline{r}$ are evaluated along the rough interface, $\underline{\underline{I}}$ is the identity matrix, and $\underline{\underline{Q}}_x$ and $\underline{\underline{Q}}_y$ are

$$\underline{\underline{Q}}_x = \begin{bmatrix} 0 & 0 & 0 & 0 & 0 & 0 \\ 0 & 0 & 0 & 0 & 0 & 0 \\ 0 & 0 & 0 & 0 & 0 & 0 \\ -\zeta\partial_x & \frac{-2\lambda\mu}{\lambda+2\mu}\partial_y & 0 & 0 & 0 & \frac{-\lambda}{\lambda+2\mu} \\ -\mu\partial_y & -\mu\partial_x & 0 & 0 & 0 & 0 \\ 0 & 0 & 0 & -1 & 0 & 0 \end{bmatrix} \tag{2.8}$$

and

$$\underline{\underline{Q}}_y = \begin{bmatrix} 0 & 0 & 0 & 0 & 0 & 0 \\ 0 & 0 & 0 & 0 & 0 & 0 \\ 0 & 0 & 0 & 0 & 0 & 0 \\ -\mu\partial_y & -\mu\partial_x & 0 & 0 & 0 & 0 \\ -\frac{2\lambda\mu}{\lambda+2\mu}\partial_x & -\zeta\partial_y & 0 & 0 & 0 & \frac{-\lambda}{\lambda+2\mu} \\ 0 & 0 & 0 & 0 & -1 & 0 \end{bmatrix} \tag{2.9}$$

The rough interface boundary conditions may then be expressed in the form

$$\hat{\underline{r}}^{(1)}(x, y; h) = \hat{\underline{r}}^{(2)}(x, y; h) \tag{2.10}$$

where superscripts indicate the respective media.

In order to relate the scattered field (the rough interface solution) to the background field (the mean planar interface solution), the scattered field at the mean planar interface $\underline{r}(0)$ is extrapolated to the rough interface by the power series expansion

$$\underline{r}(h) = \underline{r}(0) + h\underline{r}_{,z}(0) + \frac{h^2}{2!}\underline{r}_{,zz}(0) + \ldots \tag{2.11}$$

Making use of the wave equation (2.3), (2.11) is reduced to the form

$$\underline{r}(h) = (\underline{\underline{I}} + h\underline{\underline{A}} + \frac{h^2}{2!}\underline{\underline{A}}^2 + \ldots)\underline{r}(0)\,. \tag{2.12}$$

So far the formulation is exact as long as the series in (2.12) converges. It is easy to demonstrate convergence for the case of a planar interface. In this case h is constant and (2.12) can be easily Fourier transformed to the (k_x,k_y) domain to form the power series expansion of the exponential function, converging to

$$\underline{r}(k_x, k_y; h) = e^{h\underline{\underline{A}}}\underline{r}(k_x, k_y; 0)\,. \tag{2.13}$$

This is the standard form for the propagator matrix (Aki and Richards, 1980, p. 275), which is an exact extrapolation operator which forms the basis of the propagator matrix method for formulating wave equation solutions in plane layered media (Kennett, 1983).

After the displacement-stress vectors along the rough interface have been extrapolated to the mean planar interface, they are expanded in a perturbation series about $\underline{r}_0(0)$, the displacement-stress vector at the interface of the background planar interface model:

$$\underline{r}^{(j)}(0) = \underline{r}_0(0) + h\underline{r}_1^{(j)}(0) + h^2\underline{r}_2^{(j)}(0) + \ldots/;, \tag{2.14}$$

where superscripts indicate the respective media and subscripts indicate the approximation order of the field. Since $\underline{r}_0(0)$ is the displacement-stress vector for the background planar interface model, it is continuous across the planar interface and needs no superscript. The higher order terms reflect the influence of the rough interface. Combining (2.7), (2.12), and (2.14), each side of the boundary condition expressed in (2.10) can be written as (omitting the superscripts)

$$\hat{\underline{r}}(h) = (\underline{\underline{I}} + h_{,x}\underline{\underline{Q}}_x + h_{,y}\underline{\underline{Q}}_y) \tag{2.15}$$
$$\cdot\ (\underline{\underline{I}} + h\underline{\underline{A}} + \frac{h^2}{2!}\underline{\underline{A}}^2 + \ldots)$$
$$\cdot\ (\underline{r}_0 + h\underline{r}_1 + h^2\underline{r}_2 + \ldots)$$
$$\approx (\underline{\underline{I}} + h_{,x}\underline{\underline{Q}}_x + h_{,y}\underline{\underline{Q}}_y)\underline{r}_0 + h\underline{\underline{A}}\,\underline{r}_0 + h\underline{r}_1 \tag{2.16}$$
$$+\ O(h^2) + O(hh_{,x}) + O(hh_{,y})$$

where $O(\cdot)$ denotes order of accuracy.

Applying the boundary condition (2.10) to (2.16) results in

$$h(\underline{r}_1^{(2)} - \underline{r}_1^{(1)}) \approx h(\underline{\underline{A}}^{(1)} - \underline{\underline{A}}^{(2)})\underline{r}_0 + h_{,x}(\underline{\underline{Q}}_x^{(1)} - \underline{\underline{Q}}_x^{(2)})\underline{r}_0 \tag{2.17}$$
$$+\ h_{,y}(\underline{\underline{Q}}_y^{(1)} - \underline{\underline{Q}}_y^{(2)})\underline{r}_0\,,$$

which is accurate to second-order in h and its derivatives. The right-hand side of (2.17) is clearly zero in a planar interface model. The presence of interface roughness results in discontinuities in the displacement-stress vector. Such discontinuities represent sources (Aki and Richards, 1980, p. 38). Thus, to first order in h, the effects of a rough interface can be duplicated by adding sources along the mean planar interface. These sources will be designated by $\underline{s} = h(\underline{r}_1^{(2)} - \underline{r}_1^{(1)})$. This use of sources to represent material deviations from a background model is shared with standard Born theoretical developments (Wu and Aki, 1985). The mapping of heterogeneity into source terms is also used in exact formulations based on Huygen's principle (Paul and Campillo, 1988).

Fourier transforming (2.17) to the k_x, k_y domain,

$$\underline{s}\,(k_x, k_y) = \frac{1}{4\pi^2}\int_{-\infty}^{\infty} h(k_x - k'_x, k_y - k'_y)\underline{\underline{L}}\,(k_x, k_y; k'_x, k'_y)\underline{r}_0(k'_x, k'_y)\,dk'_x\,dk'_y\,, \tag{2.18}$$

where $\underline{\underline{L}}$ is defined by

$$\underline{\underline{L}} = \begin{bmatrix} 0 & 0 & 0 \\ 0 & 0 & 0 \\ ik'_x(\frac{\lambda_1}{\lambda_1+2\mu_1} - \frac{\lambda_2}{\lambda_2+2\mu_2}) & -ik'_y(\frac{\lambda_1}{\lambda_1+2\mu_1} - \frac{\lambda_2}{\lambda_2+2\mu_2}) & 0 \\ k_x k'_x(\zeta_1 - \zeta_2) + k_y k'_y(\mu_1 - \mu_2) - \omega^2(\rho_1 - \rho_2) & 2k_x k'_y(\frac{\lambda_1\mu_1}{\lambda_1+2\mu_1} - \frac{\lambda_2\mu_2}{\lambda_2+2\mu_2}) + k'_x k_y(\mu_1 - \mu_2) & 0 \\ k_x k'_y(\mu_1 - \mu_2) + 2k'_x k_y(\frac{\lambda_1\mu_1}{\lambda_1+2\mu_1} - \frac{\lambda_2\mu_2}{\lambda_2+2\mu_2}) & k_x k'_x(\mu_1 - \mu_2) + k_y k'_y(\zeta_1 - \zeta_2) - \omega^2(\rho_1 - \rho_2) & 0 \\ 0 & 0 & -\omega^2(\rho_1 - \rho_2) \end{bmatrix}$$

$$\begin{bmatrix} \frac{1}{\mu_1} - \frac{1}{\mu_2} & 0 & 0 \\ 0 & \frac{1}{\mu_1} - \frac{1}{\mu_2} & 0 \\ 0 & 0 & \frac{1}{\lambda_1+2\mu_1} - \frac{1}{\lambda_2+2\mu_2} \\ 0 & 0 & -ik_x(\frac{\lambda_1}{\lambda_1+2\mu_1} - \frac{\lambda_2}{\lambda_2+2\mu_2}) \\ 0 & 0 & -ik_y(\frac{\lambda_1}{\lambda_1+2\mu_1} - \frac{\lambda_2}{\lambda_2+2\mu_2}) \\ 0 & 0 & 0 \end{bmatrix} \tag{2.19}$$

2.3.1 Definition of the Scattering Kernel

For plane wave sources it is possible to define a factorization of the scattered field into a product of the wavenumber spectrum of the interface and a function that is called the scattering kernel. The scattering kernel is independent of the interface roughness

function, and contains the features of the scattered field related to the material contrast and the source frequency and illumination angle. For a plane wave source of the form

$$\underline{r}_0(k'_x, k'_y) = 4\pi^2 \underline{r}_p(k^p_x, k^p_y)\delta(k'_x - k^p_x, k'_y - k^p_y), \tag{2.20}$$

equation (2.18) reduces to

$$\underline{s}(k_x, k_y) = h(k_x - k^p_x, k_y - k^p_y)\underline{\underline{L}}(k_x, k_y; k^p_x, k^p_y)\underline{r}_p(k^p_x, k^p_y). \tag{2.21}$$

The scattered field source term in this case is separated into a part associated with a particular interface roughness function, $h(k_x - k^p_x, k_y - k^p_y)$, and a part associated with the material contrast and the source frequency and illumination angle, $\underline{\underline{L}}(k_x, k_y; k^p_x, k^p_y)\underline{r}_0(k^p_x, k^p_y)$. The latter part is designated as the scattering kernel.

Knowledge of the scattering kernel allows one to evaluate the scattering potential of a model independent of any particular interface. For example, the transmission scattering kernels for the two-dimensional model in Figure 2-2 are given in Figure 2-3. The source is a normally incident, planar P wave. The scattering kernels here have been resolved into down-going P and S wave scattering coefficients using a technique described in the next section. Superimposed on these plots is the Fourier transform of the interface. The scattered field is simply the product of the two curves. From these plots it is clear that an interface with a smaller correlation length, and hence a broader spectrum in the transform domain, would result in large amplitude cusps for large scattering angles in P and S. For the transmitted P wave, the scattered wave amplitude increases for scattering angles larger than the P reflection critical angle. An amplitude boost at large angles may also be seen in the P and S reflection coefficients as it will be shown later with examples. This effect has also been demonstrated by Levander and Hill (1985) using finite difference methods and by by Paul and Campillo (1988) using boundary integral equation methods.

2.3.2 Describing Reflection and Transmission

The source term given by (2.18) generates P and S waves above and below the interface. To determine the displacement coefficients of these waves requires a relation between the displacement-stress vector and the up- and down-going P, SV, and SH wave components, the form of which is given by

$$\underline{r} = \underline{\underline{F}}\,\underline{b} \ , \tag{2.22}$$

where $\underline{b} = [\grave{P}\grave{S}\grave{T}\acute{P}\acute{S}\acute{T}]^T$, the grave and acute symbols $\grave{}$ and $\acute{}$ denote down- and up-going waves, respectively, and P, S, and T are the displacement coefficients of P, SV, and SH waves, respectively. Using the reflection coefficient sign conventions of Aki and Richards (1980), $\underline{\underline{F}}$ is given by

$$\underline{\underline{F}} = \begin{bmatrix} \frac{k_x\alpha}{\omega} & \frac{k_x\nu\beta}{\omega K} & -\frac{k_y}{K} & \frac{k_x\alpha}{\omega} & \frac{k_x\nu\beta}{\omega K} & -\frac{k_y}{K} \\ \frac{k_y\alpha}{\omega} & \frac{k_y\nu\beta}{\omega K} & \frac{k_x}{K} & \frac{k_y\alpha}{\omega} & \frac{k_y\nu\beta}{\omega K} & \frac{k_x}{K} \\ \frac{\gamma\alpha}{\omega} & -\frac{K\beta}{\omega} & 0 & -\frac{\gamma\alpha}{\omega} & \frac{K\beta}{\omega} & 0 \\ \frac{2ik_x\gamma\alpha\mu}{\omega} & \frac{ik_x(\nu^2-K^2)\beta\mu}{\omega K} & -\frac{ik_y\nu\mu}{K} & -\frac{2ik_x\gamma\alpha\mu}{\omega} & -\frac{ik_x(\nu^2-K^2)\beta\mu}{\omega K} & \frac{ik_y\nu\mu}{K} \\ \frac{2ik_y\gamma\alpha\mu}{\omega} & \frac{ik_y(\nu^2-K^2)\beta\mu}{\omega K} & \frac{ik_x\nu\mu}{K} & -\frac{2ik_y\gamma\alpha\mu}{\omega} & -\frac{ik_y(\nu^2-K^2)\beta\mu}{\omega K} & -\frac{ik_x\nu\mu}{K} \\ \frac{i(\nu^2-K^2)\alpha\mu}{\omega} & -\frac{2iK\nu\beta\mu}{\omega} & 0 & \frac{i(\nu^2-K^2)\alpha\mu}{\omega} & -\frac{2iK\nu\beta\mu}{\omega} & 0 \end{bmatrix}$$

$$\cdot \begin{bmatrix} e^{i\gamma z} & 0 & 0 & 0 & 0 & 0 \\ 0 & e^{i\nu z} & 0 & 0 & 0 & 0 \\ 0 & 0 & e^{i\nu z} & 0 & 0 & 0 \\ 0 & 0 & 0 & e^{-i\gamma z} & 0 & 0 \\ 0 & 0 & 0 & 0 & e^{-i\nu z} & 0 \\ 0 & 0 & 0 & 0 & 0 & e^{-i\nu z} \end{bmatrix} \tag{2.23}$$

with $K = \sqrt{k_x^2 + k_y^2}$, $\alpha = \sqrt{(\lambda+2\mu)/\rho}$, $\beta = \sqrt{\mu/\rho}$, $\gamma = \sqrt{\omega^2/\alpha^2 - K^2}$, and $\nu = \sqrt{\omega^2/\beta^2 - K^2}$. To recover scattered field displacements from the source term note that

$$\underline{s} = \underline{r}^{(2)} - \underline{r}^{(1)} = \underline{\underline{F}}^{(2)}\underline{b}^{(2)} - \underline{\underline{F}}^{(1)}\underline{b}^{(1)} \tag{2.24}$$

and that $\underline{s}$ generates no down-going waves in the upper medium and no up-going waves in the lower medium. Hence,

$$\underline{s} = \begin{bmatrix} F_{11}^{(2)} & F_{12}^{(2)} & F_{13}^{(2)} & -F_{14}^{(1)} & -F_{15}^{(1)} & -F_{16}^{(1)} \\ F_{21}^{(2)} & F_{22}^{(2)} & F_{23}^{(2)} & -F_{24}^{(1)} & -F_{25}^{(1)} & -F_{26}^{(1)} \\ F_{31}^{(2)} & F_{32}^{(2)} & F_{33}^{(2)} & -F_{34}^{(1)} & -F_{35}^{(1)} & -F_{36}^{(1)} \\ F_{41}^{(2)} & F_{42}^{(2)} & F_{43}^{(2)} & -F_{44}^{(1)} & -F_{45}^{(1)} & -F_{46}^{(1)} \\ F_{51}^{(2)} & F_{52}^{(2)} & F_{53}^{(2)} & -F_{54}^{(1)} & -F_{55}^{(1)} & -F_{56}^{(1)} \\ F_{61}^{(2)} & F_{62}^{(2)} & F_{63}^{(2)} & -F_{64}^{(1)} & -F_{65}^{(1)} & -F_{66}^{(1)} \end{bmatrix} \begin{bmatrix} \grave{P}^{(2)} \\ \grave{S}^{(2)} \\ \grave{T}^{(2)} \\ \acute{P}^{(1)} \\ \acute{S}^{(1)} \\ \acute{T}^{(1)} \end{bmatrix} \tag{2.25}$$

$$= \underline{\underline{\hat{F}}}\,\underline{\hat{b}} \, .$$

The wave displacement coefficients generated by $\underline{s}$ are given by

$$\underline{\hat{b}} = \underline{\underline{\hat{F}}}^{-1}\underline{s} \, . \tag{2.26}$$

The inverse of $\underline{\underline{\hat{F}}}$ exists for all values of (k_x, k_y) except $(k_x, k_y) = (0, 0)$. At this point in the $\underline{k}$ plane the scattered waves are propagating normal to the mean planar surface, and SV waves are indistinguishable from SH waves. For example, consider an S plane wave traveling in the z direction with particle motion in the x direction. If the wave direction is slightly perturbed in the x direction it becomes an SV wave. A perturbation in the y direction makes it an SH wave. These distinctions are true even when the perturbations are infinitesimal. Hence, to remove the singularity of $\underline{\underline{\hat{F}}}$, an arbitrary naming convention must be adopted for vertically propagating S waves. In this paper, the x component of such waves is labeled SV, and the y component is labeled SH. The $\underline{\underline{\hat{F}}}$ matrix for vertical propagation is

$$\underline{\underline{\hat{F}}}(0,0) = \begin{bmatrix} 0 & 1 & 0 & 0 & -1 & 0 \\ 0 & 0 & 1 & 0 & 0 & -1 \\ 1 & 0 & 0 & 1 & 0 & 0 \\ 0 & i\omega\rho_2\beta_2 & 0 & 0 & i\omega\rho_1\beta_1 & 0 \\ 0 & 0 & i\omega\rho_2\beta_2 & 0 & 0 & i\omega\rho_1\beta_1 \\ i\omega\rho_2\alpha_2 & 0 & 0 & -i\omega\rho_1\alpha_1 & 0 & 0 \end{bmatrix} \tag{2.27}$$

2.4 COMPARISON WITH FINITE DIFFERENCE

The simple form of the scattered field source term (2.18) was made possible by the truncation of (2.15) to yield the second-order perturbation approximation given in (2.16). The error resulting from the exclusion of higher order terms is difficult to evaluate analytically. It is possible, though, to determine bounds on the domain of validity of this approximation. Kennett (1972) derived two conditions on the model which must hold in order for (2.18) to be valid. The first condition constrains the scattered field to be much weaker than the background field, a requirement for the single scattering approximation to apply. This condition is expressed by the relation

$$\underline{s}\,(k_x, k_y) \ll \max_{k_x,k_y} |\underline{r}_0(k_x, k_y)|, \tag{2.28}$$

where $\underline{s}$ is the scattered field source term defined by (2.18). Kennett (1972) reduced this to a simpler, but stricter, form by replacing the convolution integral in (2.18) by an upper-bound approximation, yielding

$$\frac{\kappa_0 \omega L}{\pi \beta_1} \eta_{12} \max_x |h(x)| \ll 1, \qquad \max_x |h_{,x}(x)| \ll 1, \tag{2.29}$$

where

$$\eta_{12} = \max\left\{\left|\frac{\alpha_1\rho_1 - \alpha_2\rho_2}{\alpha_1\rho_1 + \alpha_2\rho_2}\right|, \left|\frac{\beta_1\rho_1 - \beta_2\rho_2}{\beta_1\rho_1 + \beta_2\rho_2}\right|\right\},$$

L is the periodicity length of the rough interface, and the wavenumber spectrum of the incident field is bounded by $|k| \leq \kappa_0$. The second condition is that the background field must not contain wavenumbers so close to grazing incidence that shadow zones form. Shadow zones will be avoided if the radius of curvature of the interface is much longer than a wavelength. Such waves will then propagate as guided waves along the interface. This condition is expressed by

$$\frac{1}{\sqrt{\kappa_0^2 + k_z^2}} \max_x |h_{,xx}| \ll 1, \tag{2.30}$$

where k_z is the vertical wavenumber component associated with the maximum horizontal component κ_0.

These conditions are not satisfactory for practical use, however. Approximations used in the derivation of (2.29) result in a much stricter bound than is necessary, and the practical limit imposed by (2.30) needs to be better defined. In order to empirically construct more realistic constraints on interface roughness, reflection and transmission coefficients obtained using the perturbation method described above will be compared with those derived from two-dimensional finite difference solutions. By comparing results for a range of interface height and slope statistics, the domain of validity of the perturbation method can be explored.

The finite difference algorithm used here is a two-dimensional, second-order formulation. To summarize, the wave equations (2.1) and (2.2) are solved in the time-space domain by replacing the time and space derivatives by their second-order centered-difference approximations. The accuracy is improved by using a staggered mesh formulation in which horizontal and vertical displacements are represented on separate grids, each shifted by half of the grid point spacing in both coordinate directions with respect to the other. This has the added benefit of increasing the grid-point density by a factor of two. The formulation differs from that of Virieux (1986) in that we use the second-order

displacement/stress wave equations instead of the first-order velocity/stress equations. This modification improves efficiency, since the final solution was desired in terms of displacement. The stability conditions and grid dispersion relations are identical with those of Virieux's formulation. A low-order, staggered-mesh scheme was chosen because it is the most efficient method when dense grid point spacings are necessary, as is the case in our models where small interface irregularities must be represented. Higher order schemes, such as those which use fourth-order (Bayliss et al., 1986) or Fourier spatial derivative operators (Kosloff et al., 1984; Fornberg, 1988), are generally thought to be more efficient than second-order schemes, but this is not necessarily true. The dense grid point spacing used in modeling small interface perturbations puts the second-order derivative operator well within its domain of acceptable accuracy, and the short operator length makes it the most efficient scheme.

The finite difference method is known to be accurate when the wave fields and the model are both well discretized. Hence, when models with large interface irregularities are compared, the finite difference method will be used as the standard. On the other hand, the perturbation method is accurate for models with small interface height and slope irregularities and will be used as the standard for such models. The comparison with finite difference solutions will proceed in two parts. First it is necessary to show that the range of interface irregularities over which the finite difference method is accurate extends into the range over which the perturbation method is accurate. This will be done by showing that the finite difference method results match the perturbation method results for a model with very small height and slope irregularities. If the finite difference method works well in this case, results for larger interface irregularities will also be valid because they will be more accurately represented on the finite difference grid. Finite difference solutions will then be used a basis for comparison with perturbation solutions for a series of models with larger height and slope irregularities in order to probe the limits of validity of the perturbation approximation.

2.4.1 Accuracy of the Finite Difference Method

All results for scattering from a rough interface in this paper are expressed as reflection and transmission coefficients. The procedure for deriving these coefficients from the finite difference solution is similar to that described in Section 2.3.2 for the perturbation solution. In short, (2.22) is used to convert $\underline{r}$ into $\underline{b}$, and then P and S wave amplitudes in $\underline{b}$ are scaled by the source wave amplitude. The displacements and stresses in $\underline{r}$ are computed by the finite difference method in the time-space domain along a horizontal linear array of uniformly spaced receivers that do not intersect the interface at any point. The receiver array should be located between the source and the interface to allow incident waves to be separated from reflected waves based on whether they are traveling downward or upward. $\underline{r}$ is then Fourier transformed into the ω-k domain to yield a form suitable for use in (2.22). The distance of the receiver array from the interface is accounted for by the z term in the definition of $\underline{\underline{E}}$ in equation (2.23). If the finite difference model is such that reflections from the top or bottom edges of the grid will arrive within the seismogram time window, absorbing boundaries must be implemented which attenuate those reflections to a level much smaller than the reflection and transmission coefficients to be measured. Periodic boundary conditions were applied on the horizontal boundaries of the grid in order to duplicate the periodicity of the spatial Fourier transform, and the length of the array, L, was set to the horizontal dimension of the finite difference grid to take advantage of this periodicity. For a point source, L controls the range of incidence and scattering angles that are within the receiver array, and the horizontal grid size should be large enough to capture the incidence and scattering angles of interest. Since the range of incident and scattering angles detected is also dependent on the distance of the source and the receiver array from the interface, it is best to put the source and the receiver array as close to the interface as possible to minimize the grid size and the seismogram length. Receiver spacing controls the maximum representable wavenumber in $\underline{r}$, and was set equal to the grid point spacing to avoid aliasing.

The reflection and transmission coefficients obtained from finite difference modeling

are compared with analytical coefficients (Cerveny *et al.*, 1977) for the case of a planar interface model. The model is shown in Figure 2-4. The source has an 18 Hz Ricker time function of the form

$$R(t) = (1 - \frac{1}{2}\omega_0^2 t^2)e^{-\frac{1}{4}\omega_0^2 t^2}, \tag{2.31}$$

where ω_0 is the primary angular frequency of the wavelet. The source is implemented as a body force representing a point explosion source smoothed by a Gaussian with standard deviation equal to the grid point spacing. This smoothing is necessary to make the infinite bandwidth explosion source dipoles representable on the finite bandwith finite difference grid. This source isotropically radiates pure P waves. It is located 20 grid points above the interface, and the two arrays of receivers are located 10 grid points above and 10 grid points below the interface. Reflection and transmission coefficients derived from the finite difference seismograms for this model are shown in Figure 2-5 along with analytical coefficients. There is generally good agreement for both pre- and post-critical waves. The small disagreement present at the larger scattering angles results from the finite aperture of the receiver array.

The finite difference and perturbation methods will now be compared for a model with very small height and slope perturbations shown in Figure 2-2. The source is a downward propagating, planar P wave with an 18 Hz Ricker time function. The interface roughness has a Gaussian autocorrelation function with a correlation length of $L = 100$ m and an RMS height deviation of $\sigma = 16.7$ m. The interface is periodic with a period of 2.70 km, the width of the model. The finite difference sampling parameters, $\Delta x = 6.67$ m, $\Delta z = 2.22$ m, and $\Delta t = 0.00156$ s, result in a maximum phase dispersion error of -1.1 percent at 18 Hz. The two receiver arrays are located as close as possible to the interface without intersection. The Fourier transform of the interface function which has been discretized for the finite difference grid is shown in Figure 2-6a as a function of horizontal slowness evaluated at 18 Hz. The zero spectral power at the origin results from the zero mean interface deviation. Histograms of interface height and slope are

shown in Figures 2-6b and 2-6c. The largest deviation from the mean planar surface is 12 m, or 15 percent of the S wavelength in the upper medium. The largest slope is 0.16, while the mean and standard deviation of the slope are zero and 0.059, respectively. Since the maximum interface height and slope are fairly well approximated by twice their standard deviations, histograms will not be provided for the remaining rough interfaces used in this study. A comparison of the reflection and transmission coefficients derived from the finite difference and perturbation methods is shown in Figure 2-7. Agreement is very good, with both amplitude and shape predicted well by the perturbation method. "Ringing" appears to some degree in all finite difference coefficient plots, and is most apparent on the S wave coefficient plots. Another check on the accuracy of the reflection and transmission coefficient results is to plot the coefficients for the non-physical waves in the solution: the down-going S in the upper medium and the up-going S and P in the lower medium. Plots of the non-physical coefficients for the finite difference data are shown in Figure 2-8. In general, the amplitude of the non-physical waves increases with increasing scattering angle, since the wavenumbers corresponding to these larger angles are less well represented by the receiver array. The down-going P wave in the upper medium has unit amplitude at zero angle. It is clear from this figure that the maximum error is less than 0.1 percent, and that this error is associated with the S wave in the upper medium. This error is enough to explain the difference between the finite difference and perturbation results for the reflected S wave coefficient at large scattering angles.

2.4.2 Accuracy of the Perturbation Method in the ω-k Domain

The domain of validity of the perturbation method will be explored by comparing reflection and transmission coefficients generated using the perturbation method with those derived from finite difference modeling. Six rough interface models are used in this comparison, each having a Gaussian autocorrelation function and a uniform random phase. The interface functions are shown in Figures 2-9(a–f) with two times vertical exaggera-

tion. RMS interface slope ranges from 0.037 to 0.99 and RMS interface height is 0.01 km for models A–E and 0.015 km for model F. Since the accuracy of the perturbation method is sensitive to the smallest elastic wavelength in the model, interface height is measured here in terms of S wavelengths in the upper medium (S_1), and thus the relative height of the irregularities changes as the frequency changes. The bandwidth of the 18 Hz Ricker wavelet time function used in the finite difference calculation allowed reflection and transmission coefficients to be computed at three frequencies (9.93, 16.5, and 26.5 Hz) in each of the six models, for a total of 18 comparisons for each coefficient. In these comparisons, RMS interface height ranges from 0.069 to 0.28 S_1 wavelengths. RMS height, correlation length, and RMS slope for the models used are listed in Table 2.2. The material parameters are $\alpha_1 = 2.50$ km/s, $\beta_1 = 1.44$ km/s, $\rho_1 = 1.00$ g/cm^3, $\alpha_2 = 3.00$ km/s, $\beta_2 = 1.73$ km/s, and $\rho_2 = 1.00$ g/cm^3, the same as in Figure 2-2. The source is a normally incident planar P wave in layer one. Plots of these comparisons are shown for the selected models A, B, D, and E in Figures 2-10(a–d). The reflection and transmission coefficients are the displacement coefficients $\acute{P}_1$, $\acute{S}_1$, $\grave{P}_2$, and $\grave{S}_2$ are normalized so that $\grave{P}_1 = 1$.

In order to facilitate the comparison of the perturbation and finite difference coefficients, the curves are compared by finding the L_2 norm difference defined by

$$\|\acute{P}_{pt} - \acute{P}_{fd}\|_2 = 100 \times \left[\frac{\int_0^{\frac{\pi}{2}} [\acute{P}_{pt}(\theta_s) - \acute{P}_{fd}(\theta_s)]^2 d\theta_s}{\int_0^{\frac{\pi}{2}} \acute{P}_{fd}(\theta_s)^2 d\theta_s} \right]^{\frac{1}{2}}, \tag{2.32}$$

where θ_s is the scattering angle and the $\acute{P}$ coefficient is chosen for illustration. The differences between method results are plotted for each of the four coefficients in Figures 2-11(a–d) for a constant RMS interface height of 0.01 km, and in Figures 2-11(e–h) for a constant RMS interface slope of 0.1. The constant height plots show that the accuracy of the perturbation solution is not significantly degraded as RMS interface slope varies within the range tested. This L_2 norm result is verified in the coefficient comparison plots in Figures 2-10(a–d). The constant slope plots show that error increases rapidly with increasing RMS interface height, and in this particular example is acceptable for values of RMS height less than about 0.1 S_1 wavelengths.

2.4.3 Accuracy of the Perturbation Method in the t-x Domain

Error in time domain seismograms generated using the perturbation approximation cannot be directly estimated from the error results presented for the ω-k domain. This is because each seismogram contains energy from a broad spectrum of frequencies and wavenumbers. Here the time domain error will be estimated by comparing reflection seismograms generated by the perturbation method with those generated from the finite difference method. To generate reflection seismograms using the perturbation method, the scattering coefficients evaluated using the two-dimensional form of (2.26) are converted to displacement by using (2.22) with $k_y = 0$. These displacements are then Fourier transformed in ω and k to yield

$$\begin{bmatrix} u_x \\ u_z \end{bmatrix} = \frac{1}{4\pi^2} \int_{-\infty}^{\infty} e^{-i\omega t} d\omega \int_{-\infty}^{\infty} e^{ikx} dk \begin{bmatrix} F_{14} & F_{15} \\ F_{34} & F_{35} \end{bmatrix} \begin{bmatrix} \acute{P} \\ \acute{S} \end{bmatrix} . \tag{2.33}$$

Fourier transforms are evaluated using the discrete wavenumber method (Bouchon, 1977). Seismograms generated with (2.33) contain only the scattered field. The background field can be added if desired.

Seismograms were generated for each of the interface functions parameterized in Table 2.3 using both the perturbation and finite difference methods, and a subset of these are shown overlain in Figure 2-12. The source and receiver configurations and the material parameters are the same as those used in the last section. The source time function is an 18 Hz Ricker wavelet. These seismograms show that the shapes of the waveforms generated by the perturbation and finite difference methods agree fairly well for the range of models considered. Errors in amplitude and traveltime seem to be positively correlated, both being larger at receivers that are over extrema in the interface height function than at other receiver locations. This feature will be explored next using an L_2 norm error measure. Since the total waveform is composed of the background field added to the scattered field, total field perturbation method seismograms minus the source waves are

presented for comparison in Figure 2-13 for models A–I.

The L_2 norm was calculated as a measure of error between the perturbation and finite difference seismograms, using

$$\begin{aligned} E(x,\Delta t) &= \|u_z(x)^{pt} - u_z(x)^{fd}\|_2(\Delta t) \\ &= 100 \times \left[\frac{\int_{-t_{min}}^{t_{max}} dt' [u_z^{pt}(x,t'+\Delta t) - u_z^{fd}(x,t')]^2}{\frac{1}{L}\int_0^L dx \int_{t_{min}}^{t_{max}} dt' u_z^{fd}(t')^2} \right]^{\frac{1}{2}}, \end{aligned} \tag{2.34}$$

where L is the length of the receiver array and Δt is the time shift between the two seismograms. The numerator was efficiently evaluated using the fast Fourier transform since the seismograms are periodic in space. The denominator is the average power of the entire array of finite difference seismograms in order to minimize the effect of low amplitude seismograms on $E(\Delta t)$. If $E(\Delta t)$ were normalized instead to the current seismogram, globally small errors could overwhelm such low amplitude seismograms to produce large values of $E(\Delta t)$.

$E(\Delta t)$ is used to provide two separate measures of error for each seismogram: travel-time error, which is defined as the time delay $\widehat{\Delta t}$ at which E is minimum; and amplitude error, which is defined as $\hat{E} = E(\widehat{\Delta t})$. A plot of $\widehat{\Delta t}$ versus seismogram offset x for Model A is shown in Figure 2-14. Overlain on this plot is a plot of the one-way, vertical P wave traveltime associated with the interface function ($\frac{h(x)}{\alpha_1}$). In the absence of travel-time error, $\widehat{\Delta t}$ would be zero for all the seismograms. The agreement between these two curves indicates that traveltime from the interface to the receiver in the perturbation method is referenced to the mean planar interface, and not to the perturbed interface.

The reason for the traveltime error can easily be seen for the case where the interface perturbation function $h(x)$ is a constant. In this case, the perturbation expansion given by (2.15) transforms to an exact form in the ω-k domain:

$$\underline{\hat{r}}(\omega, k_x, k_y; h) = \underline{\underline{I}}(\underline{\underline{I}} + h\underline{\underline{A}} + \frac{h^2}{2!}\underline{\underline{A}}^2 + \ldots)\underline{r}(\omega, k_x, k_y; 0) \tag{2.35}$$

$$= e^{h\underline{\underline{A}}}\underline{r}(\omega, k_x, k_y; 0) \quad (2.36)$$

$$= \underline{\underline{F}} e^{h\Lambda} \underline{\underline{F}}^{-1} \underline{r}(\omega, k_x, k_y; 0). \quad (2.37)$$

Equation (2.36) is simply the definition of a propagator matrix which transforms the solution for $\underline{r}$ at depth zero to the solution at depth h. Equation (2.37) uses a diagonal factorization of $\underline{\underline{A}}$ of the form

$$\underline{\underline{A}} = \underline{\underline{F}}\,\underline{\underline{\Lambda}}\,\underline{\underline{F}}^{-1} \quad (2.38)$$

where $\underline{\underline{F}}$ is defined by (2.23) and is always invertible, and $\underline{\underline{\Lambda}}$ is a diagonal matrix whose diagonal elements in the three-dimensional case are $\Lambda_{11} = -\Lambda_{44} = i\gamma$ and $\Lambda_{22} = \Lambda_{33} = -\Lambda_{55} = -\Lambda_{66} = i\nu$. The exact form of the source term (2.18) valid for constant h is then

$$\underline{s}(\omega, k_x, k_y) = (e^{h\underline{\underline{A}}^{(1)}} - e^{h\underline{\underline{A}}^{(2)}})\underline{r}(\omega, k_x, k_y; 0) \quad (2.39)$$

$$= (\underline{\underline{F}}^{(1)} e^{h\underline{\underline{\Lambda}}^{(1)}} \underline{\underline{F}}^{(1)^{-1}} - \underline{\underline{F}}^{(2)} e^{h\underline{\underline{\Lambda}}^{(2)}} \underline{\underline{F}}^{(2)^{-1}})\underline{r}(\omega, k_x, k_y; 0) \quad (2.40)$$

$$\approx (\underline{\underline{F}}^{(1)}(h\underline{\underline{\Lambda}}^{(1)})\underline{\underline{F}}^{(1)^{-1}} - \underline{\underline{F}}^{(2)}(h\underline{\underline{\Lambda}}^{(2)})\underline{\underline{F}}^{(2)^{-1}})\underline{r}(\omega, k_x, k_y; 0) \quad (2.41)$$

$$+ \; O(h^2).$$

The phase factors of the form $e^{h\underline{\underline{\Lambda}}}$ in (2.40) are responsible for adjusting the traveltime to account for the height of the interface. The accuracy of the first order approximation $e^{h\underline{\underline{\Lambda}}} - \underline{\underline{I}} \approx h\underline{\underline{\Lambda}}$ in (2.41) controls the accuracy of the traveltime adjustment and influences the accuracy of the scattered field amplitude. The accuracy of the first and second order approximations to $e^{ih\underline{\underline{\Lambda}}} - \underline{\underline{I}}$ is illustrated in Figure 2-15. This figure shows that at least a second order approximation is required for accurate representation of phase, and therefore of traveltime, although both approximations converge to the exact solution as $h \to 0$. However, the modulus of the first order approximation is more accurate than that of the second order approximation, but this is a consequence of the non-monotonic improvement of accuracy as approximation order increases.

RMS amplitude error $\hat{E}$ in the comparison of perturbation- and finite difference-derived seismograms is shown in Figure 2-16. RMS errors of the seismograms of each

model were averaged, and these mean errors were plotted against RMS height for RMS slopes of 0.037 and 0.10, and against slope for an RMS height of 0.125 S_1 wavelengths. Contrary to the results obtained in the ω-k domain, RMS amplitude error clearly increases with increasing RMS interface slope, as well as with increasing RMS interface height. Comparison of the rates of error growth for the fixed slope and fixed height error plots shows that error increases with increasing height nearly twice as fast as it does with increasing slope.

When the time shift error is removed, amplitude error is sensitive to two factors: the amplitude scale factor and the waveform character. Waveform character refers to the general shape of the waveform including the presence and length of the coda. It is fairly well approximated in all of the nine models considered here. With the exception of small amplitude arrivals, the shapes of the first arrivals generally agree well with the finite difference results, even for models with RMS slopes as high as one, and the complexity and decay rate of the coda are also well approximated. The amplitude scale factor, however, is generally overestimated by the perturbation method. This is true to the nature of the Born approximation, which violates conservation of energy by introducing the rough interface effects via a source term whose energy is added to the energy of the background field. With these points in mind, the range of validity spans the entire range of the models tested if the error criterion is based on waveform character. On the other hand, if the error criterion is based on amplitude scale or the absolute RMS error the range is limited to RMS slopes of less than about 0.3 and RMS heights of less than about 0.25 of the smallest wavelength present in the scattered field. Notice that the latter criterion results in a less restrictive range than the RMS error analysis on scattering coefficients done in the ω-k domain.

2.5 FEATURES OF THE 3-D SCATTERED FIELD

Three-dimensional scattering examples will now be presented for the model shown in Figure 2-17. The material and interface parameters are identical to those of model D

(see Table 2.2 and Figure 2-9) with the Gaussian autocorrelation function having identical correlation lengths in the x and y directions. In general, a Gaussian rough interface whose major and minor axes coincide with the x and y axes has a Gaussian autocorrelation function of the form

$$h(k_x, k_y)h^*(k_x, k_y) \sim e^{-\frac{(k_x L_x)^2+(k_y L_y)^2}{2}}, \tag{2.42}$$

where L_x and L_y are the major- and minor-axis correlation lengths. Equation (2.42) can be generalized to allow roughness trends at an angle θ to the x axis by applying a rotation transformation to get

$$h(k_x, k_y)h^*(k_x, k_y) \sim e^{-\frac{1}{2}\left[L_x^2(k_x\cos(\theta)+k_y\sin(\theta))^2+L_y^2(-k_x\sin(\theta)+k_y\cos(\theta))^2\right]}. \tag{2.43}$$

In the first example, the source is an 18 Hz planar SV wave propagating downward along the z axis with particle motion in the x direction. The SV wave scatters into reflected and transmitted P, SV, and SH waves. The three-dimensional P, SV, and SH transmission coefficients for this model, found using the perturbation method, are given in Figure 2-18. The x and y scattering angles in these figures, referred to as ϕ_x and ϕ_y, are measured from the downward z axis in the x-z and y-z planes, respectively. They are defined by $\phi_x = \sin^{-1}(k_x v/\omega)$ and $\phi_y = \sin^{-1}(k_y v/\omega)$ where v is the body wave velocity of the transmitted wave concerned. Scattering in the z-direction, for example, is given by $\phi_x = \phi_y = 0$. The transmission coefficient plots cover scattering angles in the range $-90° \leq \phi_x \leq 90°$ and $0° \leq \phi_y \leq 90°$, and are symmetric about the $\phi_y = 0$ axis. For all three scattered wavetypes, these plots show that scattering is maximal in the direction that conserves source particle motion: for an SV source with particle motion in the x-z plane, P and SV are maximally scattered in the x-z plane, and SH is maximally scattered in the y-z plane. This effect is exaggerated by the use of the single scattering approximation. A null is present in the plane normal to maximal plane: the y-z plane for P and SV waves and the x-z plane for SH waves. An alternative display of the three-dimensional transmission coefficients is a cross-section of the coefficients for all scattering

angles at a particular azimuth, where azimuth is measured clockwise in the x-y plane from the positive x-axis, and the scattering angle is defined by $\psi = \sin^{-1}(k_z v/\omega)$. Cross-sections of the reflection and transmission coefficients for the same model and source parameters are given for azimuthal angles of 10°, 45°, and 80° in Figure 2-19.

Transmission scattering kernels for the model in Figure 2-17 are given in Figure 2-20. Comparison with the SV and SH transmission coefficients in Figure 2-18 shows that the spatially band-limited nature of this particular interface damps out the large amplitude features present at large scattering angles. The P transmission coefficient exhibits a hint of the cusps present in the kernel. Consideration of another interface roughness function requires only a visual superposition of the new interface spectrum with the kernel. For the same SV source as above and a two-dimensional rough interface with variation in the x direction, the problem is truly two-dimensional, and waves are scattered into P and SV. If the interface is rotated 90 degrees so that variation is in the y direction, the problem is fully three-dimensional, and waves are scattered into P and SH. More general interfaces whose autocorrelation functions are described by (2.43), or perhaps a von Karman or exponential function, are handled with the same approach.

The second example is the same as the first, but with the SV source replaced by a P source. The three-dimensional P and SV transmission coefficients for this model are given in Figure 2-21. Since the source particle motion and the Gaussian autocorrelation function are azimuthally invariant, the scattering coefficients are also azimuthally invariant. Deviations of the contours from circular arcs are artifacts of the contouring program. Reflection and transmission coefficient cross-sections for this model are given in Figure 2-22. Note that scattered SH waves are not generated in this example. This is a consequence of the single-scattering approximation. For a normal incidence planar P wave, a minimum of two bounces are required to generate SH.

2.6 DISCUSSION AND CONCLUSIONS

A perturbation method has been presented for computing three-dimensional body wave scattering from a rough interface. Its speed and simplicity are such that many of the examples in this thesis were generated on a Macintosh SE computer in less than two minutes. Speed is an important consideration when three-dimensional modeling is necessary. For example, many of the two-dimensional finite difference computations done for comparison required 15 Mbytes of core and 23 hours of CPU time on a Vax 8800. In three dimensions, finite difference solutions for these models are beyond our resources at present. For the class of irregular interface models with small RMS height deviations, the perturbation method is a useful alternative.

Since interface height deviations in the models presented are small, comparisons of the perturbation method with the finite difference method were preceded by careful testing of the finite difference method to show that it is valid for the small deviations used in these comparisons. It can be shown that in the limit as the finite difference grid sampling interval goes to zero, and as the numerical precision of the computer goes to infinity, the finite difference solution converges to the exact solution as $O(\Delta x)$ (Brown, 1984). However, in order for the grid sampling interval to be small enough that the finite difference solution is sufficiently close to the exact solution, the number of grid points describing a fixed model must increase as the size of the interface height perturbations decreases. Therefore, the core size and speed of a computer are constraints in the minimum interface height perturbation that can be accurately modeled using a finite difference method. Of course, a planar boundary is an exception to this limit. Another lower limit on interface perturbation size is imposed by numerical precision. As the size of interface height perturbations decreases, the amplitude of scattered seismic waves decreases. Since these scattered waves are added to the relatively large planar interface response, insignificant numerical noise in the planar interface response can be significant when compared with the scattered field. This is probably the cause of the "ringing" present in the finite difference-derived scattering coefficients. Comparisons of

finite difference-derived scattering coefficients for a planar model against an analytical solution, and for a model with small interface height and slope perturbations against a perturbation method solution, show that this "ringing" tends to oscillate about the exact solution. Hence, the smoothed finite difference scattering coefficients are useful for comparisons.

Numerous two-dimensional model comparisons of finite difference and perturbation method scattering coefficients were made in order to determine the range of validity of the perturbation method. The L_2 norms of the differences were computed for varying RMS slope and constant RMS height, and for varying RMS height and constant RMS slope. There are two major trends in the L_2 norm results. First, error increases strongly with increasing RMS height, with acceptable levels for RMS heights of less than about 0.1 shear wavelengths. Second, error appears to be roughly constant for increasing RMS slope for the tested range of 0.037 to 0.99. Smaller trends, such as the apparent increase in accuracy with increasing RMS slope, are misleading. The L_2 norm is overly sensitive to the noise in the finite difference solution being used as the standard for comparison. This is apparent when the scattering coefficient plots are examined for the trend seen in the L_2 norm plots. The L_1 norm was also calculated to see whether it is less sensitive to this noise, but the improvements were minimal. Ultimately, all trends must be confirmed by the scattering coefficient plots.

Time domain seismograms generated by the perturbation method were compared with finite difference seismograms for the same models. The perturbation method was able to accurately predict waveform character for the entire range of models considered, including the shape of the first arrival and the presence, duration, and complexity of the coda. Using RMS error analysis to determine traveltime error, it was shown that when first order perturbation theory is used, the traveltime from the interface to the receiver is referenced to the mean planar interface, and not from the perturbed interface. Hence, traveltime error increases linearly with the height of the interface. It was shown that a second order theory is required for traveltime to include the height of the perturbation.

With this traveltime error removed, the mean RMS error was determined for the perturbation seismograms in each of the models. If this mean RMS error is the criterion for determining the domain of validity of the perturbation method, it is valid for RMS slopes of less than about 0.25 and RMS heights of less than about 20 percent of the smallest wavelength in the scattered field.

Three-dimensional scattering kernels generated for an SV plane wave normally incident on a rough interface show that waves are maximally scattered in directions for which the scattered wave particle motion coincides with that of the incident wave. A P wave in the same geometry induces azimuthally isotropic radiation. In the three-dimensional scattering example it was shown that there is a null in P and SV scattering in the y direction, and a null in SH scattering in the x direction. These nulls do not exist in the time-space domain, where a receiver in any location can detect waves traveling in all directions. These scattering kernels also show that scattered wave amplitudes tend to increase for scattering angles beyond the P wave critical angle (defined with respect to the planar interface model). This confirms the results of Paul and Campillo (1988).

References

Aki, K., P.G.Richards, 1980, *Quantitative Seismology: Theory and Methods,* W. H. Freeman and Company, San Francisco, vols. 1 and 2, 932 pp.

Bayliss, A., K. Jordan, J. LeMesurier, and E. Turkel, 1986, A fourth-order accurate finite-difference scheme for the computation of elastic waves, *Bull. Seism. Soc. Am., 76,* 1115–1132.

Bouchon, M., 1977, Discrete wavenumber representation of seismic-source wave fields, *Bull. Seism. Soc. Am., 67,* 259–277.

Brown, D.L., 1984, A note on the numerical solution of the wave equation with piecewise smooth coefficients, *Math. Comp., 42,* 369–391.

Caravana, C., S.S. Stubeda, and R. Turpening, 1988, Nine-component zero offset VSP, in *Reservoir Delineation—Vertical Seismic Profiling Consortium Annual Report,* Earth Resources Laboratory, Department of Earth, Atmospheric, and Planetary Sciences, Massachusetts Institute of Technology, Cambridge, MA, 10-1–10-22.

Cerveny, V., I.A. Molokov, and I. Psencik, 1977, *Ray Method in Seismology,* Univerzita Karlova, Praha.

DeSanto, J.A., and G.S. Brown, 1986, Analytical techniques for multiple scattering from rough surfaces, in *Progress in Optics, XXIII,* E. Wolf (ed.), Elsevier Science Publishers B.V.

Fornberg, B., 1988, The pseudospectral method: Accurate representation of interfaces in elastic wave calculations, *Geophysics, 53,* 625–637.

Gilbert, F., and L. Knopoff, 1960, Seismic scattering from topographic irregularities, *J. Geophys. Res., 65,* 3437–3444.

Hudson, J.A., 1967, Scattered surface waves from a surface obstacle, *Geophys. J. R. astr. Soc., 13,* 441–458.

Kennett, B.L.N., 1972, Seismic wave scattering by obstacles on interfaces, *Geophys. J. R. astr. Soc., 28,* 249–266.

Kennett, B.L.N., 1983, *Seismic Wave Propagation in Stratified Media,* Cambridge University Press, New York, 339.

Kosloff, D., M. Reshef, and D. Loewenthal, 1984, Elastic wave calculations by the Fourier method, *Bull. Seism. Soc. Am., 74,* 875–891.

Levander, A.R., and N.R. Hill, 1985, P-SV resonances in irregular low-velocity surface layers, *Bull. Seism. Soc. Am., 75,* 847–864.

Paul, A., and M. Campillo, 1988, Diffraction and conversion of elastic waves at a corrugated interface, *Geophysics, 53,* 1415–1424.

Prange, M., 1987, Efficiency considerations from finite difference elastic wave modeling on the Connection Machine, in *Reservoir Delineation—Vertical Seismic Profiling Consortium Annual Report,* Earth Resources Laboratory, Department of Earth, Atmospheric, and Planetary Sciences, Massachusetts Institute of Technology, Cambridge, Mass.

Virieux, J., 1986, P-SV wave propagation in heterogeneous media: velocity-stress finite-difference method, *Geophysics, 51,* 889–901.

Wu, R., and K. Aki, 1985, Scattering characteristics of elastic waves by an elastic heterogeneity, *Geophysics, 50,* 582–595.

Symbol	Definition	Equation Introduced
α_j	Compressional wave speed in layer j	(2.23)
β_j	Shear wave speed in layer j	(2.23)
ρ_j	Density in layer j	(2.1)
ω	Angular frequency	(2.1)
u_j	jth component of displacement	(2.1)
$\underline{\underline{\tau}}$	Cauchy stress tensor	(2.1)
λ_j, μ_j	Lamé parameters for layer j	(2.2)
$\underline{r}$	Displacement-stress vector	(2.3)
$\underline{\underline{A}}^{(j)}$	Wave equation coefficient matrix for layer j	(2.3)
∂_j	Partial derivative w.r.t. jth component	(2.4)
ζ_j	Simplification variable for layer j	(2.4)
T_j	jth component of traction	(2.6)
$\underline{n}(x,y)$	Unit normal to interface	(2.5)
$h(x,y)$	Zero mean interface height function	(2.5)
$\underline{\underline{Q}}_x^{(j)}$, $\underline{\underline{Q}}_y^{(j)}$	Rotation matrices for layer j	(2.7)
$\underline{\underline{I}}$	Identity matrix	(2.7)
$\hat{r}^{(j)}$	Rotated displacement-stress vector in layer j	(2.7)
$\underline{r}_k^{(j)}$	kth order scattered field for layer j	(2.14)
$\underline{r}_0$	Displacement-stress vector for mean planar interface	(2.14)
$\underline{s}$	Scattered field source term	(2.18)
$\underline{\underline{L}}$	Kernel matrix for scattered field source term	(2.18)
k_x, k_y	x and y components of wavenumber	(2.18)
K	Magnitude of horizontal wavenumber	(2.23)
γ_j	Vertical component of wavenumber for a compressional wave	(2.23)
γ_j	Vertical component of wavenumber for a shear wave	(2.23)
δ	Dirac delta function	(2.20)
$\underline{b}$	Wave coefficient vector	(2.22)
$\underline{\underline{F}}$	Layer matrix	(2.22)
$\hat{\underline{b}}$	Scattering coefficient vector	(2.25)
$\hat{\underline{\underline{F}}}$	Scattering coefficient transformation matrix	(2.25)
κ_0	Maximum bound on source horizontal wavenumber	(2.29)
θ_s	Scattering angle	(2.32)
$\underline{\underline{\Lambda}}$	Diagonal eigenvalue matrix for $\underline{\underline{A}}$	(2.38)

Table 2.1: Table of symbols used in this paper.

Model	Correlation Length (km)	RMS Slope	RMS Height (km)	RMS Height in S_1 Wavelengths at 9.93 Hz	RMS Height in S_1 Wavelengths at 16.5 Hz	RMS Height in S_1 Wavelengths at 26.5 Hz
A	0.30	0.037	0.010	0.069	0.11	0.18
B	0.10	0.10	0.010	0.069	0.11	0.18
C	0.050	0.20	0.010	0.069	0.11	0.18
D	0.033	0.30	0.010	0.069	0.11	0.18
E	0.010	0.99	0.010	0.069	0.11	0.18
F	0.15	0.10	0.015	0.10	0.17	0.28

Table 2.2: Interface parameters for the rough interfaces used in the ω-k domain comparisons. The interface height functions shown plotted in Figure 2-9.

Model	Correlation Length (km)	RMS Slope	RMS Height (km)	RMS Height in S_1 Wavelengths at 18 Hz
A	0.30	0.037	0.010	0.125
B	0.10	0.10	0.010	0.125
C	0.050	0.20	0.010	0.125
D	0.033	0.30	0.010	0.125
E	0.010	0.99	0.010	0.125
F	0.15	0.10	0.015	0.188
G	0.45	0.038	0.015	0.188
H	0.60	0.039	0.020	0.25
I	0.20	0.10	0.020	0.25

Table 2.3: Interface parameters for the rough interfaces used in the t-x domain comparisons.

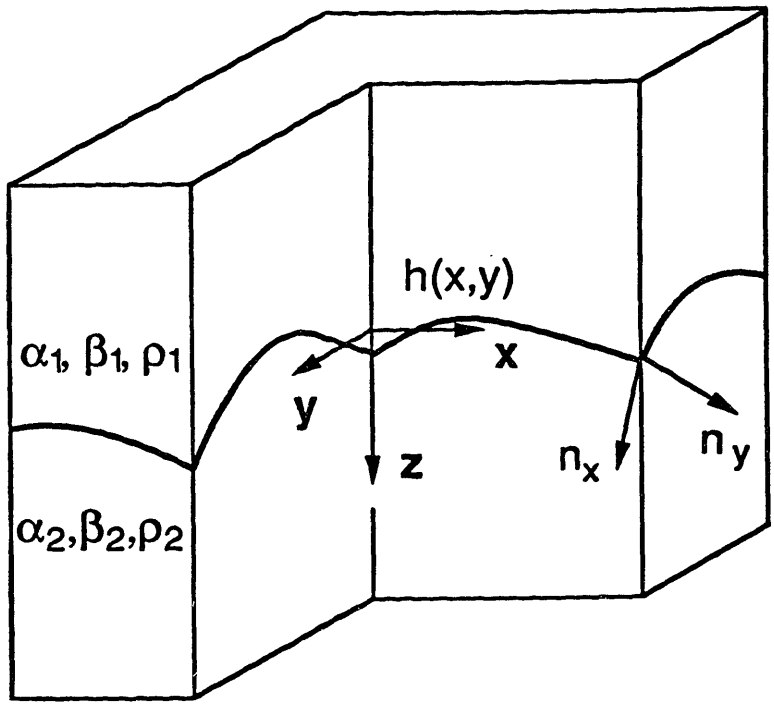

Figure 2-1: Geometry of the rough interface model. The interface is defined by $z = h(x, y)$, and the downward-pointing unit normal to this surface at each point is denoted by $\underline{n}(x, y)$. The $z = 0$ plane is defined as the mean planar surface through the rough interface. α_1, β_1, ρ_1, α_2, β_2, and ρ_2 denote the compressional and shear wave speeds and density for the materials above and below the interface, respectively.

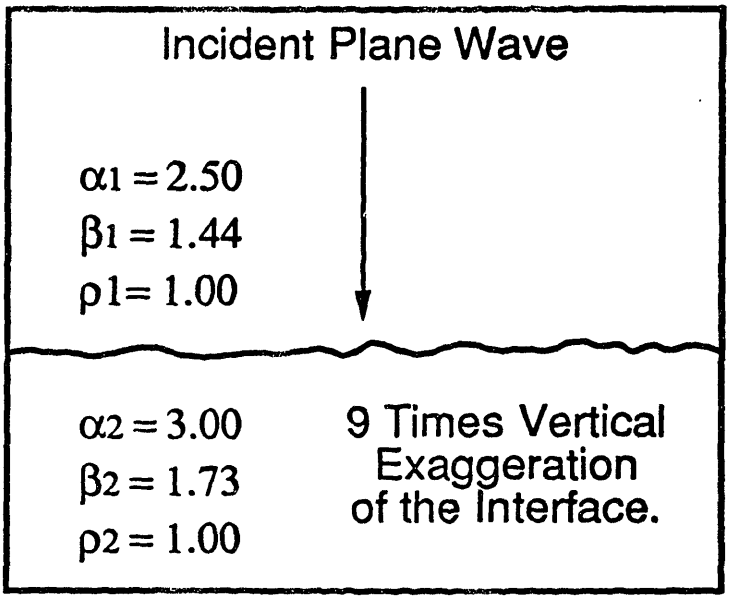

Figure 2-2: Two-dimensional rough interface model. The source is a normally incident, 18 Hz, plane wave. The rough interface has a Gaussian autocorrelation function with a correlation length of $L = 100$ m and an rms height deviation of $\sigma = 16.7$ m. The interface is periodic with a period of 2.70 km, the width of the model above.

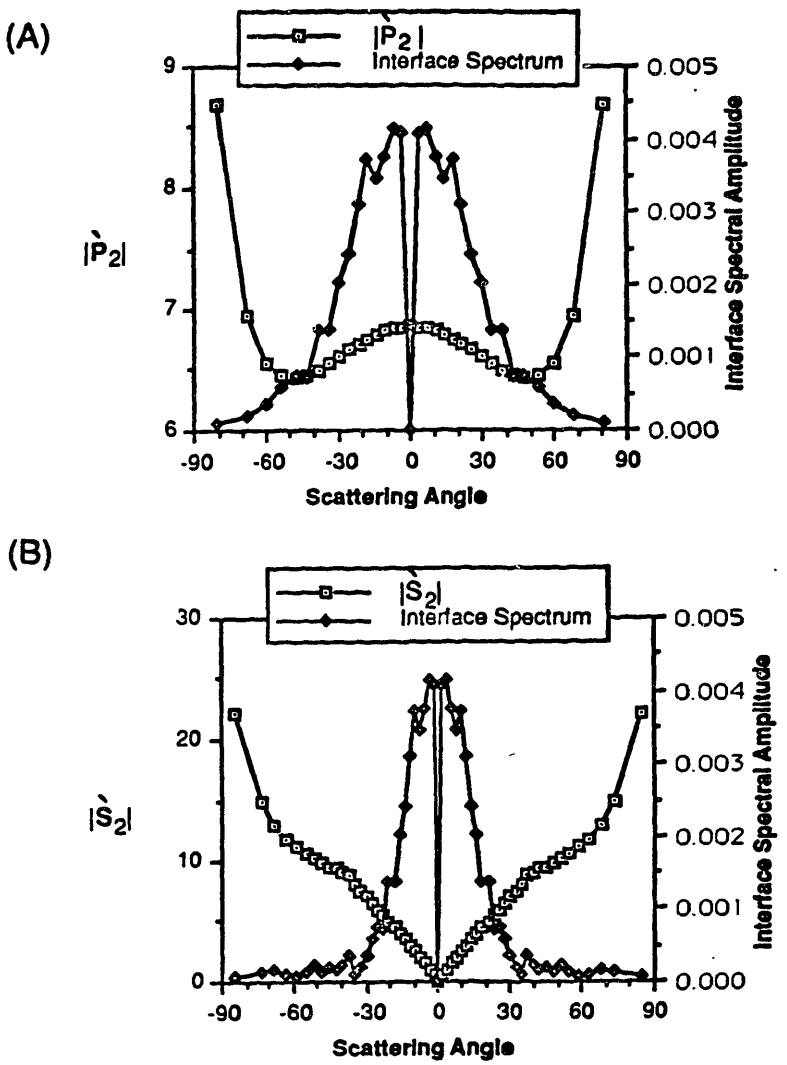

Figure 2-3: P and S wave transmission scattering kernels for a normally incident P wave for the model in Figure 2-2. The Fourier transform of the interface, mapped into scattering angle, is shown superimposed.

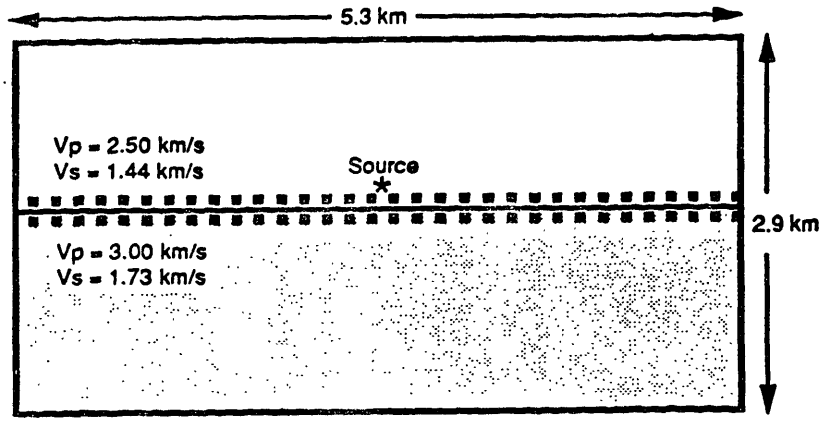

Figure 2-4: Planar interface model used to compare finite difference derived reflection and transmission coefficients with analytical solutions. The source is a point explosion with an 18 Hz Ricker wavelet time function. The sampling parameters, $\Delta x = \Delta z =$ 6.67 m and $\Delta t = 0.00156$ s, result in a maximum phase dispersion error of -1.1 percent at 18 Hz. The source is located 20 grid points above the interface, and the receiver arrays are located 10 grid points on either side of the interface. The horizontal receiver interval is two grid points. All waves within the seismogram time window are contained within the finite difference grid, eliminating the need for absorbing boundaries.

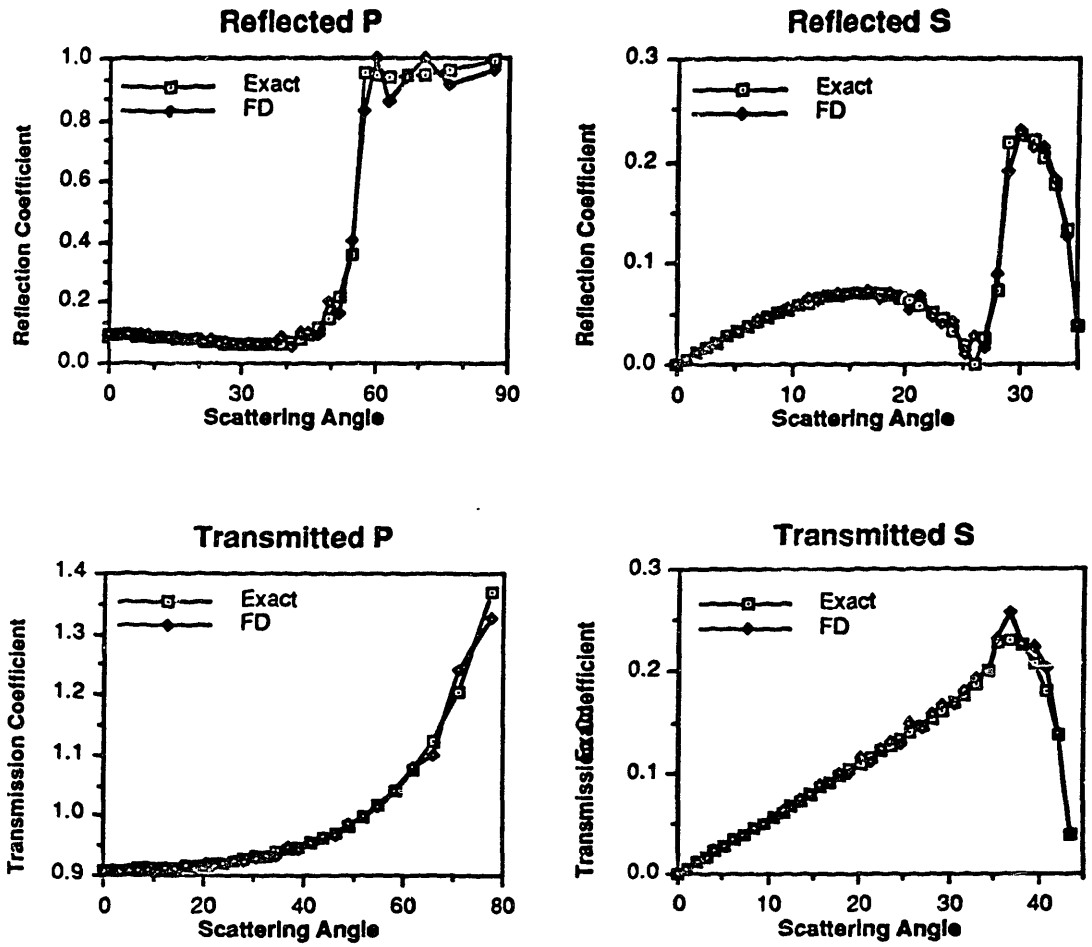

Figure 2-5: Comparison between P and S wave reflection and transmission coefficients generated by finite difference and analytic methods for a planar interface. The model is shown in Figure 2-4. The small disagreement present at the larger scattering angles is "Gibb's ringing" that results from the finite aperture of the receiver array.

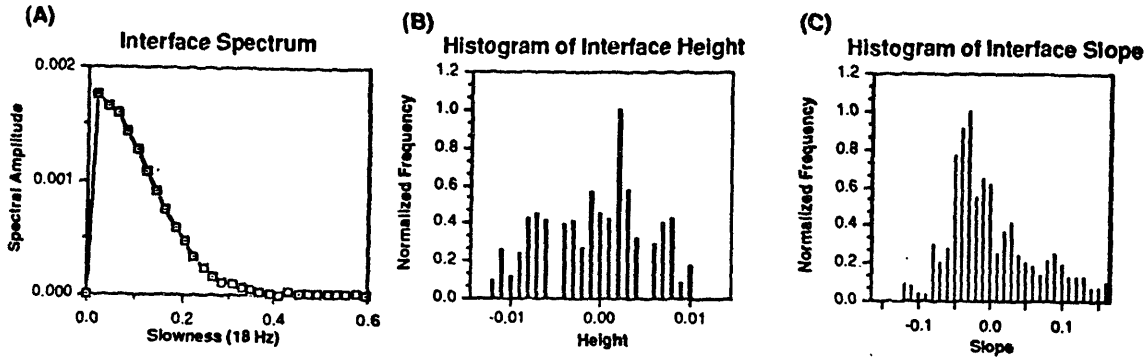

Figure 2-6: Properties of of the interface shown in Figure 2-2: (a) Fourier transform, where the horizontal slowness is evaluated for 18 Hz, and histograms of (b) interface height and (c) interface slope.

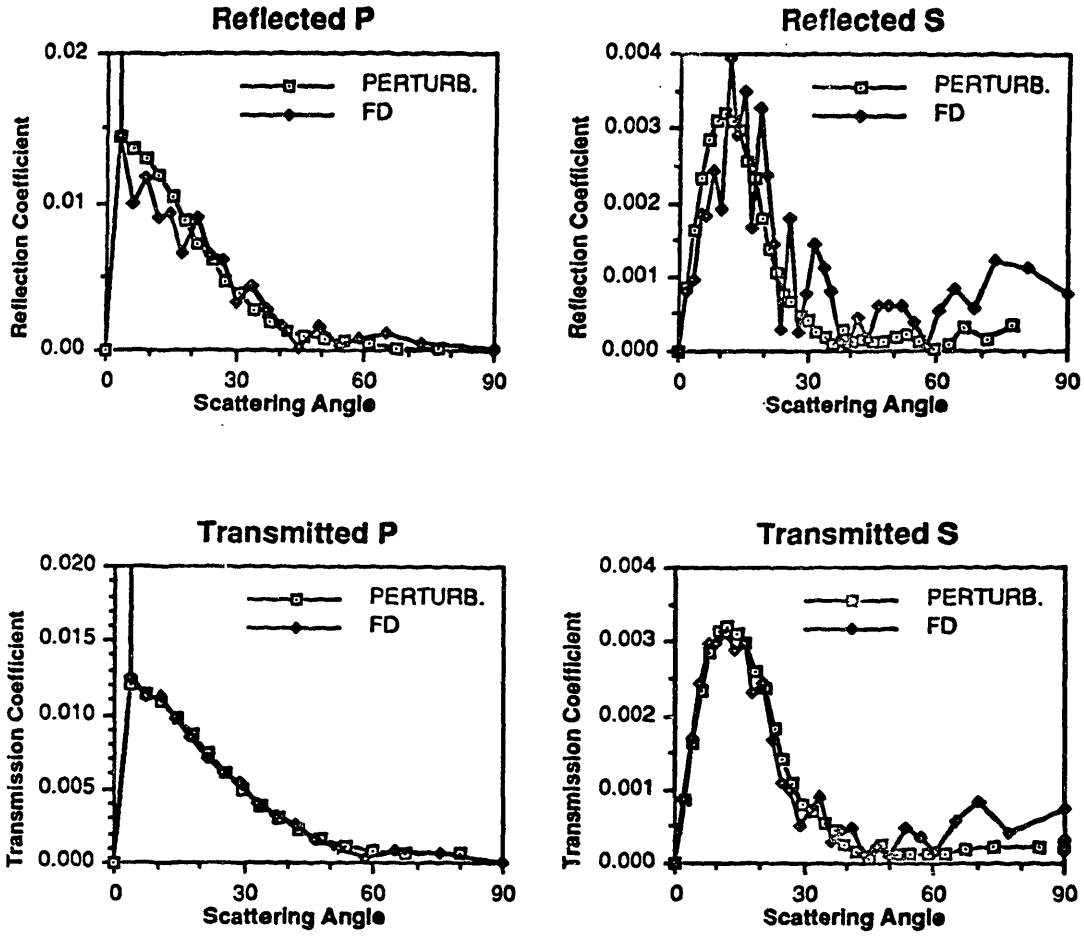

Figure 2-7: Comparison between P and S wave reflection and transmission coefficients generated from the finite difference and perturbation methods for the model shown in Figure 2-2.

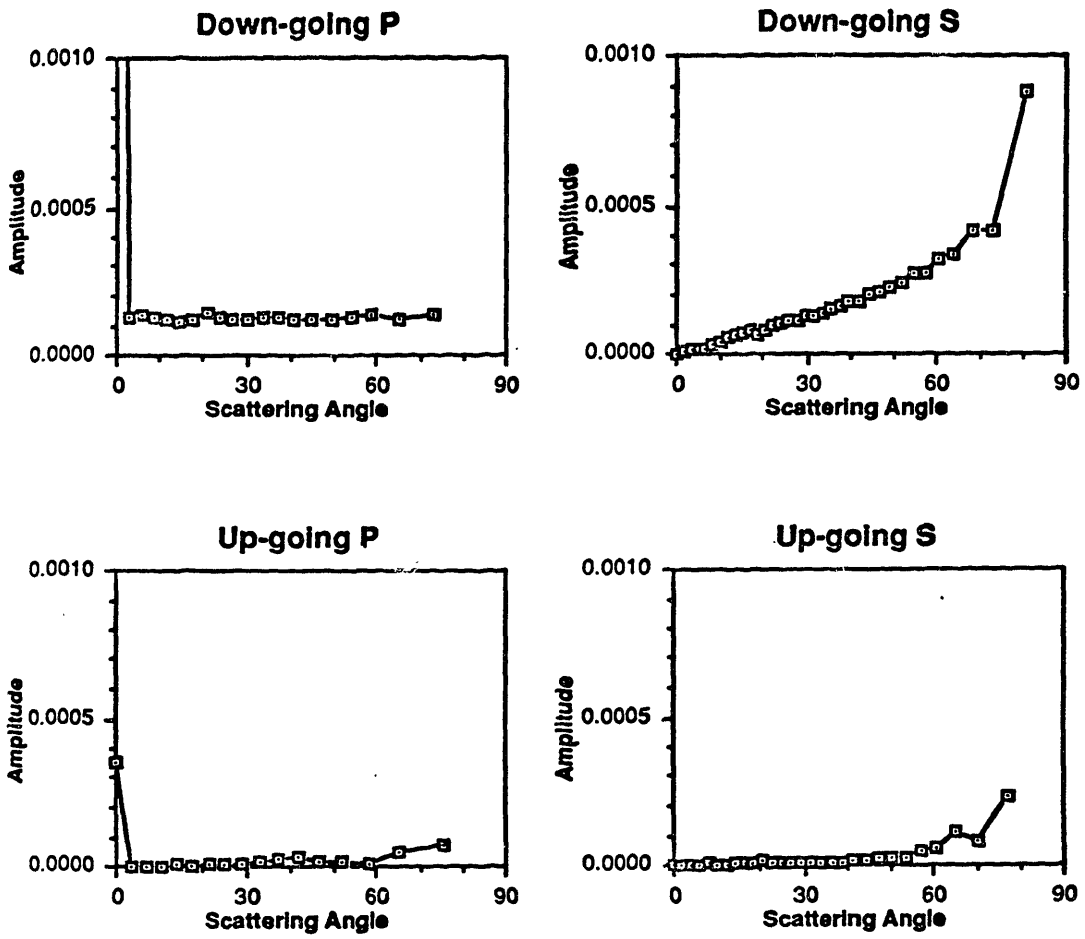

Figure 2-8: Amplitudes of waves incident on the interface corresponding to the scattered wave amplitudes shown in Figure 2-7. These are provided as a measure of the error versus angle. The down-going P wave in the upper medium has unit amplitude at zero angle.

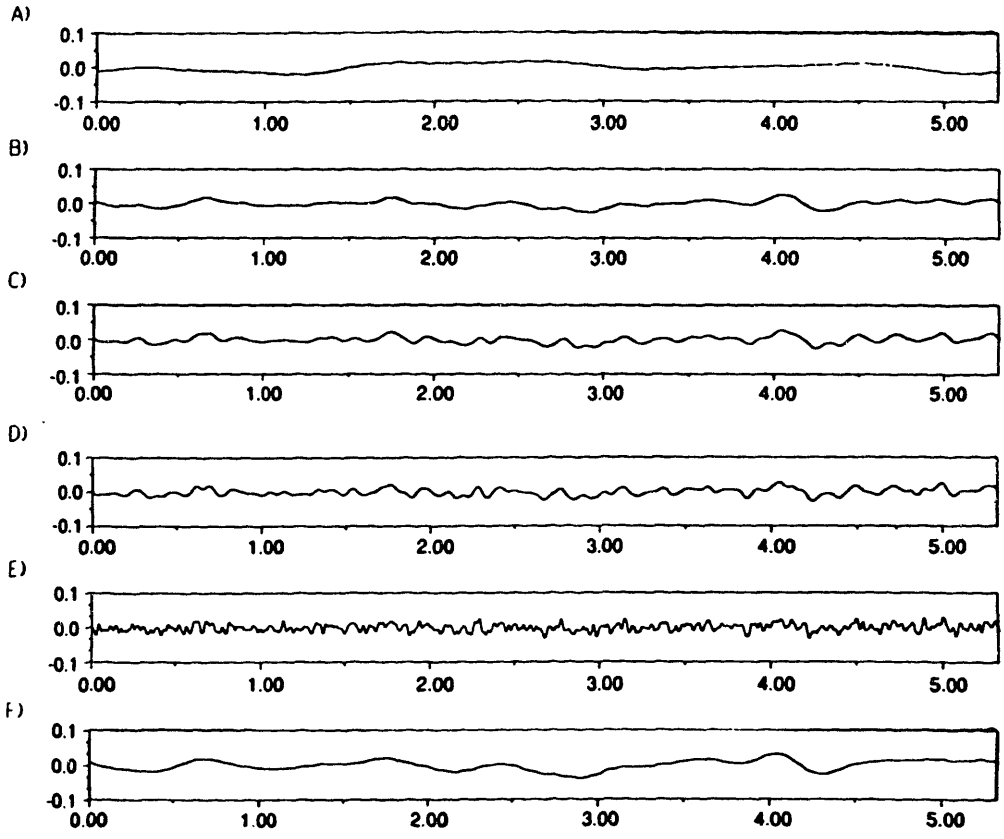

Figure 2-9: Interface functions used in comparison of reflection and transmission coefficients derived from the perturbation method with those derived from the finite difference method. The interfaces have a Gaussian autocorelation function with RMS height, correlation length, and RMS slope for each interface listed in Table 2.2. The functions are displayed in units of kilometers with two times vertical exaggeration.

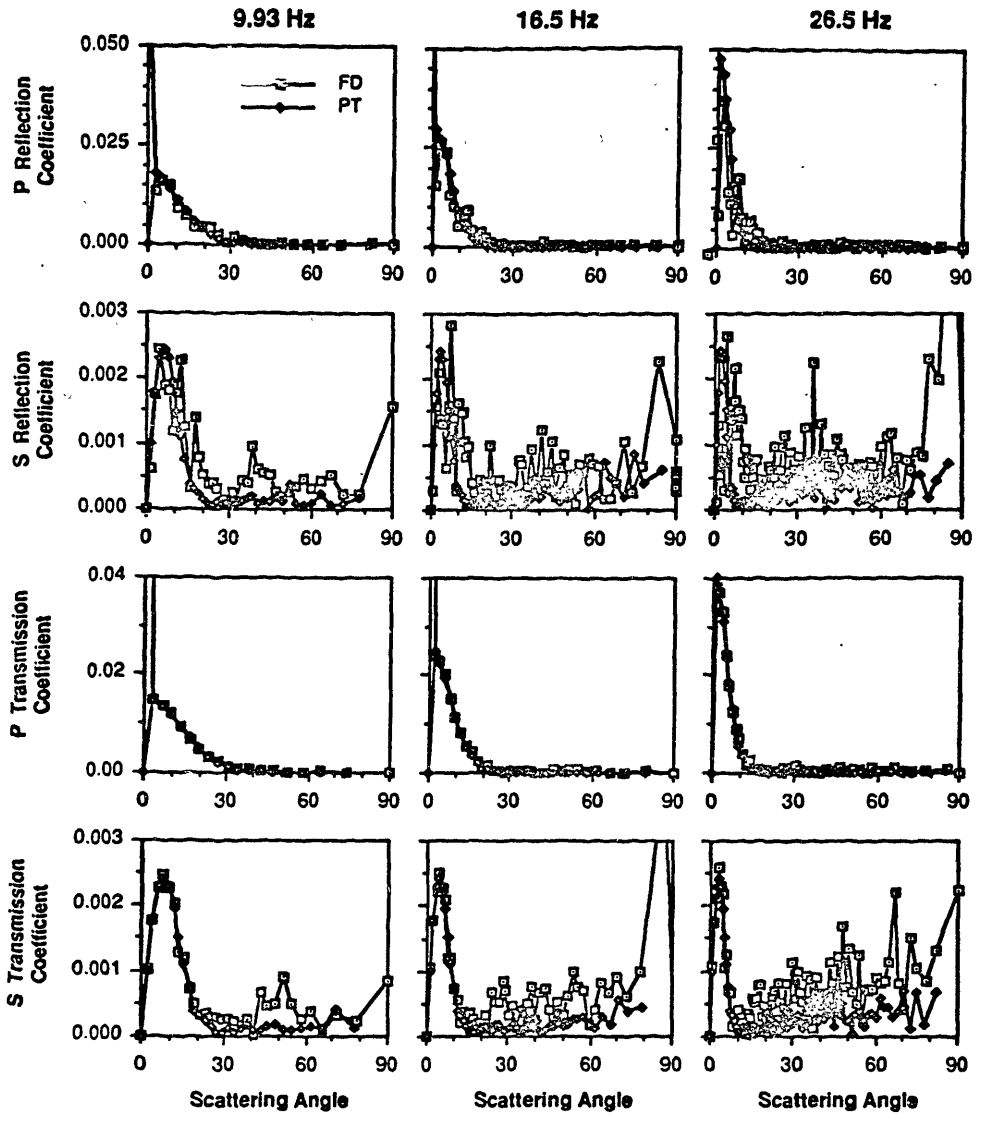

Figure 10a: Comparison of reflection and transmission coefficients derived from the perturbation and finite difference methods for model A. The parameters of the rough interface are given in Table 2.2 and the interface function is illustrated in Figure 2-9.

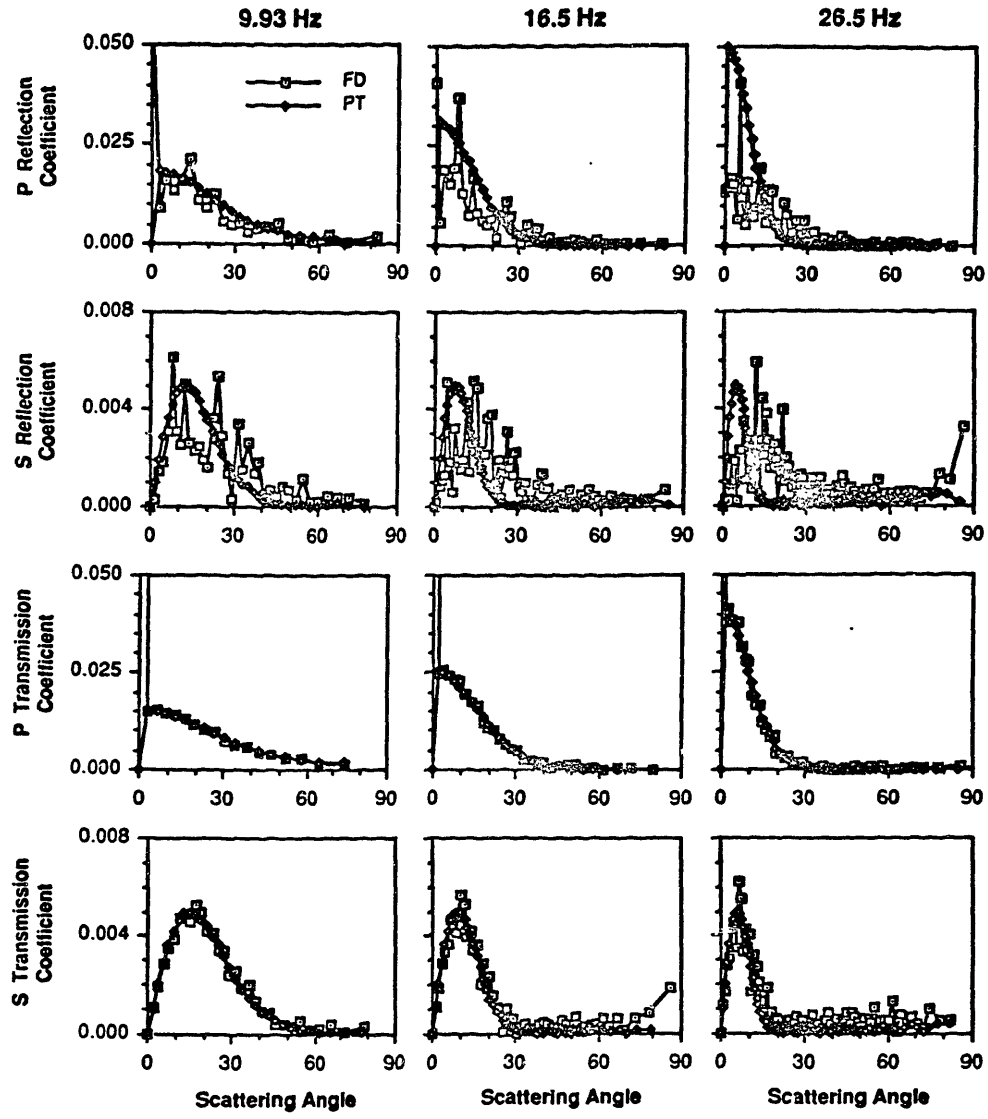

Figure 2-10b: Comparison of reflection and transmission coefficients derived from the perturbation and finite difference methods for model B. The parameters of the rough interface are given in Table 2.2 and the interface function is illustrated in Figure 2-9.

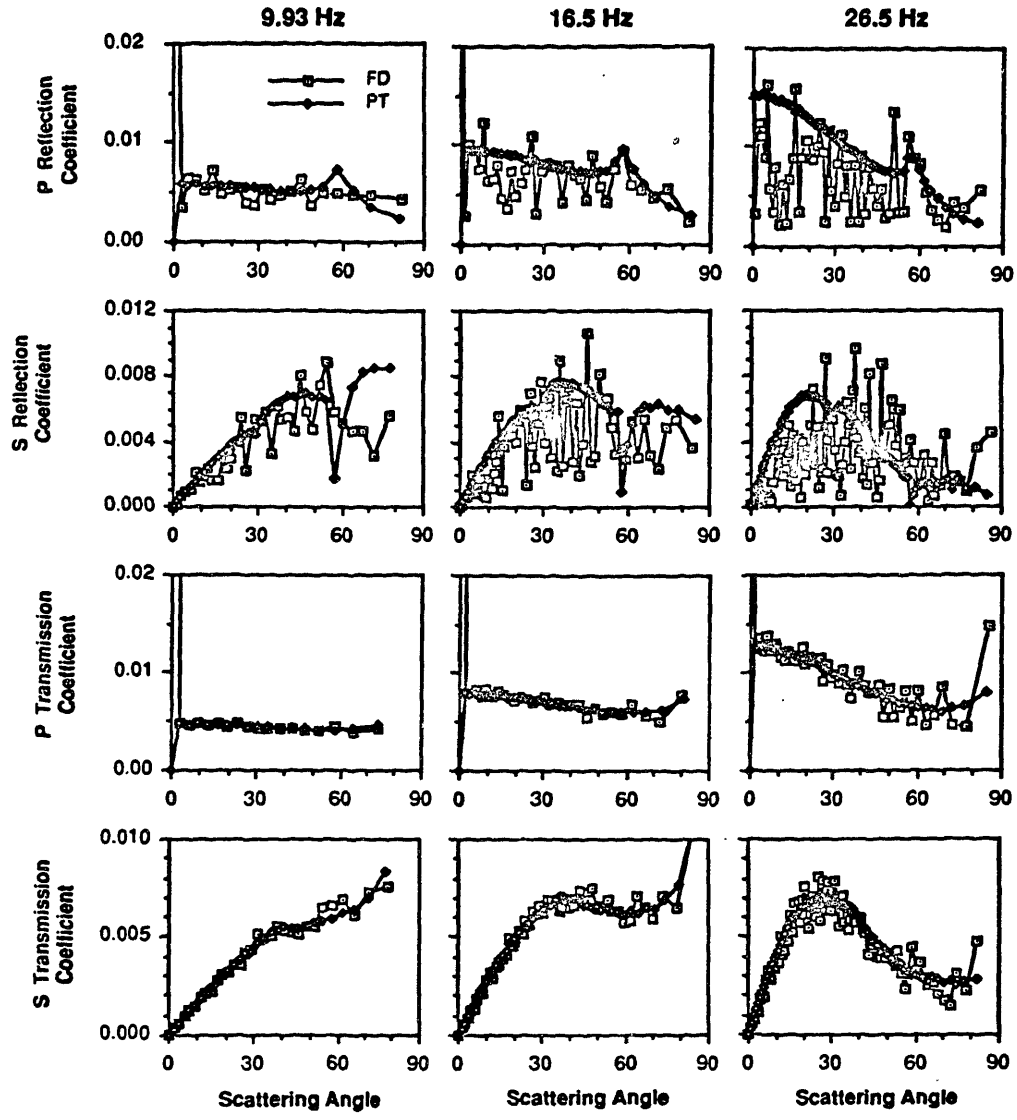

Figure 2-10c: Comparison of reflection and transmission coefficients derived from the perturbation and finite difference methods for model D. The parameters of the rough interface are given in Table 2.2 and the interface function is illustrated in Figure 2-9.

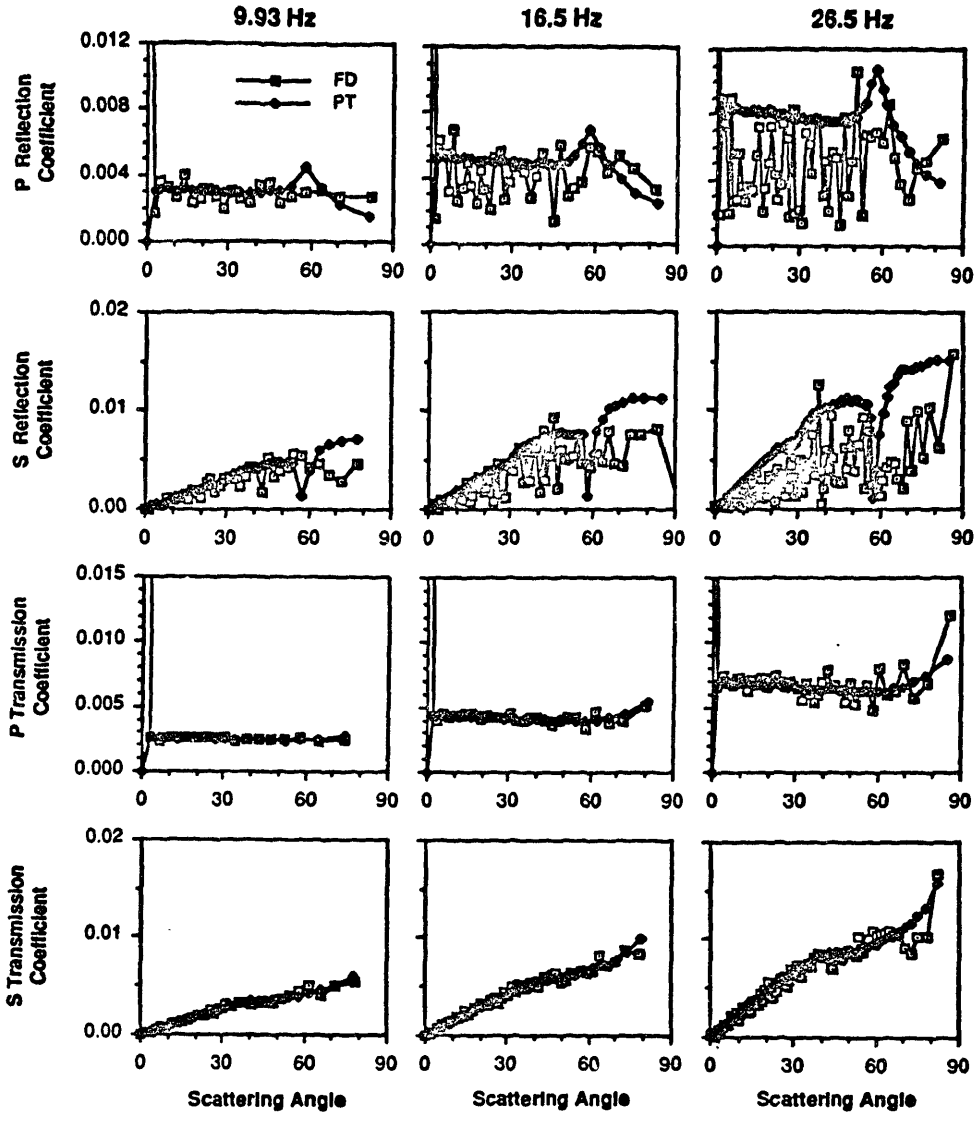

Figure 2-10d: Comparison of reflection and transmission coefficients derived from the perturbation and finite difference methods for model E. The parameters of the rough interface are given in Table 2.2 and the interface function is illustrated in Figure 2-9.

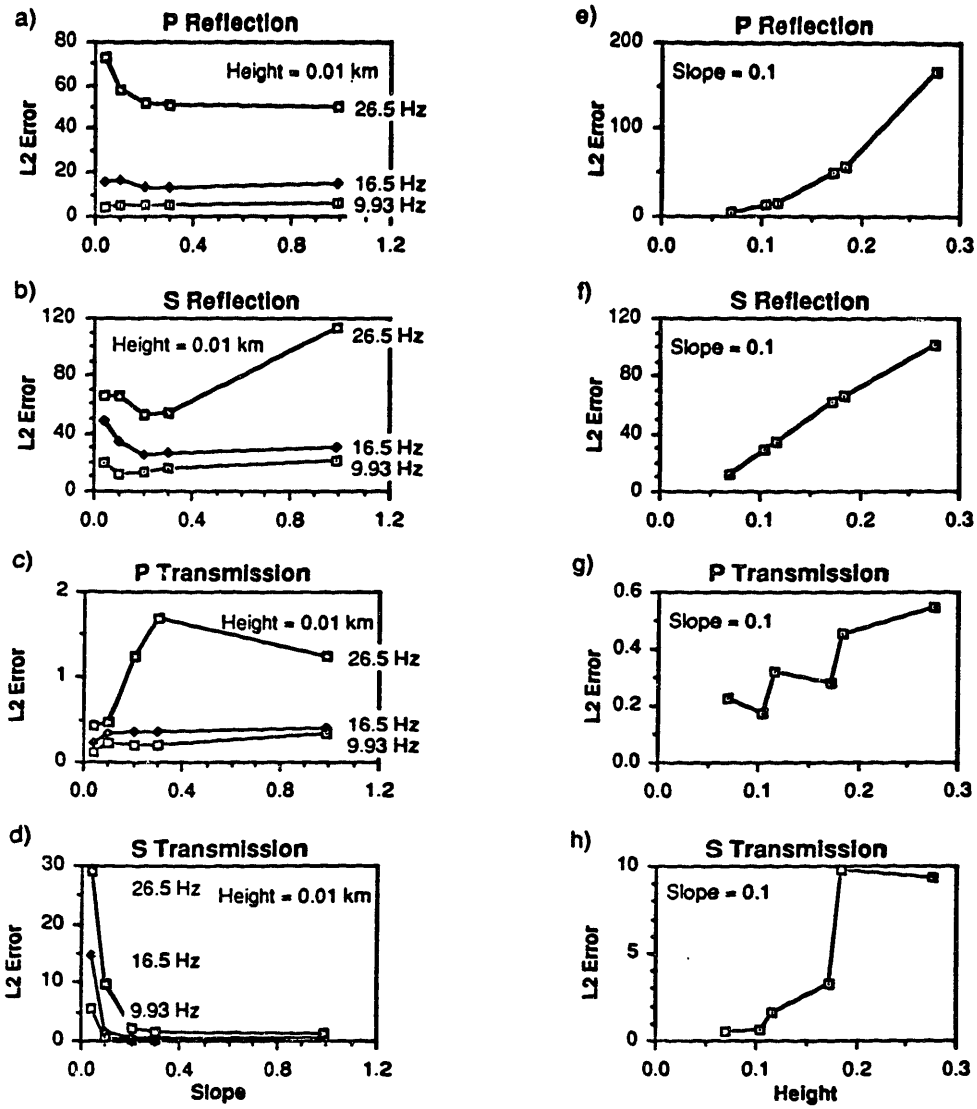

Figure 2-11: L_2 norm comparison of finite difference and perturbation method derived reflection and transmission coefficients. (a–d) RMS interface height is a constant 0.01 km and RMS slope varies from 0.037 to 0.99. RMS interface height for three frequencies can be expressed as 0.069, 0.11, and 0.18 S_1 wavelengths. (e–h) RMS interface slope is a constant 0.1 and with RMS interface height varies from 0.069 to 0.28 S_1 wavelengths.

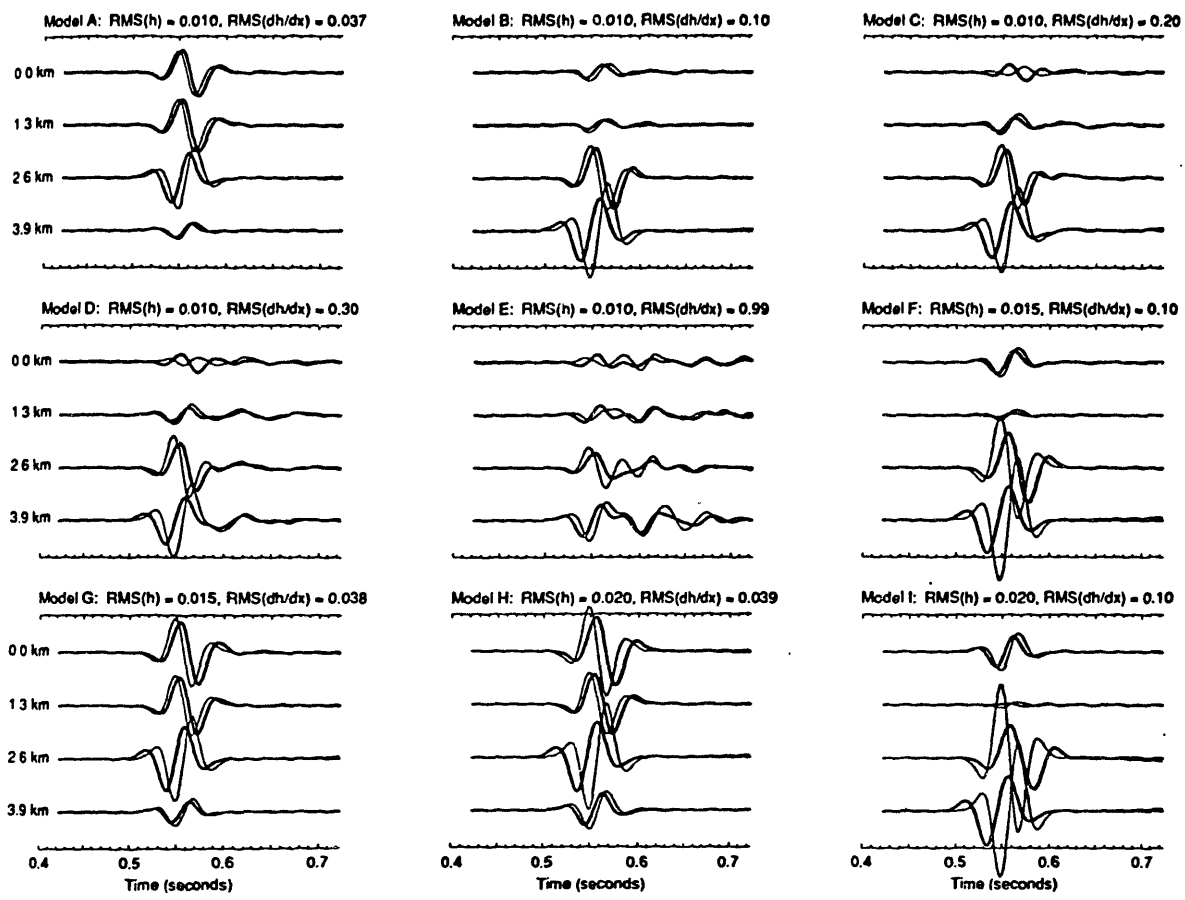

Figure 2-12: Representative scattered field seismograms generated for each of the interface functions parameterized in Table 2.3. The source is a normally incident plane wave with an 18 Hz Ricker time function. The bold curves are finite difference solutions, and the lighter curves are perturbation solutions. The four vertical component receivers are 0.0666 km above the mean planar interface at horizontal offsets of 0.0133, 1.35, 2.68, and 4.02 km. All seismograms are plotted at the same scale.

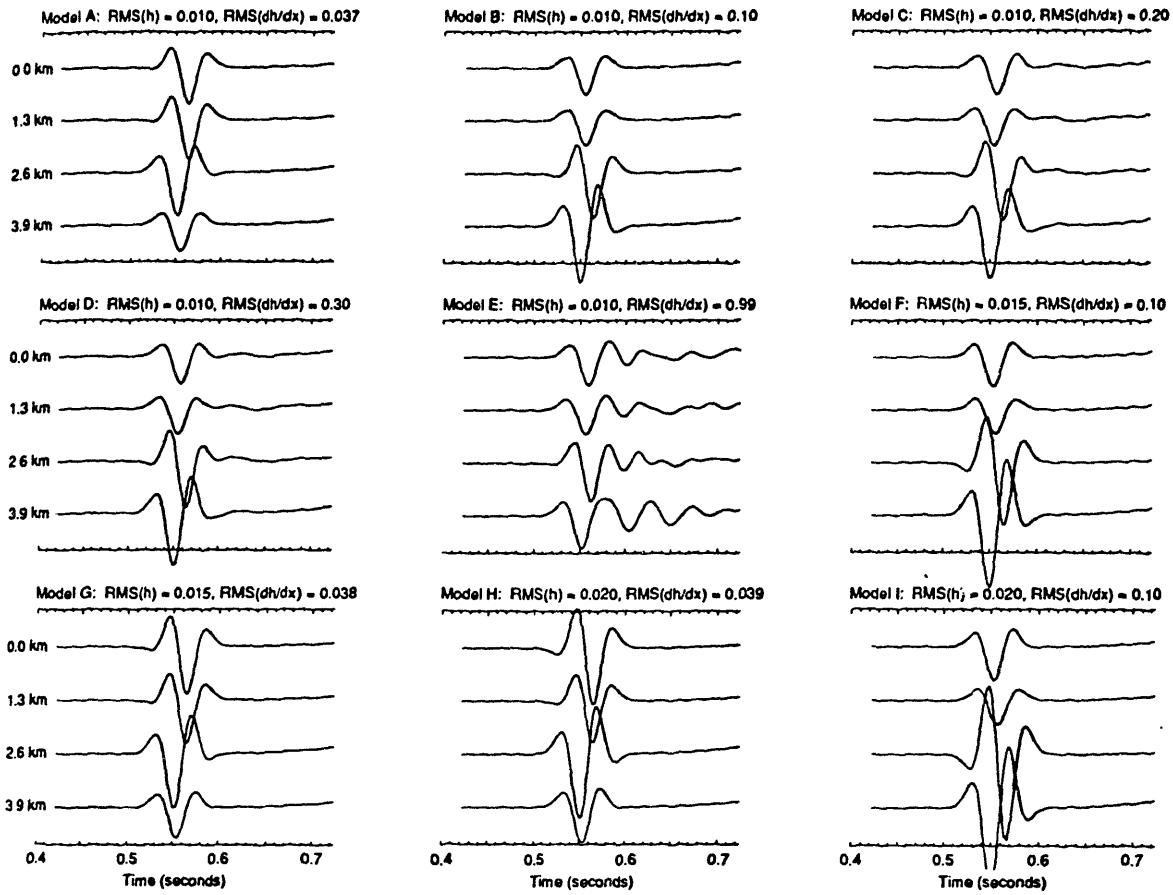

Figure 2-13: The seismograms of Figure 2-12 that were generated by the perturbation method are shown here with the background reflected field included in order to show the total waveform (minus the source wave). Plotted at the same scale as Figure 2-12.

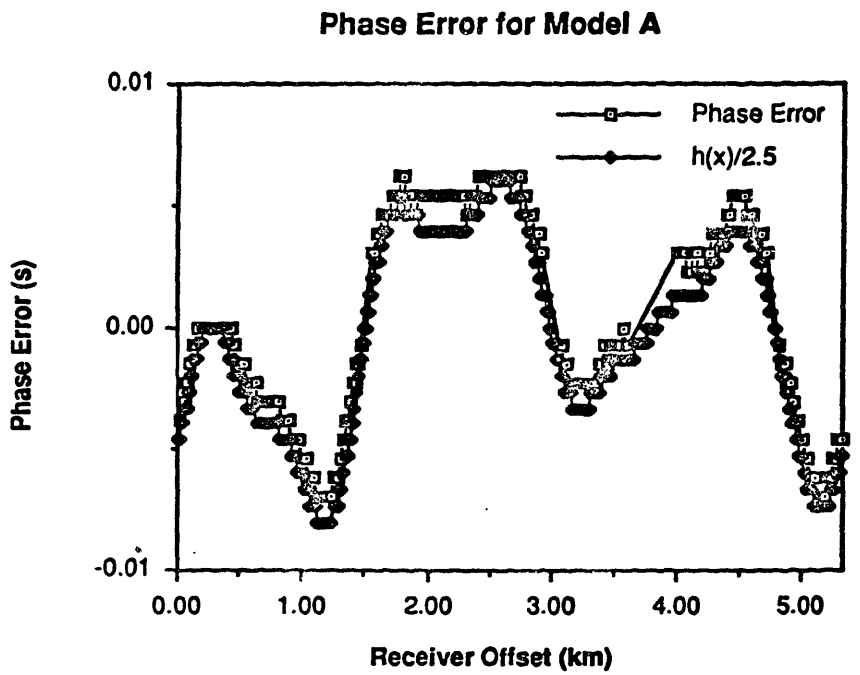

Figure 2-14: traveltime error $\widehat{\Delta t}$ plotted against seismogram offset x for Model A. Shown overlain is a plot of the one-way, vertical P wave traveltime associated with the interface function ($\frac{h(x)}{\alpha_1}$).

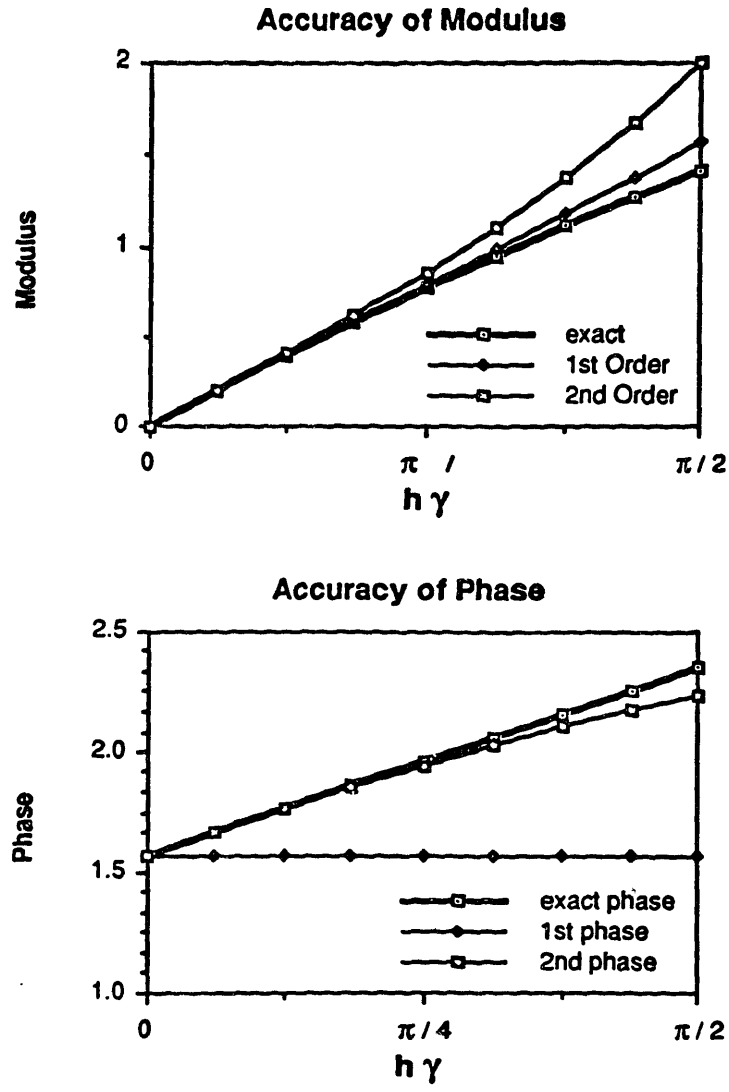

Figure 2-15: Comparison of first and second order approximations of $e^{ih\gamma} - 1$, which is the form of the term responsible for phase and amplitude shifts due to interface height. The first order approximation is $e^{ih\gamma} - 1 \approx ih\gamma$, and the second order approximation is $e^{ih\gamma} - 1 \approx ih\gamma - \frac{1}{2!}(h\gamma)^2$. (a) Modulus of the approximation. (b) Phase of the approximation in radians.

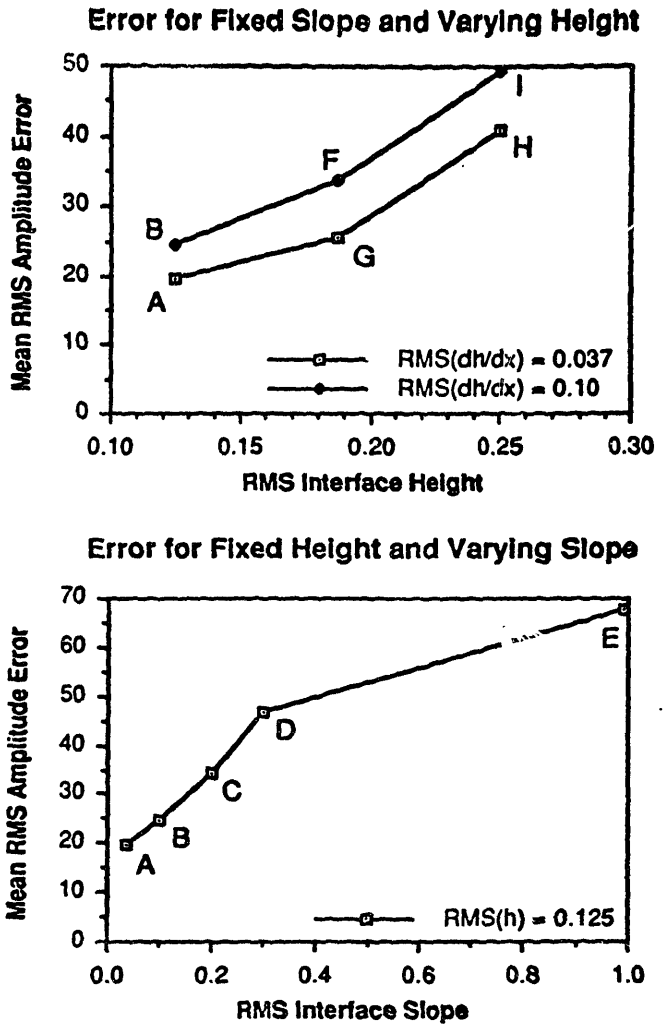

Figure 2-16: RMS amplitude error in the comparison of perturbation and finite difference derived seismograms. RMS amplitude error is measured after each perturbation method seismogram has been shifted in time relative to the complementary finite difference siesmogram such that the RMS amplitude error is minimized. The error for each model is the average of the RMS errors of the seismograms in the model. This mean error is plotted against RMS height for two values of RMS slope, and against slope for a fixed RMS height. Interface height is in units of S_1 wavelengths. The data points are labeled with their model names.

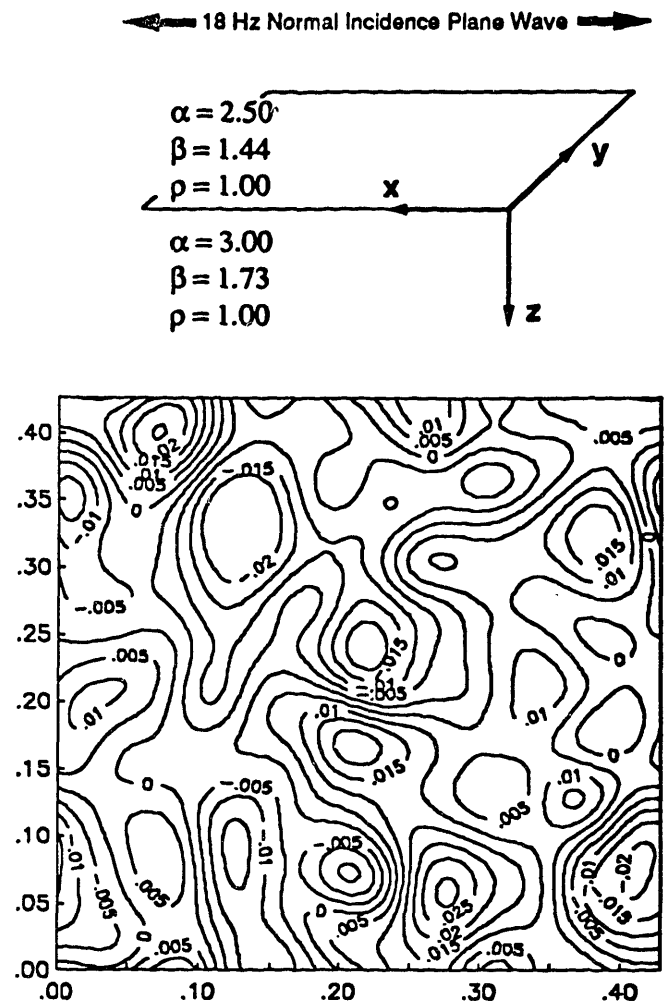

Figure 2-17: Three-dimensional rough interface scattering model. The auto-correlation function of the interface is a two-dimensional Gaussian with x and y correlation lengths of 2.4 S_1 wavelengths (0.19 km), an RMS height of 0.125 S_1 wavelengths (0.010 km), and an RMS slope of 0.30. Contours and axes are labeled in kilometers.

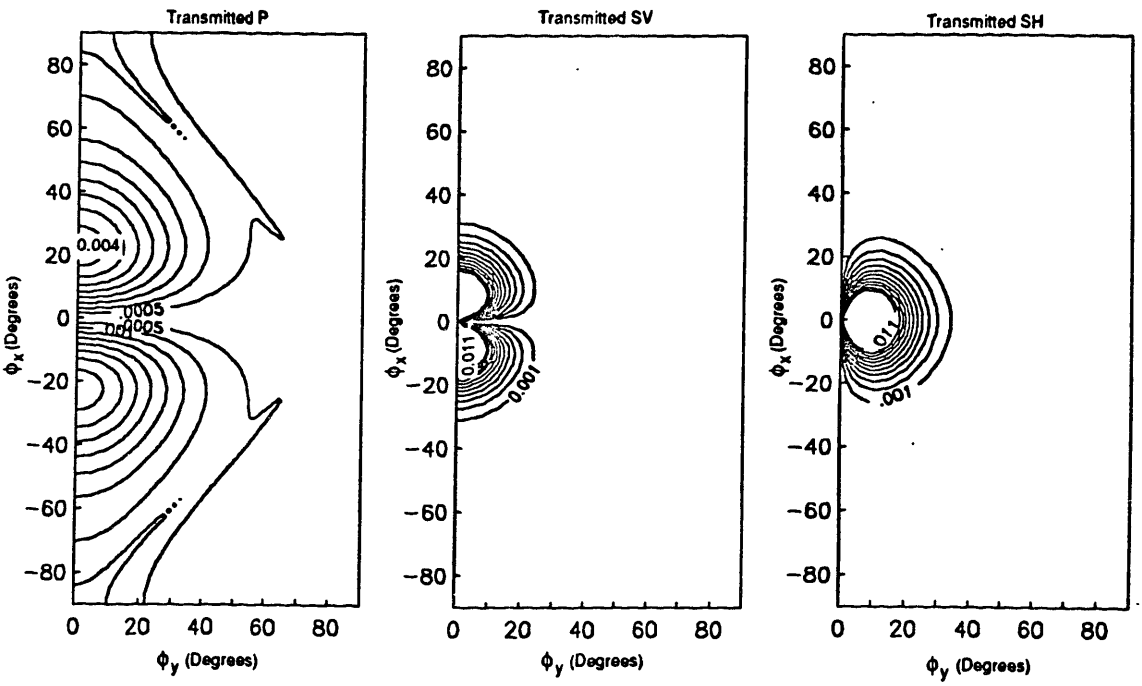

Figure 2-18: Transmission coefficients for the model in Figure 2-17. The source is an 18 Hz SV plane wave at normal incidence with particle motion in the x-direction.

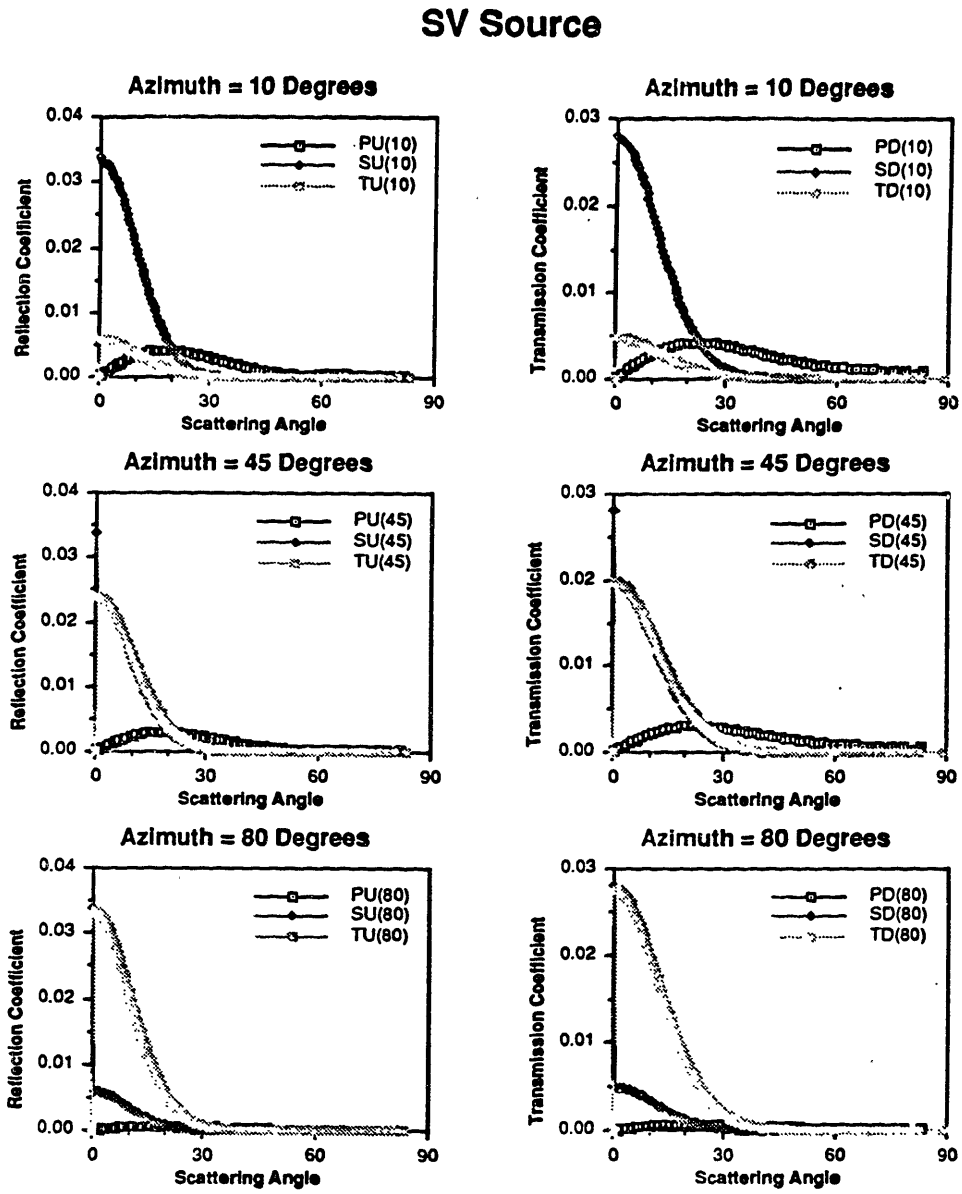

Figure 2-19: Cross-sections of the reflection and transmission coefficients in Figure 2-18 along 10°, 45°, and 80°azimuths. PU, SU, and TU and PD, SD, and TD are the up- and down-going P, SV, and SH scattering coefficients.

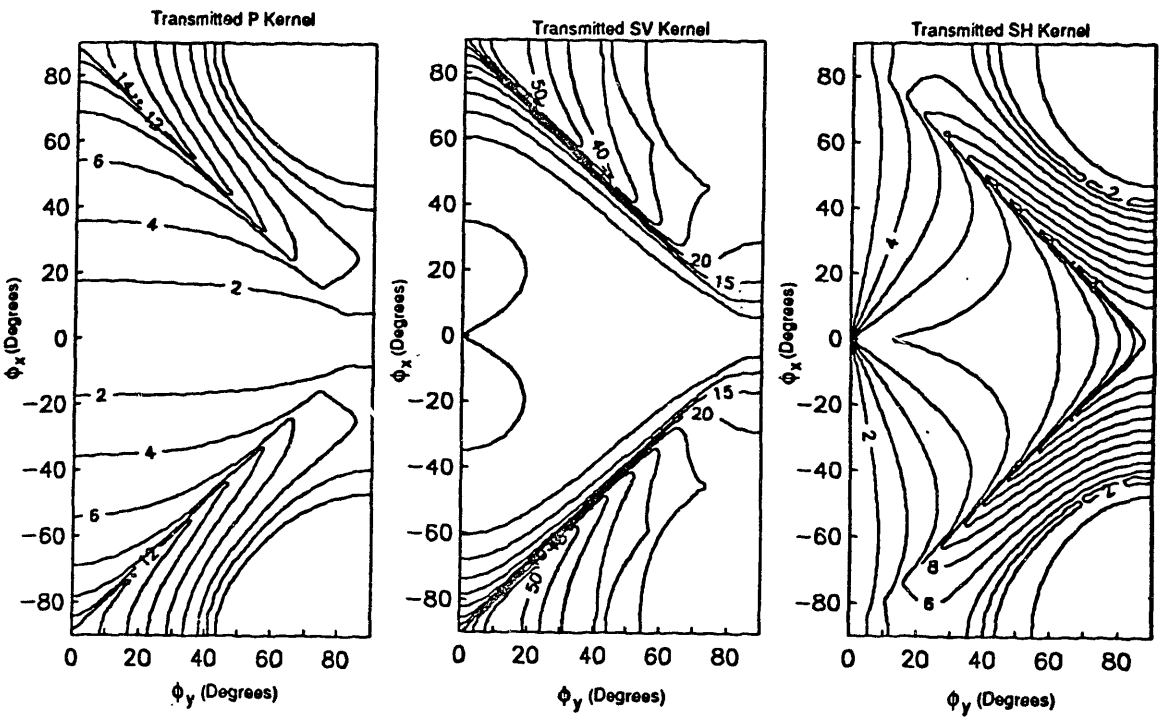

Figure 2-20: Transmission scattering kernels for the model in Figure 2-17.

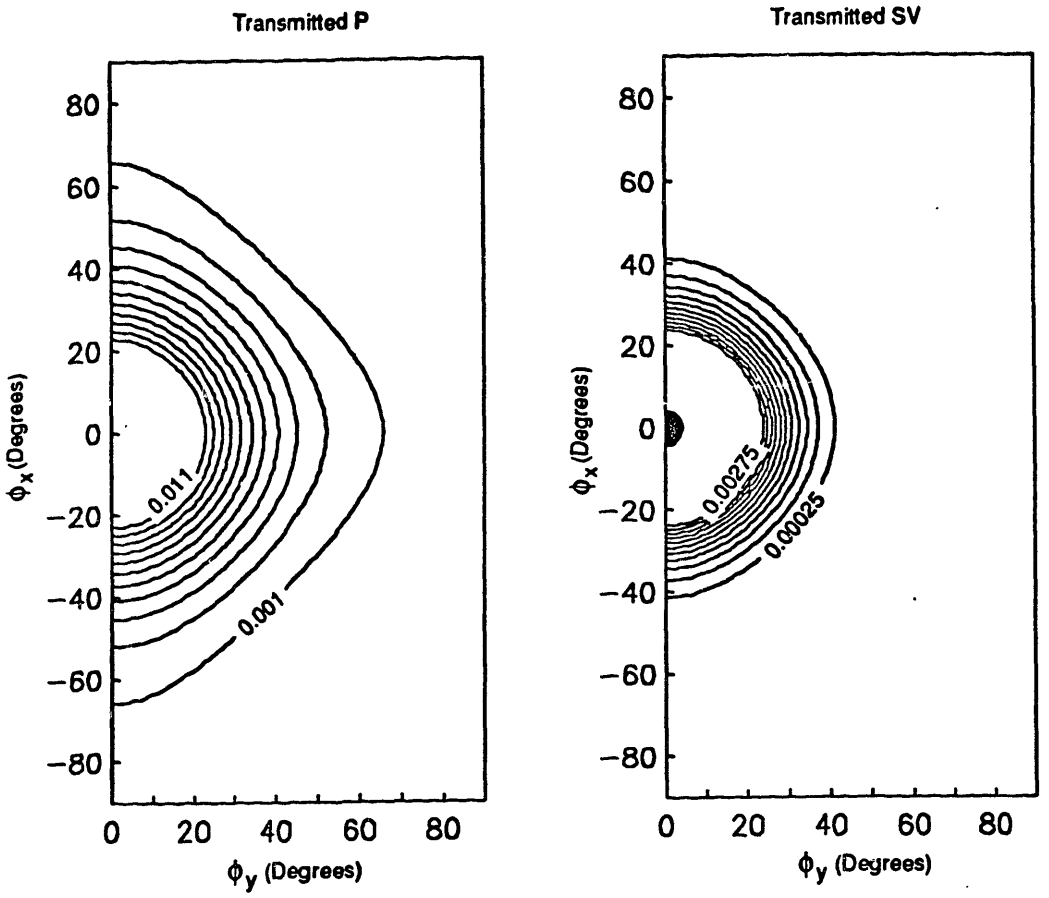

Figure 2-21: Transmission coefficients for the model in Figure 2-17. The source is an 18 Hz P plane wave at normal incidence.

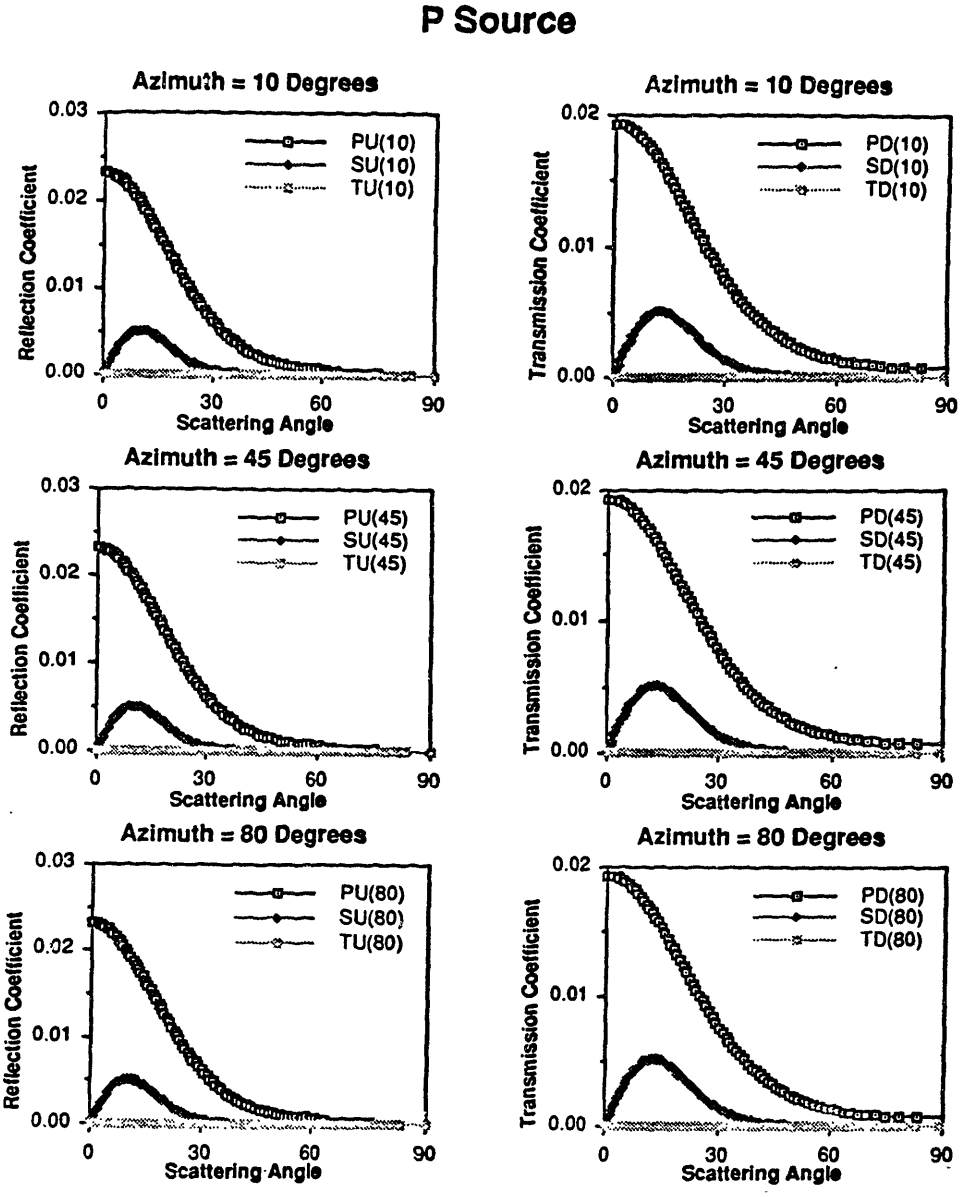

Figure 2-22: Cross-sections of the reflection and transmission coefficients in Figure 2-21 along 10°, 45°, and 80°azimuths. PU, SU, and TU and PD, SD, and TD are the up- and down-going P, SV, and SH scattering coefficients.

Chapter 3

PROPERTIES OF THE SCATTERED FIELD

3.1 ABSTRACT

The characteristics of an elastic wavefield scattered from a rough interface are controlled by the material contrast at the interface, the autocorrelation function of the interface height, and the source wave frequency and incidence angle. A perturbation method is presented here, based on small interface height and slopes and small material contrasts, which reduces the three-dimensional scattered field equations to simple linear forms which decouple the influence of contrasts in P and S velocity and density on the scattered wavefield. From these simple expressions, we discuss the three-dimensional behavior of the scattered wavefield relative to changes in interface properties.

3.2 INTRODUCTION

The complex behavior of three-dimensional waves scattered from a rough interface can be accurately modeled using approximate methods ((Kuperman and Schmidt, 1989; Prange and Toksöz, 1989)). Although these methods provide fast ways to generate scattering coefficients and seismograms, the 6×6 matrix operations necessary to obtain the solution

hide the underlying features of the equations which control the sensitivity of the scattered wave field to material contrasts and source wavelet. In this chapter we further simplify the perturbation equations by making a small material contrast approximation. In these new equations, the scattered wave field is composed of a sum of three terms corresponding to the contributions of $\frac{\Delta\alpha}{\alpha}$, $\frac{\Delta\beta}{\beta}$, and $\frac{\Delta\rho}{\rho}$ to the scattered wave field. These equations allow us to isolate the effects of the three material contrast parameters.

3.3 FIRST ORDER ANALYSIS

In this section we derive simple formulae relating the P, SV, and SH scattering kernels to the interface material contrast. From these simple formulae, the dependence of scattered field phase and radiation patterns on the interface material contrast can be shown. The complete formulae for the perturbation approximation to the scattered field were presented in chapter 2. These will be summarized, and then reduced to a more compact and more easily interpreted form by using a first order analysis which assumes a small scattering angle and small material contrast at the interface.

3.3.1 The Perturbation Equations

A brief review is presented here of the perturbation equations in chapter 2 that are relevant to the first order analysis to be performed. Using the methods of propagator matrix theory (Kennett, 1983), a three-dimensional elastic wave field can be described by a six-element displacement-stress vector $\underline{r}$ whose members are the three components of displacement and the three Cauchy stresses which are continuous across a welded horizontal planar interface:

$$\underline{r} = [u_x \; u_y \; u_z \; \tau_{xz} \; \tau_{yz} \; \tau_{zz}]^T, \tag{3.1}$$

where a superscript T denotes a matrix transpose, and where the interface is normal to the z-axis. Another way to represent an elastic wave field is by a six-element scattering

coefficient vector $\underline{b}$ whose members are the amplitude coefficients of the down- and up-going P, SV, and SH waves:

$$\underline{b} = [\grave{P}\ \grave{S}\ \grave{T}\ \acute{P}\ \acute{S}\ \acute{T}]^T. \tag{3.2}$$

$\underline{b}$ is related to $\underline{r}$ in the frequency-wavenumber domain by the formula

$$\underline{b} = \underline{\underline{F}}^{-1}\underline{r}, \tag{3.3}$$

where

$$\underline{\underline{F}}^{-1} = \begin{bmatrix} \frac{k_x\beta^2}{\alpha\omega} & \frac{k_y\beta^2}{\alpha\omega} & \frac{\beta^2(\nu^2-K^2)}{2\alpha\gamma\omega} & \frac{-ik_x}{2\alpha\gamma\rho\omega} & \frac{-ik_y}{2\alpha\gamma\rho\omega} & \frac{-i}{2\alpha\rho\omega} \\ \frac{k_x\beta(\nu^2-K^2)}{2\nu\omega K} & \frac{k_y\beta(\nu^2-K^2)}{2\nu\omega K} & \frac{-K\beta}{\omega} & \frac{-ik_x}{2K\beta\rho\omega} & \frac{-ik_y}{2K\beta\rho\omega} & \frac{iK}{2\beta\nu\rho\omega} \\ \frac{-k_y}{2K} & \frac{k_x}{2K} & 0 & \frac{ik_y}{2K\beta^2\nu\rho} & \frac{-ik_x}{2K\beta^2\nu\rho} & 0 \\ \frac{k_x\beta^2}{\alpha\omega} & \frac{k_y\beta^2}{\alpha\omega} & \frac{-\beta^2(\nu^2-K^2)}{2\alpha\gamma\omega} & \frac{ik_x}{2\alpha\gamma\rho\omega} & \frac{ik_y}{2\alpha\gamma\rho\omega} & \frac{-i}{2\alpha\rho\omega} \\ \frac{k_x\beta(\nu^2-K^2)}{2\nu\omega K} & \frac{k_y\beta(\nu^2-K^2)}{2\nu\omega K} & \frac{K\beta}{\omega} & \frac{ik_x}{2K\beta\rho\omega} & \frac{ik_y}{2K\beta\rho\omega} & \frac{iK}{2\beta\nu\rho\omega} \\ \frac{-k_y}{2K} & \frac{k_x}{2K} & 0 & \frac{-ik_y}{2K\beta^2\nu\rho} & \frac{ik_x}{2K\beta^2\nu\rho} & 0 \end{bmatrix} \tag{3.4}$$

The Fourier transform convention used here is given by

$$f(k_x,k_y,\omega) = \int\int_{-\infty}^{\infty}\int f(x,y,z)e^{i(-k_xx-k_yy+\omega t)}dxdydt \tag{3.5}$$

$$f(x,y,t) = \frac{1}{(2\pi)^3}\int\int_{-\infty}^{\infty}\int f(k_x,k_y,k_z)e^{i(k_xx+k_yy-\omega t)}dk_xdk_yd\omega \tag{3.6}$$

In the perturbation approximation to scattering from a rough interface, a zero-mean rough interface height perturbation $h(x,y)$ is defined relative to a planar interface. The total field is then expressed as the sum of a background field $\underline{r_0}$ and the scattered field $\underline{r_s}$, where $\underline{r_0}$ is the solution for the planar interface model and $\underline{r_s}$ is the perturbation to

$\underline{r}_0$ which accounts for the interface roughness. This scattered field is expressed as the field resulting from an equivalent source $\underline{s}$ at the mean depth of the rough interface. This source has the form (2.18; Chapter 2)

$$\underline{s}(k_x, k_y) = \frac{1}{4\pi^2}\int_{-\infty}^{\infty} h(k_x - k'_x, k_y - k'_y)\underline{\underline{L}}(k_x, k_y; k'_x, k'_y)\underline{r}_0(k'_x, k'_y)\, dk'_x\, dk'_y \quad (3.7)$$

$$= \underline{r}_{s2} - \underline{r}_{s1}, \quad (3.8)$$

where $\underline{\underline{L}}(k_x, k_y; k'_x, k'_y)$ is defined by (2.19; Chapter 2), and $\underline{r}_{s1}$ and $\underline{r}_{s2}$ are the values of the displacement-stress vectors in media 1 and 2 at the depth of the mean planar interface. $\underline{s}$ is dependent on the interface roughness function, the material contrast at the interface, and the source which illuminates the interface.

To study reflection and transmission coefficients we require a plane-wave source. Hence, the background field $\underline{r}_0$ has the form

$$\underline{r}_0(k'_x, k'_y) = 4\pi^2 \bar{\underline{r}}_0(k^0_x, k^0_y)\delta(k'_x - k^0_x, k'_y - k^0_y), \quad (3.9)$$

where $\bar{\underline{r}}_0$ is the plane-wave background field displacement-stress vector, $4\pi^2$ scales the wave to have unit amplitude in the space domain, and the frequency dependence is implied. Substituting (3.9) into (3.7) yields an equivalent source of the form

$$\underline{s}(k_x, k_y) = h(k_x - k^0_x, k_y - k^0_y)\underline{\underline{L}}(k_x, k_y; k^0_x, k^0_y)\bar{\underline{r}}_0(k^0_x, k^0_y). \quad (3.10)$$

From (3.10) we see that the equivalent source in this case can be factored into two terms: one which is the interface roughness function h, and the other dependent only on the material contrast and the source. The latter term is called the scattering kernel (Prange and Toksöz, 1989), and is denoted by

$$\underline{\underline{\Phi}}(k_x, k_y; k^p_x, k^p_y) = \underline{\underline{L}}(k_x, k_y; k^p_x, k^p_y)\bar{\underline{r}}_0(k^p_x, k^p_y) \quad (3.11)$$

In our discussions of rough interface transmission and reflection coefficients, scattering kernels will be used to separate interface roughness effects from source and material

contrast effects.

3.3.2 First Order Analysis

In order to evaluate reflection coefficients, we will consider two infinite half-spaces joined at a welded rough interface whose average depth is taken to be $z = 0$, and whose height function is specified by $h(x, y)$. A plane wave source is in medium one, the upper medium. The P and S wave velocities and densities of the two media are given by α_1, β_1, ρ_1 and α_2, β_2, ρ_2. The material contrast between the two media is small, and is expressed in terms of the perturbation parameters $\Delta\alpha = \alpha_2 - \alpha_1$, $\Delta\beta = \beta_2 - \beta_1$, and $\Delta\rho = \rho_2 - \rho_1$, which apply to the average parameters α, β, and ρ. Substituting these perturbations into the definition of $\underline{\underline{L}}$, (2.19; Chapter 2), and keeping only first order terms,

$$\underline{\underline{L}} = \frac{\Delta\alpha}{\alpha}\underline{\underline{L}}_\alpha + \frac{\Delta\beta}{\beta}\underline{\underline{L}}_\beta + \frac{\Delta\rho}{\rho}\underline{\underline{L}}_\rho \tag{3.12}$$

where $\underline{\underline{L}}_\alpha$, $\underline{\underline{L}}_\beta$, and $\underline{\underline{L}}_\rho$ are defined by

$$\underline{\underline{L}}_\alpha = \begin{bmatrix} 0 & 0 & 0 & 0 & 0 & 0 \\ 0 & 0 & 0 & 0 & 0 & 0 \\ -4ik'_x\frac{\beta^2}{\alpha^2} & 0 & 0 & 0 & 0 & \frac{2}{\rho\alpha^2} \\ -8k_xk'_x\rho\frac{\beta^4}{\alpha^2} & 0 & 0 & 0 & 0 & 4ik_x\frac{\beta^2}{\alpha^2} \\ -8k_yk'_x\rho\frac{\beta^4}{\alpha^2} & 0 & 0 & 0 & 0 & 4ik_y\frac{\beta^2}{\alpha^2} \\ 0 & 0 & 0 & 0 & 0 & 0 \end{bmatrix} \tag{3.13}$$

$$\underline{\underline{L}}_\beta = \begin{bmatrix} 0 & 0 & 0 & \frac{2}{\rho\beta^2} & 0 & 0 \\ 0 & 0 & 0 & 0 & \frac{2}{\rho\beta^2} & 0 \\ 4ik'_x\frac{\beta^2}{\alpha^2} & 0 & 0 & 0 & 0 & 0 \\ -8k_xk'_x\rho\frac{\beta^2}{\alpha^2}(\alpha^2-2\beta^2) & -2k_yk'_x\rho\beta^2 & 0 & 0 & 0 & -4ik_x\frac{\beta^2}{\alpha^2} \\ 4k_yk'_x\rho\frac{\beta^2}{\alpha^2}(4\beta^2-\alpha^2) & -2k_xk'_x\rho\beta^2 & 0 & 0 & 0 & -4ik_y\frac{\beta^2}{\alpha^2} \\ 0 & 0 & 0 & 0 & 0 & 0 \end{bmatrix} \tag{3.14}$$

$$\underline{\underline{L}}_\rho = \begin{bmatrix} 0 & 0 & 0 & \frac{1}{\rho\beta^2} & 0 & 0 \\ 0 & 0 & 0 & 0 & \frac{1}{\rho\beta^2} & 0 \\ 0 & 0 & 0 & 0 & 0 & \frac{1}{\rho\alpha^2} \\ \omega^2\rho - 4k_xk'_x\rho\frac{\beta^2}{\alpha^2}(\alpha^2-\beta^2) & -k_yk'_x\rho\beta^2 & 0 & 0 & 0 & 0 \\ -2k_yk'_x\rho\frac{\beta^2}{\alpha^2}(\alpha^2-2\beta^2) & \omega^2\rho - k_xk'_x\rho\beta^2 & 0 & 0 & 0 & 0 \\ 0 & 0 & \omega^2\rho & 0 & 0 & 0 \end{bmatrix} \tag{3.15}$$

Substituting this decomposition of $\underline{\underline{L}}$ into (3.10) yields

$$\underline{s}(k_x,k_y) = h(k_x-k_x^0,k_y-k_y^0)[\frac{\Delta\alpha}{\alpha}\underline{\underline{L}}_\alpha + \frac{\Delta\beta}{\beta}\underline{\underline{L}}_\beta + \frac{\Delta\rho}{\rho}\underline{\underline{L}}_\rho]\underline{\bar{r}}_0 \tag{3.16}$$

$$= h(k_x-k_x^0,k_y-k_y^0)[\frac{\Delta\alpha}{\alpha}\underline{\Phi}_\alpha + \frac{\Delta\beta}{\beta}\underline{\Phi}_\beta + \frac{\Delta\rho}{\rho}\underline{\Phi}_\rho] \tag{3.17}$$

where the analog of (3.11) was used to define the α, β, and ρ components of the scattering kernel Φ as $\underline{\Phi}_{\{\alpha,\beta,\rho\}} = \underline{\underline{L}}_{\{\alpha,\beta,\rho\}}\underline{r}_0$.

Since this first-order approximation of $\underline{\underline{L}}$ contains no zero-order terms, a first-order approximation of $\underline{s} = h\underline{\underline{L}}\underline{r}_0$ requires only a zero-order approximation of $\underline{\bar{r}}_0$. To zero

order, the background field $\underline{r}_0$ is approximated by the incident field in the absence of scattering, yielding

$$\underline{r}_0 = \underline{\underline{F}}\,\underline{b}_0 \tag{3.18}$$

where $\underline{\underline{F}}$ uses the average material parameters (a zero-order approximation) and $\underline{b}_0$, the wave coefficient vector defined in (3.2), is $[1\ 0\ 0\ 0\ 0\ 0]^T$ for a P source, $[0\ 1\ 0\ 0\ 0\ 0]^T$ for an SV source, and $[0\ 0\ 1\ 0\ 0\ 0]^T$ for an SH source. Results for P and SV sources will be presented in two separate sections.

The equivalent source (3.16) will be converted into scattering coefficients using (3.8) and (3.3). This is done by solving the equation

$$\begin{aligned}
\underline{s} &= \underline{r}_{s2} - \underline{r}_{s1} = \underline{\underline{F}}_2\underline{b}_2 - \underline{\underline{F}}_1\underline{b}_1 && (3.19)\\
&\approx \underline{\underline{F}}(\underline{b}_2 - \underline{b}_1) && (3.20)\\
&= \underline{\underline{F}}\begin{bmatrix} 1 & 0 & 0 & 0 & 0 & 0\\ 0 & 1 & 0 & 0 & 0 & 0\\ 0 & 0 & 1 & 0 & 0 & 0\\ 0 & 0 & 0 & -1 & 0 & 0\\ 0 & 0 & 0 & 0 & -1 & 0\\ 0 & 0 & 0 & 0 & 0 & -1 \end{bmatrix}\hat{\underline{b}} && (3.21)\\
&= \underline{\underline{\hat{F}}}\,\hat{\underline{b}} && (3.22)
\end{aligned}$$

where the radiation conditions require that $\underline{b}_1 = [0\ 0\ 0\ \acute{P}_1\ \acute{S}_1\ \acute{T}_1]$ and $\underline{b}_2 = [\grave{P}_2\ \grave{S}_2\ \grave{T}_2\ 0\ 0\ 0]$, and $\hat{\underline{b}} = [\grave{P}_2\ \grave{S}_2\ \grave{T}_2\ \acute{P}_1\ \acute{S}_1\ \acute{T}_1]$ contains the non-zero wave coefficients of $\underline{b}_1$ and $\underline{b}_2$. The step from (3.19) to (3.20) approximates the radiation from a source at an interface of small material contrast by the radiation from a source in an unbounded medium of average material properties. This is done to reduce the inverse operator to a known simple form of $\underline{\underline{F}}^{-1}$ given in (3.4). Using (3.17) and (3.22), $\hat{\underline{b}}$ can be expressed as

$$\hat{\underline{b}}(k_x, k_y) = h(k_x - k_x^0, k_y - k_y^0)\left(\frac{\Delta\alpha}{\alpha}\hat{\underline{b}}_\alpha + \frac{\Delta\beta}{\beta}\hat{\underline{b}}_\beta + \frac{\Delta\rho}{\rho}\hat{\underline{b}}_\rho\right), \tag{3.23}$$

where $\hat{\underline{b}}_\alpha$, $\hat{\underline{b}}_\beta$, and $\hat{\underline{b}}_\rho$ are defined in terms of the scattering kernels Φ_α, Φ_β, and Φ_ρ by

$$\begin{aligned} \hat{\underline{b}}_\alpha &= \hat{\underline{\underline{F}}}^{-1}\underline{\Phi}_\alpha \\ \hat{\underline{b}}_\beta &= \hat{\underline{\underline{F}}}^{-1}\underline{\Phi}_\beta \\ \hat{\underline{b}}_\rho &= \hat{\underline{\underline{F}}}^{-1}\underline{\Phi}_\rho \end{aligned} \tag{3.24}$$

P Source

If the background field $\bar{\underline{r}}_0$ in (3.18) is associated with a planar P wave source, then when it is substituted into (3.16), the scattering kernels are

$$\underline{\Phi}^P_\alpha, \underline{\Phi}^P_\beta, \underline{\Phi}^P_\rho = \tag{3.25}$$

$$\begin{bmatrix} 0 \\ 0 \\ \frac{2i\beta^2}{\alpha\omega}(\nu_1^{0^2} - 3k_x^{0^2}) \\ \frac{-4\rho\beta^2 k_x\omega}{\alpha} \\ \frac{-4\rho\beta^2 k_y\omega}{\alpha} \\ 0 \end{bmatrix}, \quad \begin{bmatrix} \frac{2i\alpha\gamma_1^0 k_x^0}{\omega} \\ 0 \\ \frac{4i\beta^2 k_x^{0^2}}{\alpha\omega} \\ \frac{4\beta^2 k_x\rho[2k_x^{0^2}(\beta^2-\alpha^2)+\omega^2]}{\alpha\omega} \\ \frac{4\beta^2 k_y\rho[k_x^{0^2}(2\beta^2-\alpha^2)+\omega^2]}{\alpha\omega} \\ 0 \end{bmatrix}, \quad \begin{bmatrix} \frac{2i\alpha\gamma_1^0 k_x^0}{\omega} \\ 0 \\ \frac{i\beta^2(\nu_1^{0^2}-k_x^{0^2})}{\alpha\omega} \\ \frac{\alpha k_x^0\rho}{\omega}[\omega^2 - 4\frac{\beta^2}{\alpha^2}k_x k_x^0(\alpha^2-\beta^2)] \\ \frac{-2\beta^2 k_x^{0^2} k_y\rho(\alpha^2-2\beta^2)}{\alpha\omega} \\ \alpha\gamma_1^0\rho\omega \end{bmatrix}$$

For a normal incidence planar P wave source, the scattering coefficients $\hat{\underline{b}}^P_\alpha$, $\hat{\underline{b}}^P_\beta$, and $\hat{\underline{b}}^P_\rho$ are given by

$$\underline{\hat{b}}_{\alpha}^{P}, \underline{\hat{b}}_{\beta}^{P}, \underline{\hat{b}}_{\rho}^{P} = \begin{bmatrix} \frac{i\omega^2}{\alpha^2\gamma} \\ 0 \\ 0 \\ \frac{i\omega^2}{\alpha^2\gamma} \\ 0 \\ 0 \end{bmatrix}, \begin{bmatrix} \frac{-2i\beta^2K^2}{\alpha^2\gamma} \\ \frac{-2i\beta K}{\alpha} \\ 0 \\ \frac{-2i\beta^2K^2}{\alpha^2\gamma} \\ \frac{-2i\beta K}{\alpha} \\ 0 \end{bmatrix}, \begin{bmatrix} \frac{-i\omega}{2a} + \frac{i\beta^2(\nu^2-K^2)}{2a^2\gamma} \\ \frac{iK\omega}{2\beta\nu} - \frac{iK\beta}{\alpha} \\ 0 \\ \frac{i\omega}{2a} + \frac{i\beta^2(\nu^2-K^2)}{2a^2\gamma} \\ \frac{-iK\omega}{2\beta\nu} - \frac{iK\beta}{\alpha} \\ 0 \end{bmatrix} \tag{3.26}$$

where the superscript P indicates a P wave source. When the scattering angles are real, it is valid to make substitutions into (3.26) of $\gamma = \frac{\omega}{\alpha}\cos\theta_P$, $\nu = \frac{\omega}{\beta}\cos\theta_S$, and $K = \frac{\omega}{\alpha}\sin\theta_P = \frac{\omega}{\beta}\sin\theta_S$, where θ_P and θ_S are the P or S scattering angles. This yields

$$\underline{\hat{b}}_{\alpha}^{P}, \underline{\hat{b}}_{\beta}^{P}, \underline{\hat{b}}_{\rho}^{P} = \begin{bmatrix} \frac{i\omega}{\alpha\cos\theta_P} \\ 0 \\ 0 \\ \frac{i\omega}{\alpha\cos\theta_P} \\ 0 \\ 0 \end{bmatrix}, \begin{bmatrix} -2i\omega\frac{\beta^2\sin^2(\theta_P)}{\alpha^3\cos\theta_P} \\ -2i\omega\frac{\sin\theta_S}{\alpha} \\ 0 \\ -2i\omega\frac{\beta^2\sin^2(\theta_P)}{\alpha^3\cos\theta_P} \\ -2i\omega\frac{\sin\theta_S}{\alpha} \\ 0 \end{bmatrix}, \begin{bmatrix} \frac{i\omega}{2\alpha\cos\theta_P}[1 - \cos\theta_P - 2\frac{\beta^2}{\alpha^2}\sin^2(\theta_P)] \\ \frac{i\omega}{2\beta}[\tan\theta_S - 2\frac{\beta}{\alpha}\sin\theta_S] \\ 0 \\ \frac{i\omega}{2\alpha\cos\theta_P}[1 + \cos\theta_P - 2\frac{\beta^2}{\alpha^2}\sin^2(\theta_P)] \\ \frac{i\omega}{2\beta}[-\tan\theta_S - 2\frac{\beta}{\alpha}\sin\theta_S] \\ 0 \end{bmatrix} \tag{3.27}$$

Three features of the scattered wave field are immediately obvious from (3.27). Firstly, a normally incident P wave scatters into P and SV waves, but not into SH waves. More precisely, a contrast in α generates only P waves, whereas contrasts in β or ρ generate both P and SV waves. Secondly, the scattering coefficients are azimuthally isotropic, *i.e.*, the wavenumber spectrum is completely described by K, with no reference to k_x

or k_y. Azimuthal variation, however, will result when the spectrum of the interface roughness function $h(k_x, k_y)$ varies azimuthally. Thirdly, the shape of the scattered field wavelet in the time domain for a single scattered plane wave is proportional to the time derivative of the incident field wavelet. Such changes to the wavelet are determined by the frequency dependence of the terms in (3.27), and this is simply described by the factor $i\omega$ which is present in all of the terms. A factor of $i\omega$ in the frequency domain denotes a time derivative in the time domain. Since the time-domain scattered field response is actually a summation over all scattered field plane waves, the final seismogram will be a summation of such derivative wavelets scattered from the entire interface, partially obscuring the derivative nature of the wavelets.

Example seismograms for Model A in Figure 3-1 by the 8 three-component seismograms shown in Figure 3-2. Model A has material parameters $\alpha = 1$ km/s, $\beta = 1/\sqrt{3}$ km/s, $\rho = 1$ g/cm^3, $\Delta\alpha/\alpha = 0.1$ km/s, $\Delta\beta/\beta = 0.1$ km/s, and $\Delta\rho/\rho = 0.1$ g/cm^3. The source is a normally incident, planar P wave in medium one. The rough interface $h(x, y)$ has a Gaussian autocorrelation function with correlation lengths of 0.563 km in the x-direction and 1.0 km in the y-direction, and an RMS height of 0.113 km. The RMS slope for this interface is 0.2 and the RMS height is 20 percent of the shortest wavelength in the model. Hence, from the results of Chapter 2, the perturbation method is valid for this model. The seismograms were generated by inserting the source term (3.7) into a propagator matrix-based formulation such as that described by Kennett (1983), and then Fourier transforming these frequency-wavenumber domain results to the time-space domain using the discrete wavenumber method (Bouchon, 1977).

The accuracy of the simple formulae in (3.27) is examined in Figures 3-3, 3-4, and 3-5 by plotting the components of $\hat{\underline{b}}^P_\alpha$, $\hat{\underline{b}}^P_\beta$, and $\hat{\underline{b}}^P_\rho$ against scattering results generated directly from (3.11) for the three models Model B, Model C, and Model D. Note that these scattering coefficients are derived from the scattering kernel and do not include the influence of a specific interface roughness function. These three models have the same average parameters as Model A, but only α is perturbed in Model B, only β is

perturbed in Model C, and only ρ is perturbed in Model D. The overall agreement is quite good, with the simple expressions of (3.27) giving smooth approximations to the results generated from (3.11). For all curves the agreement is good when the scattering angle is less than about 45 degrees. In several cases the agreement is good for the entire range of angles tested. In regions where the scattering coefficient changes rapidly, the coefficient is smoothly approximated.

SV Source

Substituting the background field for an SV plane wave source (3.18) into (3.16), the scattering kernels in (3.17) are defined by

$$\underline{\Phi}^S_\alpha, \underline{\Phi}^S_\beta, \underline{\Phi}^S_\rho = \begin{bmatrix} 0 \\ 0 \\ \frac{-8ik_x^0\nu_1^0\beta^3}{\omega\alpha^2} \\ 0 \\ 0 \\ 0 \end{bmatrix}, \begin{bmatrix} \frac{2i\beta}{\omega}(\nu_1^{0^2} - k_x^{0^2}) \\ 0 \\ \frac{4ik_x^0\nu_1^0\beta^3}{\omega\alpha^2} \\ \frac{-8\rho\beta^3 k_x k_x^0 \nu_1^0(\alpha^2-\beta^2)}{\omega\alpha^2} \\ \frac{-4\rho\beta^3 k_y k_x^0 \nu_1^0(\alpha^2-2\beta^2)}{\omega\alpha^2} \\ 0 \end{bmatrix}, \begin{bmatrix} \frac{i\beta}{\omega}(\nu_1^{0^2} - k_x^{0^2}) \\ 0 \\ \frac{-2i\beta^2 k_x^0\nu_1^0}{\omega\alpha^2} \\ \frac{\rho\beta\nu_1^0}{\omega}[\omega^2 - 4\frac{\beta^2}{\alpha^2}(\alpha^2-\beta^2)k_x k_x^0] \\ -2\rho\beta^3 k_y k_x^0 \frac{\nu_1^0}{\omega\alpha^2}(\alpha^2-2\beta^2) \\ -\rho\beta\omega k_x^0 \end{bmatrix} \tag{3.28}$$

For a normal incidence planar SV wave source, the scattering coefficients $\hat{\underline{b}}^S_\alpha$, $\hat{\underline{b}}^S_\beta$, and $\hat{\underline{b}}^S_\rho$ are given by

$$\hat{\underline{b}}^S_\alpha, \hat{\underline{b}}^S_\beta, \hat{\underline{b}}^S_\rho = \begin{bmatrix} 0 \\ 0 \\ 0 \\ 0 \\ 0 \\ 0 \end{bmatrix}, \begin{bmatrix} \frac{2i\beta k_x}{\alpha} \\ \frac{ik_x(\nu^2-K^2)}{\nu K} \\ \frac{-ik_y\omega}{K\beta} \\ \frac{-2ik_x\beta}{\alpha} \\ \frac{-ik_x(\nu^2-K^2)}{\nu K} \\ \frac{ik_y\omega}{K\beta} \end{bmatrix}, \begin{bmatrix} \frac{ik_x}{\alpha}(\beta - \frac{\omega}{2\gamma}) \\ \frac{ik_x}{2K\nu}(\nu^2 - \frac{\omega}{\beta}\nu - K^2) \\ \frac{ik_y\omega(\omega-\beta\nu)}{2K\beta^2\nu} \\ -\frac{ik_x}{\alpha}(\beta + \frac{\omega}{2\gamma}) \\ -\frac{ik_x}{2K\nu}(\nu^2 + \frac{\omega}{\beta}\nu - K^2) \\ \frac{ik_y\omega(\omega+\beta\nu)}{2K\beta^2\nu} \end{bmatrix} \tag{3.29}$$

Since (3.29) refers to k_x and k_y independently of K these scattering coefficients vary with azimuth. Expressing the scattering coefficients in terms of θ_P, θ_S, and the azimuthal angle ψ, we make the substitutions $\gamma = \frac{\omega}{\alpha}\cos\theta_P$, $\nu = \frac{\omega}{\beta}\cos\theta_S$, $K = \frac{\omega}{\alpha}\sin\theta_P = \frac{\omega}{\beta}\sin\theta_S$, $k_x = \frac{\omega}{\alpha}\sin\theta_P\cos\psi = \frac{\omega}{\beta}\sin\theta_S\cos\psi$, and $k_y = \frac{\omega}{\alpha}\sin\theta_P\sin\psi = \frac{\omega}{\beta}\sin\theta_S\sin\psi$, to get

$$\hat{\underline{b}}^S_\alpha, \hat{\underline{b}}^S_\beta, \hat{\underline{b}}^S_\rho = \begin{bmatrix} 0 \\ 0 \\ 0 \\ 0 \\ 0 \\ 0 \end{bmatrix}, \begin{bmatrix} \frac{2i\beta\omega}{\alpha^2}\sin\theta_P\cos\psi \\ \frac{i\omega\cos 2\theta_S\cos\psi}{\beta\cos\theta_S} \\ \frac{-i\omega}{\beta}\sin\psi \\ \frac{-2i\beta\omega}{\alpha^2}\sin\theta_P\cos\psi \\ \frac{-i\omega\cos 2\theta_S\cos\psi}{\beta\cos\theta_S} \\ \frac{i\omega}{\beta}\sin\psi \end{bmatrix}, \begin{bmatrix} \frac{-i\omega}{2\alpha^2}\tan\theta_P\cos\psi(\alpha - 2\beta\cos\theta_P) \\ \frac{-i\omega}{2\beta}\cos\psi(1 - \frac{\cos 2\theta_S}{\cos\theta_S}) \\ \frac{i\omega}{2\beta\cos\theta_S}\sin\psi(1 - \cos\theta_S) \\ \frac{-i\omega}{2\alpha^2}\tan\theta_P\cos\psi(\alpha + 2\beta\cos\theta_P) \\ \frac{-i\omega}{2\beta}\cos\psi(1 + \frac{\cos 2\theta_S}{\cos\theta_S}) \\ \frac{i\omega}{2\beta\cos\theta_S}\sin\psi(1 + \cos\theta_S) \end{bmatrix} \tag{3.30}$$

From (3.30) we see that a normally incident SV wave is associated with P, SV, and SH scattering. To first order such scattering is not influenced by $\Delta\alpha$. Scattered P and SV waves have a cosine-shaped azimuthal variation with a maximum in the direction of the

incident SV particle motion, and scattered SH waves vary sinusoidally with azimuth with a maximum in the direction normal to the incident SV particle motion. Cross-sections of $\hat{\underline{b}}_{\beta}^{S}$ and $\hat{\underline{b}}_{\rho}^{S}$ for the azimuth of maximum amplitude are shown in Figures 3-6 and 3-7 along with the more complete solutions derived from (3.11) for comparison. The solution of (3.11) for $\hat{\underline{b}}_{\alpha}^{S}$ is not shown since it is three orders of magnitude below $|\hat{\underline{b}}_{\beta}^{S}|$ and $|\hat{\underline{b}}_{\rho}^{S}|$. As with the P wave source, the results are good for scattering angles of less than about 45 degrees.

3.4 EXAMPLES FOR A GAUSSIAN ROUGH INTERFACE

The scattering kernel describes the variation in the scattered field that is due to the source and the material contrast at the interface. The influence of a particular rough interface function must be included using (3.23) to obtain the actual scattered field. A random rough interface is typically described by its autocorrelation function. There are three classes of autocorrelation functions that are generally considered in the geophysical literature: Gaussian, exponential, and von Karman (Frankel and Clayton, 1986). These functions are given in the following table.

Type	$R(x,y)$
Gaussian	$\exp[-(\frac{x}{a_x})^2-(\frac{y}{a_y})^2]$
Exponential	$\exp[-\sqrt{(\frac{x}{a_x})^2+(\frac{y}{a_y})^2}]$
von Karman	$K_0(\sqrt{(\frac{x}{a_x})^2+(\frac{y}{a_y})^2})$

To generate one realization of a random interface from these autocorrelation functions it is necessary to specify two correlation lengths, a_x and a_y, and an RMS height deviation, and to have a random number generator capable of generating uniform random numbers within a real interval. Since the autocorrelation function is defined as the power spectrum

of the interface function, *i.e.*, $R(k_x, k_y) = h(k_x, k_y)h^*(k_x, k_y)$, the modulus of the interface function is given by $|h| = \sqrt{R}$, with the value at $k_x = k_y = 0$ being zero in order to obtain a zero-mean interface. The phase is a random quantity specified by $\exp(i\phi)$, where ϕ is a uniform random number between 0 and 2π. The discrete interface function so constructed, $h(k_x, k_y)$, is then normalized so that the RMS height of $h(x, y)$ is equal to the desired value. This method for generating a random interface function in the wavenumber domain is equivalent to a space domain method where a discrete field of uniform random numbers is convolved with the square root of the autocorrelation function and then normalized to the specified RMS value.

3.4.1 Normalization of the Interface Spectrum

Our example uses the Gaussian autocorrelation function to produce the rough interface shown in Figure 3-1. In order to have closed-form expressions for scattering coefficients for an arbitrary interface with a Gaussian autocorrelation function, we must derive an expression for the normalization factor which scales the interface height function to have a desired RMS value. The same procedure can be used to derive analogous expressions for exponential and von Karman autocorrelation functions.

Consider an interface which is periodic of period $2L_x$ in the x-direction and $2L_y$ in the y-direction. The Fourier series representation of this interface is

$$h(x,y) = \sum_{m=-M}^{M} \sum_{n=-N}^{N} h_{mn} e^{ik_x^m x} e^{ik_y^n y} \tag{3.31}$$

where $k_x^m = \frac{\pi m}{L_x}$, $k_y^m = \frac{\pi m}{L_y}$, and

$$h_{mn} = \frac{1}{4L_xL_y} \int_{-L_y}^{L_y} \int_{-L_x}^{L_x} h(x,y) e^{-ik_x^m x} e^{-ik_y^n y} dx\, dy \tag{3.32}$$

The autocorrelation of $h(x, y)$ is defined by

$$r(x,y) = \frac{1}{4L_xL_y} \int_{-L_y}^{L_y} \int_{-L_x}^{L_x} h(x',y')h(x+x', y+y')dx'dy', \tag{3.33}$$

which yields the expected expression

$$r_{mn} = h^*_{mn} h_{mn}. \tag{3.34}$$

when $h(x,y)$ is defined by (3.31). The Fourier transform of the Gaussian autocorrelation function

$$r(x,y) = e^{-(\frac{x}{a_x})^2 - (\frac{y}{a_y})^2} \tag{3.35}$$

is given by

$$\begin{aligned} r_{mn} &= \frac{a_x a_y \pi}{4 L_x L_y} e^{-(\frac{k_x^m a_x}{2})^2 - (\frac{k_y^n a_y}{2})^2} \\ &\bullet \ \mathrm{Re}\{\mathrm{erf}(\frac{L_x}{a_x} + \frac{i k_x^m a_x}{2})\} \, \mathrm{Re}\{\mathrm{erf}(\frac{L_y}{a_y} + \frac{i k_y^n a_y}{2})\}, \end{aligned} \tag{3.36}$$

where erf() is the error function defined by

$$\mathrm{erf}(z) = \frac{2}{\sqrt{\pi}} \int_0^z e^{\xi^2} d\xi. \tag{3.37}$$

For $\frac{2L}{a} > 3$ it is safe to approximate (3.36) by

$$r_{mn} = \frac{a_x a_y \pi}{4 L_x L_y} e^{-(\frac{k_x^m a_x}{2})^2 - (\frac{k_y^n a_y}{2})^2}. \tag{3.38}$$

In this regime, the unbounded growth of the error functions in (3.36) for large k is held in check by the damping provided by the Gaussian exponential term. The error resulting for such an approximation is illustrated by a contour plot in Figure 3-8a. Figures 3-8b and 3-8c show comparisons of the exact and approximate expressions evaluated at $2L/a = 2$ and $2L/a = 3$. As expected, the error behaves like a sinc function.

It remains to relate the RMS height deviation σ in the space domain to $h(k_x, k_y)$. The zero-mean RMS height deviation is given by

$$\sigma^2 = \frac{1}{4L_xL_y}\int_{-L_y}^{L_y}\int_{-L_x}^{L_x}[h(x,y)-\bar{h}]^2 dx\,dy \tag{3.39}$$

$$= \frac{1}{4L_xL_y}\int_{-L_y}^{L_y}\int_{-L_x}^{L_x} h^2(x,y)dx\,dy - \bar{h}^2 \tag{3.40}$$

where $\bar{h}$ is the mean of $h(x,y)$. The first term in (3.40), by (3.33), is simply $r(0,0)$, the spatial autocorrelation function evaluated at the origin. The second term, by (3.32) and (3.34), is $r_{0,0}$, the Fourier transform of the autocorrelation function (3.38) evaluated at the origin. Substituting these values into (3.40) yields

$$\sigma^2 = 1 - \frac{a_x a_y \pi}{4L_xL_y}. \tag{3.41}$$

Hence the form of h_{mn} which is normalized to yield an RMS height deviation of σ_0 is

$$h_{mn} = \sqrt{r_{mn}} = \left[\sigma_0^2 \frac{\frac{a_x a_y \pi}{4L_xL_y}}{1-\frac{a_x a_y \pi}{4L_xL_y}} e^{-(\frac{k_x^m a_x}{2})^2-(\frac{k_y^n a_y}{2})^2}\right]^{\frac{1}{2}}. \tag{3.42}$$

3.4.2 Normally Incident P Source

Three-dimensional radiation patterns which include the effects of interface roughness are shown in Figures 3-9 and 3-10. The source is a normally incident planar P wave in medium 1 and the rough interface model is shown in Model A of Figure 3-1. Figure 3-9 shows the nine P, SV, and SH up-going components of $\frac{\Delta\alpha}{\alpha}h\underline{\hat{b}}_\alpha^P$, $\frac{\Delta\beta}{\beta}h\underline{\hat{b}}_\beta^P$, and $\frac{\Delta\rho}{\rho}h\underline{\hat{b}}_\rho^P$ in the upper medium, and Figure 3-10 shows the nine down-going components in the lower medium. The plots are independently scaled to fill the plot frame, and a maximum amplitude for each plot is indicated for comparison.

All of the plots show that scattering occurs over a broader range of angles in the x-direction than in the y-direction. This results directly from the smaller autocorrelation length in the x-direction (0.563 km) than in the y-direction (1.00 km), and agrees with the intuitive result that azimuths of greater RMS interface slope are associated with more diffuse scattering. If a_x and a_y were the same length, the scattering scattering

coefficients would be azimuthally isotropic. From the plots in Figure 3-9 it is clear that, for up-going waves, $\Delta\alpha$ and $\Delta\rho$ contribute most to reflected P wave scattering, and result in equal amounts of backscattering at $\theta_P = 0$. For non-zero θ_P, however, a contrast in P wave velocity generates more backscattered energy than a contrast in density. Scattering into SV waves is influenced nearly equally by $\Delta\beta$ and $\Delta\rho$. The results for down-going waves (Figure 3-10) equal those for up-going waves for contrasts in the P and S wave velocities, but differ greatly for contrasts in density. Density contrasts produce significant backscattering into the source medium, but almost no forward scattering.

Wu and Aki (1985) examined the effect of material contrast on the relative dominance of forward or backward scattering from volume scatterers. Applying the Born approximation in the low-frequency range (Rayleigh scattering), they found that the scattered field can be decomposed into an impedance-type and a velocity-type scattered field. Impedance-type scattering is seen in its purest form when there is zero velocity contrast at the scatterer, and is associated with a predominant backscattered lobe. Impedance-type scattering is illustrated by the $\Delta\rho$ components of scattering in Figures 3-9 and 3-10. Velocity-type scattering is seen in its purest form when there is zero impedance contrast at the scatterer, and is associated with a predominant forward scattered lobe. The conditions for zero impedance contrast are

$$\rho_1\alpha_1 - \rho_2\alpha_2 = 0 \tag{3.43}$$

$$\rightarrow \frac{\Delta\alpha}{\alpha} = -\frac{\Delta\rho}{\rho} \tag{3.44}$$

and

$$\rho_1\beta_1 - \rho_2\beta_2 = 0 \tag{3.45}$$

$$\rightarrow \frac{\Delta\beta}{\beta} = -\frac{\Delta\rho}{\rho}. \tag{3.46}$$

Under these conditions the back-scattered lobes in (3.27) largely cancel, permitting the forward-scattered lobes to dominate.

The time-domain representation of the scattering results presented in Figures 3-9 and 3-10 is given by the three-component seismograms in Figures 3-11, 3-12, and 3-13. Figure 3-11 shows the scattered field measured by a linear array of 8 three-component receivers in each medium. In both arrays, the receivers are evenly spaced along the $x = 0$ line between $y = 0$ and $y = 5.6$ km (inclusive), and are at a distance of 2 km from the mean planar interface. Figures 3-12 and 3-13 display a decomposition of the Figure 3-11 seismograms into their $\Delta\alpha$, $\Delta\beta$, and $\Delta\rho$ components. The $\Delta\alpha$ component was generated from Model B, the $\Delta\beta$ component from Model C, and the $\Delta\rho$ component from Model D. The maximum amplitudes of these seismograms are much larger than the maximum amplitudes of the related scattering coefficients because the seismograms represent the summation of scattered waves over all scattering angles.

The areal distribution of downward scattered and upward scattered wave amplitudes is illustrated by contour maps in Figures 3-14, 3-15, and 3-16. These maps were generated from two horizontal two-dimensional arrays of three-component receivers which were placed 2 km above and 2 km below the interface. The maximum amplitude (measured as an absolute value) on each component of each receiver was then contoured. Comparison of these contour maps with the interface height contour map provides an indication of the sensitivity of the seismogram amplitudes to interface height. In Figure 3-9 we can see that the z components in the upper and lower media primarily represent P waves scattered from contrasts in P wave velocity and density. Since the direction of maximum scattering is vertical in this case, a map of maximum amplitudes is quite similar to the interface height contour map. The x and y components are dominated by obliquely scattered P and SV waves, resulting in the lack of correspondence of these maps with the interface height contour map.

3.4.3 Normally Incident SV Source

We will now provide the same analysis for a normally incident SV wave as we did above for the P wave source. In interpreting the following plots, keep in mind that the incident SV

particle motion is in the x direction. Three-dimensional radiation patterns which include the effects of interface roughness are shown in Figures 3-17 and 3-18. The azimuth of maximum scattering in the P and SV kernels coincides with the smallest correlation length of the interface, emphasizing scattering in the x direction. For up-going waves, the scattered field in the normal direction is composed of equal amounts of SV and SH waves. This scattering is equally sensitive to the contrast in S wave velocity and the contrast in density, while to first order the contrast in P wave velocity produces no scattered waves. As the scattering angle increases, P waves become increasingly prominent with respect to the S waves, dominating the scattered field at scattering angles greater than about 45 degrees.

The time-domain representation of these scattering results is given in the three-component seismograms in Figures 3-19, 3-20, and 3-21. The receiver arrays are configured as they were for the P source analysis in the preceding section. As we saw in the scattering coefficient plots, there is an abundance of energy in the x component which includes normally scattered SV waves and obliquely scattered P waves. The y component contains primarily SH waves. Although the maximum amplitude of the SH scattering coefficient equals that of the SV scattering coefficient, the total energy scattered into SH, measured as the volume enclosed by the scattering coefficient surface, is smaller than that of the SV wave. Thus the y components display smaller amplitudes than the x components. Contributions to the x components by obliquely scattering P waves increase the discrepancy in magnitude between these two components.

The areal distribution of forward- and backward-scattered wave amplitudes is illustrated by contour maps in Figures 3-22, 3-23, and 3-24. The similarity between the contours of the x components and the interface height contours indicates that this component of the scattered field is dominated by normal scattering from the surface, which Figures 3-17 and 3-18 show us must be SV waves. If obliquely scattered P waves were dominant in the x-component, the correspondance could not be nearly as good. Furthermore, the maps show that the scattered field is contributed to equally by $\Delta\beta$ and

$\Delta\rho$.

3.4.4 Obliquely Incident P Source

Scattering coefficients were generated for planar P waves incident on model A in Figure 3-1 at angles of 0, 20, 40, and 60 degrees. These coefficients were generated directly from (3.7), with no further approximations. Three-dimensional plots of the coefficients for the up- and down-going waves are shown in Figures 3-25 and 3-26. The propagation direction of the incident wave in these models is in the x-z plane. Comparisons of relative shapes and amplitudes of these coefficients is facilitated by cross-sectional plots of the three-dimensional coefficients, where the cross-section is taken in the x-z plane for P and SV coefficients, and in the y-z plane for SH coefficients. Cross-sectional plots for Figures 3-25 and 3-26 are shown in Figures 3-27 and 3-28.

Several major features of these plots bear mentioning. The amplitudes of the primary (smooth) lobe of scattered P and SH waves decrease with increasing incidence angle, while the primary lobe of the scattered SV wave increases in amplitude with increasing incidence angle. This is true for both up- and downgoing waves. Scattered SH waves have maximum amplitude near the vertical for upgoing waves, while for downgoing waves the direction of maximum scattering is more sensitive to the source incidence angle. The up-going P and SV wave coefficients have cusps at the P to P and S to S critical angles of $\sin^{-}1(\alpha_1/\alpha_2) = \sin^{-}1(\beta_1/\beta_2) \approx 65$ degrees, and the SV wave coefficients have additional cusps at the P to S and S to P critical angles of $\sin^{-1}(\beta_1/\alpha_2) = \sin^{-1}(\beta_2/\alpha_1) \approx$ 34 degrees. These cusps are invariant with incidence angle. They are present in the scattering kernel and thus are independent of any particular interface function. Similar peaks were observed by Paul and Campillo (1988) , who used a boundary integral equation method to compute the exact solution for two-dimensional elastic wave scattering from a rough interface. They observed that the P to S wave backscattering coefficient has a dramatic increase as the scattering angle increases past the P to P critical angle.

When P waves are scattered, the angle of maximum scattering coincides with the inci-

dence angle only in the case of normal incidence. This can be understood by considering the scattering coefficient as a product of the interface spectrum with the scattering kernel, where the interface spectrum is shifted so that the zero wavenumber value coincides with the specular angle (see equation 3.7). Although the maximum of the interface spectrum is at the specular angle, the scattering kernel generally will not have any extrema at the specular angle. Hence, the product will generally not have any extrema at the specular angle. In all cases, of course, specular scattering will dominate when the background field is included.

3.4.5 Obliquely Incident SV Source

Scattering coefficients were generated for planar SV waves incident on model A in Figure 3-1 at angles of 0, 20, 40, and 60 degrees. As for a P wave source, these coefficients were generated directly from (3.7), with no further approximations. Three-dimensional plots of these coefficients for the up- and down-going waves are shown in Figures 3-29 and 3-30, and cross-sections of these plots are shown in Figures 3-31 and 3-32. The propagation direction and particle motion of the incident SV wave in these models is in the x-z plane. Cusps appear at the same scattering angles that as found in the case of the obliquely incident P wave. This confirms our observation that the cusps are associated with the critical angles (the material contrast), and not with the source wave type. Beyond these critical angles the scattering coefficients tend to increase, with larger incidence angles associated with larger increases.

3.5 SUMMARY AND CONCLUSIONS

The perturbation equations developed in chapter 2 allow one to quickly generate scattering coefficients and seismograms for a three-dimensional rough interface model for which the RMS interface height and RMS slope is sufficiently small. In this chapter these equations are further simplified by use of a small material contrast approximation

in order to isolate and study the influence of contrasts in α, β, and ρ on scattered P, SV, and SH waves. In these equations it was possible to entirely factor out the material contrast terms $\frac{\Delta\alpha}{\alpha}$, $\frac{\Delta\beta}{\beta}$, and $\frac{\Delta\rho}{\rho}$ from the scattering coefficients, expressing the scattered field coefficients as a weighted sum of $\Delta\alpha$, $\Delta\beta$, and $\Delta\rho$ contributions. For the case of a normally incident plane wave source, these coefficients have an even more compact form than planar interface scattering coefficients. The degradation of solution accuracy due to the small material contrast approximation was tested by comparing these simple solutions with those derived from the equations of chapter 2 for a rough interface model with a 10 percent velocity contrast. It was found that the small scattering angle approximation implicit in the small material contrast approximation is accurate to suprisingly large angles, with the accuracy dependent on the particular scattered wave type being compared. Aki and Richards (1980, p. 153) came to very similar conclusions in their discussion of the accuracy of small material contrast approximations to reflection and transmission coefficients for a planar interface. The simplified scattering coefficients for normally incident waves also give insight into the shape of the scattered field wavelet. The form of these coefficients makes it clear that the scattered field wavelet is proportional to the time derivative of the incident field wavelet. This observation was verified in synthesized seismograms.

Modeling of obliquely incident P and SV waves on an interface with a Gaussian autocorrelation function show that the scattered wave amplitudes are not necessarily maximum in the direction of specular scattering. Furthermore, there are cusps in the scattering coefficient at scattering angles equal to the critical angles for P and S wave scattering on a planar interface. Such phenomenon has also been reported for exact solutions of rough interface scattering models which were based generated by finite difference and boundary integral equation methods (Levander and Hill, 1985; Paul and Campillo, 1988).

References

Aki, K., P.G.Richards, 1980, *Quantitative Seismology: Theory and Methods,* W. H. Freeman and Company, San Francisco, vols. 1 and 2, 932 pp.

Frankel, A. and R. Clayton, 1986, Finite difference simulation of seismic wave scattering: implications for the propagation of short-period seismic waves in the crust and models of crustal heterogeneity, *J. Geophys. Res.*, 91, 6465–6489.

Kuperman, W., and H. Schmidt, 1989, Self-consistent perturbation approach to rough surface scattering in stratified elastic media, submitted to *J. Acoust. Soc. Am.*

Levander, A.R., and N.R. Hill, 1985, P-SV resonances in irregular low-velocity surface layers, *Bull. Seism. Soc. Am., 75,* 847–864.

Paul, A. and M. Campillo, 1988, Diffraction and conversion of elastic waves at a corrugated interface, *Geophysics,* 53, 1415–1424.

Prange, M., and M. N. Toksöz, 1989, Perturbation approximation of 3-D seismic scattering, submitted to *Geophysical Journal.*

Wu, R., and K. Aki, 1985, Scattering characteristics of elastic waves by an elastic heterogeneity, *Geophysics,* 50, 582–595.

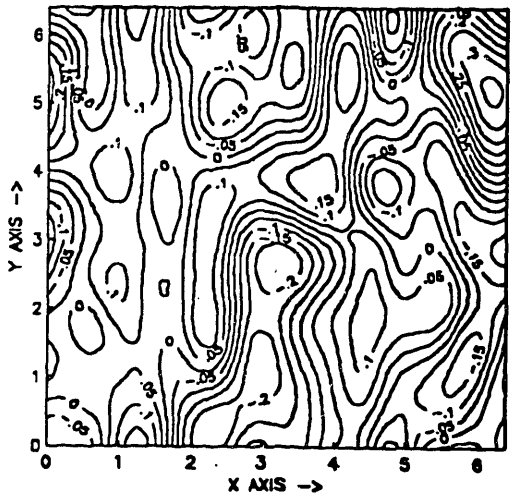

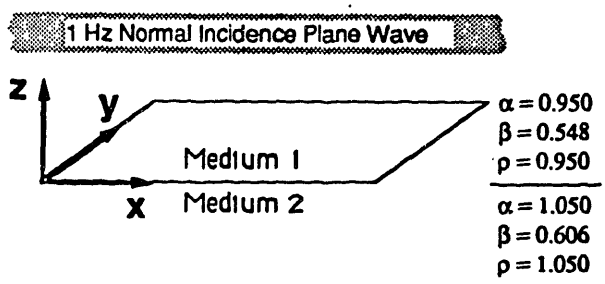

Figure 3-1: Contour map of the interface height function. The rough interface $h(x,y)$ has a Gaussian autocorrelation function with correlation lengths of 0.563 km in the x-direction and 1.0 km in the y-direction, and an RMS height of 0.113 km. The RMS slope for this interface is 0.2 and the RMS height is 20 percent of the shortest wavelength in the model. The source is a normally incident 1 Hz plane wave with a Ricker wavelet time function of the form $R(t) = [1-(\omega_0 t)^2/2]\exp(-(\omega_0 t)^2/4)$, where $\omega_0 = 2\pi$. The source is 2 units above the mean planar interface. The materials in this interface model are varied to yield the models given in the table below.

Model	α	β	ρ	$\Delta\alpha/\alpha$	$\Delta\beta/\beta$	$\Delta\rho/\rho$
Model A	1.00	$1./\sqrt{3}$	1.00	0.10	0.10	0.10
Model B	1.00	$1./\sqrt{3}$	1.00	0.10	0.00	0.00
Model C	1.00	$1./\sqrt{3}$	1.00	0.00	0.10	0.00
Model D	1.00	$1./\sqrt{3}$	1.00	0.00	0.00	0.10

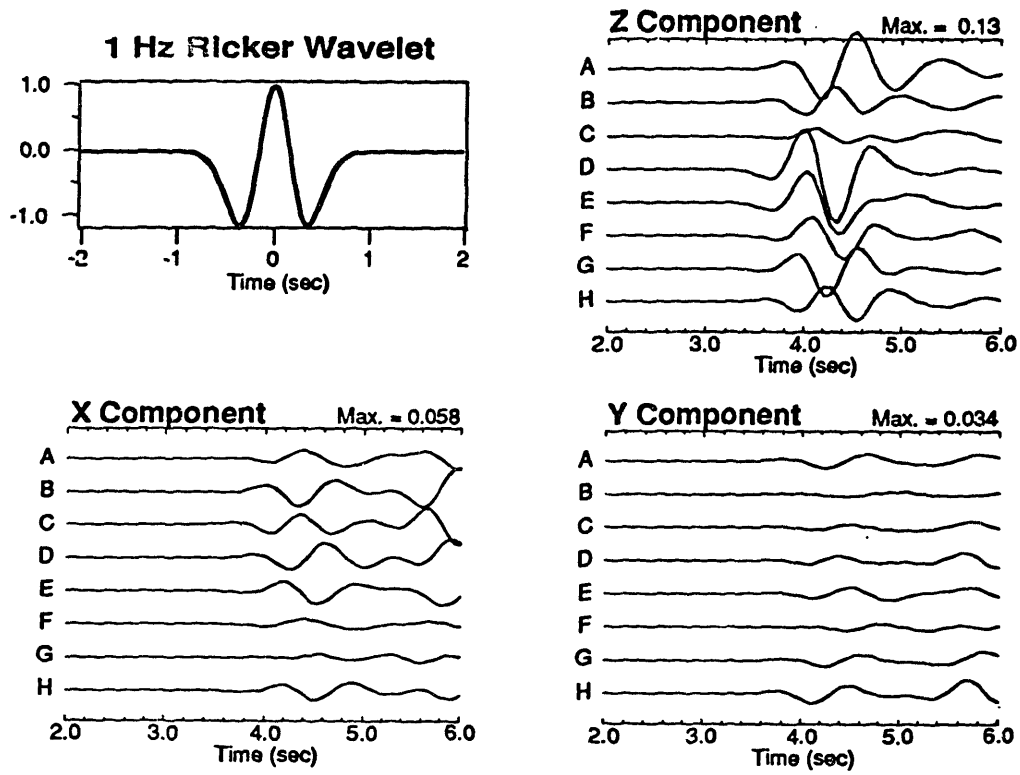

Figure 3-2: Representative three-component scattered field seismograms for Model A. The three components are plotted at the same scale. The 8 receivers, labeled A–H, are located along the x-axis from $x = 0$ to $x = 5.6$, and are 2 units above the mean planar interface. The source wavelet is shown for comparison.

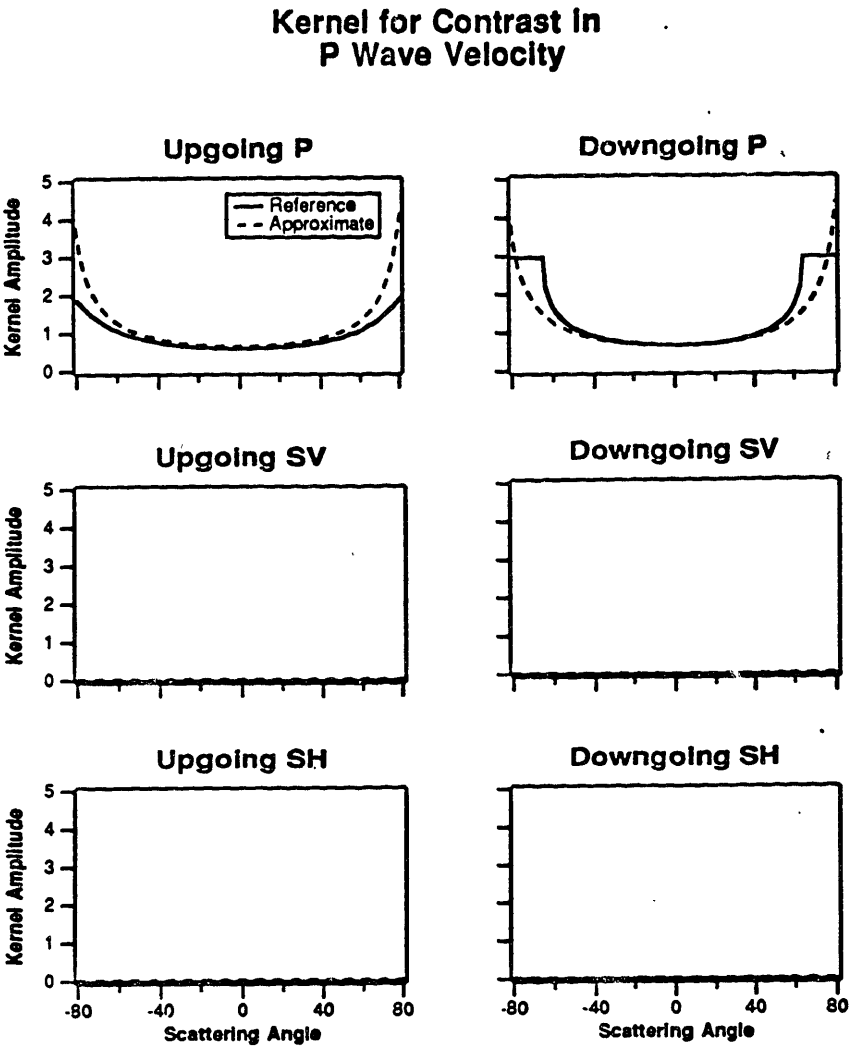

Figure 3-3: Comparison of the components of $\frac{\Delta\alpha}{\alpha}\underline{\hat{b}}_{\alpha}^{P}$ generated by (3.27) and by the direct solution of (3.11). The SV and SH components in this case are exactly zero. The curves are a cross-section of the azimuthally symmetric pattern. The model parameters are taken from Model B in Figure 3-1, where $\Delta\alpha/\alpha = 0.10$ and $\Delta\beta/\beta = \Delta\rho/\rho = 0$. The source is a normally incident 1 Hz planar P wave. These curves do not include the influence of a specific interface roughness function.

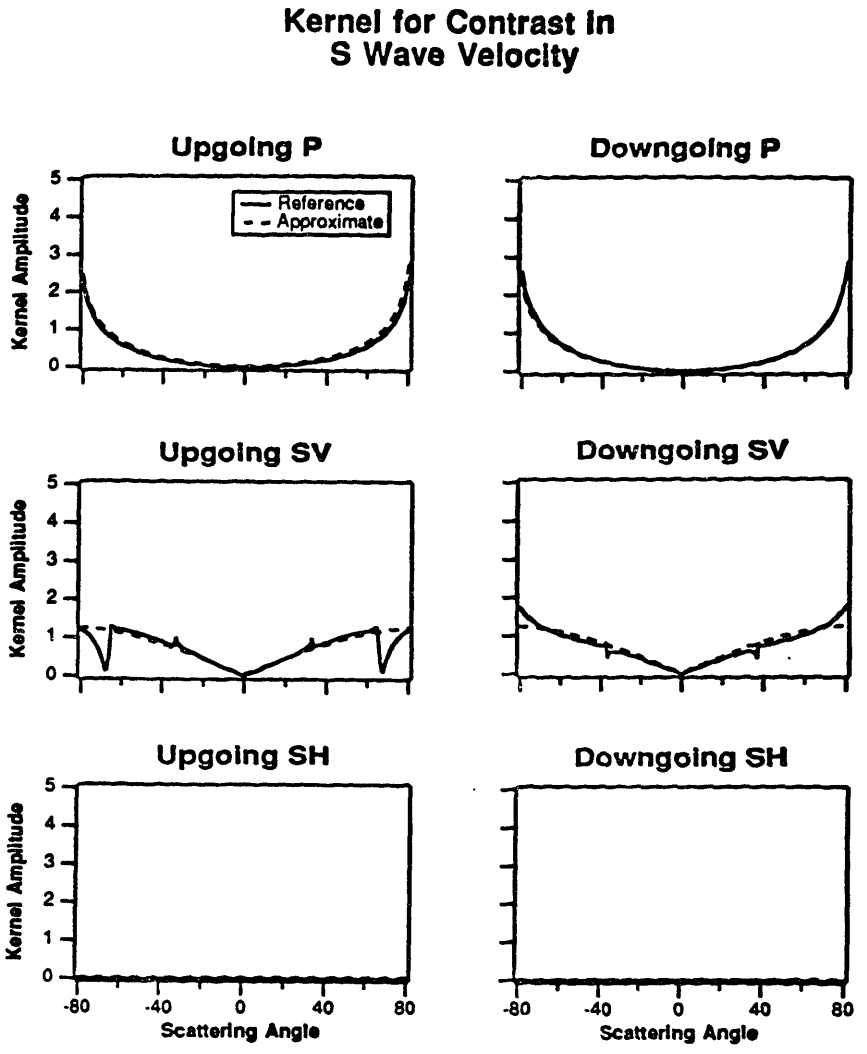

Figure 3-4: Comparison of the components of $\frac{\Delta\beta}{\beta}\hat{\underline{b}}^P_\beta$ generated by (3.27) and by the direct solution of (3.11). The SH component in this case is exactly zero. The curves are a cross-section of the azimuthally symmetric pattern. The model parameters are taken from Model C in Figure 3-1, where $\Delta\beta/\beta = 0.10$ and $\Delta\alpha/\alpha = \Delta\rho/\rho = 0$. The source is a normally incident 1 Hz planar P wave.

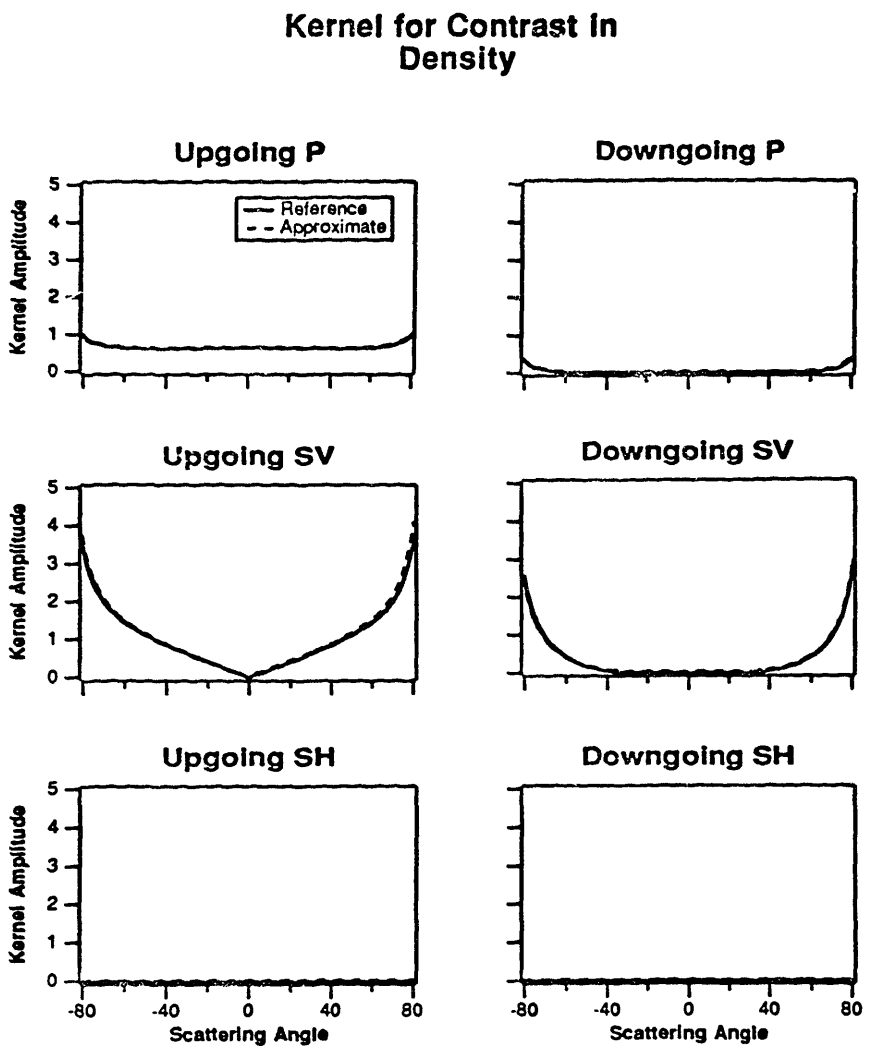

Figure 3-5: Comparison of the components of $\frac{\Delta\rho}{\rho}\underline{\hat{b}}_{\rho}^{P}$ generated by (3.27) and by the direct solution of (3.11). The SH component in this case is exactly zero. The curves are a cross-section of the azimuthally symmetric pattern. The model parameters are taken from Model D in Figure 3-1, where $\Delta\rho/\rho = 0.10$ and $\Delta\alpha/\alpha = \Delta\beta/\beta = 0$.

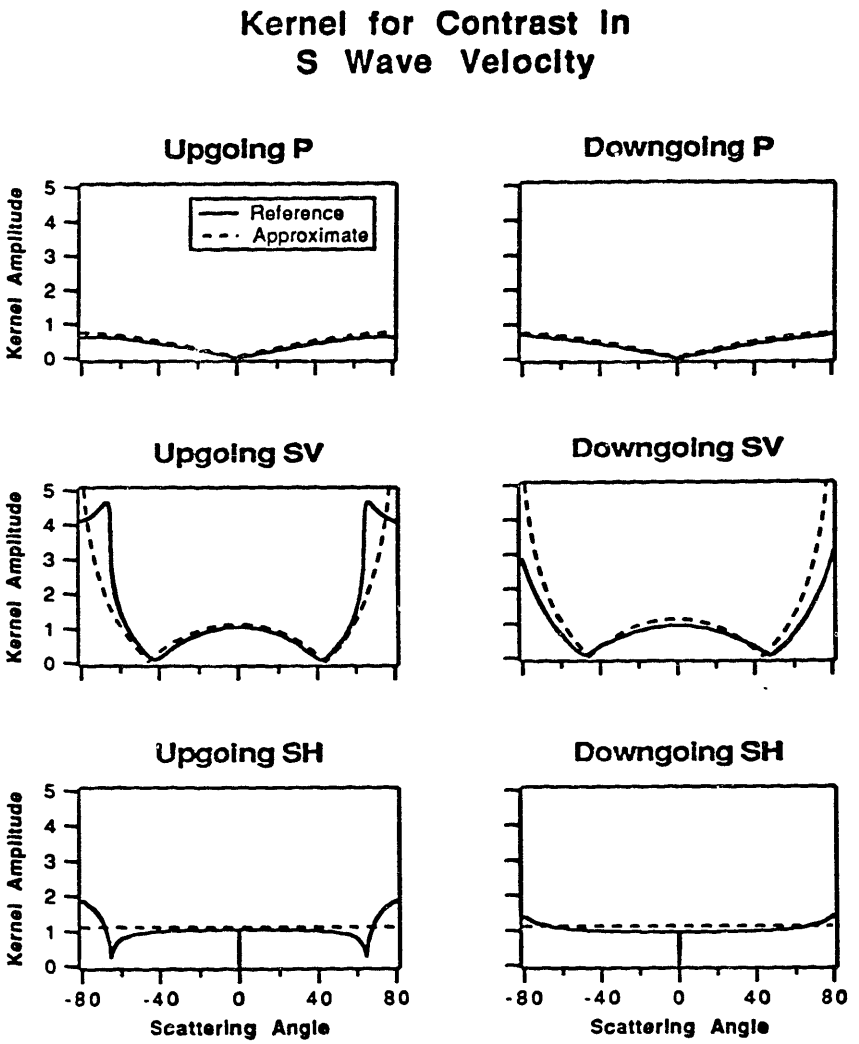

Figure 3-6: Comparison of the P, SV and SH wave components of $\frac{\Delta\beta}{\beta}\hat{\underline{b}}\frac{S}{\beta}$ generated by (3.30) and by the direct solution of (3.11). The curves are cross-sections of the azimuthally anisotropic patterns in the azimuthal direction of maximum scattering: for P and SV waves this is in the direction of the incident SV particle motion, and for SH waves it is normal to this direction. The model parameters are taken from Model C in Figure 3-1, where $\Delta\beta/\beta = 0.10$ and $\Delta\alpha/\alpha = \Delta\rho/\rho = 0$. The source is a normally incident, 1 Hz planar SV wave.

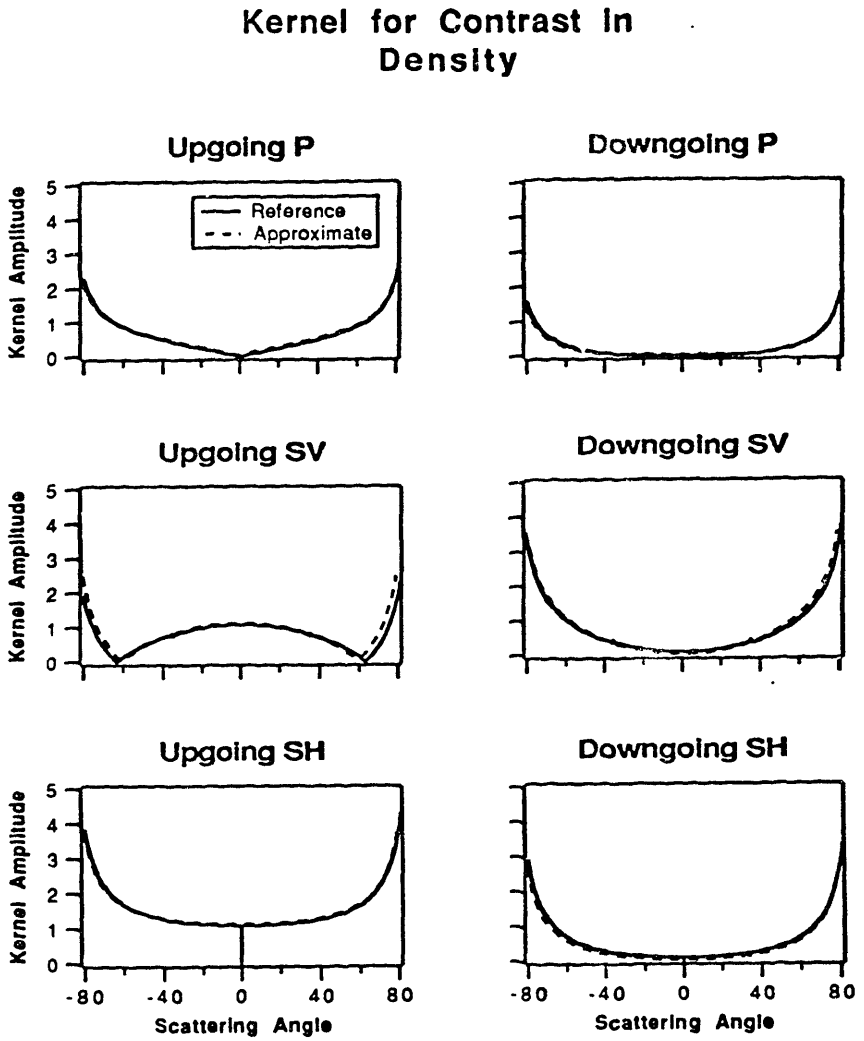

Figure 3-7: Comparison of the P, SV and SH wave components of $\frac{\Delta\rho}{\rho}\underline{\hat{b}}\frac{S}{\rho}$ generated by (3.30) and by the direct solution of (3.11). The curves are cross-sections of the azimuthally anisotropic patterns in the azimuthal direction of maximum scattering: for P and SV waves this is in the direction of the incident SV particle motion, and for SH waves it is normal to this direction. The model parameters are taken from Model D in Figure 3-1, where $\Delta\rho/\rho = 0.10$ and $\Delta\alpha/\alpha = \Delta\beta/\beta = 0$. The source is a normally incident, 1 Hz planar SV wave.

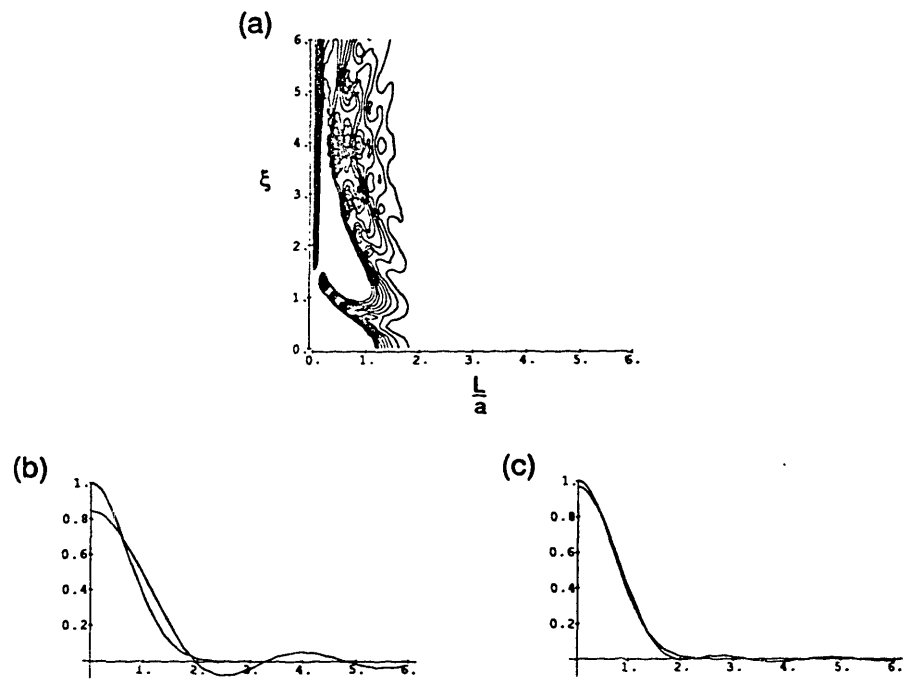

Figure 3-8: (a) Contour plot of $|e^{-\xi^2} - e^{-\xi^2}\,\mathrm{Re}\{\mathrm{erf}(\frac{L}{a} + i\xi)\}|$ with contours at intervals of 0.01 between 0.0 and 0.1. It illustrates that (3.38) is a valid approximation of (3.36) when $2L/a > 3$. (b) and (c) are comparisons of $e^{-\xi^2}$ and $e^{-\xi^2}\,\mathrm{Re}\{\mathrm{erf}(\frac{L}{a} + i\xi)\}$ evaluated at $2L/a = 2$ and $2L/a = 3$, respectively.

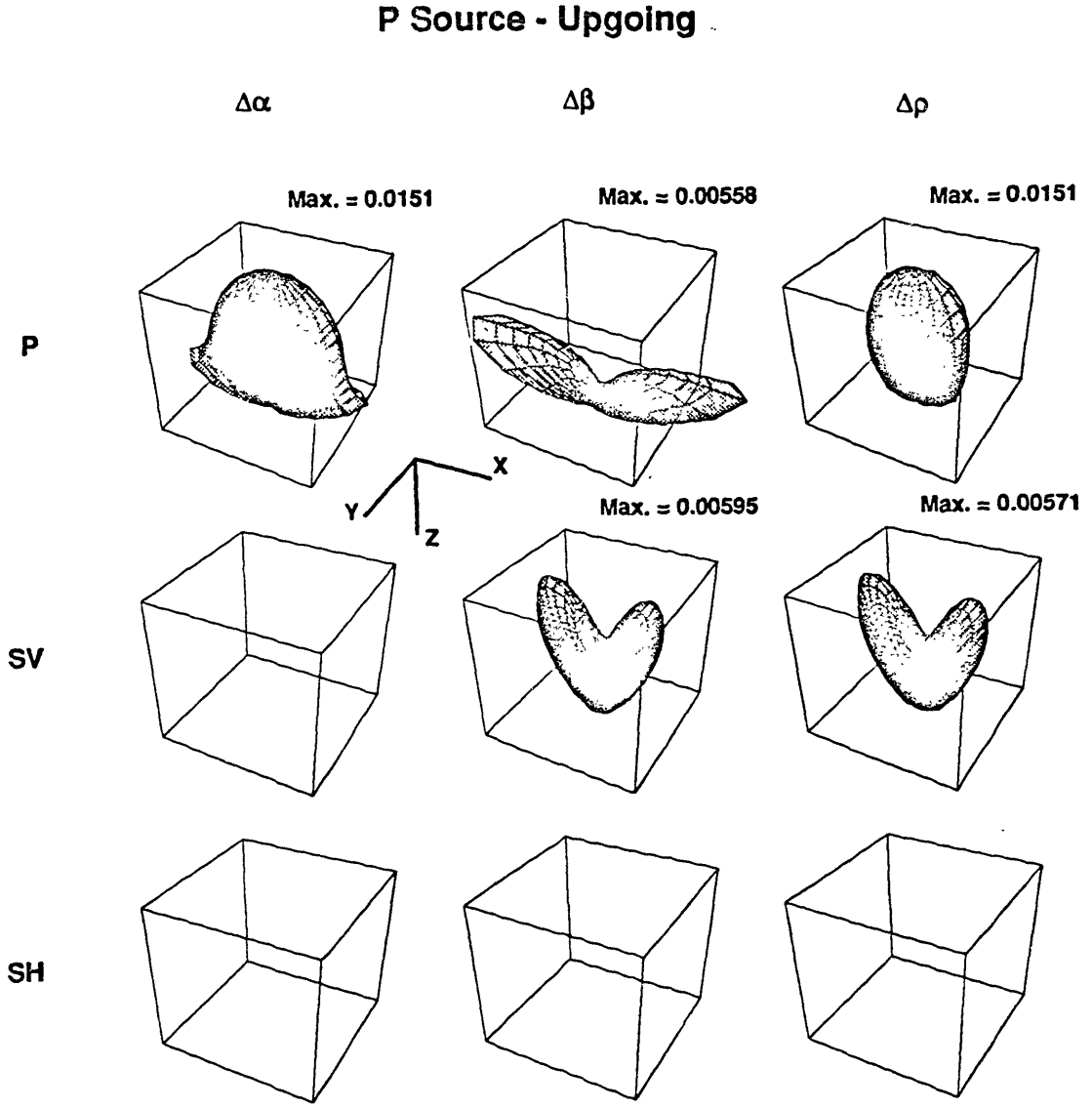

Figure 3-9: Three-dimensional plots of the up-going P, SV, and SH components of the scattered field for the rough interface model of Figure 3-1 and a normally incident planar P wave source. The leftmost column corresponds with Model B, the center column with Model C, and the rightmost column with Model D. The maximum amplitude is shown above each plot. Summing across a row produces the P, SV, or SH component of scattering in Model A.

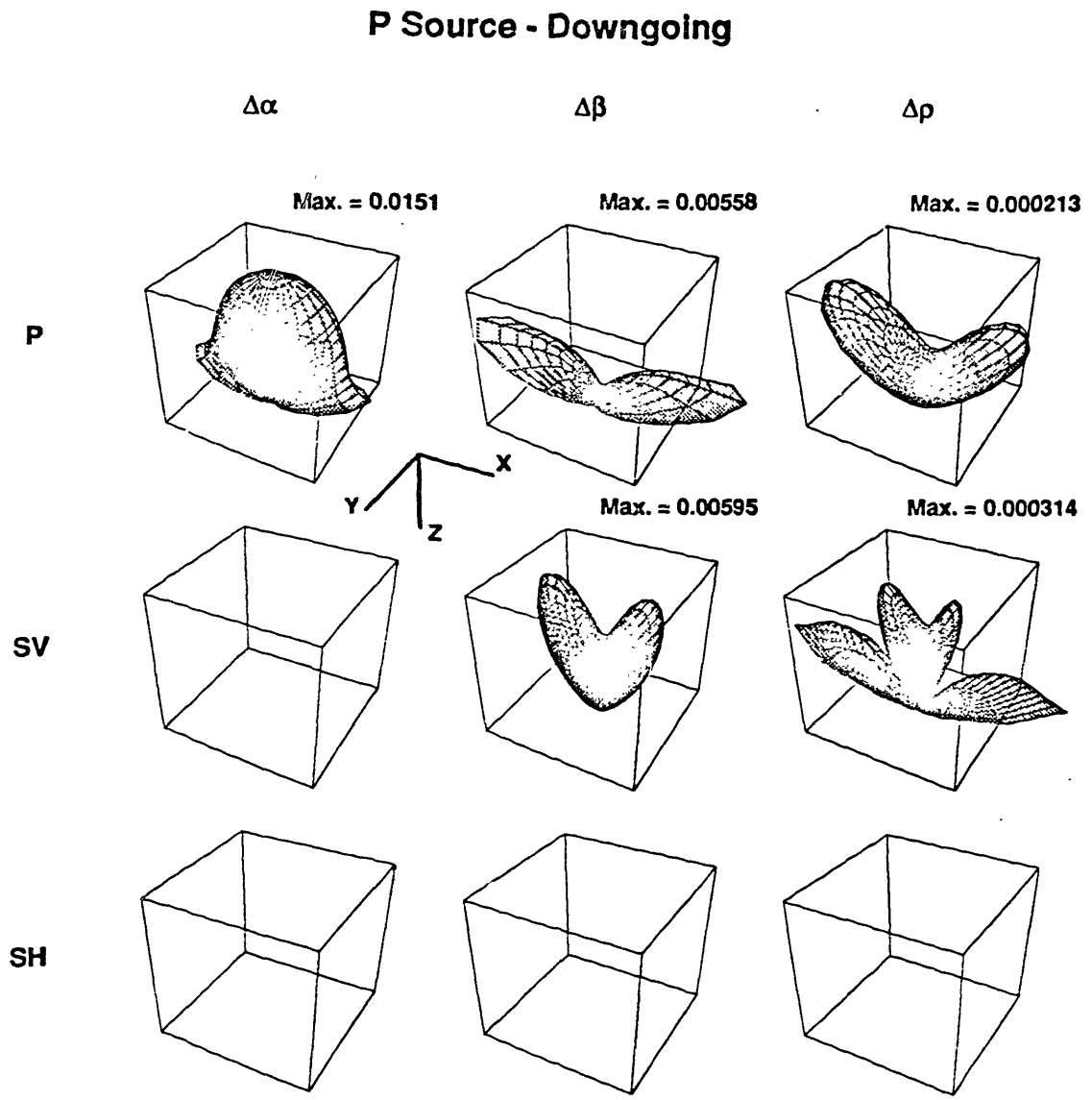

Figure 3-10: Three-dimensional plots of the down-going P, SV, and SH components of the scattered field for the rough interface model of Figure 3-1 and a normally incident planar P wave source. The leftmost column corresponds with Model B, the center column with Model C, and the rightmost column with Model D. The maximum amplitude is shown above each plot. Summing across a row produces the P, SV, or SH component of scattering in Model A.

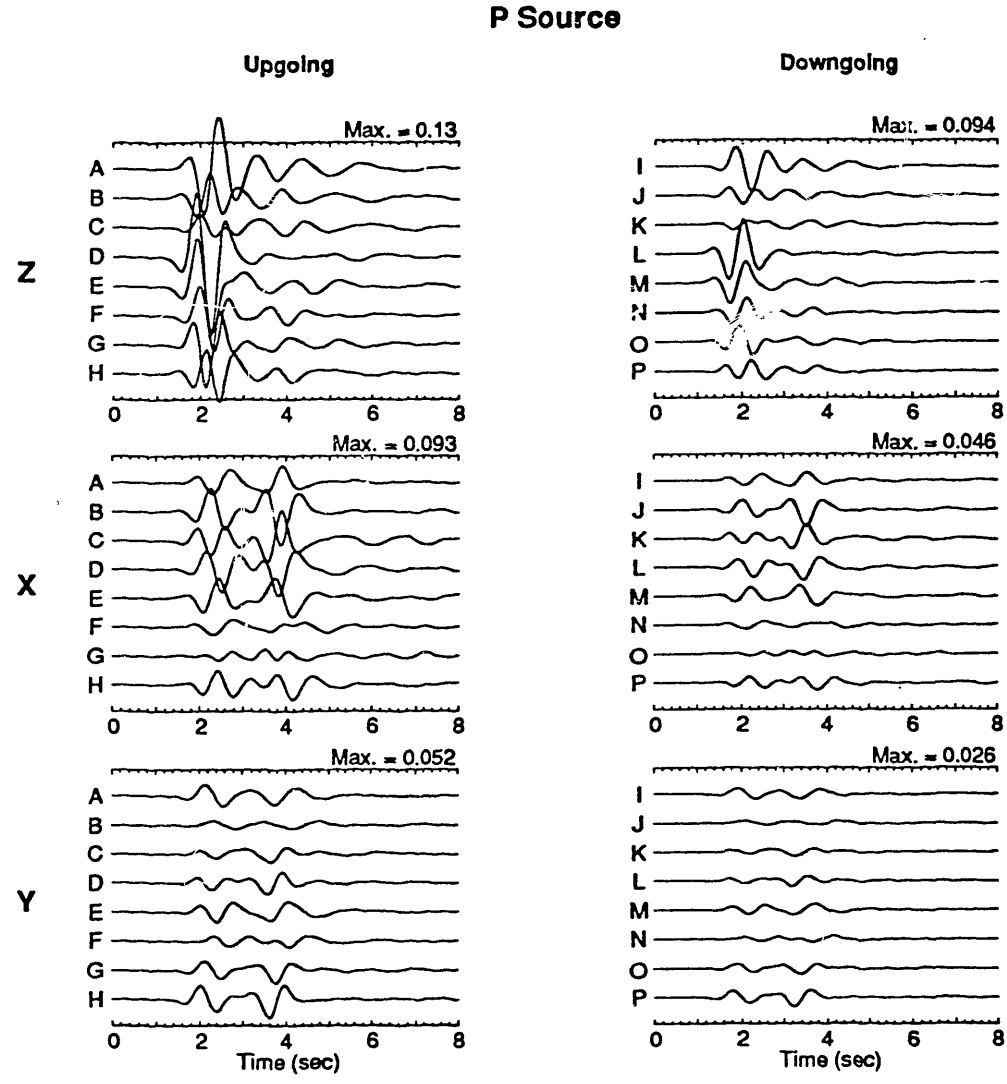

Figure 3-11: Representative seismograms for the scattered field of Model A. The source is a normally incident planar P wave. The up-going field is measured by 8 three-component receivers, labeled A–H, evenly spaced along the $x = 0$ line between $y = 0$ and $y = 5.6$ km (inclusive) and at an elevation above the mean planar interface of 2 km. The down-going field is measured by an identical array, labeled I–P, displaced 2 km below the mean planar interface. The seismograms are all plotted at the same scale, and the maximum amplitude is indicated on each plot.

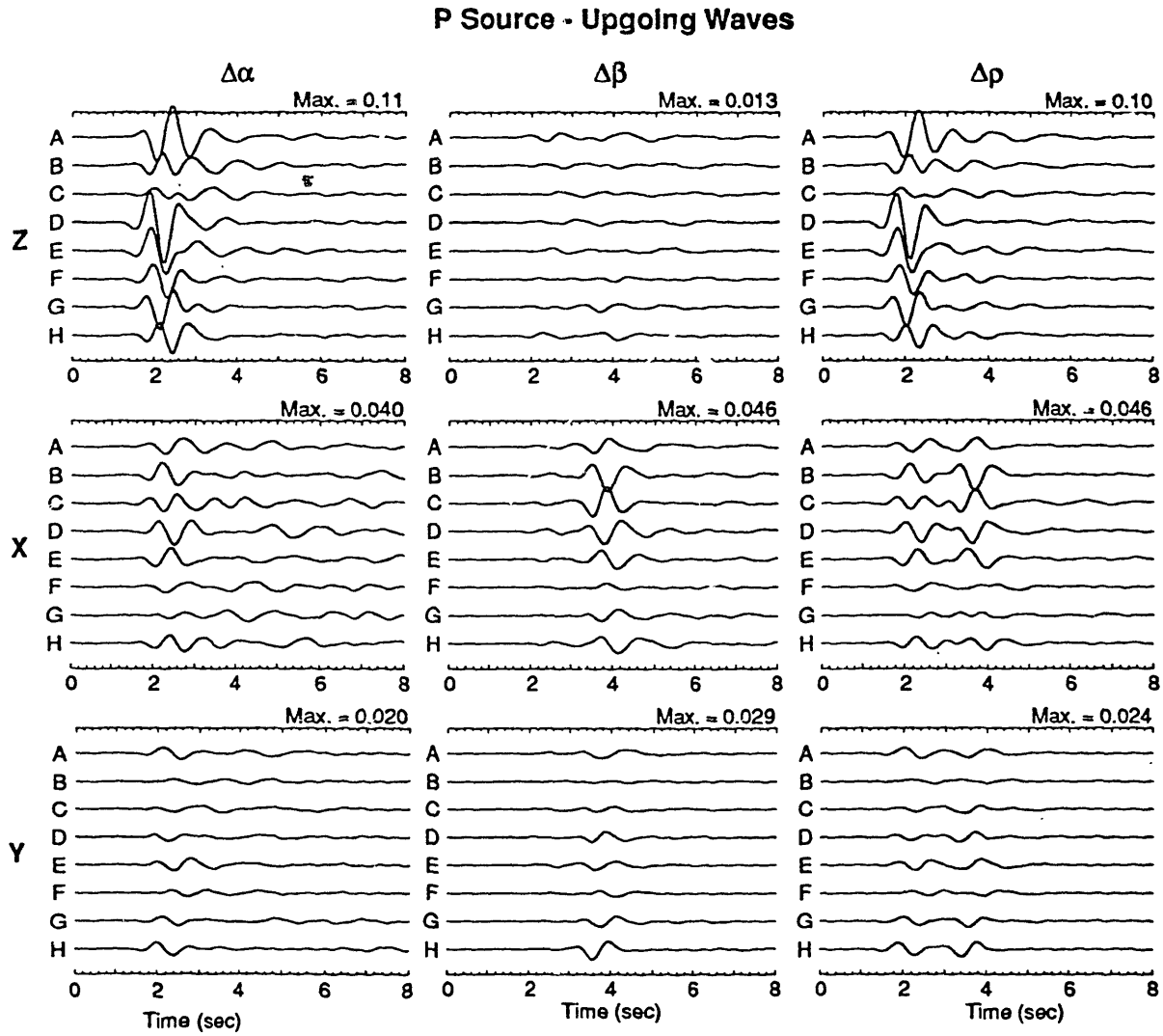

Figure 3-12: Representative three-component seismograms for the up-going scattered field in Figure 3-11 decomposed into its $\Delta\alpha$, $\Delta\beta$, and $\Delta\rho$ components. The $\Delta\alpha$ component was generated from Model B, the $\Delta\beta$ component from Model C, and the $\Delta\rho$ component from Model D. The scale is the same as that in Figure 3-11.

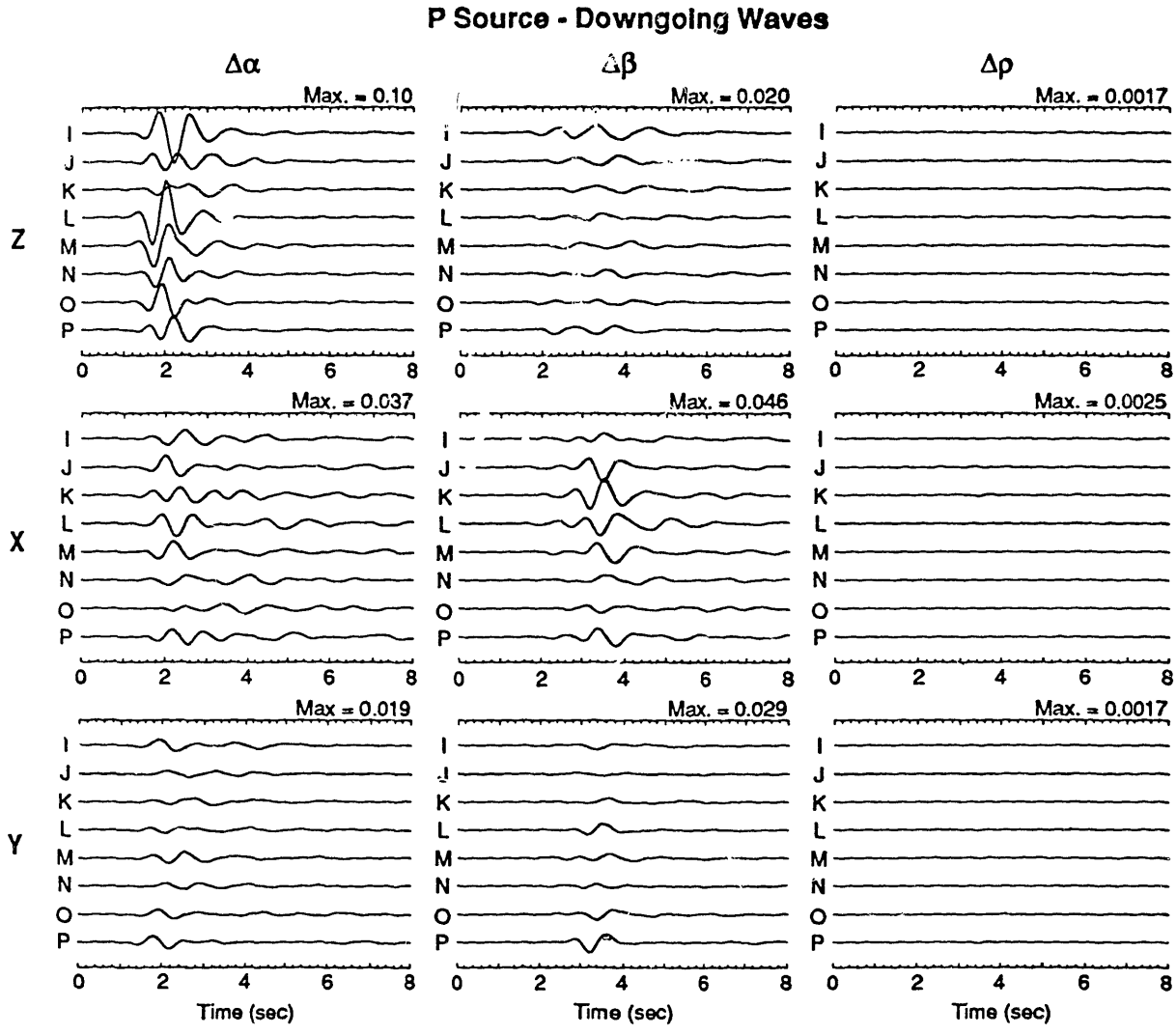

Figure 3-13: Representative three-component seismograms for the down-going scattered field in Figure 3-11 decomposed into its $\Delta\alpha$, $\Delta\beta$, and $\Delta\rho$ components. The $\Delta\alpha$ component was generated from Model B, the $\Delta\beta$ component from Model C, and the $\Delta\rho$ component from Model D. The scale is the same as that in Figure 3-11.

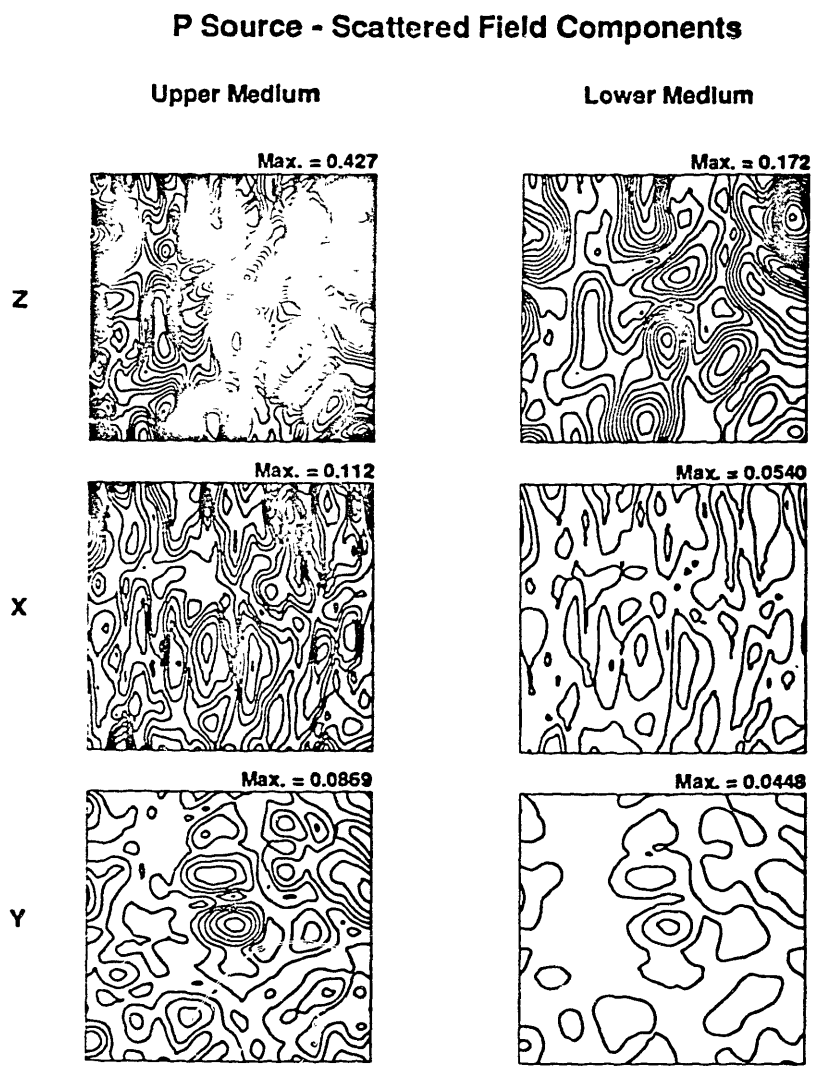

Figure 3-14: The areal distribution of forward scattered and backward scattered waves amplitudes measured at 2 km above and 2 km below the mean planar interface. The maximum amplitude (measured as an absolute value) on each component of each receiver is shown contoured. The source is a normally incident planar P wave traveling in Model A. The contour interval is 0.01, where the incident wave has unit amplitude.

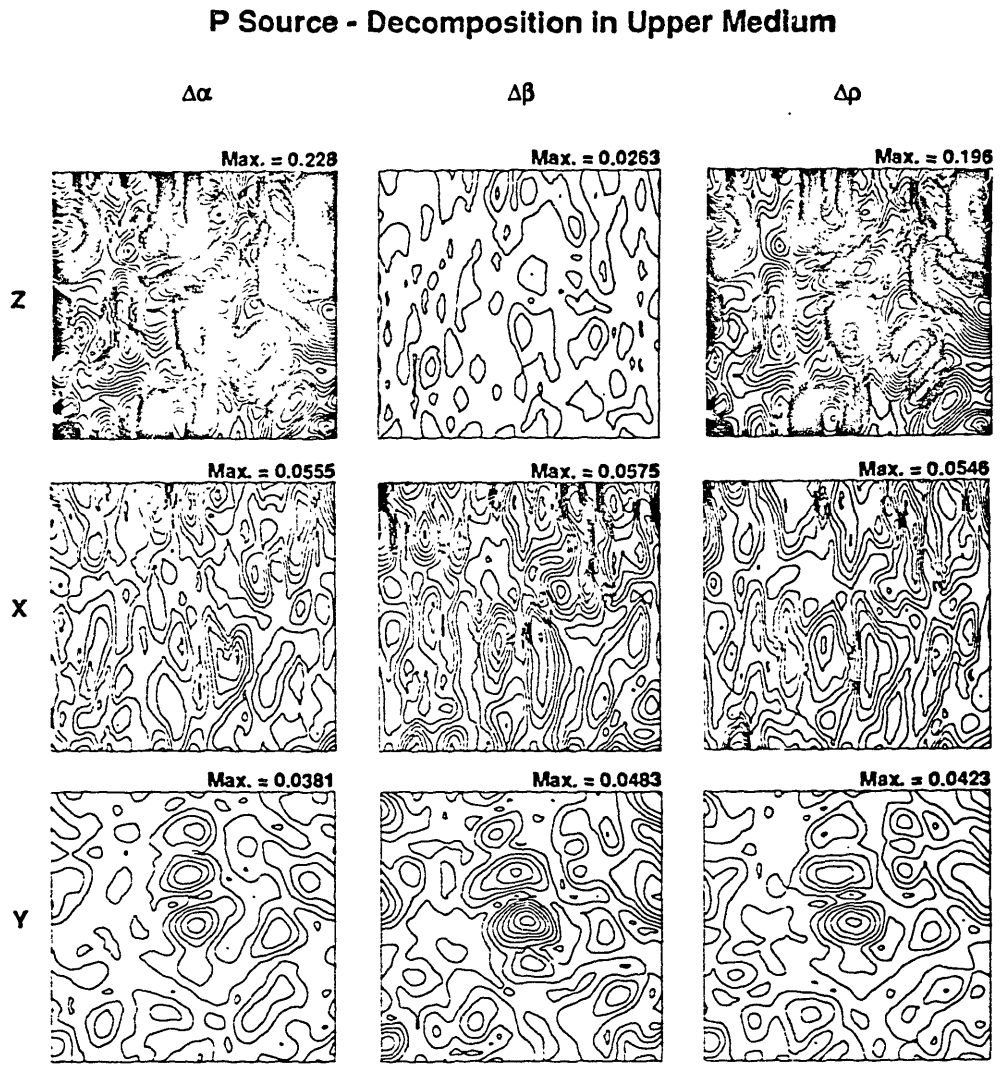

Figure 3-15: The areal distribution of backward scattered wave amplitudes measured at 2 km above the mean planar interface. The maximum amplitude (measured as an absolute value) on each component of each receiver is shown contoured. The source is a normally incident planar P wave traveling in Models B, C, and D to produce the $\Delta\alpha$, $\Delta\beta$, and $\Delta\rho$ components, respectively. The maximum amplitude is indicated for each contour map. The contour interval is 0.005, where the incident wave has unit amplitude.

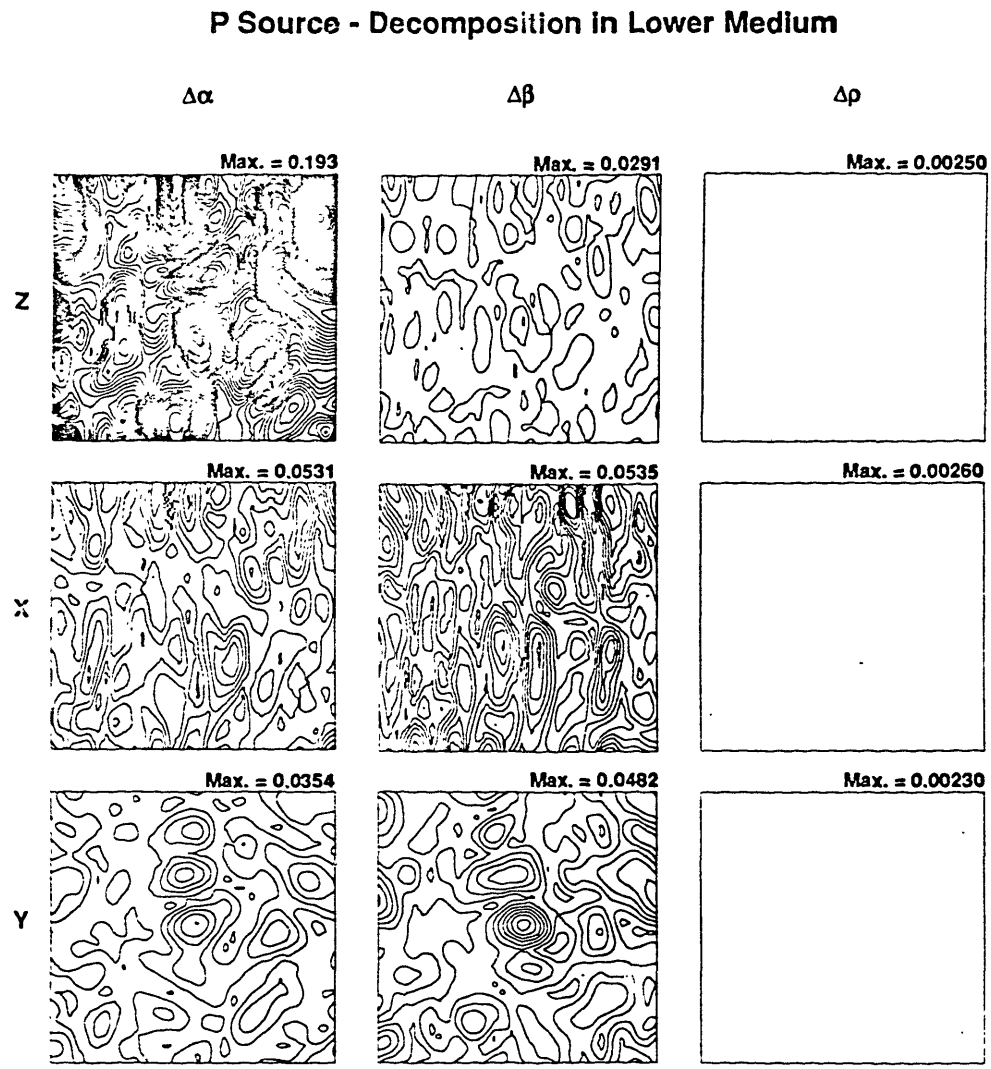

Figure 3-16: The areal distribution of forward scattered wave amplitudes measured at 2 km below the mean planar interface. The maximum amplitude (measured as an absolute value) on each component of each receiver is shown contoured. The source is a normally incident planar P wave traveling in Models B, C, and D to produce the $\Delta\alpha$, $\Delta\beta$, and $\Delta\rho$ components, respectively. The maximum amplitude is indicated for each contour map. The contour interval is 0.005, where the incident wave has unit amplitude.

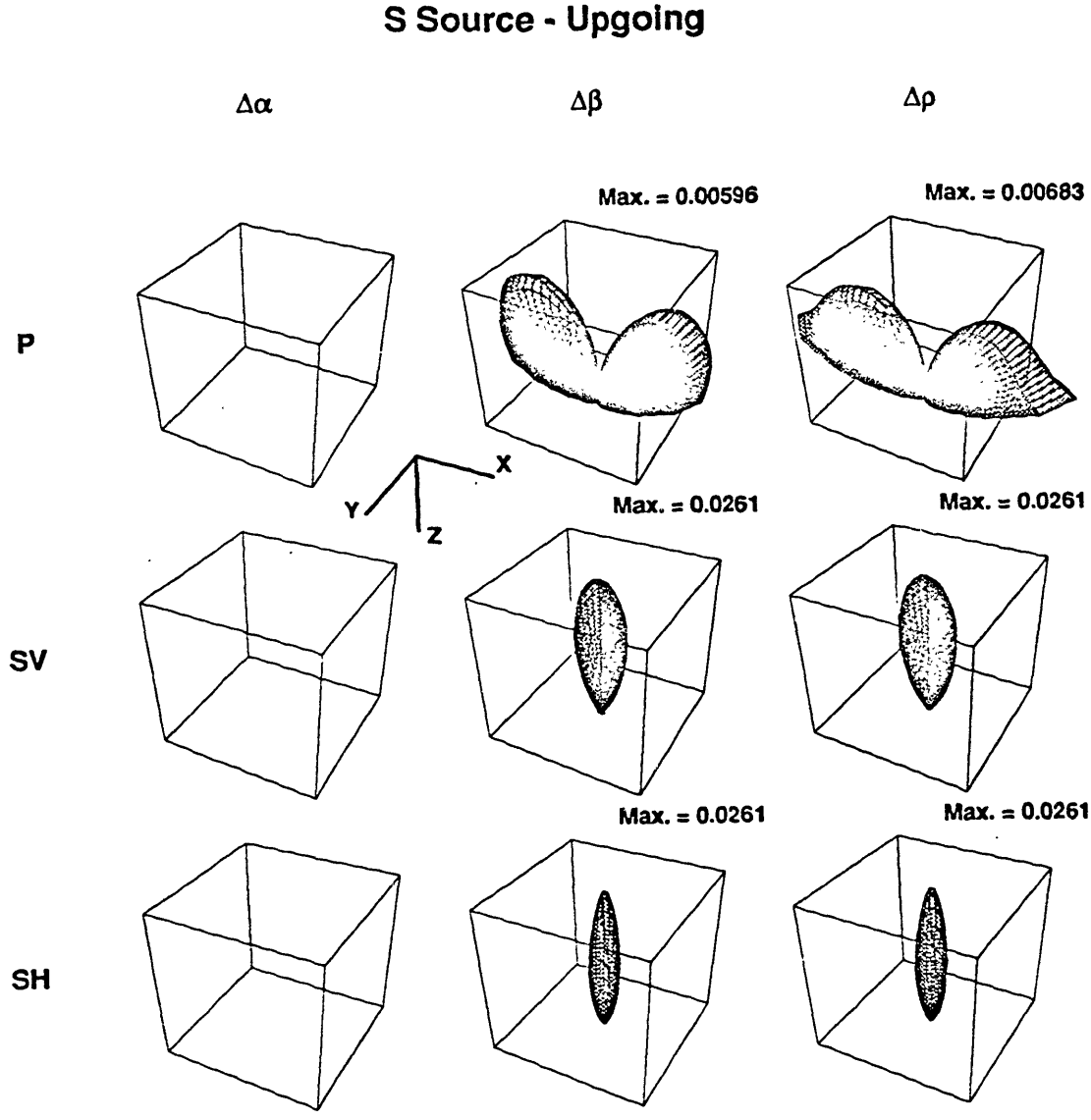

Figure 3-17: Three-dimensional plots of the up-going P, SV, and SH components of the scattered field for the rough interface model of Figure 3-1 and a normally incident planar SV wave with particle motion in the x direction. The leftmost column corresponds with Model B, the center column with Model C, and the rightmost column with Model D. The maximum amplitude is shown above each plot. Summing across a row produces the P, SV, or SH component of scattering in Model A.

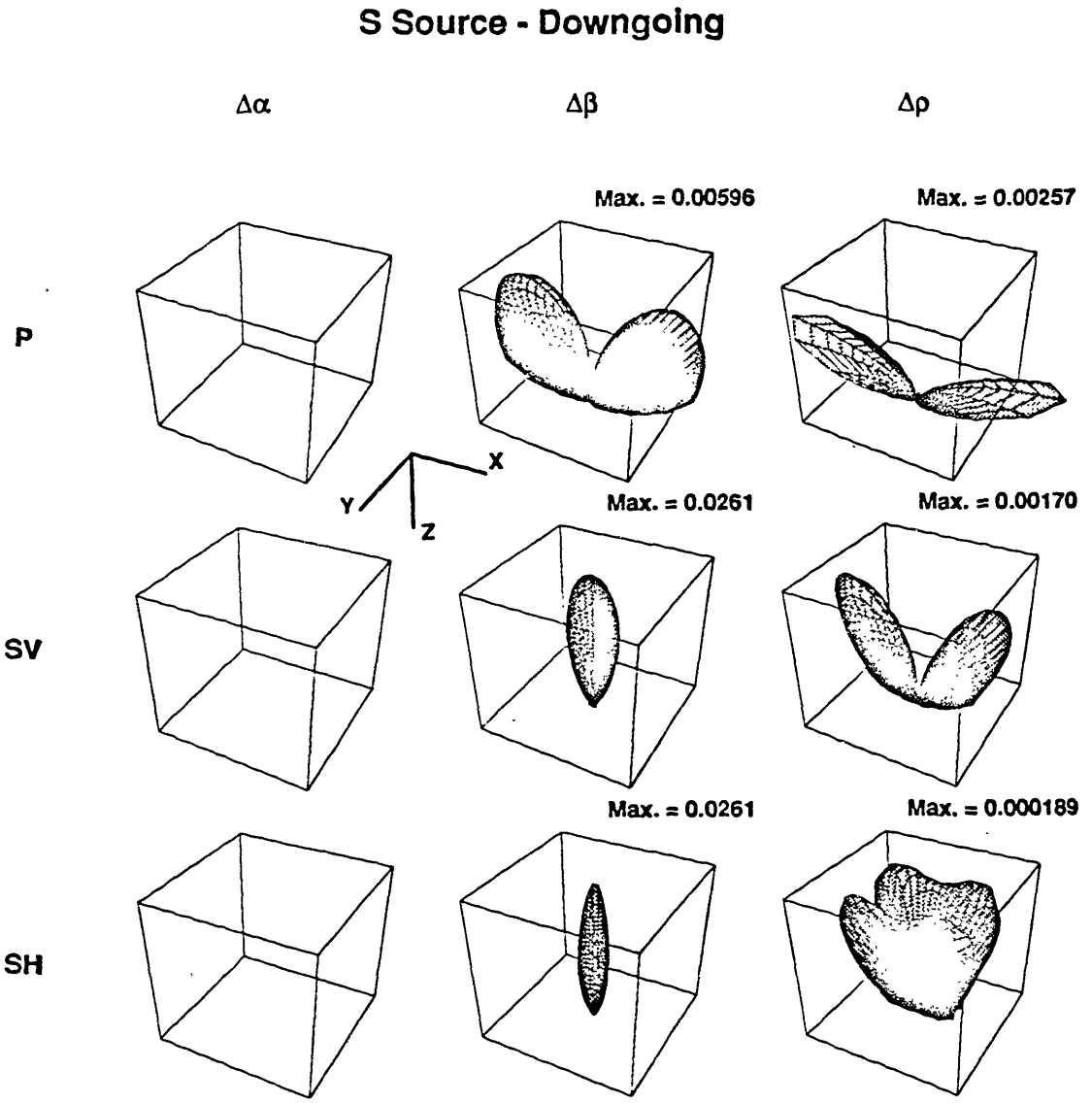

Figure 3-18: Three-dimensional plots of the down-going P, SV, and SH components of the scattered field for the rough interface model of Figure 3-1 and a normally incident planar SV wave with particle motion in the x direction. The leftmost column corresponds with Model B, the center column with Model C, and the rightmost column with Model D. The maximum amplitude is shown above each plot. Summing across a row produces the P, SV, or SH component of scattering in Model A.

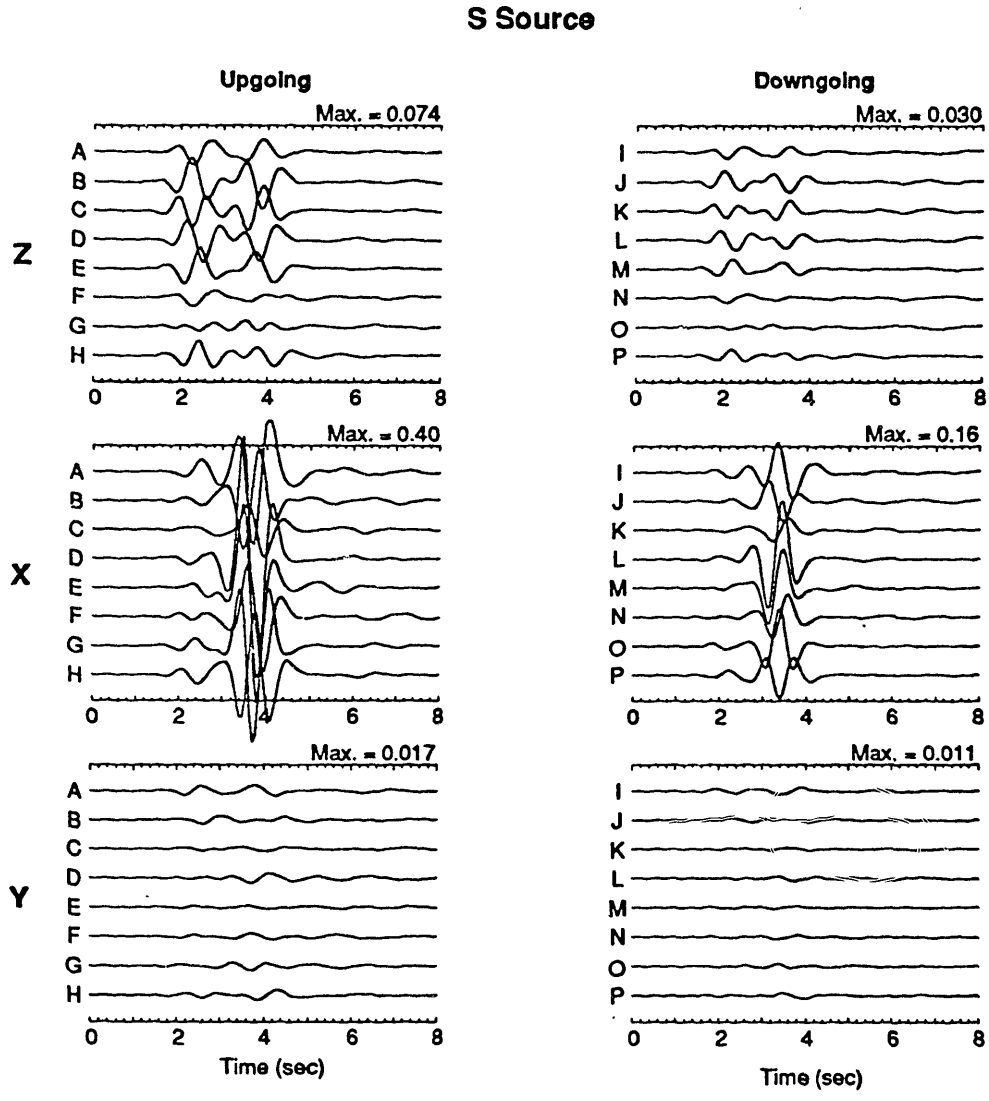

Figure 3-19: Representative seismograms for the scattered field of Model A. The source is a normally incident planar SV wave with particle motion in the x direction. The receiver locations and seismogram scale factors are the same as those in Figure 3-11.

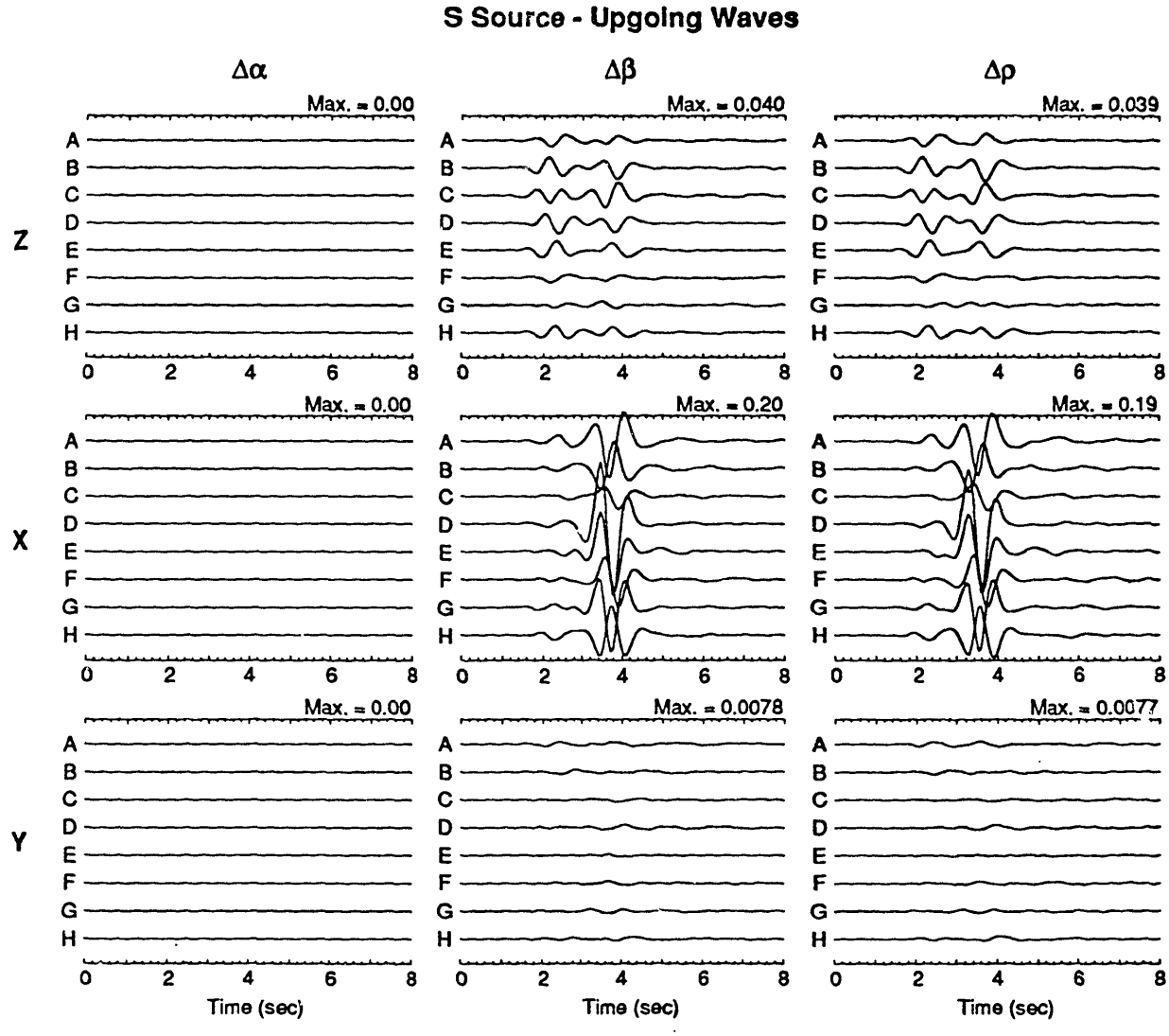

Figure 3-20: Representative three-component seismograms for the up-going scattered field in Figure 3-19 decomposed into its $\Delta\alpha$, $\Delta\beta$, and $\Delta\rho$ components. The $\Delta\alpha$ component was generated from Model B, the $\Delta\beta$ component from Model C, and the $\Delta\rho$ component from Model D. The scale is the same as that in Figure 3-19.

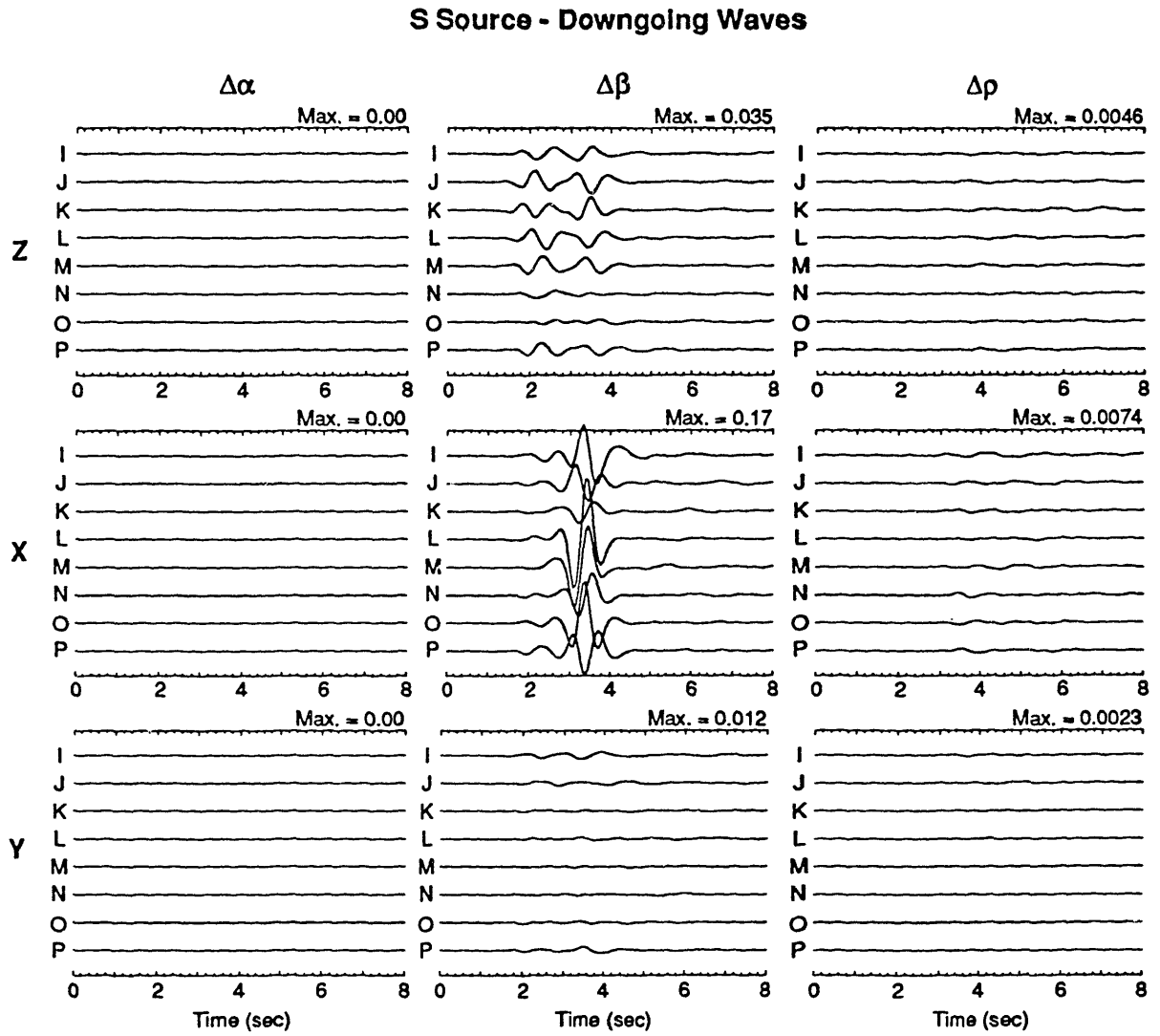

Figure 3-21: Representative three-component seismograms for the down-going scattered field in Figure 3-19 decomposed into its $\Delta\alpha$, $\Delta\beta$, and $\Delta\rho$ components. The $\Delta\alpha$ component was generated from Model B, the $\Delta\beta$ component from Model C, and the $\Delta\rho$ component from Model D. The scale is the same as that in Figure 3-19.

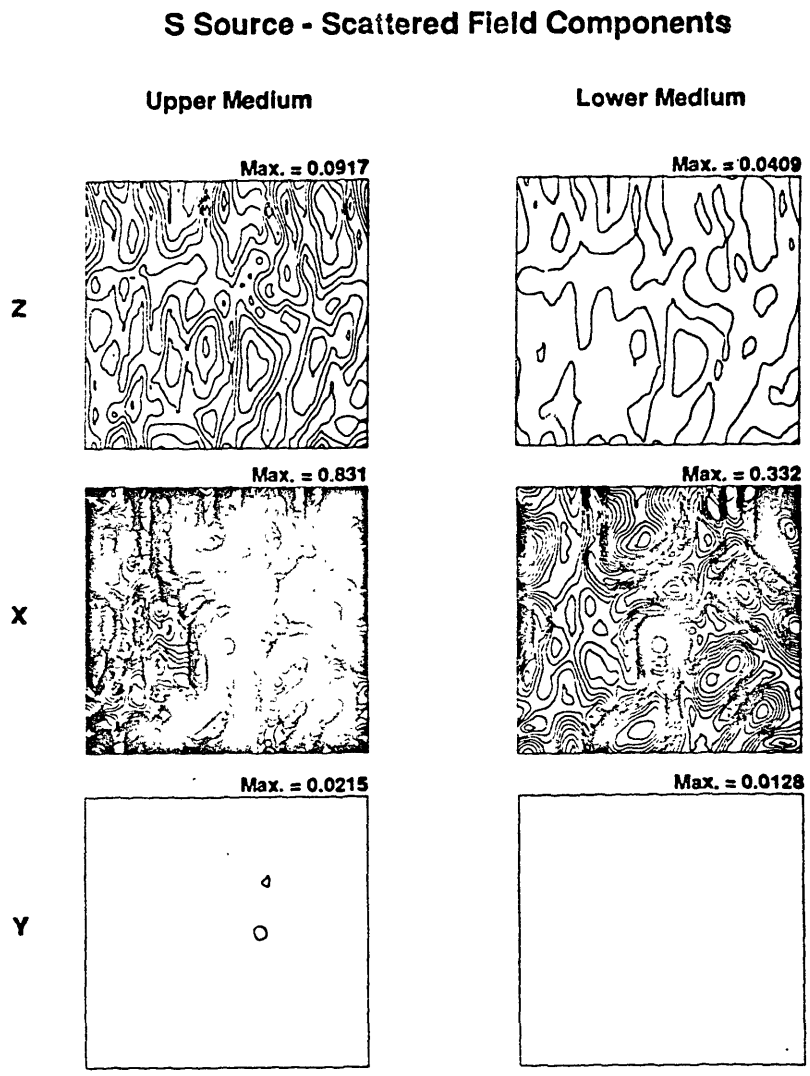

Figure 3-22: The areal distribution of forward scattered and backward scattered waves amplitudes measured at 2 km above and 2 km below the mean planar interface. The maximum amplitude (measured as an absolute value) on each component of each receiver is shown contoured. The source is a normally incident planar SV wave traveling in Model A with particle motion in the x-direction. The contour interval is 0.01, where the incident wave has unit amplitude.

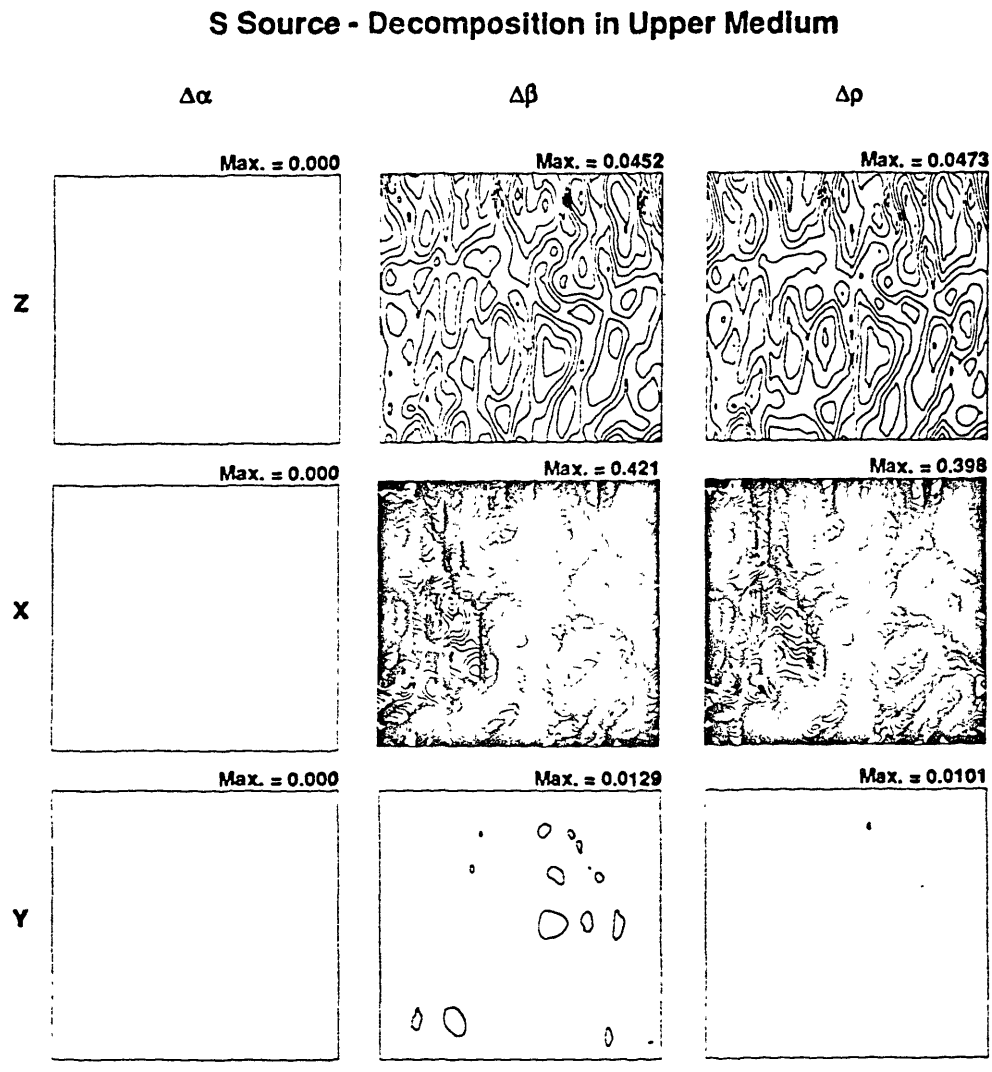

Figure 3-23: The areal distribution of backward scattered wave amplitudes measured at 2 km above the mean planar interface. The maximum amplitude (measured as an absolute value) on each component of each receiver is shown contoured. The source is a normally incident planar SV wave traveling in Models B, C, and D to produce the $\Delta\alpha$, $\Delta\beta$, and $\Delta\rho$ components, respectively. The source particle motion is in the x-direction. The maximum amplitude is indicated for each contour map. The contour interval is 0.005, where the incident wave has unit amplitude.

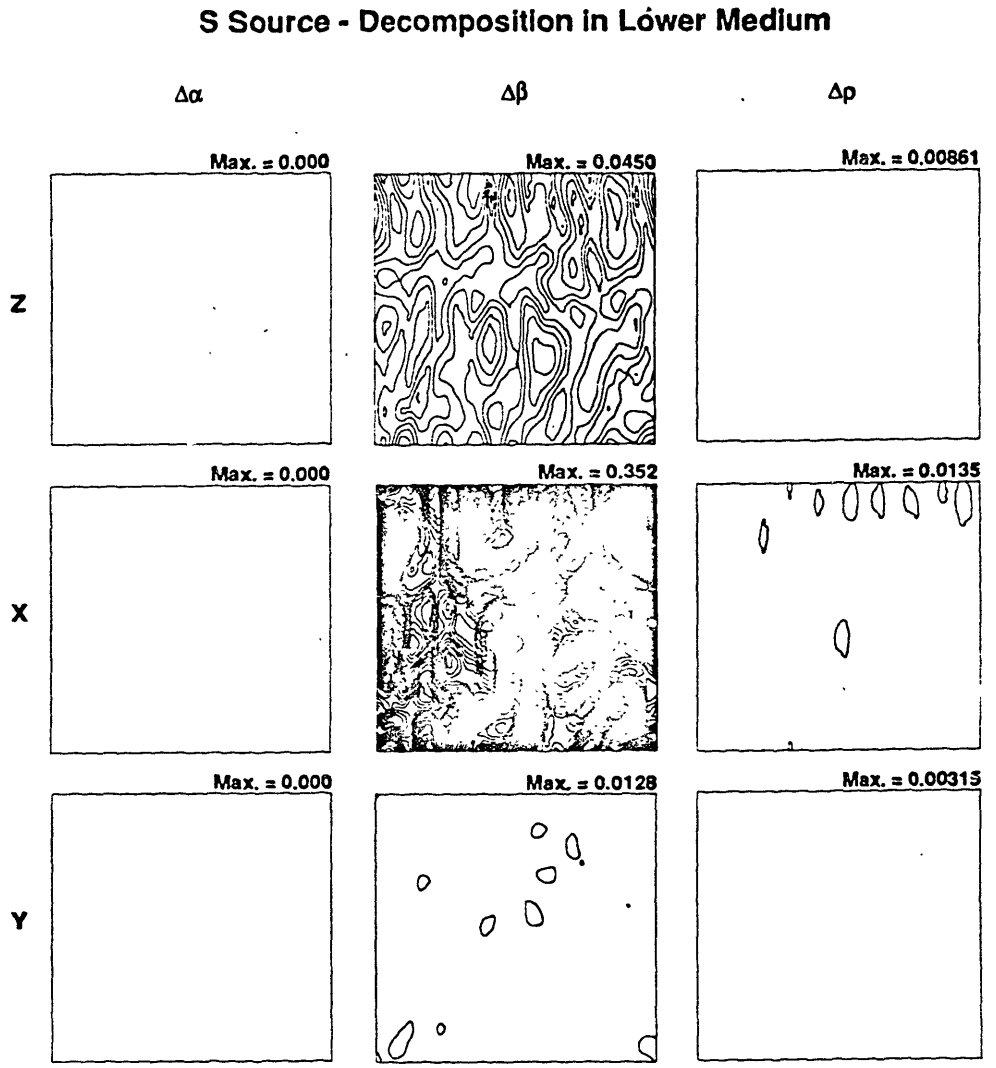

Figure 3-24: The areal distribution of forward scattered wave amplitudes measured at 2 km below the mean planar interface. The maximum amplitude (measured as an absolute value) on each component of each receiver is shown contoured. The source is a normally incident planar SV wave traveling in Models B, C, and D to produce the $\Delta\alpha$, $\Delta\beta$, and $\Delta\rho$ components, respectively. The source particle motion is in the x-direction. The maximum amplitude is indicated for each contour map. The contour interval is 0.005, where the incident wave has unit amplitude.

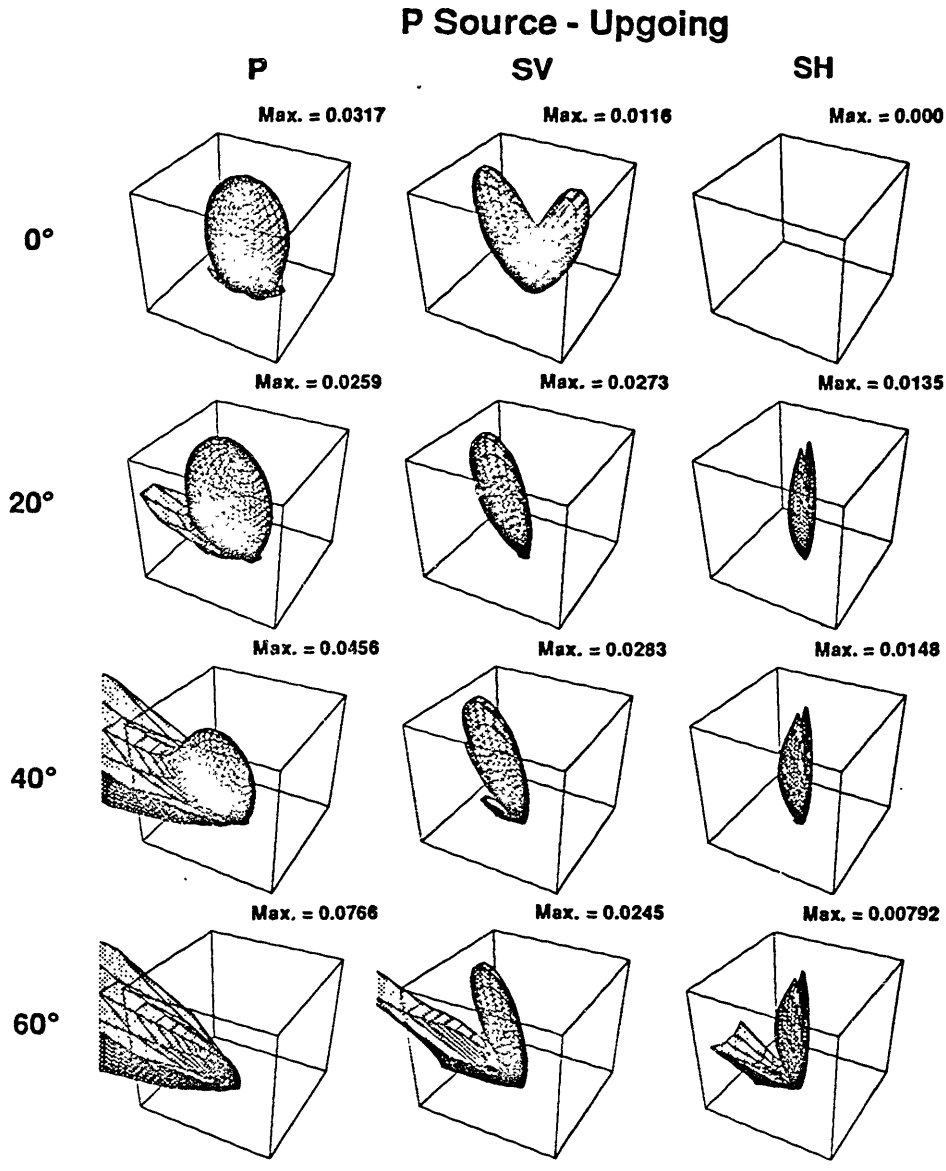

Figure 3-25: Up-going wave scattering coefficients for planar P waves incident in the x-z plane in model A at incidence angles of 0, 20, 40, and 60 degrees. The maximum amplitude of each coefficient is indicated.

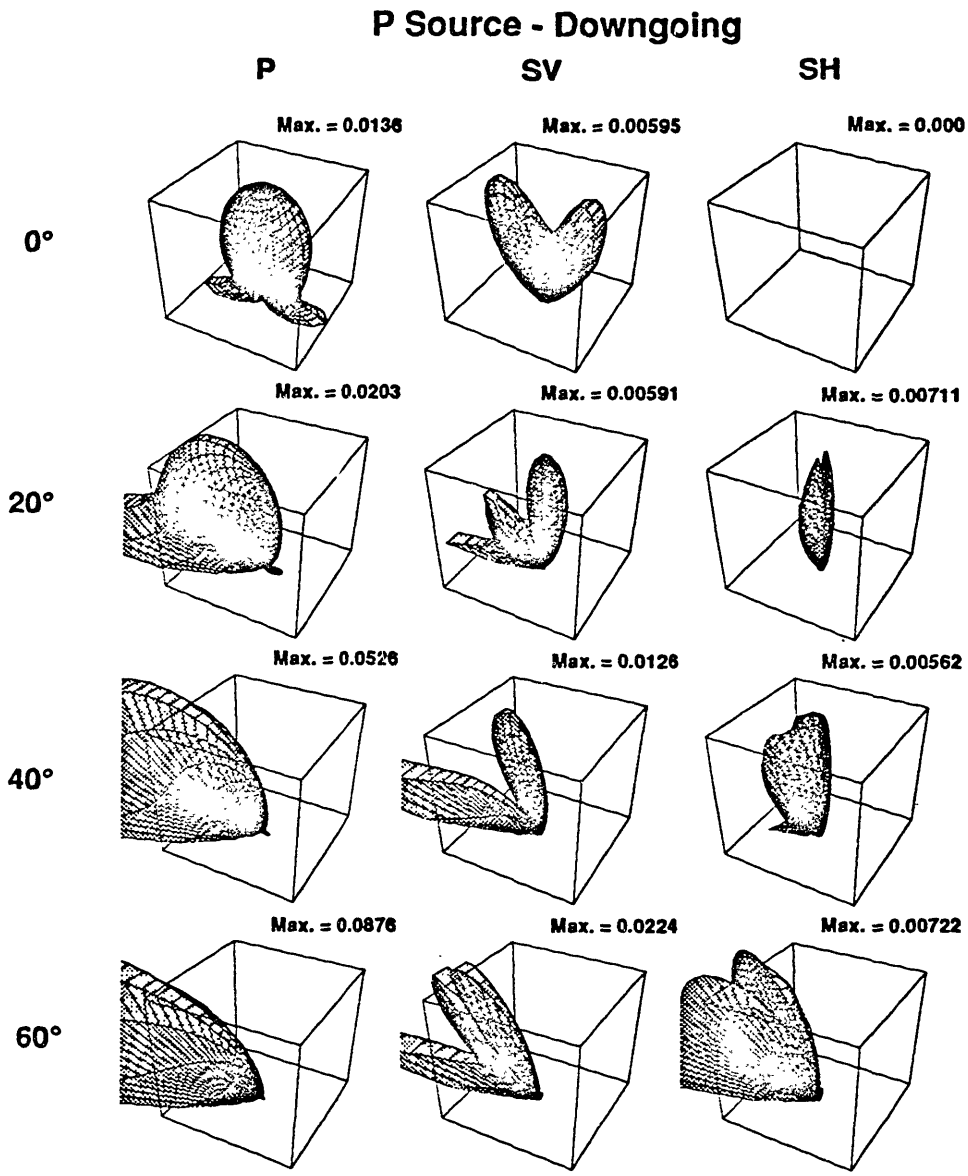

Figure 3-26: Down-going wave scattering coefficients for planar P waves incident in the x-z plane in model A at incidence angles of 0, 20, 40, and 60 degrees. The maximum amplitude of each coefficient is indicated.

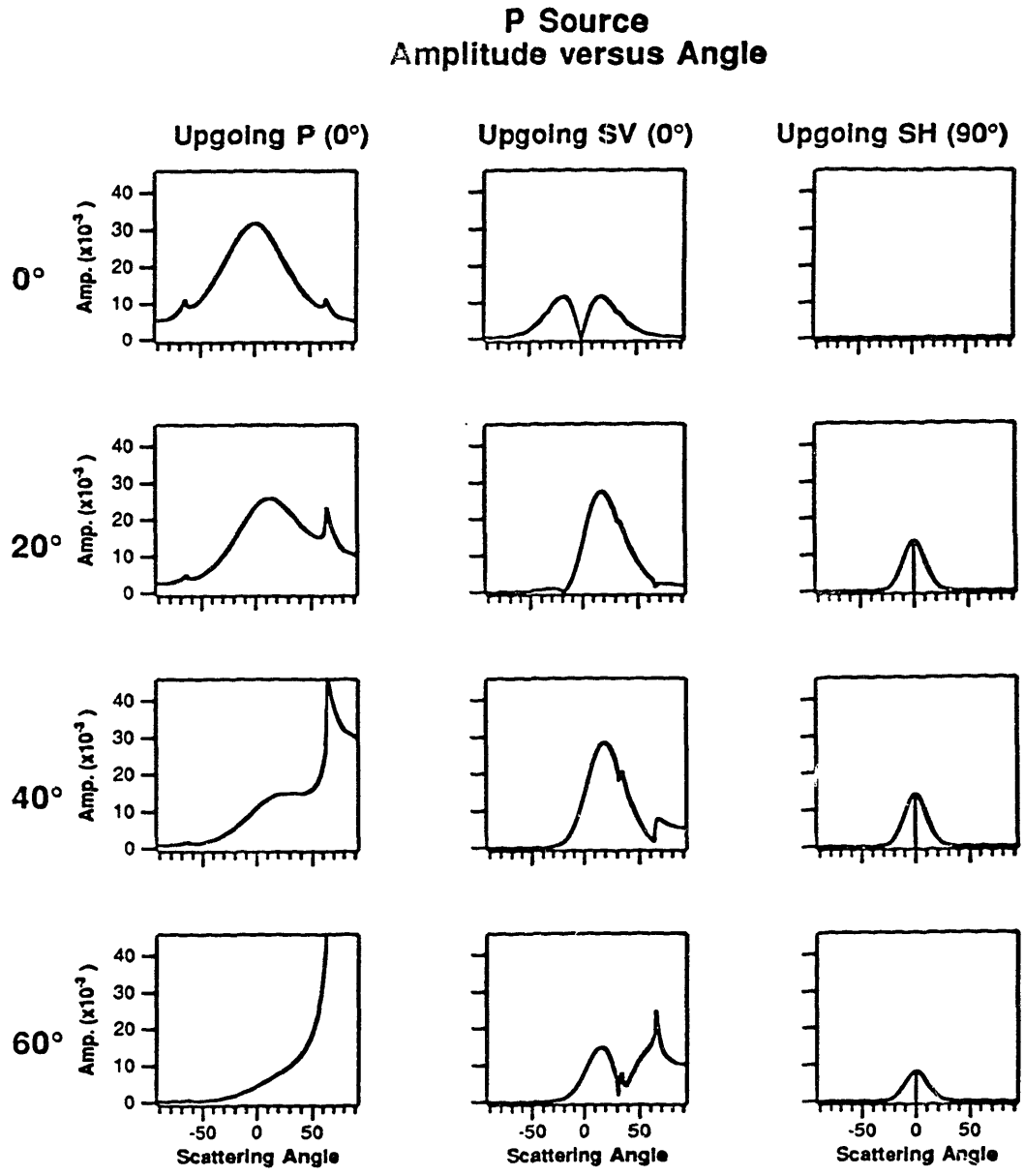

Figure 3-27: Cross-sectional plots for the three-dimensional scattering coefficients shown in Figure 3-25. P and SV cross-sections were taken in the x-z plane, and SH cross-sections were taken in the y-z plane. All plots have the same scale. Positive scattering angles indicate forward scattering.

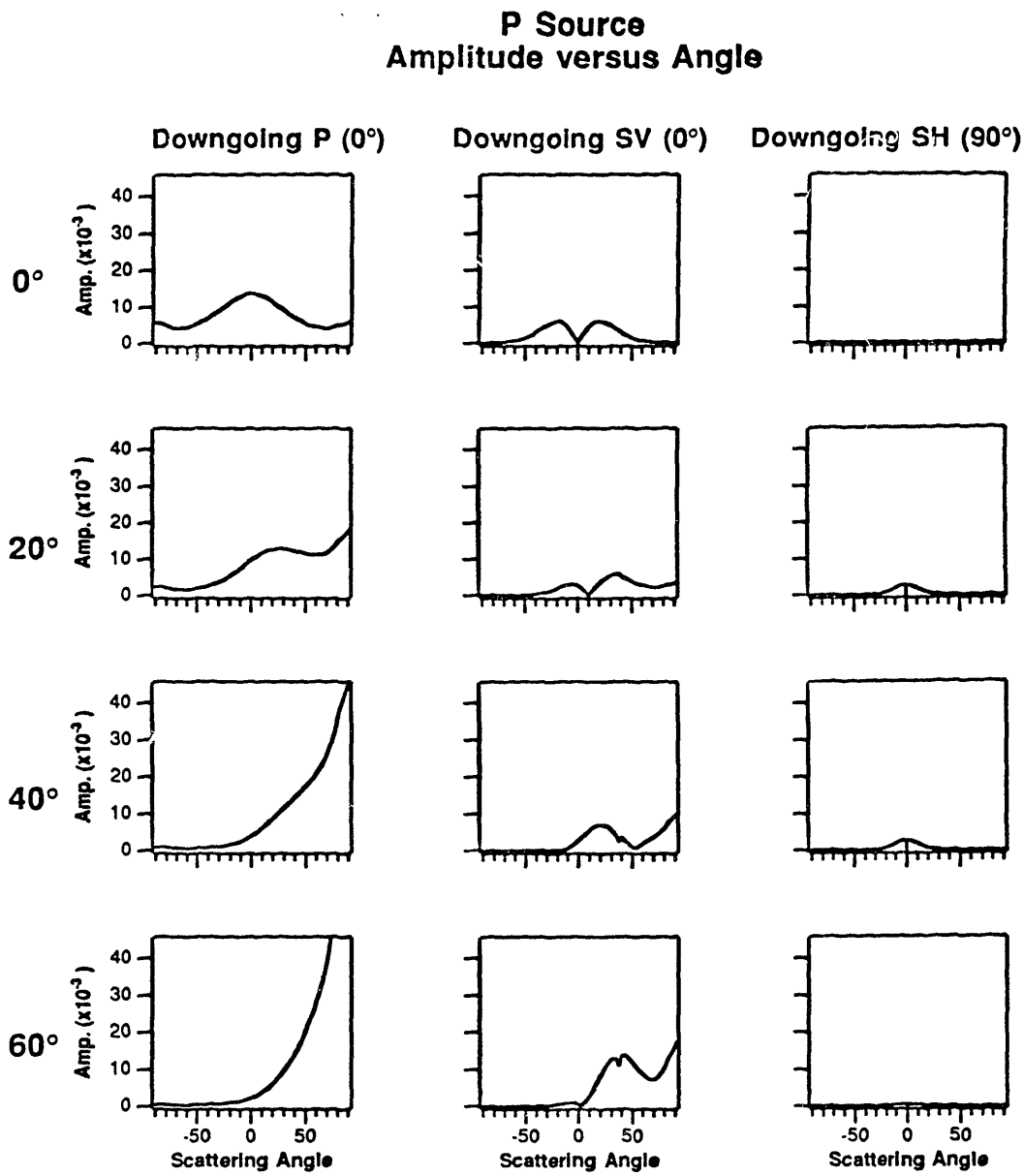

Figure 3-28: Cross-sectional plots for the three-dimensional scattering coefficients shown in Figure 3-26. P and SV cross-sections were taken in the x-z plane, and SH cross-sections were taken in the y-z plane. All plots have the same scale. Positive scattering angles indicate forward scattering.

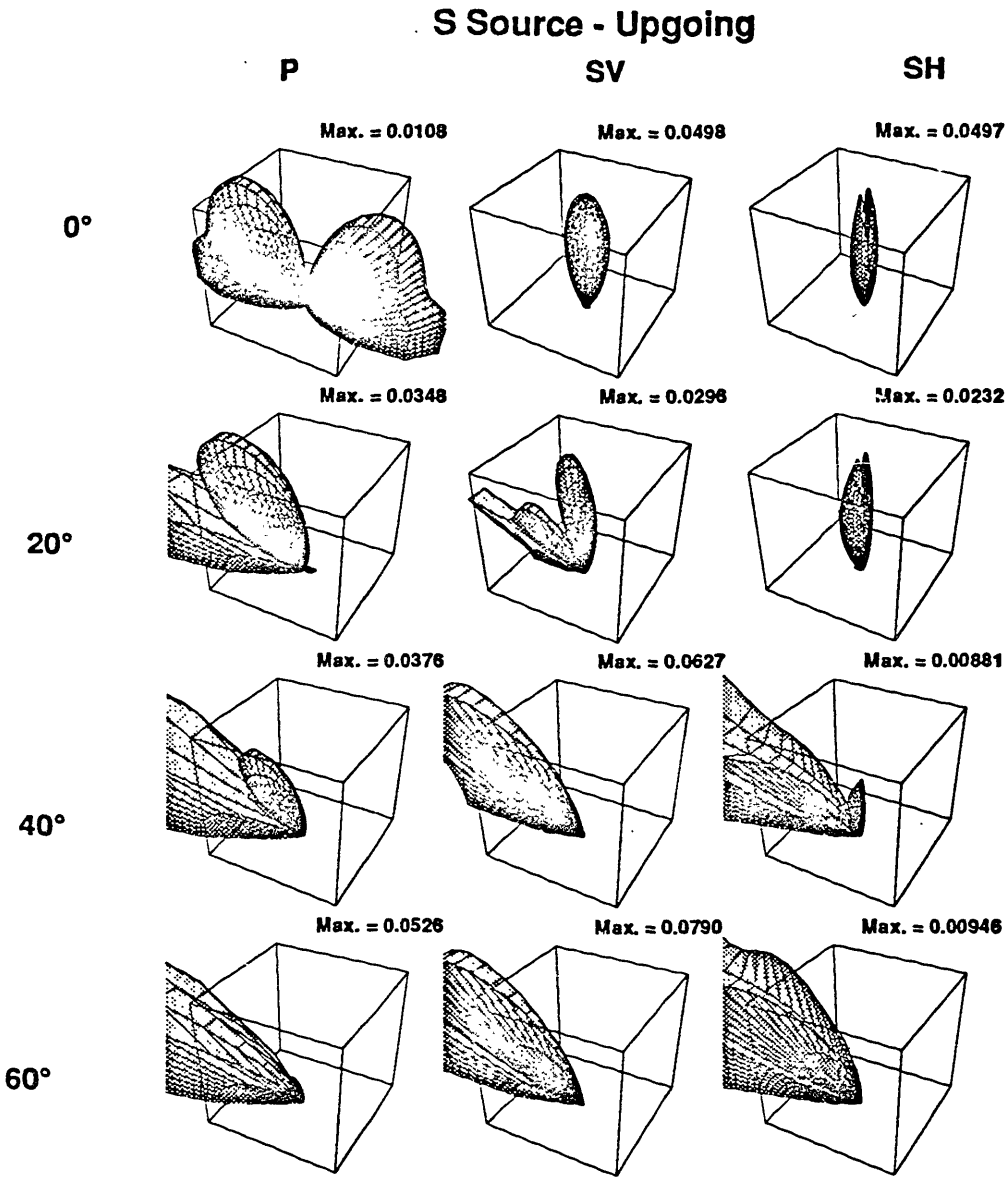

Figure 3-29: Up-going wave scattering coefficients for planar SV waves incident in the x-z plane in model A at incidence angles of 0, 20, 40, and 60 degrees. The maximum amplitude of each coefficient is indicated.

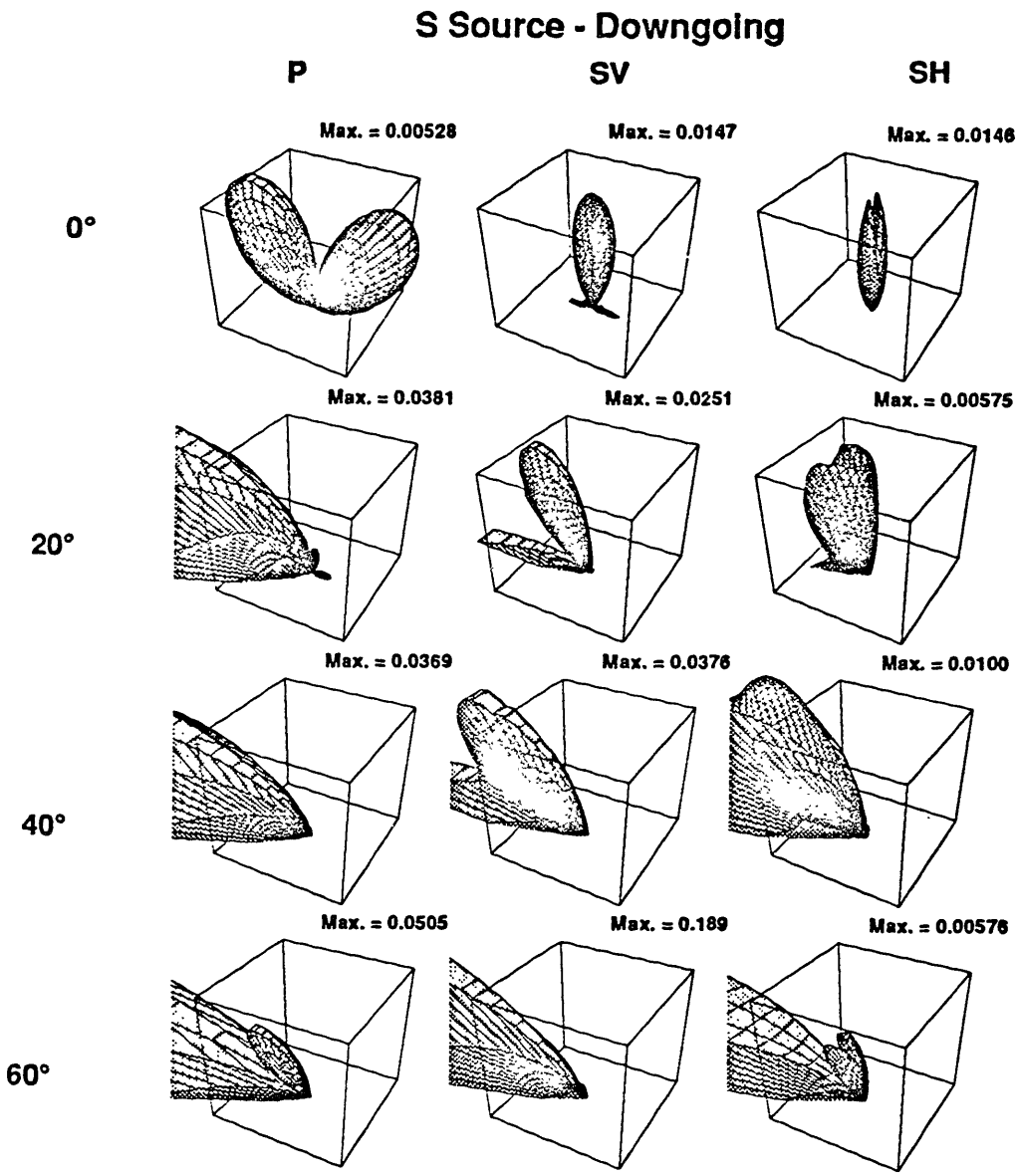

Figure 3-30: Down-going wave scattering coefficients for planar SV waves incident in the x-z plane in model A at incidence angles of 0, 20, 40, and 60 degrees. The maximum amplitude of each coefficient is indicated.

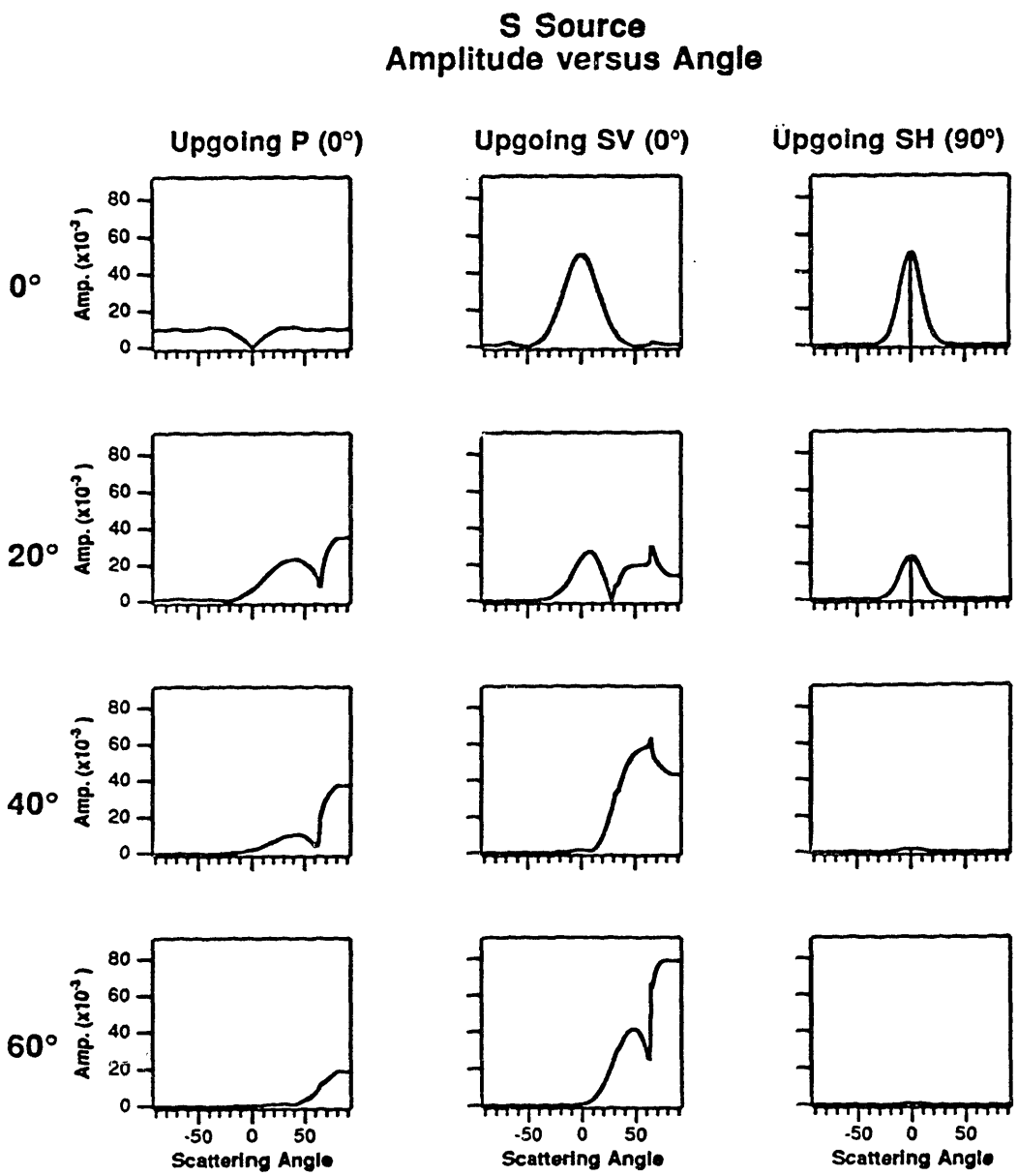

Figure 3-31: Cross-sectional plots for the three-dimensional scattering coefficients shown in Figure 3-29. P and SV cross-sections were taken in the x-z plane, and SH cross-sections were taken in the y-z plane. All plots have the same scale. Positive scattering angles indicate forward scattering.

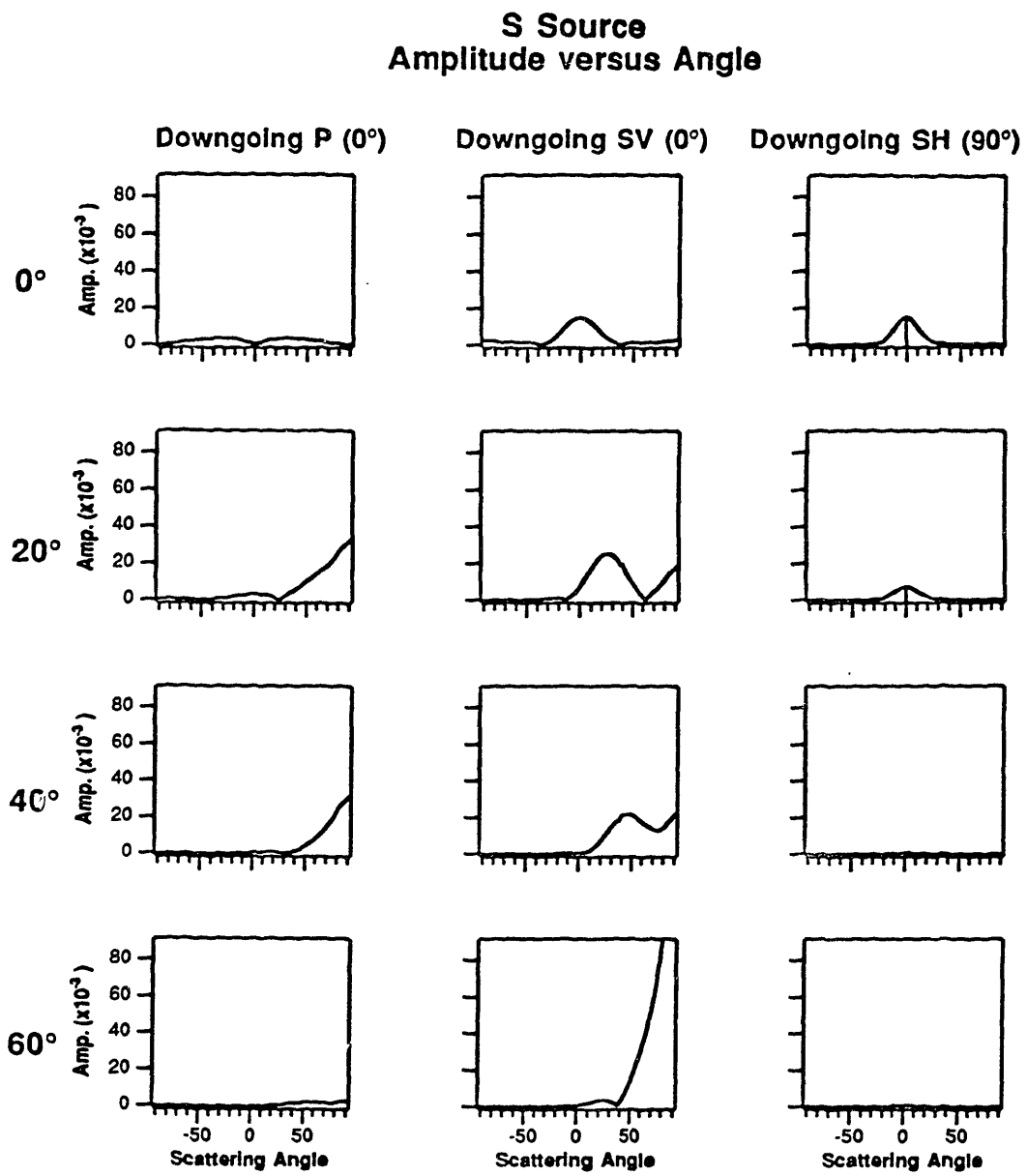

Figure 3-32: Cross-sectional plots for the three-dimensional scattering coefficients shown in Figure 3-30. P and SV cross-sections were taken in the x-z plane, and SH cross-sections were taken in the y-z plane. All plots have the same scale. Positive scattering angles indicate forward scattering.

Chapter 4

APPLICATION TO VSP DATA

4.1 INTRODUCTION

An SH wave vertical seismic profile[1] (VSP) was obtained in 1989 as part of an overall experiment to obtain a full nine-component (three-component source and three-component receiver) seismic data set which could be used to study anisotropy and scattering effects at an MIT experimental borehole site (MIT/Birch 1-20A) in Manistee County, Michigan. In an SH wave vertical seismic profile, the source is a traction applied at the surface of the Earth in direction normal to the sagittal plane. Within the sagittal plane of a model composed of horizontal, planar interfaces, such a source would propagate only as SH waves, with particle motions in the tangential direction only. The observed seismograms for this experiment contained significant energy in the vertical and radial components. Two plausible explanations for this anomalous energy are dipping planar interfaces and scattering. We apply the perturbation method of chapter 2 to show that the scattering produced by a rough interface can satisfactorily explain much of the observed anomalous energy.

[1] A vertical seismic profile (VSP) is a seismic experiment in which a source is located at or near the surface of the earth and receivers are located in a borehole. For an indepth discussion of the VSP geometry and the associated interpretational techniques, see Gal'perin (1974) or Balsh *et al.*, (1982).

4.2 SITE DESCRIPTION

The borehole site location is indicated in Figure 4-1. This site is in the northeastern part of the Michigan basin. The regional dip of this basin is less than 1°. A lithologic cross-section of the strata pierced by the borehole is given in Figure 4-2, with velocities and densities indicated for the region of interest. The top three layers are composed of glacial till, and their P wave velocities were determined from a seismic refraction survey performed by Marathon Oil Company (Caravana, *et al.*, 1987). The slow topmost layer, as described in drillers' logs, is composed of sand, gravel, and clay. These logs, kept while drilling numerous shallow (< 45 m deep) boreholes in the region, record the drillers' observations of changes in sediment color and texture noted as the hole is bored. Both the refraction survey and the driller's logs indicated that the interfaces in and at the base of the glacial till are rough on a vertical scale of several meters.

4.3 EXPERIMENT DESCRIPTION

The experimental configuration is illustrated in Figure 4-3. In our terminology, the radial direction is defined as the vector contained in the sagittal plane which is perpendicular to the vertical direction, and the tangential direction is defined by the vector which is normal to the sagittal plane. The orientation of the VSP three-component receivers is determined by an on-board gyroscopic compass, allowing the seismograms to be accurately rotated into the vertical, radial, tangential coordinate system. For the data presented in this study, the down-hole receivers were spaced every 9.16 m between the depths of 9.16 m and 201.6 m.

An SH source is synthesized in a two step process using a 45° inclined force provided by an OmniPulse truck from Bolt Technology Inc (Figure 4-4). The truck first applies an impulsive force at 45° to the positive tangential direction with a hydraulic piston (the right source). The resulting waves are recorded by two three-component receivers, the VSP receiver and a fixed-position monitor phone. Without moving the receiver,

the piston is rotated by 90° and the force is applied at 45° to the negative tangential direction (the left source). The resulting "left" VSP seismogram is adjusted so that its first P wave arrival occurs at the same time, and has the same amplitude, as that in the "right" VSP seismogram to compensate for variations in the source. After every left-right source pair, the VSP receiver is moved. The VSP seismograms from all depths are normalized to a common time and amplitude scale using the time and amplitude deviations of the first arrival of the P wave observed at the fixed monitor phone. Since the corrected left-right seismogram pairs are generated by equal vertical tractions and opposite tangential tractions, they can be subtracted to yield seismograms resulting from an equivalent tangential traction of twice the original strength.

This approach depends on the validity of using the P wave for zero-time and amplitude correction. Corrections in amplitude and zero-time should be made with respect to the least contaminated wave in the seismograms, namely first P wave arrival. Zero-time adjustments for this arrival are also valid for S-wave arrivals because the source-receiver distance doesn't change between the left and right shots for a given VSP receiver depth,or between the source and the fixed monitor phone. The amplitude correction seems based on the assumption that source P wave amplitude is representative of source S wave amplitude, *i.e.*, since P waves result primarily from the vertical component of traction, and SH waves in the sagittal plane result from the tangential component of traction, it appears that we assume in scaling the seismograms by their P-wave amplitudes that the rotation of the source from the left to the right position changes the vertical and tangential components of traction by the same factor. However, this scaling is applied in large part to allow removal of the vertical component of traction, producing the effect of a purely tangential source. The amplitude of the first P wave arrival is completely controlled by the vertical component of traction, so subtraction of the seismograms resulting from the left and right sources after they have been scaled by P-wave amplitude will effectively eliminate this component of traction. If the tangential component of traction varies with source rotation by a slightly different factor, it will simply change the effective amplitude

of the tangential traction for the subtracted seismograms, not the vector direction of the traction.

4.4 FEATURES OF THE DATA

The vertical, radial, and tangential components of the subtracted VSP data between the depths of 9.1 m and 201.6 m are shown in Figures 4-5a,b,c. The significant features of the tangential component are a refracted SH wave which appears as the first arrival at receivers above 46 m, a strong reverberation in the upper layer, and a clearly defined downgoing SH wave propagating to the base of the till layer at 165 m. The SH reflection from the base of the till is weak. The vertical and radial components show excellent cancellation of the direct P wave arrival. Below 46 m, a clearly defined downgoing SV wave is apparent in the radial component, along with its strong reflection from the base of the till. In comparison with the vertical and tangential components, this component has the greatest complexity. The vertical component also shows the downgoing SV wave, but there is no obvious reflection from the base of the till.

Phase identification in this VSP is facilitated by comparing the data with synthetic VSP seismograms computed for a planar interface model with a point tangential traction source (Figure 4-6). These seismograms were generated by a discrete wavenumber formulation of the propagator matrix method, and present a complete solution of the wave equation including all body wave multiple reflections and interface waves (Mandal, 1986; Prange, 1985; Kennett, 1983). These seismograms are intended to provide a reference for understanding arrival times and amplitudes in the VSP experiment, and a simple 25 Hz Ricker wavelet is used. Downgoing SH wave travel times from the synthetic seismograms agree well with the experimental data. However, the strong reflection from the base of the glacial till present in the synthetic data is not visible in the experimental data. Since this interface is known from well logs to mark an abrupt change in material properties, the diminished amplitude of the observed reflected SH wave suggests that this interface is rough enough to attenuate the reflected wave. In the time window between the direct SH

and this reflected arrival, only one multiply reflected arrival appears in the synthesized data, while the experimental data contains numerous arrivals, some of which appear to be multiply reflected. Because they do not match the arrival times of any phases in our planar interface model of the site, we attribute these arrivals to scattering. The downgoing SH wave in the transverse component of the VSP data is significantly broader in time than the corresponding wave in the radial or vertical components, or in the synthetic seismograms. This effect could be explained by the influence of a rough interface of the scattered wavefield. Pulse broadening can occur when the field scattered from the rough interface, which has been advanced or delayed in time due the height variations in the interface, is added to the planar interface background field.

In the rest of this study we will focus on the wave field in the layer of glacial till between the depths of 45.8 m and 165 m. The wave velocities in this region are relatively well known, as was verified by the travel time comparison between the data and synthetic seismograms. Waves in this region do not appear to be contaminated by the reverberations apparent in the shallower layers. Representative seismograms for this region (at depth intervals of 18.3 m) are shown in detail in Figures 4-7a,b,c,d,e,f. Each of these figures displays three views of the data from a given depth: (1) the three pairs of unsubtracted vertical, radial, and tangential component seismograms, with each pair overlain in order to illustrate the effectiveness of the P wave cancellation; (2) the three components after subtraction; and (3) hodograms[2] for the vertical-radial and tangential-radial planes within a time window around the first S wave arrival. Comparison of first arrival amplitudes shows that the vertical component amplitudes are approximately 60 percent of radial component amplitudes, and radial component amplitudes are are approximately 50 percent of tangential component amplitudes.

Hodograms are especially important since particle motion is critical for accurate phase identification. For waves propagating in the sagittal plane, SH waves will appear as particle motion in the tangential direction of the radial-tangential plane, and P and

[2]A hodogram is a two-dimensional graph of particle motion in a specified plane.

SV waves will appear in the radial-vertical plane, with P wave particle motion in the direction of P wave propagation and SV waves perpendicular to the direction of SV wave propagation. Hodograms produced from our data, as displayed in Figures 4-7a,b,c,d,e,f, show the SH wave to be the dominant component. The SH wave particle motion is linear in the tangential direction for receivers above about 46 m, but is rotated by 5°–7° from purely tangential motion for receivers below this depth. This effect is attributed to the interaction of the SH waves with a shallow interface in the glacial till.

One or more SV waves arrive within the time window about the SH wave arrival, as can be deduced from the presence of energy in the radial-vertical plane. These SV arrivals have one-half to one-third the amplitude of the SH arrivals. The presence of a single SV arrival could be explained by the transmission of the incident SH wave through a planar interface with an out-of-plane dip, resulting in a single S arrival with components in both radial-tangential and radial-vertical planes. Clo (1989) used three-dimensional ray tracing to investigate the effect of an interface with out-of-plane dip on the conversion of SH waves into SV and P waves. His model, a simplified version of our model, is shown in Figure 4-8. The results at three receivers for an interface with a 5° dip are plotted in Figure 4-9. Here an SH source wave with a free-space radiation pattern — *i.e.*, no free surface effects — transmits through a dipping interface and develops energy in the radial and vertical components. Four effects are observed in this ray-theoretical modeling: (1) the magnitude of energy in the vertical component is always larger than that in the radial component, with this difference growing smaller with increasing receiver depth; (2) the energy in the cross-components increases with increasing receiver depth; (3) at a given receiver depth, energy in the cross-components is largest when the azimuth angle is large; and (4) converted P wave amplitudes are less than 1.5 percent of transmitted S amplitudes. Only the fourth of these effects is observed in the experimental data. There are several other characteristics of the data which are inconsistent with a simple out-of-plane dip hypothesis. Firstly, the incidence angles of the SV arrivals vary unpredictably from receiver to receiver, whereas changes in particle motion due to out-of-plane dip

would have angles easily predictable using Snell's law, and would vary smoothly from receiver to receiver. Also, the observed broadening of the direct SH wavelet relative to the corresponding SV wavelet, and the complexity of the radial component arrivals in a large time window following the direct SV arrival, cannot be a result of out-of-plane dip. A scattering mechanism is clearly indicated by the data. Of course, there could be some out-of-plane dip of the mean planar interface associated with the rough interface scattering.

4.5 OBSERVATIONS FROM MODELING

In order to test whether the observed scattered field can be attributed to rough interface scattering, the perturbation method of chapter 2 was used to generate synthetic seismograms which model the features of an SH wave transmitted through a rough interface. To facilitate the modeling, some simplifying assumptions were made. First of all, although scattering coefficients may be generated with source waves with any incidence angle, synthetic seismograms were only produced for a normally incident source wave. This is a limitation of the theory when applied to plane wave sources, and will not exist in future point source implementations. Since we find by applying Snell's law to the planar interface model in Figure 4-2 that the incidence angle for an S wave would be near 20° from the vertical for receivers in the range of interest, we cannot expect to exactly model rough interface scattering in the experimental geometry with a normally incident source wave. We can, however, provide insight into the expected coupling of incident SH waves into SV and P waves for the material contrasts and frequency used in the experiment. Secondly, the model was simplified to include just a single interface at a depth of 46 m. The velocity model is illustrated in Figure 4-8. Hence, multiple reflections will not be included in the synthetic seismograms. These multiples form an insignificant part of the seismograms, as can be seen from the discrete wavenumber synthetic seismograms presented in Figure 4-6.

The interface height functions used in the modeling were constrained to have Gaussian

autocorrelation functions with RMS height deviations of 1.53 m. This RMS height is 22 percent of the wavelength of an SH wave in the upper medium, which is the upper limit for accurate solutions from the perturbation modeling method. Different interface height functions were then generated by varying the x and y autocorrelation lengths between 4.58 m and 18.33 m. The lower bound on an acceptable autocorrelation length is controlled by the maximum permissible RMS slope for accurate solutions from the perturbation modeling method. Another set of interface height functions was prepared by simply rotating the above set of height functions by 45° in azimuth. Representative interface height functions illustrating these two sets of functions are shown in Figure 4-10.

Scattering coefficients for source waves with 0° and 20° incidence angles show the angular distribution of scattered P, SV, and SH waves for an SH plane wave source (Figure 4-11). Coefficients were calculated for each of these angles of incidence on a model with x and y autocorrelation lengths of 9.16 m, and for 20°-incident waves on an interface with autocorrelations lengths of 9.16 m in the x direction and 18.32 m in the y direction. Comparing scattering coefficients derived for normal incidence with those for a 20° incidence angle provides insight into differences between the experimental and synthesized seismograms. In the normal incidence case, the SV and SH scattering coefficients are tightly focused in the direction normal to the interface, and are nearly equal in maximum amplitude. The P wave scattering coefficient is 77 percent smaller in maximum amplitude than scattered SV and SH waves. This maximum occurs in the direction parallel the interface, making the vertical component of its propagation velocity less than that of scattered S waves. The combined effects of small amplitude and late arrival matches the observed absence of P waves in the experimental data (Figure 4-5a,b,c). Non-normal incidence angle acts to increase the the magnitude of the scattering coefficients over that of the normal-incidence scattering coefficient for the corresponding normal incidence model. Hence, the synthetic seismograms will tend to underestimate the scattered wave amplitudes. The SH scattering coefficient, however, has a value of 0.13 at the zero scattering angle, which is similar to the normally incident source case. The

maximum amplitude of the SH scattering coefficient relative to that of the SV scattering coefficient has increased dramatically over the normal incidence case, but if the scattering coefficients are compared within the domain of scattering angles less than 45°in order to isolate scattered waves which will arrive within the time window of the synthetic seismograms, the maximum amplitude of the SH scattering coefficient is reduced to 0.6. Scattering coefficients for the two interface height functions have similar shapes, with the coefficients for smoother interface being of lower amplitude in general, and more compact in the y direction.

Synthetic seismograms for a SH wave normally incident on nine different interface models are presented in Figures 4-12a,b,c. The complexity and amplitude of the vertical component seismograms increases with decreasing y autocorrelation length, and is relatively insensitive to changes in the x autocorrelation length. This behavior is expected from the shape of the scattering coefficients shown in Figure 4-11. There it can be seen that P wave scattering is relatively small in comparison with SV scattering, and SV waves generate significant energy on the vertical component only for large scattering angles. The SV scattering coefficient shows that these large scattering angles are only possible for scattering azimuths in the vicinity of the y direction, resulting in the insensitivity of the vertical component to changes in the x autocorrelation length. Since changing the source wave incidence angle to 20° shifts the scattering coefficients in the x direction, seismograms for a source incident at 20° should show greater sensitivity of the vertical component to the x autocorrelation length. The radial component seismograms are sensitive to changes in both the x and y autocorrelation lengths. This also follows from the scattering coefficients. The amount of SV wave energy displayed on the radial component is dependent on the azimuth of the scattered SV wave, and is maximum for small scattering angles. Small changes in the x autocorrelation length can extend the azimuthal reach of the scattering coefficient in the x direction in the neighborhood of the zero scattering angle, allowing SV waves to scatter more efficiently into the radial component. Again, changing the source wave incidence angle to 20° will increase the

energy in the radial component. The tangential components increase in complexity and decrease in amplitude as the y autocorrelation length is decreased.

The above relationships between amplitude and autocorrelation length, determined from normal incidence synthetic seismograms, are quantified by the contour plots in Figure 4-13a,b. The first column in Figure 4-13a contains three plots, each presenting the average maximum absolute amplitude of one component of the synthetic seismograms versus x and y autocorrelation length. The maximum amplitude of each seismogram is found within an S wave time window beginning at the first arrival of the S wave and ending at the end of the seismogram. The average of these maxima is then taken over an 8 by 8 array of receivers at a depth of 61.1 m beneath the mean depth of the interface. The second column contains similar plots using the same source and receiver locations, but the interface height function is rotated in azimuth by 45°. Figure 4-13b displays the results for a P wave time window beginning a the start of the seismograms and ending at the first arrival of the S wave. The amplitudes observed in the VSP data do not match the amplitudes in the synthetic data for any of the models. Data from the VSP experiment has more energy in the radial and vertical components relative to the tangential component than was observed in the synthetic data. Better agreement in this respect could be obtained by increasing the RMS interface height. Increased RMS height, however, does not reduce the discrepancy in the energies of the vertical and radial components of the observed and synthetic data. In the synthetic data, the vertical components consistently have more energy than the radial components, whereas in the experimental data the radial and vertical components have nearly equal energy. To resolve some of these discrepancies we will have to calculate rough interface synthetic seismograms for oblique incidence angles that more accurately model the experimental field geometry.

4.6 DISCUSSION

We offered two plausible explanations for the energy appearing on the vertical and radial components in our SII VSP experiment: a near-surface interface which is dipping or rough. The complexity of the observed waveforms cannot be satisfactorily explained by a dipping interface model. Such an interface would split the SII source wavelet into SV and SII waves, but these would have the same complexity as the source wavelet. Synthetic seismograms generated for rough interface models using the perturbation method presented in chapter 2 successfully modeled the observed waveform complexity. Interface roughness, however, failed to explain the amplitudes observed in the vertical and radial components relative to the tangential components. In the experimental data, vertical component amplitudes were approximately 60 percent of the corresponding radial component amplitudes, whereas in the synthetic seismograms the vertical component was consistently larger in amplitude than the radial component, even for interface models which were rotated 45° in azimuth from the incident SH particle motion. The ratio of the radial component amplitude to the tangential component amplitude in the synthetic seismograms is smaller by a factor of 4 than the observed ratio. Since current limitations in the modeling method limit the source wave to normal incidence, it is important to consider how the synthetic seismograms would change if the source incidence angle were changed to a more realistic incidence angle of 20°. This can be done by examining the scattering coefficients for a 20° incidence angle. The SV scattering coefficient in this case indicates that the SV scattering wave field will increase in magnitude relative to the normal incidence case, and will also contribute more to the radial component relative the the vertical component. However, since the scattered wave amplitudes from these scattering coefficients must be summed over all scattering angles to produce a seismogram, a more precise statement about the expected amplitudes on each component for a 20° incidence angle cannot be made until synthetic seismograms can be produced for this case. If radial component amplitudes are still small relative to vertical and tangential component amplitudes, the introduction of out-of-plane dip to the mean planar interface

can be used to adjust the relative amplitudes, while keeping the waveform complexity intact.

References

Balsh, A., M.W. Lee, J.J.Miller, and R.T. Ryder, 1982, The use of vertical seismic profiles in seismic investigations of the Earth, *Geophysics,* 47, 906–918.

Caravana, C., R. Turpening, and S. Stubeda, 1988, Nine-component zero offset VSP — Data handling and qualitative observations, *1988 Annual Report of the Reservoir Delincation — Vertical Seismic Profiling Consortium,* M.I.T. Earth Resources Laboratory, Cambridge, MA.

Clo, A., 1989, Cross-component energy in VSP data, in *Vertical Seismic Profiling, Interim Report.* Earth Resources Laboratory, Department of Earth, Atmospheric, and Planetary Sciences, Mass. Instit. or Tech.

Gal'perin, E.I., 1974, *Vertical Seismic Profiling,* Society of Exploration Geophysicists, Special Publication No. 12, Tulsa, Okla. (originally published in Russian by Nedra, Moscow, USSR, 1971).

Kennett, B.L.N., 1983, *Seismic Wave Propagation in Stratified Media,* Cambridge University Press, Cambridge, 342 pp.

Mandal, B., 1986, Complete seismogram synthesis for transversely isotropic media, *J. Geophys.,* 59, 149–156.

Prange, M., 1985, A numerically stable method for computing high frequency sub-surface seismograms in layered media using the discrete wavenumber method, in *Vertical Seismic Profiling, Interim Report,* Earth Resources Laboratory, Department of Earth, Atmospheric, and Planetary Sciences, Mass. Instit. or Tech.

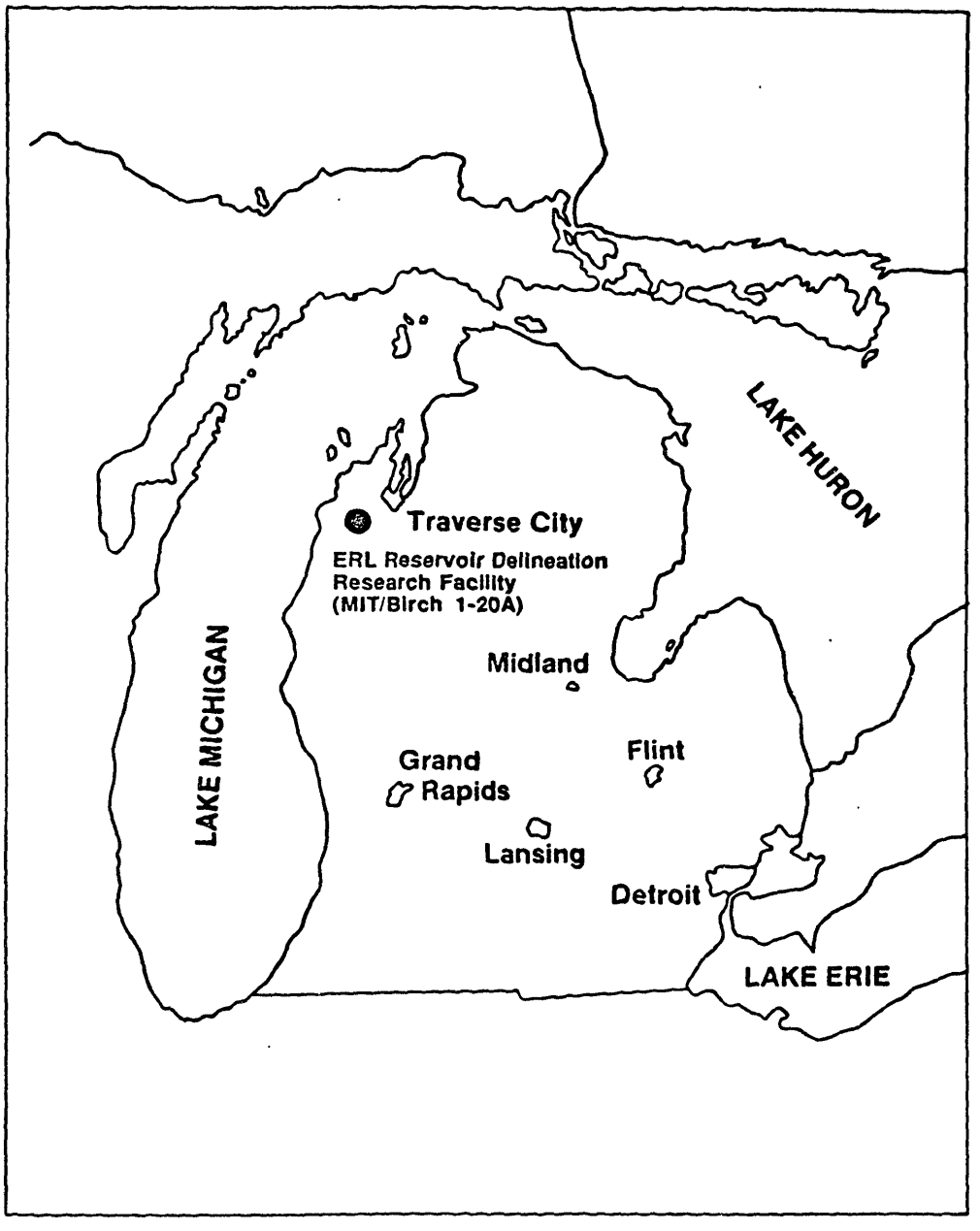

Figure 4-1: Map showing the site of the MIT/Birch 1-20A borehole.

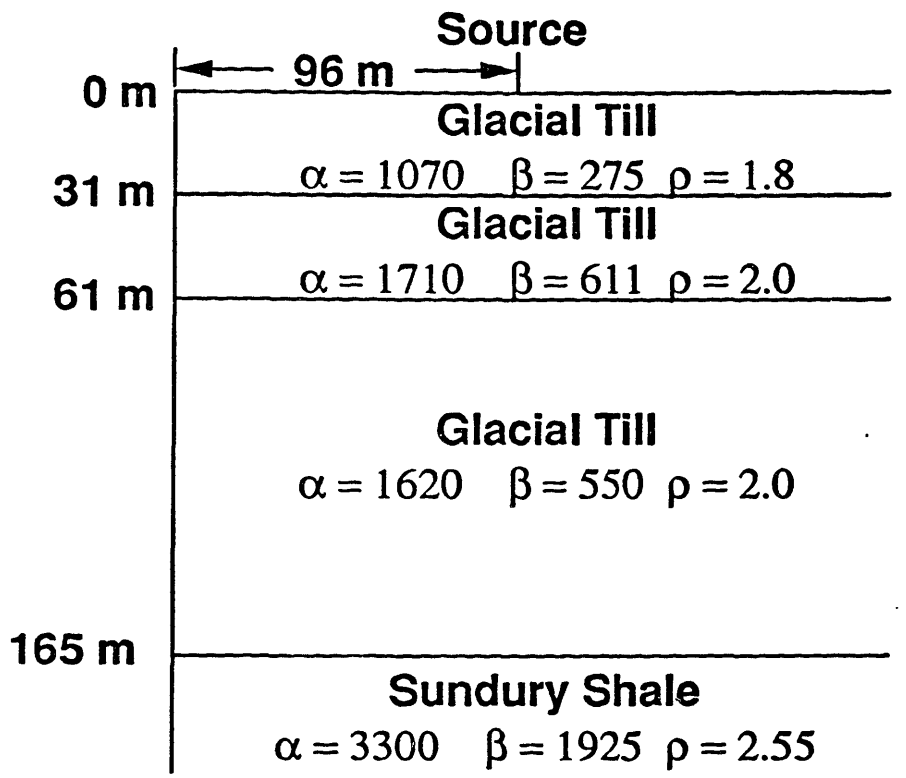

Figure 4-2: Lithological cross-section and velocity/density model of the borehole site.

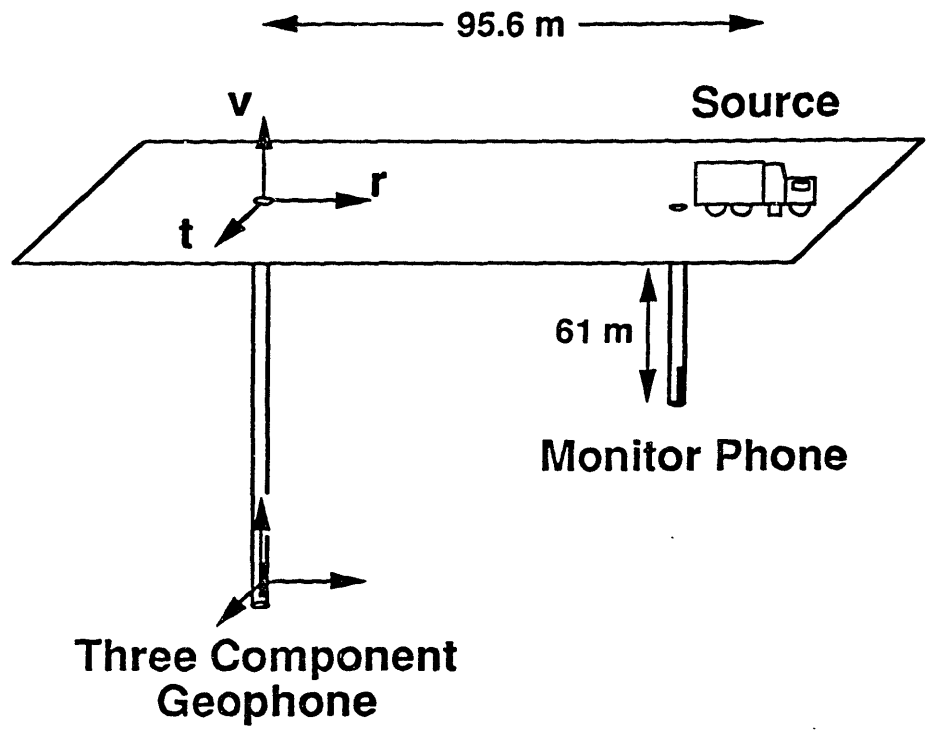

Figure 4-3: Geometry of the VSP experiment. The source is used to generate tangential tractions. The three-component monitor phone is fixed in place for the duration of the experiment. The orientation of the three-component geophone is precisely determined with an onboard gyroscope.

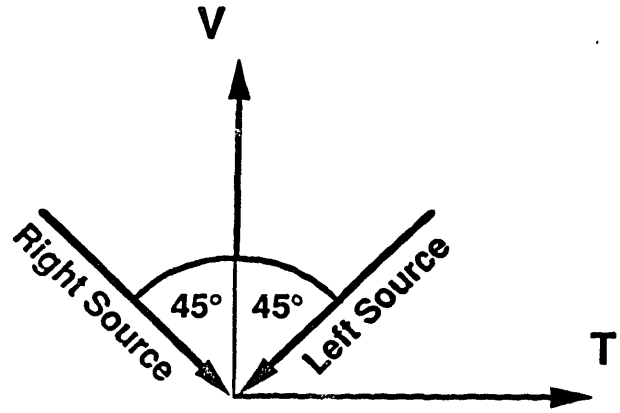

Figure 4-4: Geometry of the force vectors for the left and right sources as viewed from the borehole.

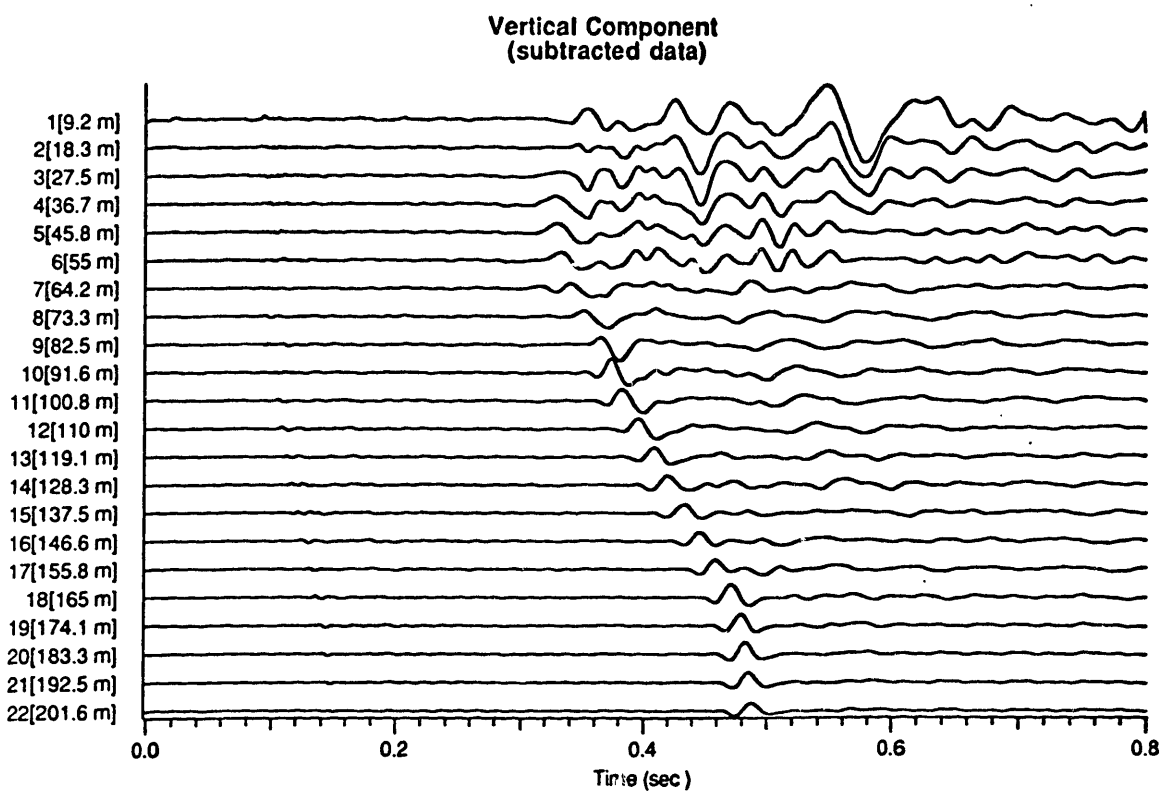

Figure 4-5a Vertical component of data (after subtraction) from the VSP experiment between the depths of 9.1 m and 201.6 m.

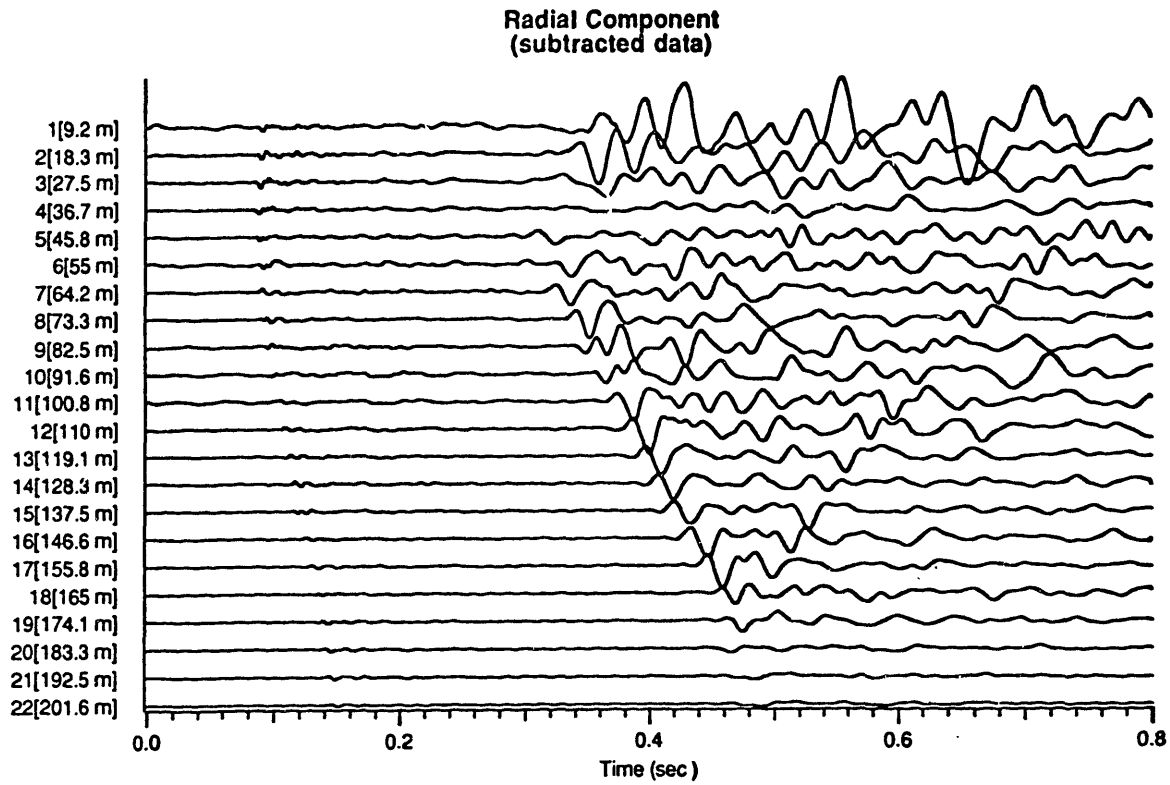

Figure 4-5b: Radial component of data (after subtraction) from the SH VSP experiment between the depths of 9.1 m and 201.6 m. Displayed at the same scale as Figure 4-5a.

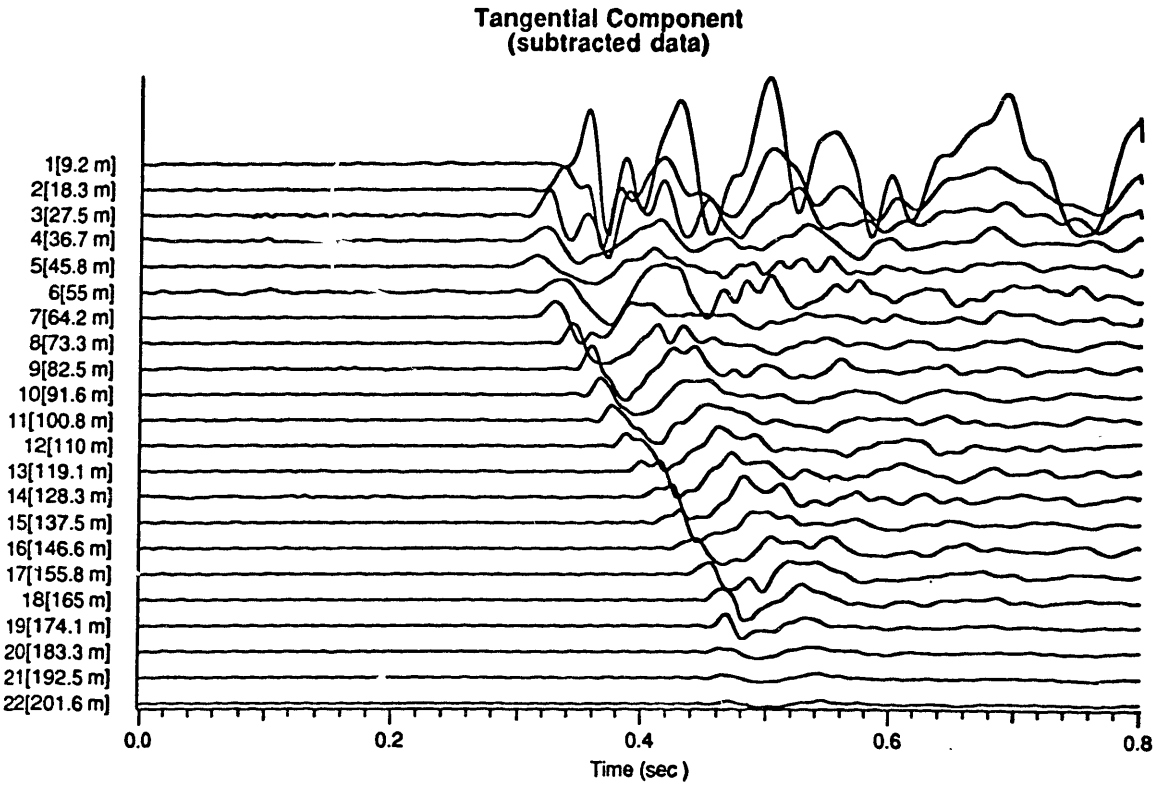

Figure 4-5c: Tangential component of data (after subtraction) from the SH VSP experiment between the depths of 9.1 m and 201.6 m. Displayed at one half the scale of Figures 4-5a,b.

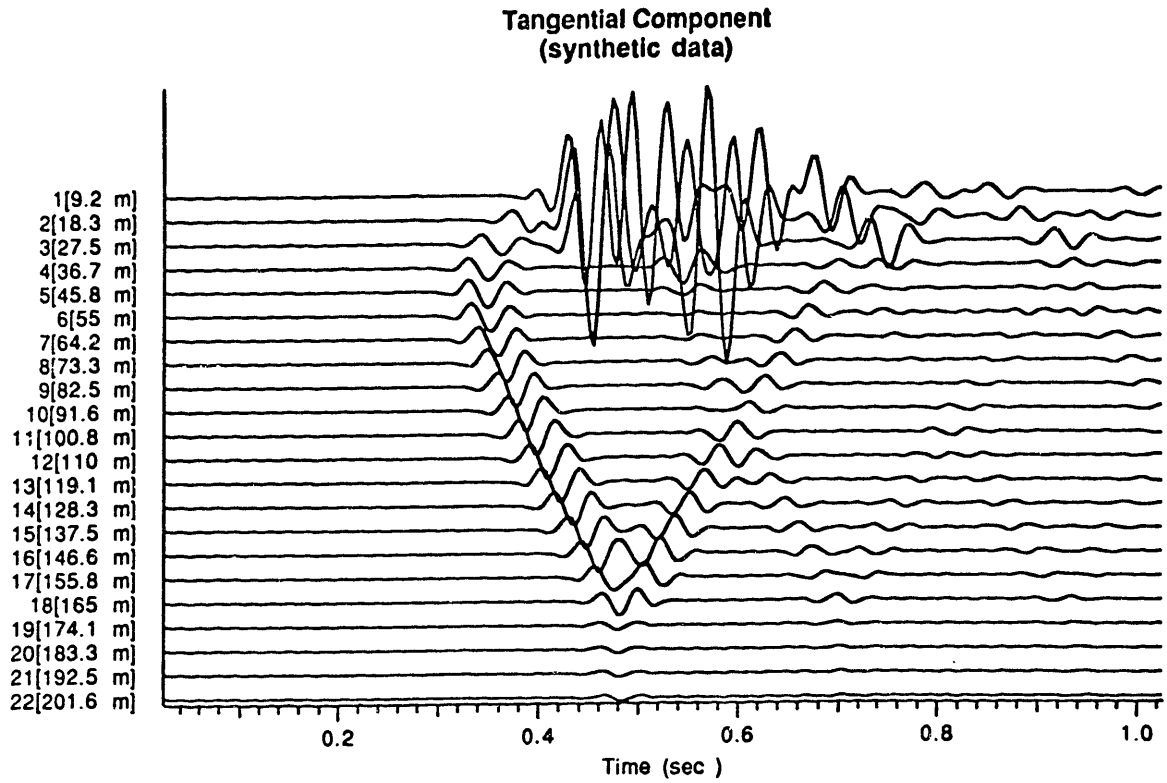

Figure 4-6: Tangential component of synthetic seismograms generated from the model in Figure 4-2. For this model the vertical and radial components are exactly zero. The seismograms were generated by a discrete wavenumber formulation of the propagator matrix method, and present a complete solution of the wave equation including all body wave multiple reflections and interface waves. The vertical scale was adjusted to match as closely as possible that of Figure 4-5c for the first SH arrival on receivers below 55 m.

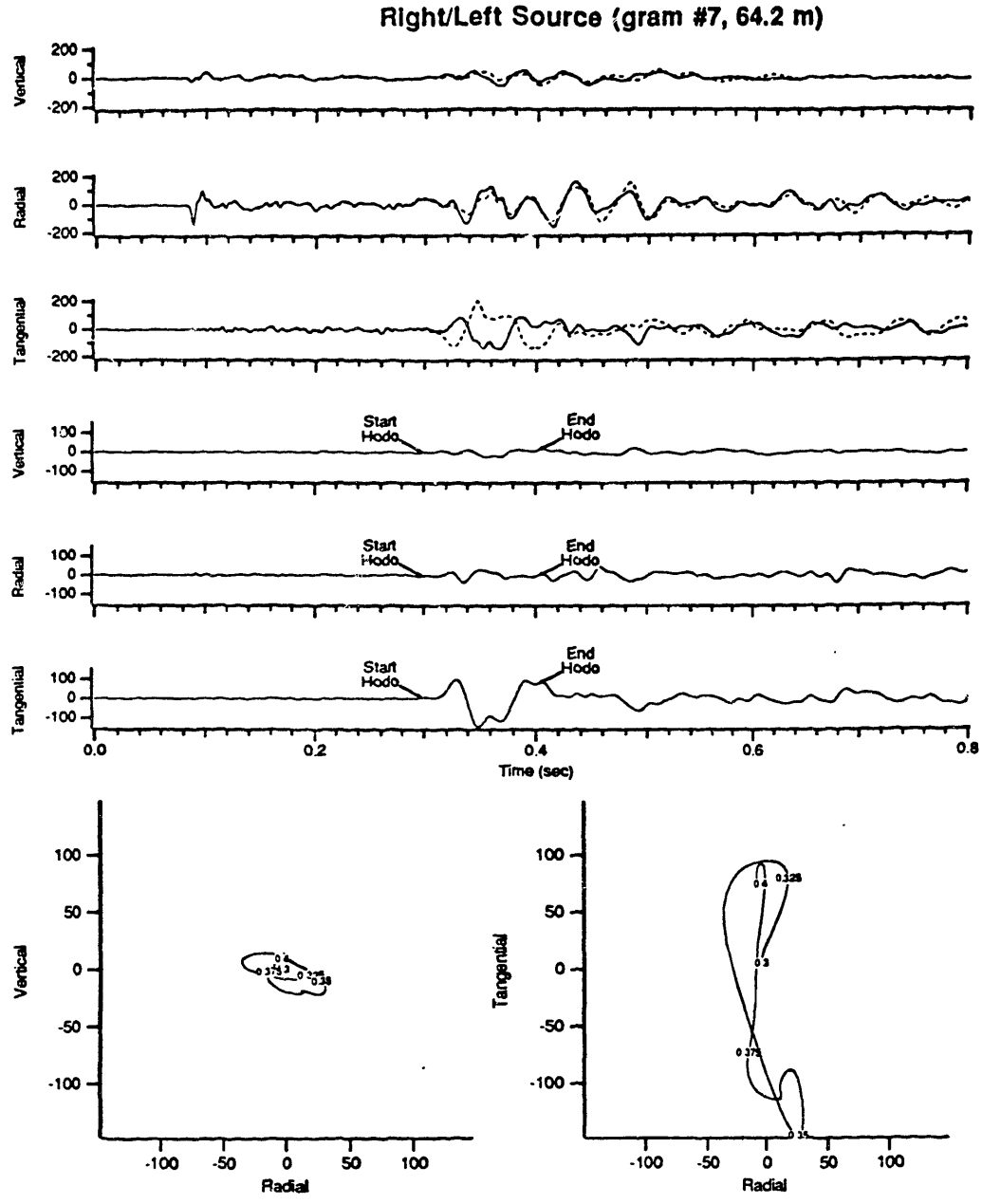

Figure 4-7a: VSP data for the receiver at depth 64.2 m. The top three seismograms are the overlain raw data for the left and right sources, the middle seismograms are the subtracted data, and the two hodograms are in the radial-vertical and radial-tangential planes.

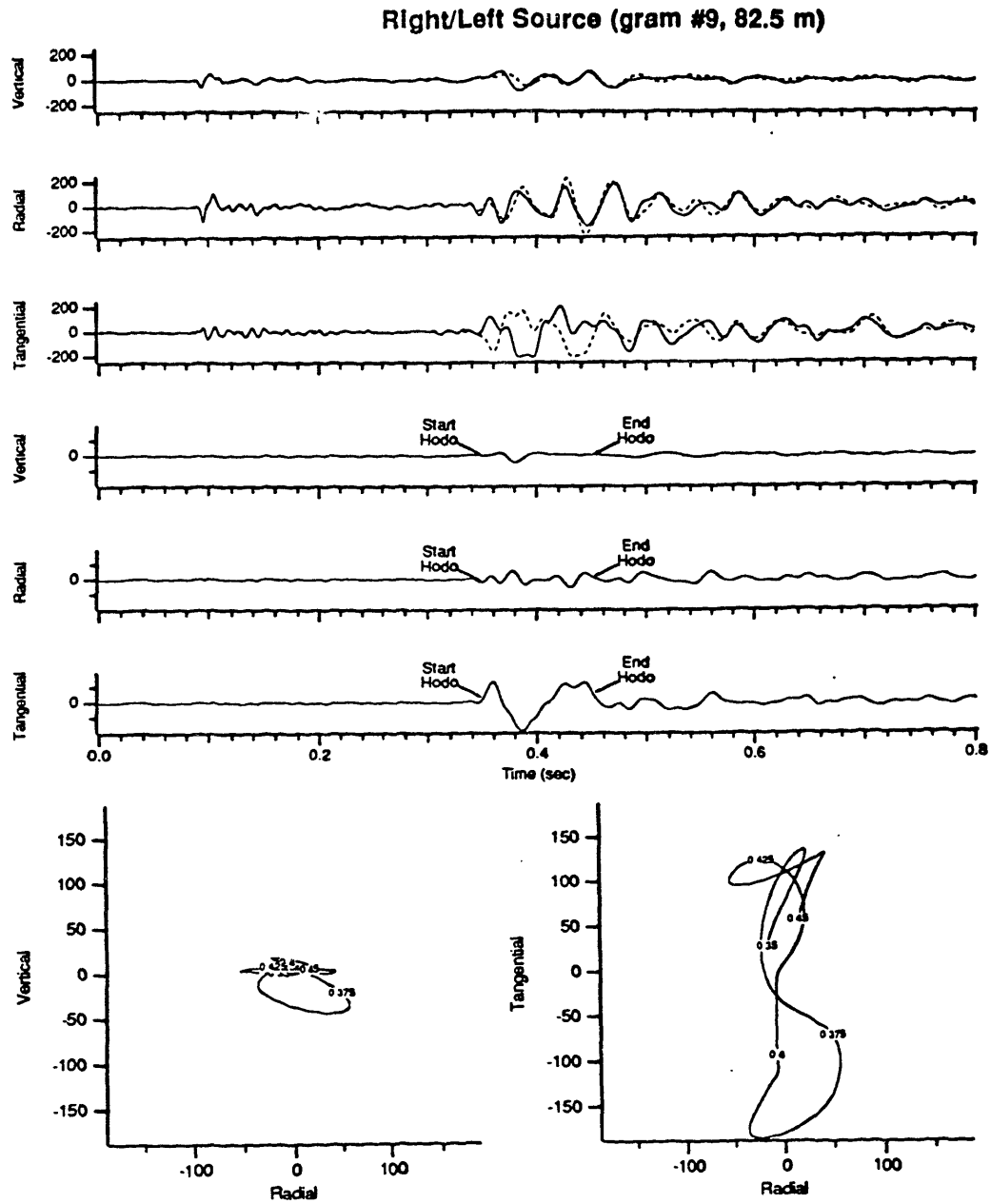

Figure 4-7b: VSP data for the receiver at depth 82.5 m. The top three seismograms are the overlain raw data for the left and right sources, the middle seismograms are the subtracted data, and the two hodograms are in the radial-vertical and radial-tangential planes.

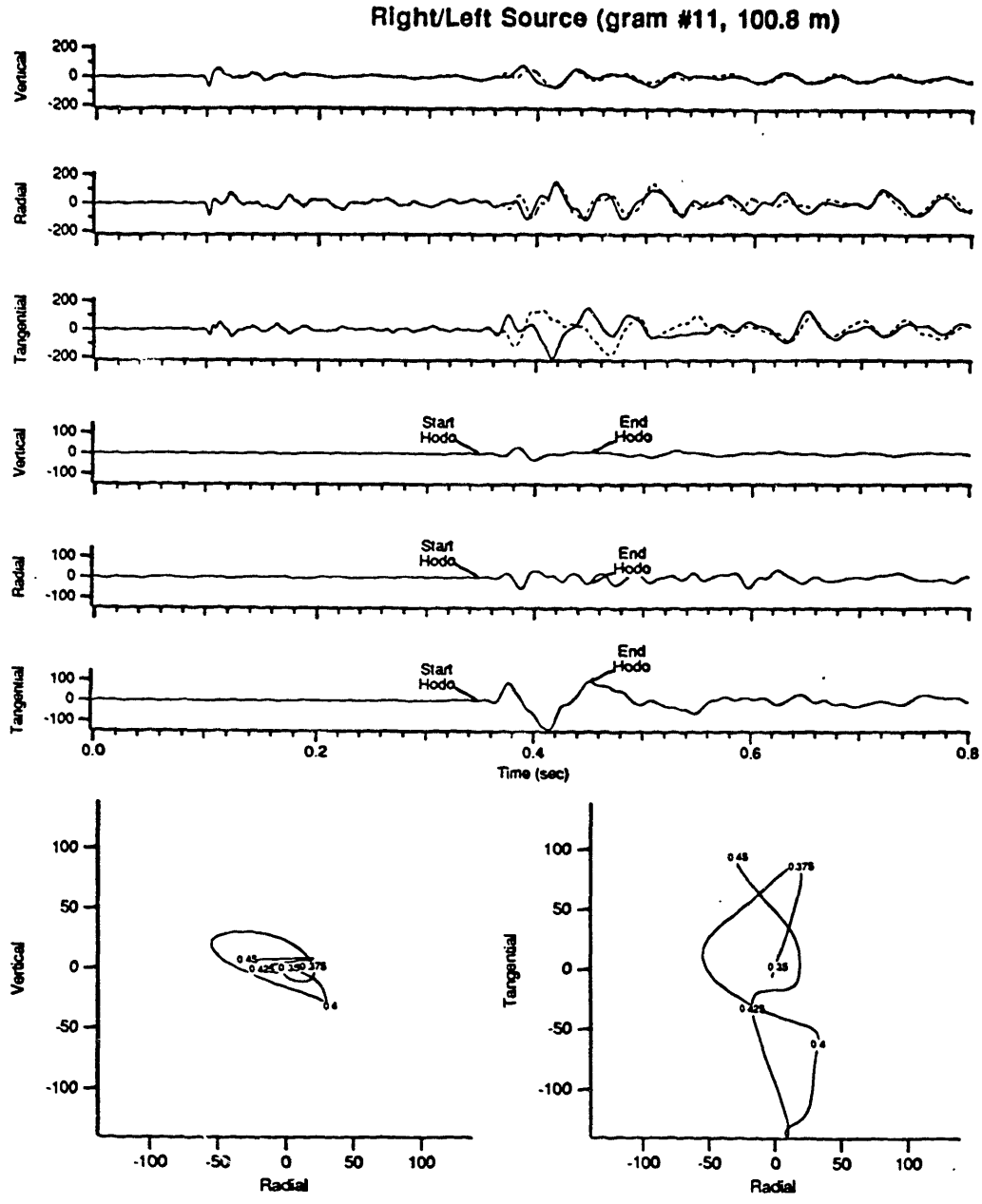

Figure 4-7c: VSP data for the receiver at depth 100.8 m. The top three seismograms are the overlain raw data for the left and right sources, the middle seismograms are the subtracted data, and the two hodograms are in the radial-vertical and radial-tangential planes.

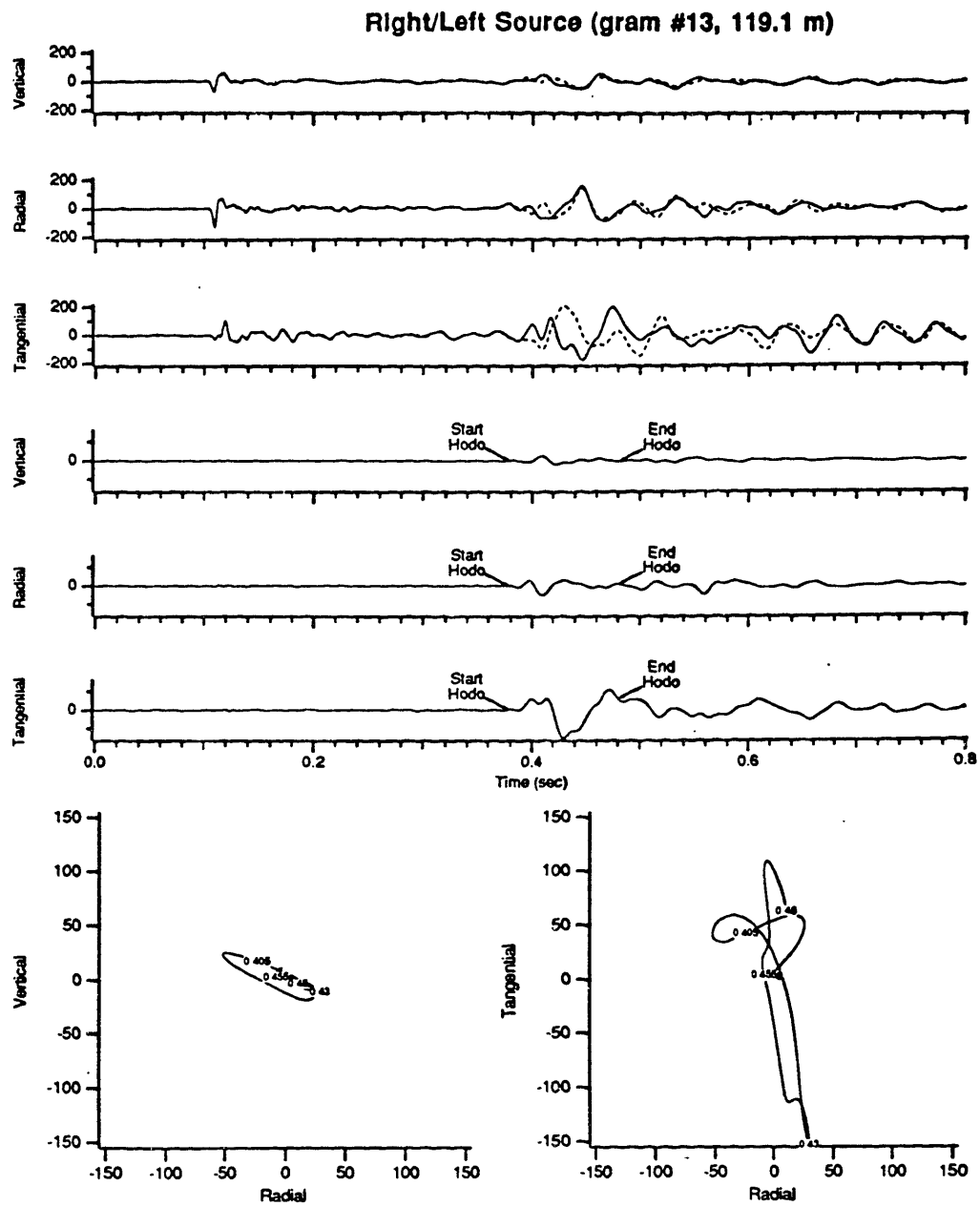

Figure 4-7d: VSP data for the receiver at depth 119.1 m. The top three seismograms are the overlain raw data for the left and right sources, the middle seismograms are the subtracted data, and the two hodograms are in the radial-vertical and radial-tangential planes.

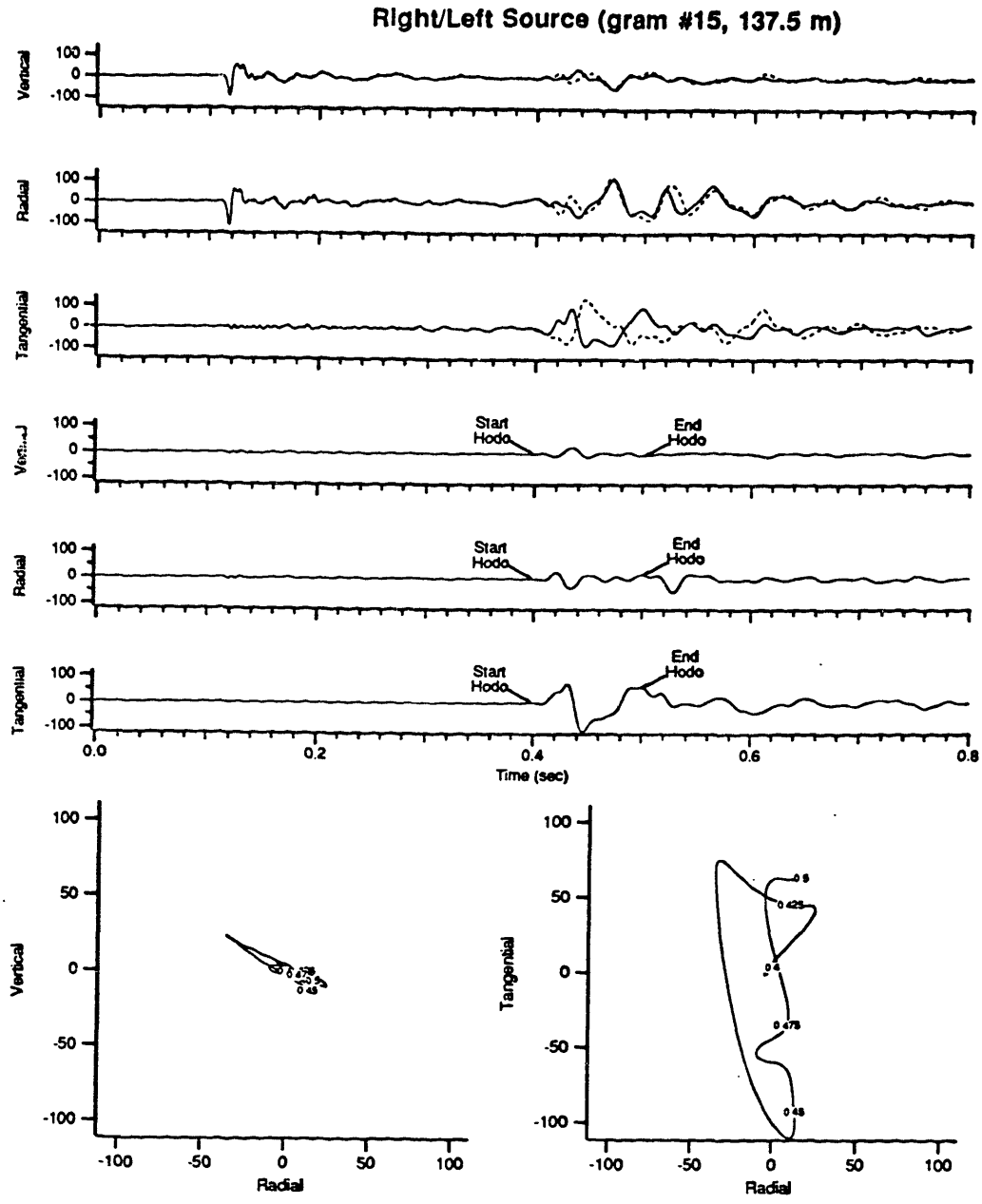

Figure 4-7e: VSP data for the receiver at depth 137.5 m. The top three seismograms are the overlain raw data for the left and right sources, the middle seismograms are the subtracted data, and the two hodograms are in the radial-vertical and radial-tangential planes.

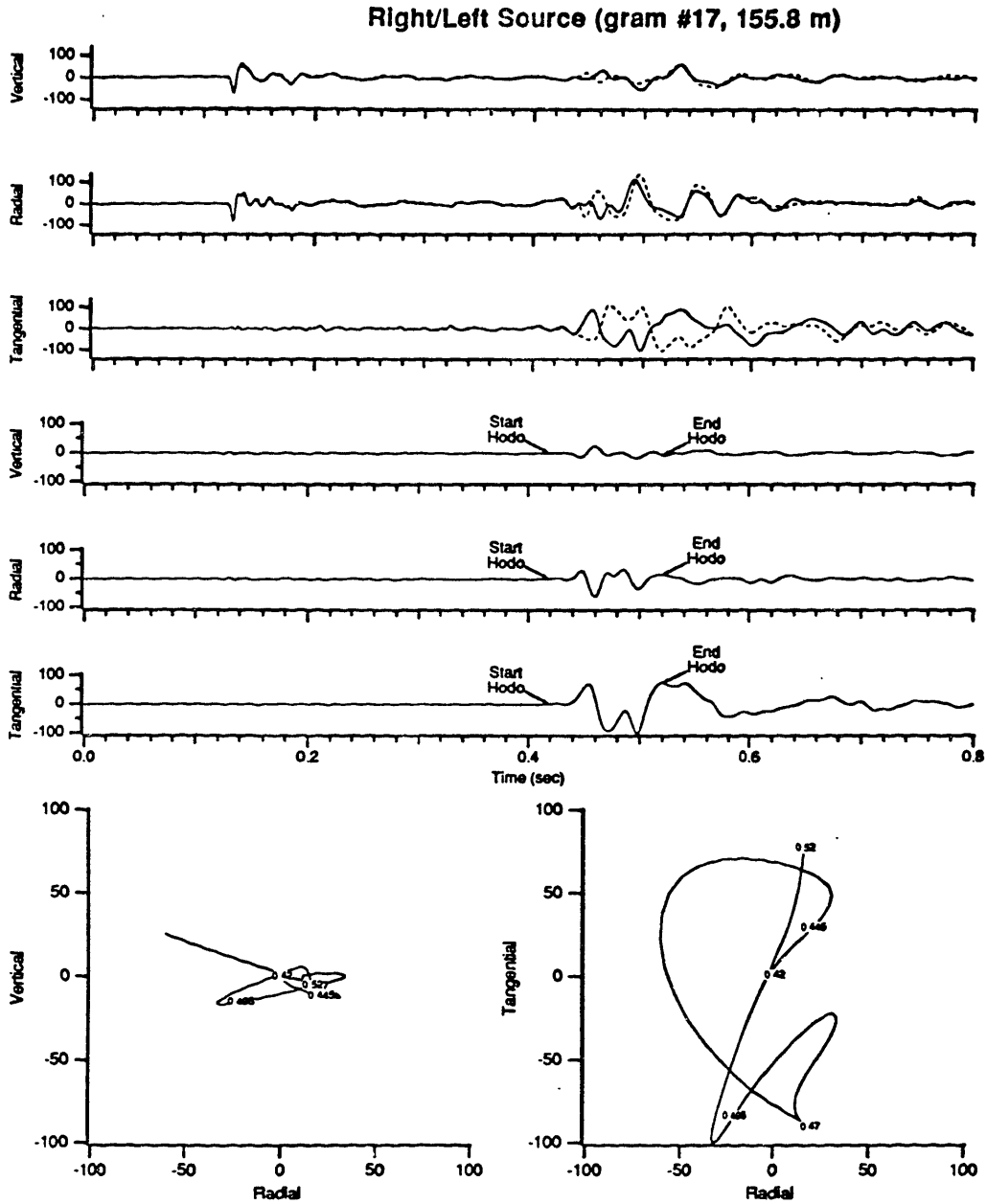

Figure 4-7f: VSP data for the receiver at depth 155.8 m. The top three seismograms are the overlain raw data for the left and right sources, the middle seismograms are the subtracted data, and the two hodograms are in the radial-vertical and radial-tangential planes.

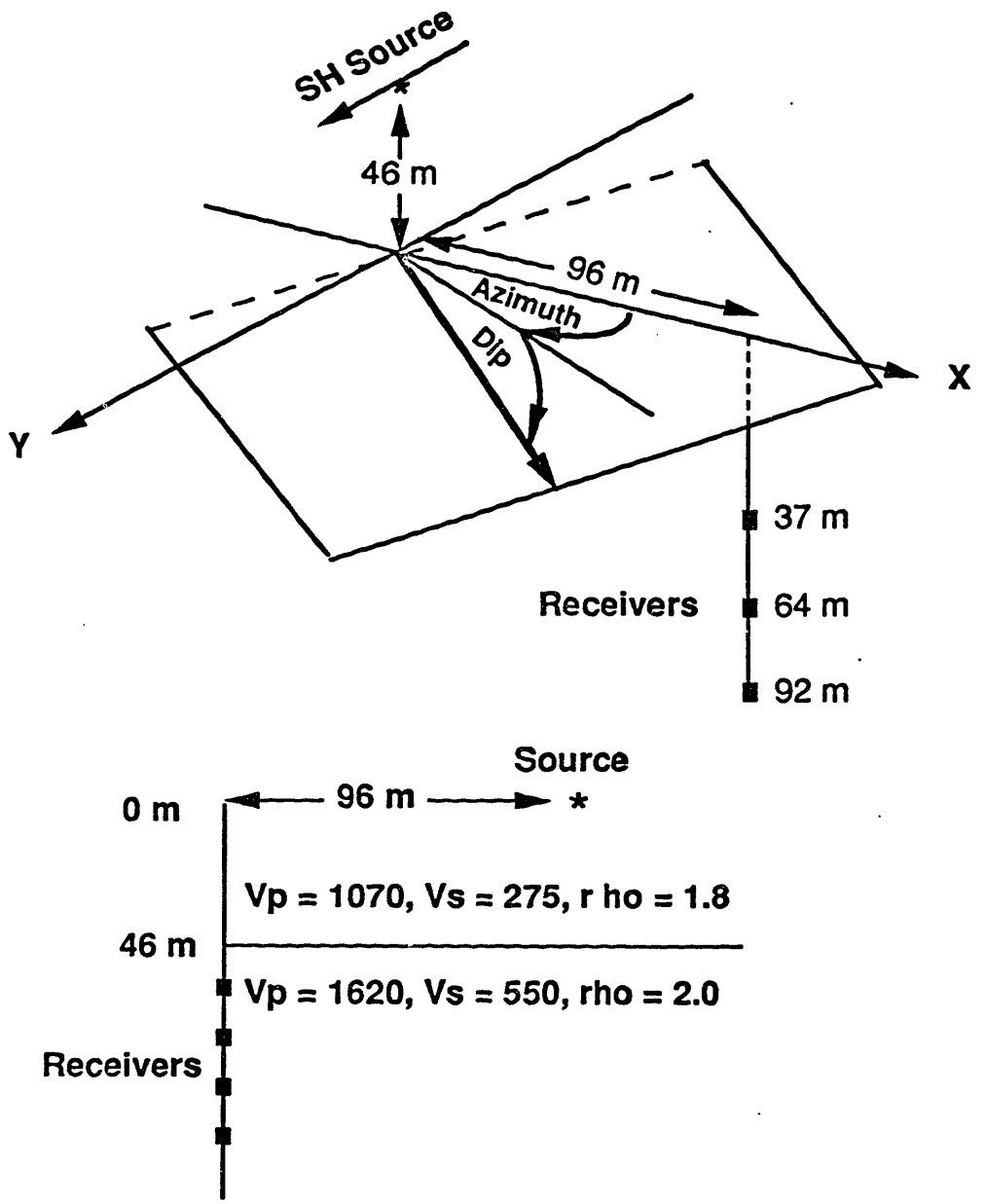

Figure 4-8: Simplified model for wave propagation through a dipping glacial till interface. The upper figure defines the geometry of the model, and the lower figure defines the simplified velocity model.

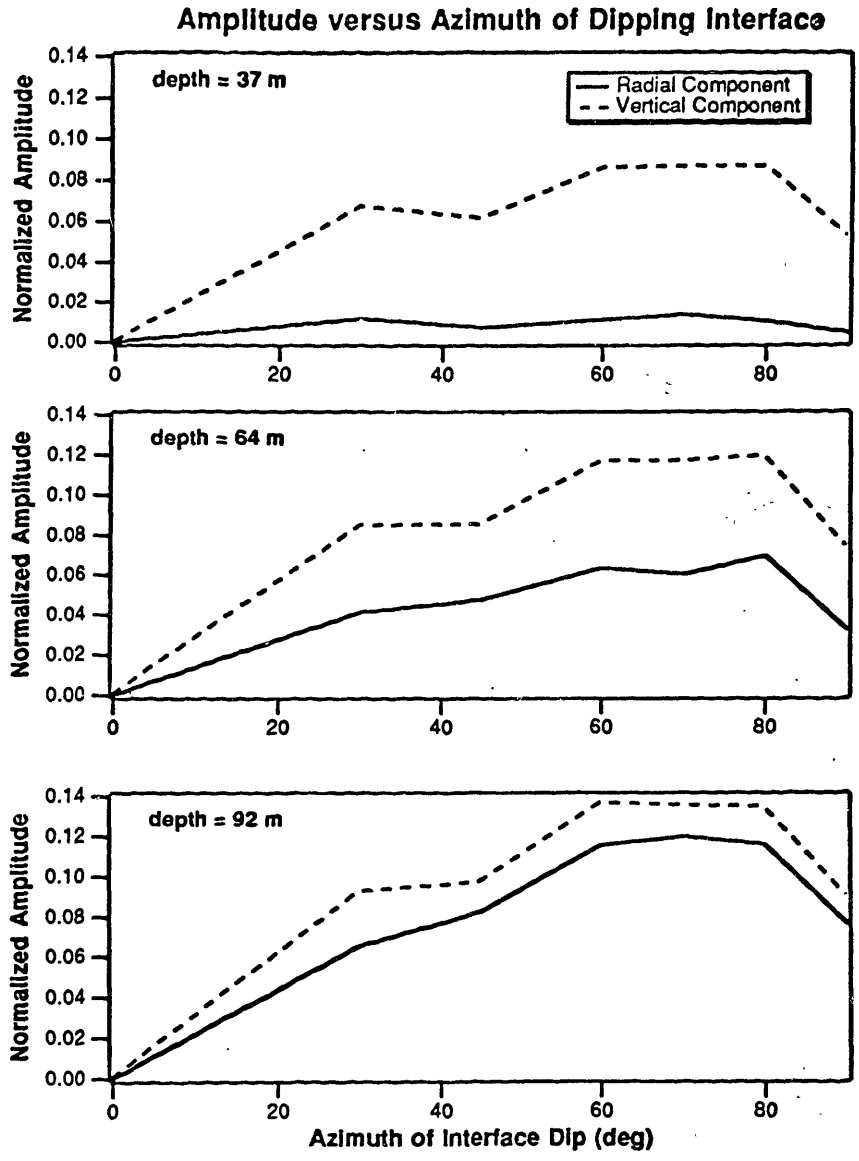

Figure 4-9: The effect of an interface with a 5° dip out-of-plane dip and several dip azimuths on the conversion of SH waves into SV waves for a simplified version of our model shown in Figure 4-8(Clo, 1989). Radial and vertical component amplitudes are normalized to the tangential component amplitude at each of three receiver depths.

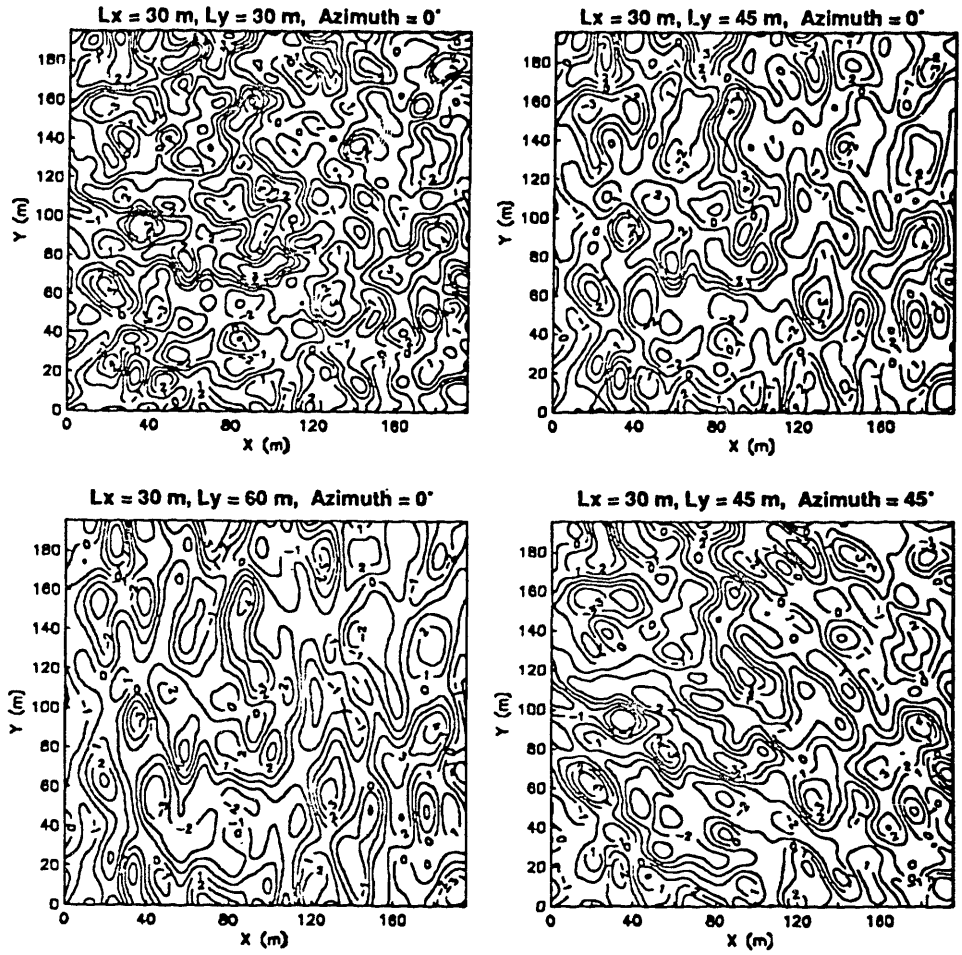

Figure 4-10: Contour plots of representative interface height functions. The indicated x and y autocorrelation lengths refer to the height function before azimuthal rotation.

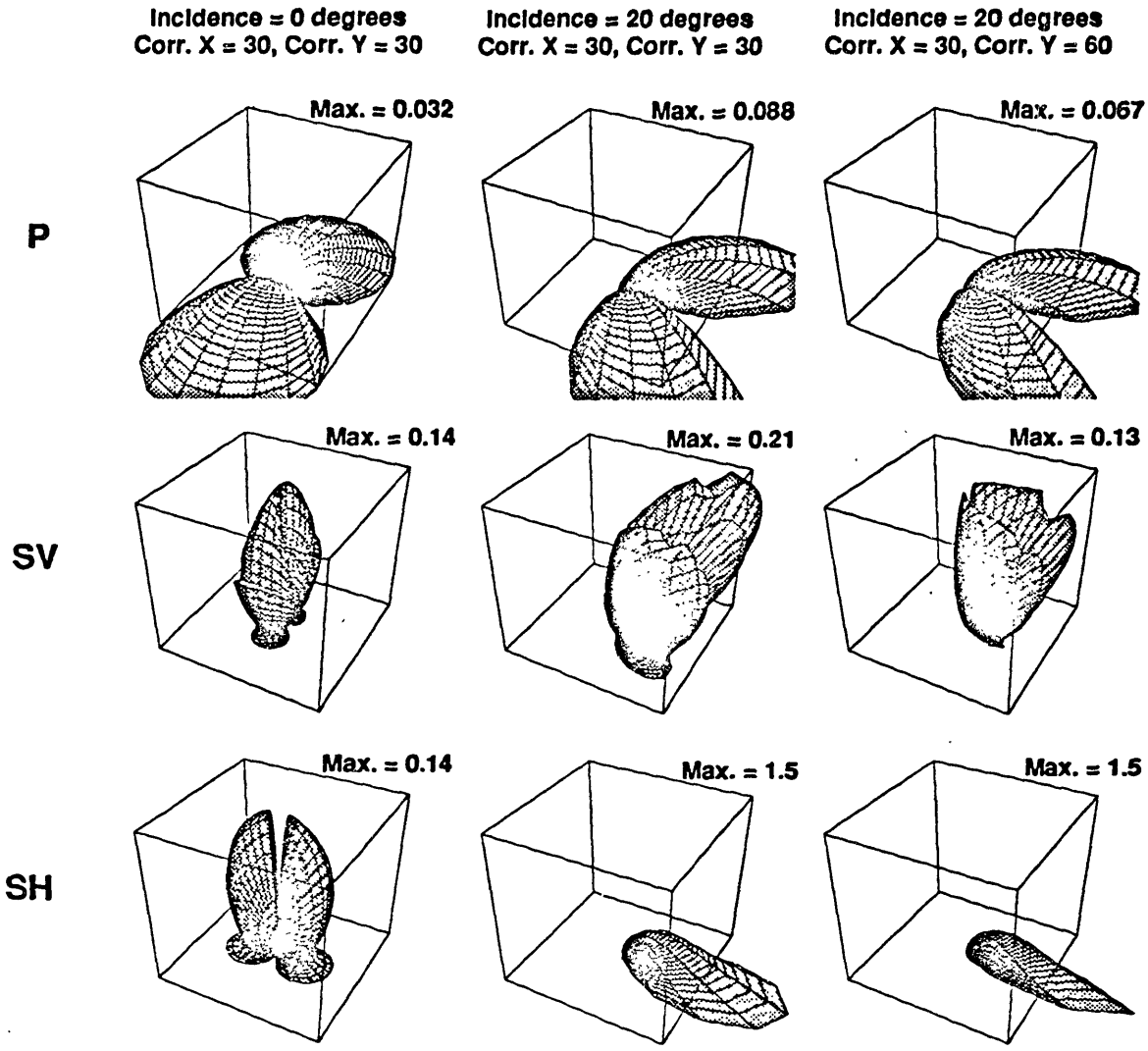

Figure 4-11: Transmitted P, SV, and SH wave scattering coefficients for an SH plane wave with an incidence angle of 20 degrees. The maximum amplitude of each scattering coefficient is indicated.

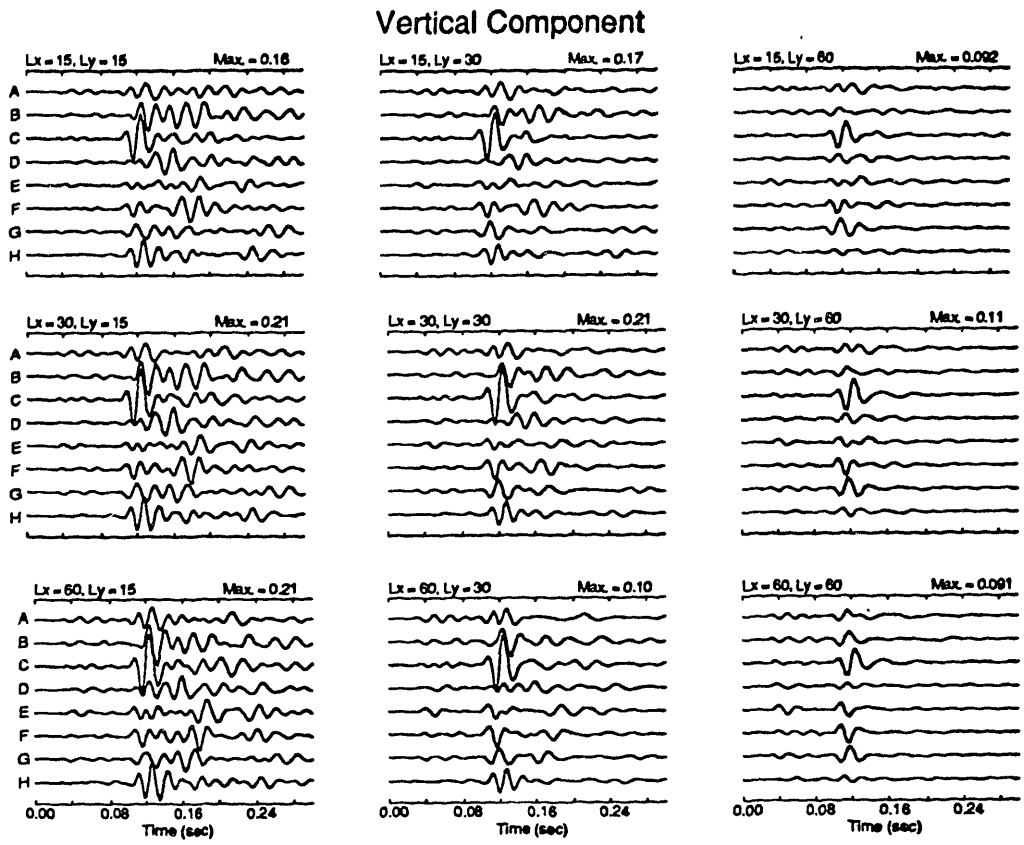

Figure 4-12a: Vertical component of representative synthetic seismograms for nine rough interface models. The source is a normally incident SH wave incident on the 45 m interface of the model in Figure 4-2. The source wavelet is a 40 Hz Ricker wavelet. The RMS interface height is 1.53 m and the x and y autocorrelation lengths are indicated. The receivers are 61 m beneath the mean interface depth. The seismograms are all plotted at the same scale. The maximum amplitude in each panel is indicated.

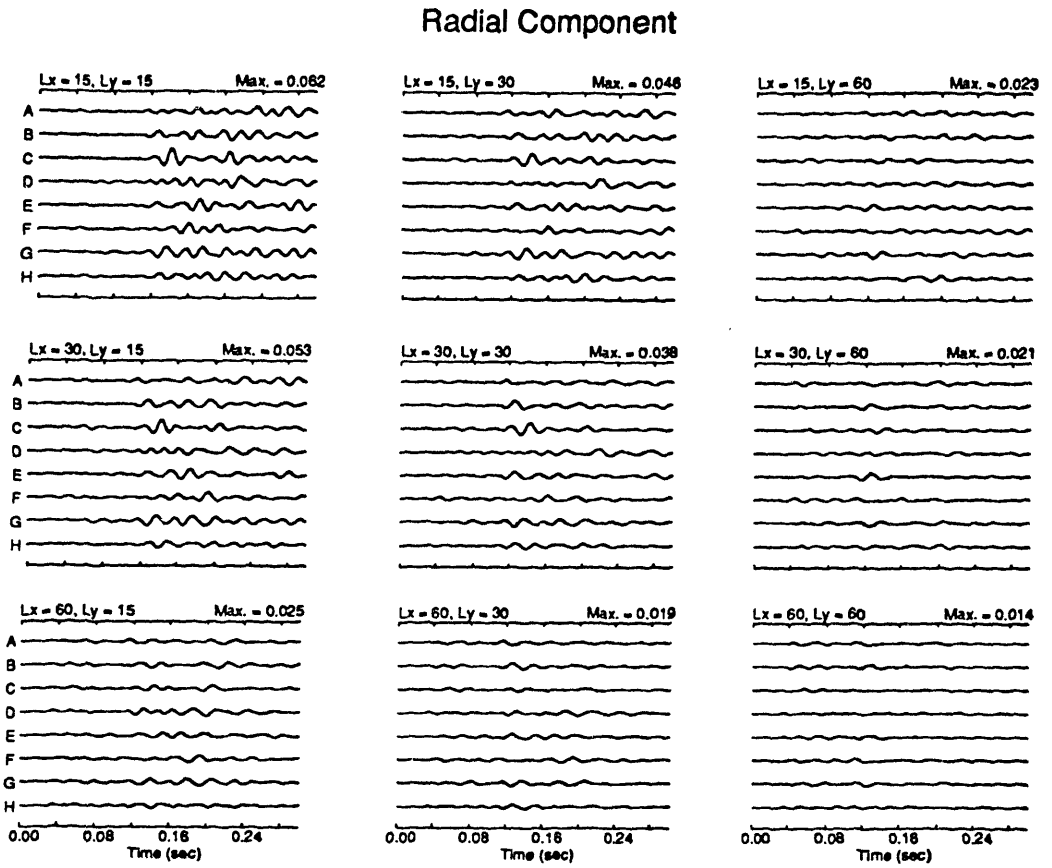

Figure 4-12b: Radial component of the synthetic seismograms shown in Figure 4-12a (plotted at the same scale).

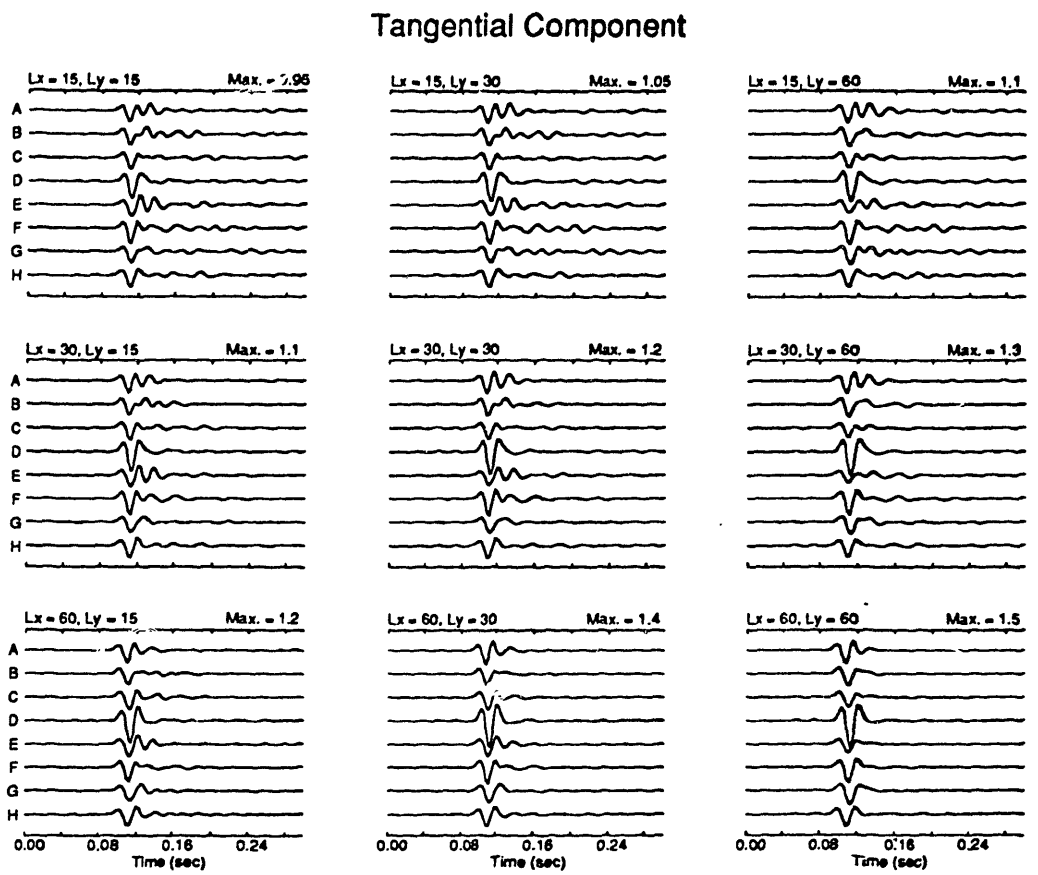

Figure 4-12c: Tangential component of the synthetic seismograms shown in Figure 4-12a (seismogram amplitudes are reduced in size by a factor of 8 relative to those in Figures 4-12a,b).

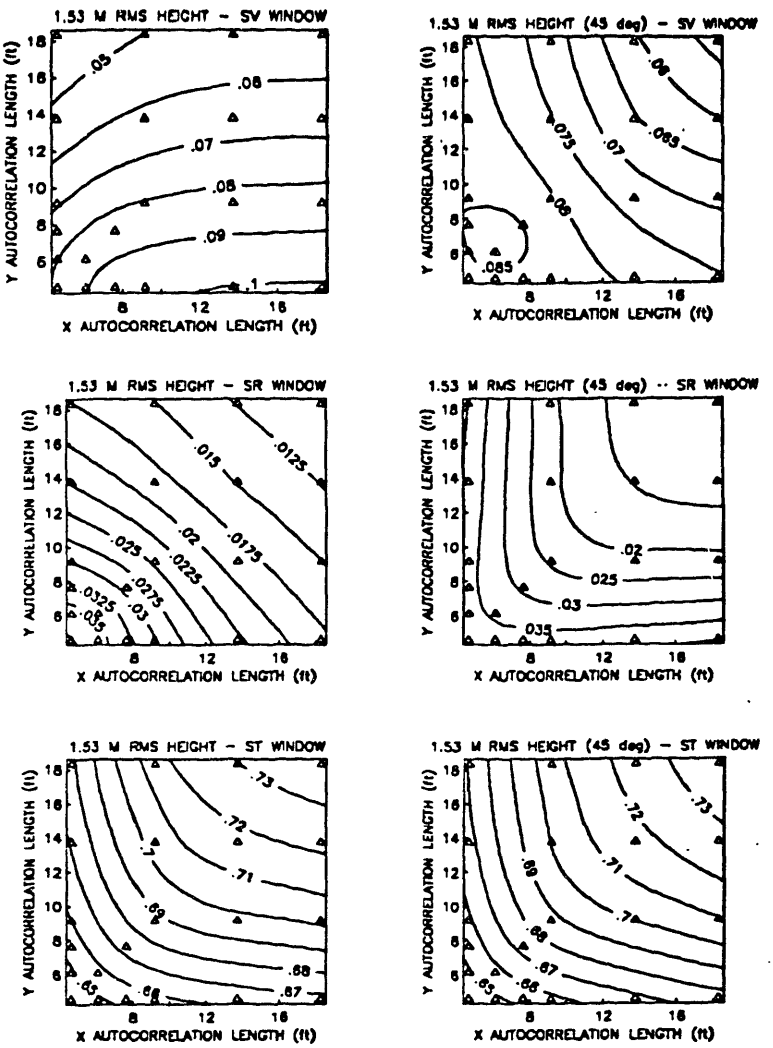

Figure4-13a: Contour plots of the average maximum absolute amplitude of each component versus x and y autocorrelation length, measured in an S wave time window beginning at the first arrival of the S wave and ending at the end of the seismogram. The average is taken over an 8 by 8 array of receivers at a depth of 61.1 m beneath the mean depth of the interface. In the second column, the interface height function is rotated in azimuth 45° relative to the first column. Contours were derived from the synthetic data points marked by triangles.

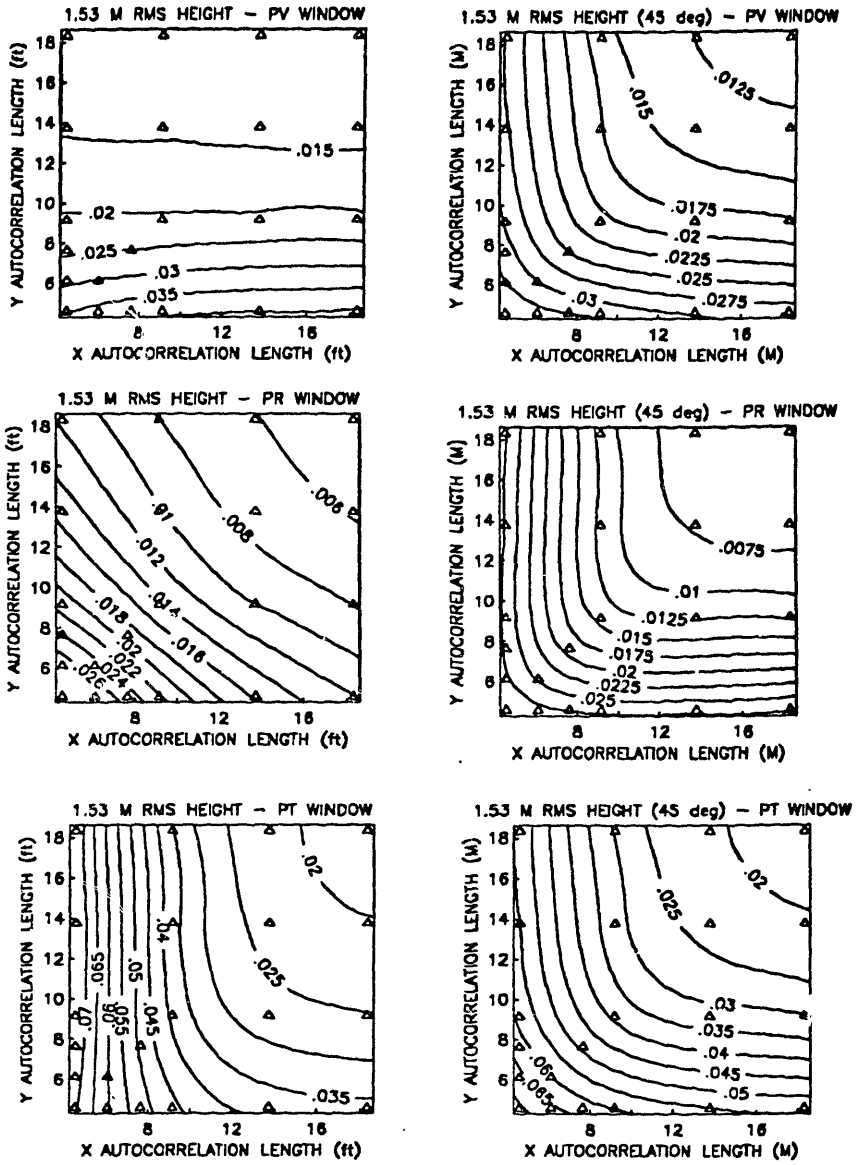

Figure 4-13b: Contour plots of the average maximum absolute amplitude of each component versus x and y autocorrelation length, measured in a P wave time window beginning at the first arrival of the P wave and ending at the first arrival of the S wave. Contours were derived from the synthetic data points marked by triangles.

Chapter 5

GENERAL DISCUSSION AND CONCLUSIONS

We have presented a perturbation method for modeling three-dimensional elastic wave scattering from rough interfaces. The primary advantages of this approximate formulation over exact formulations are its great computational speed, the ease with which the rough interface scattering solutions can be integrated into standard programs for exact wave propagation in stratified media, and the simple analytical form of the solution. The computational speed is sufficient to remove dimensional limitations, allowing fully three-dimensional scattering problems to be studied. The easy integration of this perturbation method into standard exact stratified media formulations provides a convenient mechanism for increasing model complexity of a standard one-dimensional model. The simple analytical form of the perturbation formulation allows the scattered wavefield to be analyzed in terms of scattering kernels, scattering coefficients, and scattered field seismograms.

Constraints on the domain of validity of the method were determined by comparison of scattering coefficients and seismograms generated by the perturbation formulation with those generated by a finite difference formulation for a suite of models with a 20 percent contrast on P and S wave velocity across rough interfaces with RMS heights

ranging from 0.069 to 0.28 S wavelengths and RMS slopes ranging from 0.037 to 0.99. In the scattering coefficient comparisons, the perturbation method is accurate for RMS interface height deviations of less than about 10 percent of the smallest wavelength in the scattered field. This result is independent of RMS interface slope within the tested range. Comparisons of seismograms generated by the two methods show that error does increase with increasing RMS slope, but at half the rate of error growth with increasing height. From these tests we determined that the perturbation solution amplitudes are reliable for RMS heights of less than about 0.20 S wavelengths and RMS slopes of less than about 0.25. The perturbation formulation reliably predicts waveform shapes for a larger domain including the entire range of interface models tested.

Three-dimensional scattering kernels were generated for P and SV waves normally incident on a rough interface. Scattering kernels represent the scattered field response to a delta function interface height function. They must be convolved with an interface height function in order to produce scattering coefficients, but by themselves illustrate the general scattering behavior of an interface contrast and source configuration independent of any particular interface roughness function. The kernels we generated show that waves are maximally scattered in directions for which the scattered wave particle motion coincides with that of the incident wave. An incident SV wave with particle motion in the x direction scatters P and SV waves maximally in the x direction and SH waves maximally in the y direction. A P wave in the same geometry induces azimuthally isotropic radiation because it has no preferred azimuthal orientation. Similarly, for incident SV waves there is a null in P and SV scattering in the y direction, and a null in SH scattering in the x direction. These nulls do not appear in seismograms because a receiver in any location can detect waves traveling in all directions, scattering from many points on the interface. Scattering kernels also show that the critical angles in rough interface scattering, *i.e.*, those angles at which amplitude maxima or minima appear, correspond to the critical angles of the mean planar interface problem with one qualification: since the spectrum of the interface height function modulates the scattering kernel, an interface

whose spectrum does not contain energy at the critical angles will not have these maxima or minima in its scattering coefficient. Furthermore, unlike scattering from planar interfaces, interface roughness produces non-specular scattering, and waves incident from any angle can scatter in the direction of the critical angle.

By assuming material contrasts across the interface are small, further approximations can be made, yielding simple equations for the scattering coefficients in which $\frac{\Delta\alpha}{\alpha}$, $\frac{\Delta\beta}{\beta}$, and $\frac{\Delta\rho}{\rho}$ appear as scaling factors for three new kernels which describe the scattering contributions of each of the material contrasts. When the source is a normally incident plane wave, these coefficients have an even more compact form than planar interface scattering coefficients. From these simple forms it is seen that the scattered field wavelet is the time derivative of the source field wavelet. Scattering coefficients and seismograms for normally incident waves were used to illustrate the relative contributions of the separate material contrasts on the scattered wavefield. Scattering coefficients for obliquely incident waves show that the scattered wave amplitudes, excluding the background specular field, are not necessarily maximum in the direction of specular scattering.

In the final chapter, I presented seismic data from an SH wave vertical seismic profile experiment which contains evidence of rough interface scattering. The experiment was conducted at a site in the Michigan Basin generally thought to have a horizontally stratified velocity structure. If this were so, waves would only be detected on the tangential component of the gyroscopically oriented receivers. However, the observed seismograms contain SV as well as SH arrivals, and the complexity of these arrivals requires a scattering mechanism which we model as scattering from a rough interface. By generating scattering coefficients and seismograms for several rough interface models, we explored the particular scattering mechanism at work at this site. We found that synthetic seismograms generated for the rough interface scattering mechanism underestimated scattering of the incident SH wave into SV waves, but successfully modeled waveform complexity. However, since synthetic seismograms in this investigation were limited to normally incident source waves, synthetic seismograms were primarily useful for comparisons with

waveform complexity in the observed seismograms. Amplitudes could only be estimated from scattering coefficients generated for the correct incidence angle.

We have demonstrated the value of our perturbation formulation for modeling elastic wave scattering in rough interface problems. Current implementation considers only plane wave sources. Future work includes the extension of the synthetic seismogram computer program to handle point sources and multilayered models with acoustic and elastic layers. This will allow us to continue with testing of the method for more realistic models. Experimental data with which to compare the results of this theory must be obtained. Water tank models with fluid-elastic rough interfaces provide a controlled environment for such testing. This work has already begun. From such testing, the range over which RMS height and slope, incidence angles, and material contrasts can vary while maintaining acceptable solution accuracy can be experimentally determined for three-dimensional models. Such physical model experiments will also be useful for testing other promising approximate modeling techniques such as the ray-born method.

Appendix A

Finite-Difference Modeling

A.1 Introduction

The purpose of this appendix is to present an accurate and efficient implementation of the finite difference method for modeling elastic wave scattering from rough interfaces. The finite difference (FD) method is a useful tool for generating seismograms where approximate or simple solutions are not applicable. It involves replacing the space and time derivatives in the continuum elastic wave equation by their FD approximations. The resulting wave equation relates displacement values at grid points in space to displacement values at previous discrete time points. This time stepping scheme is initialized by specifying the source wave field for two consecutive time steps.

Traditional FD formulations (Alterman and Karal, 1968; Alford et al., 1974; Kelly et al., 1976) are accurate to second order in space and time, where order of accuracy refers to the asymptotic form of the error term in the approximation of derivatives. Higher-order FD formulations, such as those which use fourth-order (Vidale et al., 1985; Bayliss et al., 1986) or Fourier spatial derivative operators (Gazdag, 1981; Kosloff et al., 1984; Fornberg, 1987), permit the wavefield to be sampled more sparsely than the second order schemes but require more machine calculations per derivative evaluation. The optimum order of accuracy must strike a balance between model size and number of calculations

per derivative evaluation, while providing an acceptable level of accuracy. For serial computers this balance generally favors order four schemes. However, the small interface perturbations of our model require an unusually dense grid point spacing, putting the second-order derivative operator well within its domain of acceptable accuracy, and its short operator length makes it the most efficient scheme. Accuracy and grid point density are further improved by using a staggered mesh formulation in which horizontal and vertical displacements are represented on separate grids, each shifted by half of the grid point spacing in both coordinate directions with respect to the other (Figure A-1). The formulation is similar to the scheme of Virieux (1986), but differs from it in that we use second-order displacement-stress equations instead of first-order velocity-stress equations. This modification improves efficiency, since the final solution is desired in terms of displacement.

A.2 The Finite Difference Scheme

The wave equations for a linearly elastic, isotropic, heterogeneous medium are

$$\begin{aligned} \rho\partial_{tt}u &= \partial_x[(\lambda+2\mu)\partial_x u + \lambda\partial_z w] + \partial_z[\mu(\partial_z u + \partial_x w)] \\ \rho\partial_{tt}w &= \partial_z[(\lambda+2\mu)\partial_z w + \lambda\partial_x u] + \partial_x[\mu(\partial_z u + \partial_x w)]. \end{aligned} \tag{A.1}$$

$u(x,z,t)$ and $w(x,z,t)$ are the horizontal and vertical components of displacement, and λ, μ, and ρ are the Lamé parameters and density. The equations throughout this paper are given in their two-dimensional forms for compatibility with the numerical examples. The formal extension to three dimensions is straightforward.

To obtain an FD formulation of (A.1), each of the derivatives is replaced by a formula which depends only on the field values at grid points. Since the values of these are only known at discrete points, the derivative operation consists of the assumption of an interpolation function, followed by the exact differentiation of this function. FD derivatives are traditionally computed using Lagrange interpolation, in which the field

about a grid point is expanded in terms of a truncated Taylor series. The resulting formula is a weighted sum of neighboring grid values.

When a staggered mesh is used, derivatives are always evaluated at the midpoints of grid intervals. D^x_{2p} and D^z_{2p}, the staggered mesh derivative operators of FD order $2p$ with respect to x and z, have the form

$$D^x_{2p}f(x) = \frac{1}{\Delta x}\sum_{\nu=1}^{p} A_{p,\nu}[f(x+(\nu-\frac{1}{2})\Delta x) - f(x-(\nu-\frac{1}{2})\Delta x)] \qquad (A.2)$$

$$D^z_{2p}f(z) = \frac{1}{\Delta z}\sum_{\nu=1}^{p} A_{p,\nu}[f(x+(\nu-\frac{1}{2})\Delta x) - f(x-(\nu-\frac{1}{2})\Delta x)]. \qquad (A.3)$$

For second order spatial derivatives,

$$A_{1,1} = 1. \qquad (A.4)$$

The numerical derivative coefficients $A_{p,\nu}$ for $p > 1$ can be obtained from the differentiated Lagrange interpolation function (c.f. Abramowitz and Stegun (1972) 25.2.6). The time derivative terms $\partial_{tt}u$ and $\partial_{tt}w$ in (A.1) are approximated by second order finite differences, regardless of the spatial order of the formulation. The second order formula is

$$D^{tt}_2 f(t) = \frac{1}{(\Delta t)^2}[f(t+\Delta t) - 2f(t) + f(t-\Delta t)]. \qquad (A.5)$$

This formula may be derived from (A.2) and (A.4) by replacing x and Δx by t and Δt, and applying the resulting derivative formula twice to get the second derivative. Note that, although the formula for first derivatives involves field values between grid points, when it is applied twice only values on grid points are needed.

Substituting FD derivative operators into (A.1) and isolating the term representing the value at $t + \Delta t$ yields

$$
\begin{aligned}
u(t+\Delta t) &= 2u(t) - u(t-\Delta t) \qquad \text{(A.6)} \\
&+ \frac{(\Delta t)^2}{\rho}\left\{D^x_{2p}[(\lambda+2\mu)D^x_{2p}u(t) + \lambda D^z_{2p}w(t)] + D^z_{2p}[\mu(D^z_{2p}u(t) + D^x_{2p}w(t))]\right\} \\
w(t+\Delta t) &= 2w(t) - w(t-\Delta t) \\
&+ \frac{(\Delta t)^2}{\rho}\left\{D^z_{2p}[(\lambda+2\mu)D^z_{2p}w(t) + \lambda D^x_{2p}u(t)] + D^x_{2p}[\mu(D^z_{2p}u(t) + D^x_{2p}w(t))]\right\},
\end{aligned}
$$

where the half-order p is a value between 1 and ∞. In the limit as $p \to \infty$, these equations describe the Fourier, or pseudospectral method. In this limit, however, the summations are actually evaluated using an algorithm based on the fast Fourier transform.

Addition or multiplication of terms in (A.6) requires that they lie on the same point in space. This might appear to be a problem in a method in which the two components, u and w, are specified on separate grids, and which results in or requires values at the midpoints of grid intervals in forming derivatives. However, it was noted in deriving the form of the time derivative term that in spite of the use of grid midpoint values in the computation of first derivatives, a second derivative uses only values on grid points, and does not require the values at the midpoints of the grid intervals. Similarly, on a staggered mesh, when the spatial derivative in the z direction of a field on one grid is followed by a spatial derivative in the x direction, the results of the derivative calculation are found on points aligned with the other grid. Because the wave equation contains only pairs of spatial derivatives, it is ideally suited for the staggered mesh method.

A.3 Numerical Dispersion

Such properties of solutions to the discrete wave equation (A.6) as stability and convergence are characterized by its dispersion equation (Trefethen, 1982). The need to limit the effects of numerical dispersion constitutes the primary constraint on time and space grid step sizes. Hence, the efficiency of a scheme is controlled in large part by its dispersion equation. In this section, the dispersion equation for (A.6) in a homogeneous

medium is derived. This result is useful in defining optimum Δt and Δx for homogeneous media, and these can be used as a guide in the case of heterogeneous media.

The dispersion equation is derived by transforming (A.6) to the Fourier domain and reducing the wave equation to an eigenvalue problem relating wavenumber and frequency. Since the medium parameters are assumed constant here, the Fourier transform is performed by replacing the derivative operators in (A.6) by their transforms. This can be done by substituting a phase factor of the form $e^{i(kx+\gamma z-\omega t)}$ into (A.2), (A.3), and (A.5), the transformed derivative operators are

$$D^x_{2p}e^{ikx} = i\left\{\frac{2}{\Delta x}\sum_{\nu=1}^{p} A_{p,\nu}\sin(\frac{\nu k\Delta x}{2})\right\}e^{ikx} = i\mathcal{K}_{2p}e^{ikx} \tag{A.7}$$

$$D^z_{2p}e^{i\gamma z} = i\left\{\frac{2}{\Delta z}\sum_{\nu=1}^{p} A_{p,\nu}\sin(\frac{\nu\gamma\Delta z}{2})\right\}e^{i\gamma z} = i\Gamma_{2p}e^{i\gamma z} \tag{A.8}$$

$$D^{tt}_{2}e^{i\omega t} = -\left\{\frac{2}{\Delta t}\sin(\frac{\omega\Delta t}{2})\right\}^2 e^{i\omega t} = -(\Omega_2)^2e^{i\omega t}. \tag{A.9}$$

The terms in braces, labeled $\mathcal{K}_{2p}$, Γ_{2p} and Ω_2, are identified as FD approximations of the spatial and temporal frequencies k, γ, and ω, respectively. The Taylor series expansions of $\mathcal{K}_{2p}$ and Γ_{2p} equal k and γ to order $2p$. Replacing D^x_{2p}, D^z_{2p}, and D^{tt}_2 in (A.6) by $i\mathcal{K}_{2p}$, $i\Gamma_{2p}$, and $-(\Omega_2)^2$, the FD elastic wave equation in the Fourier domain for a homogeneous medium is

$$(\Omega_{2p})^2\begin{bmatrix} u \\ w \end{bmatrix} = \begin{bmatrix} \alpha^2(\mathcal{K}_{2p})^2+\beta^2(\Gamma_{2p})^2 & (\alpha^2-\beta^2)\mathcal{K}_{2p}\Gamma_{2p} \\ (\alpha^2-\beta^2)\mathcal{K}_{2p}\Gamma_{2p} & \alpha^2(\Gamma_{2p})^2+\beta^2(\mathcal{K}_{2p})^2 \end{bmatrix}\begin{bmatrix} u \\ w \end{bmatrix} \tag{A.10}$$

where $\alpha = \sqrt{(\lambda+2\mu)/\rho}$ and $\beta = \sqrt{\mu/\rho}$ are the compressional and shear wave speeds. This is an eigenvalue problem where the eigenvalues, $(\Omega_2)^2$, are given by

$$(\Omega_2)^2 = \begin{cases} \alpha^2((\mathcal{K}_{2p})^2+(\Gamma_{2p})^2) \\ \beta^2((\mathcal{K}_{2p})^2+(\Gamma_{2p})^2). \end{cases} \tag{A.11}$$

Compressional and shear waves are clearly decoupled in a homogeneous medium. Solving for ω,

$$\omega = \frac{2}{\Delta t}\sin^{-1}\left[\frac{v\Delta t}{2}\sqrt{(\mathcal{K}_{2p})^2 + (\Gamma_{2p})^2}\right], \tag{A.12}$$

where $v \in \{\alpha, \beta\}$. Substitution of (A.12) into the phase velocity equation $C(k,\gamma) = \omega/\sqrt{k^2+\gamma^2}$ gives the phase velocity dispersion equation, and the group velocity dispersion equation is $U(k,\gamma) = d\omega/d\sqrt{k^2+\gamma^2}$. When $\Delta x = \Delta z$, phase and group velocities are greatest for waves propagating 45 degrees to the grid axes ($k = \gamma$). The dispersion equations for this case are

$$C_{2p}(k) = \frac{\sqrt{2}v}{\Theta k\Delta x}\sin^{-1}\left[\sqrt{2}\Theta\sum_{\nu=1}^{p}A_{p,\nu}\sin(\frac{\nu k\Delta x}{2})\right] \tag{A.13}$$

$$U_{2p}(k) = \frac{v\sum_{\nu=1}^{p}\nu A_{p,\nu}\cos(\frac{\nu k\Delta x}{2})}{\sqrt{1-2\Theta^2[\sum_{\nu=1}^{p}A_{p,\nu}\sin(\frac{\nu k\Delta x}{2})]^2}}. \tag{A.14}$$

where $\Theta = v\Delta t/\Delta x$.

Stability of the FD formulation (A.6) is guaranteed when the argument of arcsine in (A.12) is less than or equal to one. Otherwise, ω is complex, resulting in the exponential growth of the solution with time. For $\Delta x = \Delta z$, the stability condition is

$$\Theta \le \Theta^c_{2p} \equiv \min\left[\frac{1}{\sqrt{2}\sum_{\nu=1}^{p}A_{p,\nu}\sin(\frac{\nu k\Delta x}{2})}\right]. \tag{A.15}$$

The stability condition and dispersion equations for a second order finite difference formulation are

$$C_2 = \frac{\sqrt{2}v}{\Theta k\Delta x}\sin^{-}1\left[\sqrt{2}\Theta\sin(\frac{k\Delta x}{2})\right] \tag{A.16}$$

$$U_2 = \frac{v\cos(\frac{k\Delta x}{2})}{\sqrt{1-2\Theta^2\sin^2(\frac{k\Delta x}{2})}} \tag{A.17}$$

$$\Theta^c_2 = \frac{1}{\sqrt{2}}. \tag{A.18}$$

Graphical representations of velocity error due to the phase and group dispersion relations derived above are given in Figure A-2. The numerical velocity error ϵ is defined by $v_d = v_0(1 + \epsilon)$, where v_d is the numerically dispersed velocity and v_0 is the undispersed velocity.

A.4 Interface Boundary Conditions

The FD wave equation (A.6) was derived with the tacit assumption that the model parameters vary smoothly within the grid. This assumption is necessary because sharp changes in medium parameters result in infinite spatial frequency components that the FD spatial derivatives cannot resolve. It is possible to explicitly include boundary conditions in the FD formulation at each interface (Kelly et al., 1976), but this would require changes in the computer program for each rough interface model. The alternative that we employ represents interfaces by using the smooth parameter formulation (A.6), in which velocities change abruptly between the adjacent grid points across an interface. Brown (1984) has shown that the reflection and transmission coefficient errors of a smooth parameter formulation are order (1/PPW), regardless of p, where PPW is points per wavelength. Since second-order formulations require a larger number of PPW for a given dispersion error than higher-order formulations, the error in reflection and transmission coefficients is correspondingly smaller. This conclusion was verified by numerical modeling experiments.

References

Abramowitz, M., and I.A. Stegun, 1972, *Handbook of Mathematical Functions,* Dover Publications, Inc., New York, 1046 pp.

Alford, R. M., K. R. Kelly, and D. M. Boore, 1974, Accuracy of finite-difference modeling of the acoustic wave equation, *Geophysics, 39,* 834–842.

Alterman, Z. S. and F. C. Karal, 1968, Propagation of elastic waves in layered media by finite difference methods, *Bull. Seism. Soc. Am, 58,* 367–398.

Bayliss, A., K. E. Jordan, J. LeMesurier, and E. Turkel, 1986, A fourth-order accurate finite-difference scheme for the computation of elastic waves, *Bull. Seism. Soc. Am., 76,* 1115–1132.

Brown, D. L., 1984, A note on the numerical solution of the wave equation with piecewise smooth coefficients, *Math. Comp., 42,* 369–391.

Fornberg, B., 1987, The pseudo-spectral method: Comparisons with finite differences for the elastic wave equation, *Geophysics, 52,* 483–501.

Gazdag, J., 1981, Modeling of the acoustic wave equation with transform methods, *Geophysics, 46,* 854–859.

Kelly, K. R., R. W. Ward, S. Treitel, and R. M. Alford, 1976, Synthetic seismograms: A finite-difference approach, *Geophysics, 41,* 2–27.

Kosloff, D., M. Reshef, and D. Loewenthal, 1984, Elastic wave calculations by the Fourier method, *Bull. Seism. Soc. Am., 74,* 875–891.

Trefethen, L. N., 1982, Group velocity in finite difference schemes, *SIAM Review, 24,* 113–136.

Vichnevetsky, R. and B. Peiffer, 1975, Error waves in finite element and finite difference methods for hyperbolic equations, in *Advances in Computer Methods for Partial Differential Equations,* edited by R. Vichnevetsky, pp. 53–58, A.I.C.A.

Vidale, J., D. V. Helmberger, and R. W. Clayton, 1985, Finite-difference seismograms for SH waves, *Bull. Seism. Soc. Am., 75,* 1765–1782.

Virieux, J., 1986, P-SV wave propagation in heterogeneous media: velocity-stress finite-difference method, *Geophysics, 51,* 889–901.

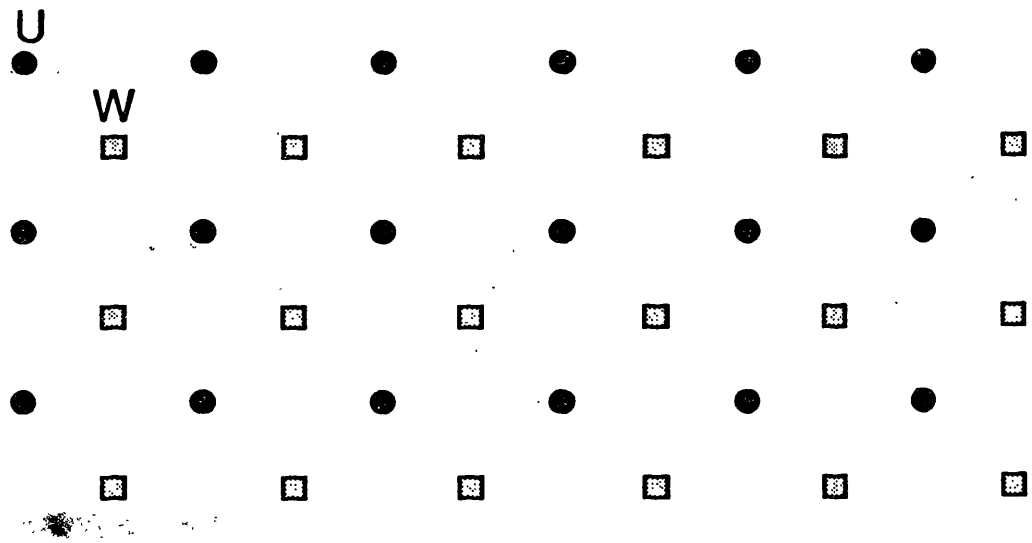

Figure A-1: Illustration of the staggered mesh on which the finite difference formulation is based.

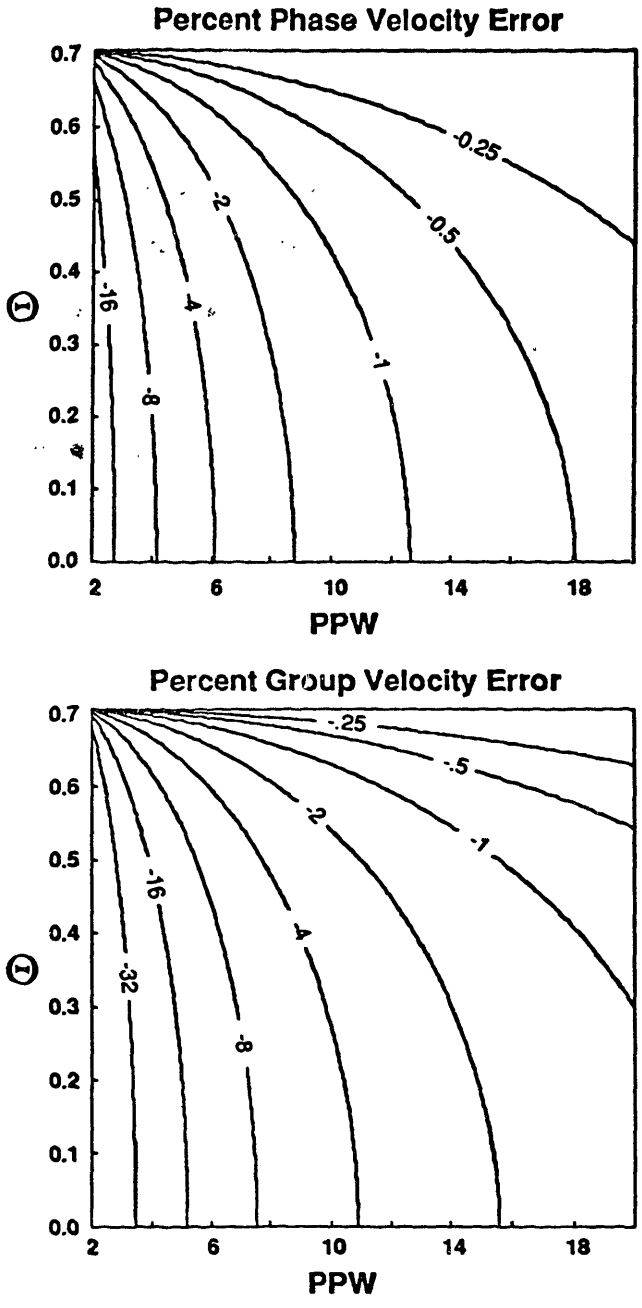

Figure A-2: Percent phase and group velocity dispersion plotted against grid points per wavelength (PPW) and $\Theta \equiv v\Delta t/\Delta x$.